Properties of Chiral Self-Assembled Monolayers at the Solid–Liquid Interface Investigated by FT-IR ATR Spectroscopy

---

Thèse présentée à la Faculté des Sciences

Institut de Microtechnique

Université de Neuchâtel

Par

Marco Bieri

Acceptée sur proposition du jury:

Prof. T. Bürgi, directeur de thèse

Prof. F. Stoeckli, rapporteur

Prof. U. P. Fringeli, rapporteur

Soutenue le 2 février 2007

Université de Neuchâtel

2007

Properties of Chiral Self-Assembled Monolayers at the Solid–Liquid Interface Investigated by FT-IR ATR Spectroscopy

---

Thèse présentée à la Faculté des Sciences

Institut de Microtechnique

Université de Neuchâtel

Par

Marco Bieri

Acceptée sur proposition du jury:

Prof. T. Bürgi, directeur de thèse

Prof. F. Stoeckli, rapporteur

Prof. U. P. Fringeli, rapporteur

Soutenue le 2 février 2007

Université de Neuchâtel

2007

Université de Neuchâtel

FACULTE DES SCIENCES
Secrétariat-Décanat de la faculté
- Rue Emile-Argand 11
- CP 158
- CH-2009 Neuchâtel

IMPRIMATUR POUR LA THESE

Properties of Chiral Self-Assembled Monolayers at the Solid-Liquid Interface Investigated by FT-IR ATR Spectroscopy

Marco BIERI

UNIVERSITE DE NEUCHATEL

FACULTE DES SCIENCES

La Faculté des sciences de l'Université de Neuchâtel,
sur le rapport des membres du jury

MM. T. Bürgi (directeur de thèse),
F. Stöckli
et U.P. Fringeli (Vienne, A)

autorise l'impression de la présente thèse.

Neuchâtel, le 9 février 2007

Le doyen :
T. Ward

■ Téléphone : +41 32 718 21 00 ■ Fax : +41 32 718 21 03 ■ E-mail : secretariat.sciences@unine.ch ■ www.unine.ch/sciences

How on earth are you ever going to explain in terms of chemistry and physics so important a biological phenomenon as first love?

Albert Einstein (1879–1955)

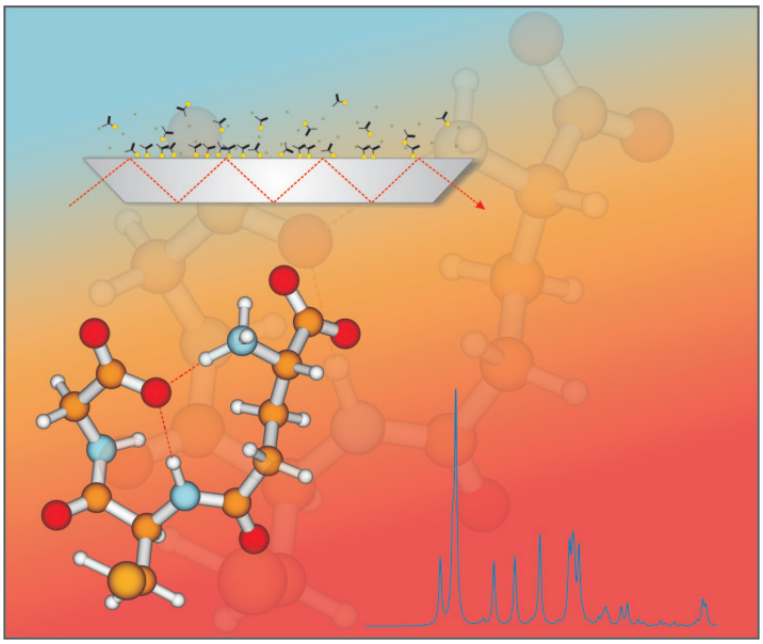

Previous page:

Front cover picture of Phys. Chem. Chem. Phys. volume 8(4), 2006.
The related article is found in Part II, Chapter 2 on page 45.

Table of Contents

List of Figures

List of Tables

List of Abbreviations

AFM	Atomic Force Microscopy
ATR-IR	Attenuated Total Reflection Infrared
BOMD	Born–Oppenheimer Molecular Dynamics
BVD	Butterworth–Van Dyke
DFT	Density Functional Theory
FEM	Finite Element Method
FT-IR	Fourier Transform Infrared
HF	Hartree–Fock (Method)
HK	Hohenberg–Kohn (Theorem)
IRE	Internal Reflection Element
KS	Kohn–Sham (Equations)
MES	Modulation Excitation Spectroscopy
PCM	Polarizable Continuum Model
PEM	Photoelastic Modulator
PM-IRRAS	Polarization-Modulation Infrared Reflection-Absorption Spectroscopy
PSD	Phase-Sensitive Detection
QCM	Quartz Crystal Microbalance
SAM	Self-Assembled Monolayer
UHV	Ultra-High Vacuum

Chemicals

EtOH	Ethanol
GSH	Glutathione
NAC	*N*-Acetyl-cysteine
PEN	Penicillamine

Keywords

Solid–Liquid Interface, Self-Assembled Monolayer, Attenuated Total Reflection Infrared Spectroscopy, Chirality, Enantiodiscrimination

Mots Clés

Interface Solide–Liquide, Monocouche Auto-Assemblée, Spectrométrie Infrarouge à Réflexion Totale Atténuée, Chiralité, Discrimination Enantiomerique

Thesis Abstract

The main distinctive feature of modern surface science is that it deals with single crystal surfaces, which are well-defined from the viewpoint of their structure and composition. In other words, these surfaces are either clean and adsorbate-free on the atomic level, or, in the case of adsorbate-covered surfaces, contain adsorbate species added intentionally in amounts controlled also on the atomic level. Thus, surface science experiments are typically performed in ultra-high vacuum (UHV), as this is the only possible environment where such surfaces can be prepared and maintained. For these reasons, the solid–vacuum and solid–vapor interfaces still are the main areas of interest for surface studies.

However, preparation of crystal surfaces and analysis, the requirement of UHV equipment, greatly limits applications. Perhaps one of the most important applications of surfaces is found in heterogeneous catalysis. While single crystal surfaces have contributed to a fundamental understanding of reactants and intermediates in model catalytic reactions, industrial catalysis is performed on porous materials and nanoparticles, almost exclusively. In addition, structure, reactivity and composition can be different in UHV and under real conditions. This example shows a discrepancy between fundamental research and practical applications often encountered. While atomically clean surfaces analyzed under artificial measurement conditions still play an important role for fundamental understanding, it should also be the goal of modern surface science to explore the role of surfaces under realistic conditions.

Indeed, in recent years, surface science is moving to more complicated materials and to studies of the solid–liquid interface. The latter has great relevance in biological processes and technological applications, *e.g.* catalysis, lubrication and corrosion prevention. Also, the modification of surfaces by self-assembled monolayers (SAMs) is an important process taking place at the solid–liquid interface.

SAMs are ordered molecular assemblies formed by the adsorption of an active surfactant on a solid surface. Based on the constituent surfactant, a variety of SAMs with different properties and functionalities can easily be prepared with potential applications in various branches of surface technology, such as passivation, lubrication, surface engineering, development of (bio-)sensors and biocompatibility. Furthermore, SAMs are excellent model systems amenable to investigating competing surfactant–substrate and surfactant–surfactant intermolecular interactions.

Up to the present, SAMs have been mostly investigated at the solid–gas interface using *ex situ* techniques. The latter have the disadvantage that the dynamics of self-assembly or kinetics of adsorption are not sensed but only the final state of the SAM is analyzed. The main goal of this thesis is to provide insight into the formation of SAMs at the solid–liquid interface by using *in situ* experimental techniques.

Fourier-transform infrared spectroscopy (FT-IR) applied in the attenuated total internal reflection (ATR) mode was used as the prime technique to probe the self-assembly of chiral peptides or derivatives thereof from the liquid phase to gold surfaces. It is demonstrated that ATR is an excellent *in situ* analysis method that provides rich molecular-level information, such as kinetics of adsorption, structural changes and orientation of molecules within the SAM.

The insight was further broadened by using ATR in combination with modulation excitation spectroscopy (MES). The latter benefits from highlighting spectral changes due to the periodic stimulation of the sample by an external parameter. In contrast to conventional differential spectroscopy, the signal-to-noise ratio in spectra recorded by MES is significantly increased by about one order of magnitude. Furthermore, disentanglement of complex spectra and detection of overlapped or hidden signals is possible for species in the system with different kinetics. MES was used to further explore the structure of SAMs and it was shown that the latter may undergo significant reversible structural changes by periodically stimulating the molecules within the adsorbate layer.

One of the most interesting and valuable properties a chiral SAM or surface can have is its ability to discriminate between enantiomers of a chiral compound, which is crucial for heterogeneous enantioselective catalysis and chiral recognition. It is therefore desirable to develop techniques that can not only quantify enantiodiscrimination but also shed light on its origin. Such techniques should ideally provide molecular-level information and combine (surface-) sensitivity with selectivity for the chiral information, a combination of criteria that is difficult to meet simultaneously.

It is demonstrated that ATR in combination with MES is a powerful technique to meet these requirements. For the first time, enantiodiscrimination between chiral SAMs and an analyte molecule was probed and unique molecular-level insight on the origin of chiral recognition was obtained.

Additional experimental techniques used for this work were quartz crystal microbalance (QCM) and polarization-modulation infrared reflection-absorption spectroscopy (PM-IRRAS). QCM is extremely sensitive to mass uptake on the sensor surface and the technique was used to investigate adsorption kinetics and self-assembly of molecules from the liquid phase *in situ*. In addition, QCM provides information on the viscoelastic properties of SAMs which allows to detect multilayer growth. Since, in contrast to infrared spectroscopy, QCM signals are not affected by structural changes, the technique is an excellent complement to ATR. PM-IRRAS, an infrared spectroscopy method based on external reflection, was used to analyze adsorbate layers *ex situ* after hours or days of self-assembly.

Furthermore, computational methods showed themselves to be a powerful support. Density functional theory (DFT) calculations were routinely used for vibrational analysis of surfactant molecules and calculations helped to interpret experimental spectra. Specifically, on the basis of DFT, a model was proposed for the interaction between *N*-acetyl-L-cysteine and proline that makes electrostatic interactions responsible for enantiodiscrimination. Furthermore, for the analysis of orientation of adsorbed molecules a novel method relying fully on DFT was developed. Finally, a model based on finite element method (FEM) was developed and used to quantitatively assess surface reaction rates such as kinetics of adsorption and desorption, respectively, fully accounting

for mass transport of surfactant molecules from the bulk liquid phase to the surface.

This thesis is divided into five parts. Part I is intended to give an introduction on SAMs and chirality in nature (Chapter 1) and on the experimental and theoretical methods (Chapter 2) used for this work. Part II is dedicated to adsorption and self-assembly. Herein, Chapters 1 and 2 deal with L-glutathione adsorption on gold. It was shown that this tripeptide undergoes significant reversible structural changes upon acid/base stimuli (Chapter 1). Chapter 2 gives insight into structural changes within the adsorbate layer during self-assembly and addresses the kinetics of adsorption. Chapter 3 is dedicated to the adsorption and self-assembly of *N*-acetyl-L-cysteine on gold. In this study, the orientation of adsorbed molecules was assessed by simulating the surface spectrum. This novel approach relies on the transition dipole moments derived from DFT calculations. Finally, Chapter 4 deals with D-penicillamine SAMs and explains the molecule's superior properties as metal ligand.

Part III gives insight into enantiodiscrimination probed by ATR-IR MES. In Chapter 1 chiral recognition of an L-glutathione SAM toward the analyte molecule proline was investigated. By using a transport and adsorption model based on FEM it was further possible to extract the relative adsorption and desorption kinetics of the proline enantiomers on/from the L-glutathione SAM, fully accounting for mass transport of molecules within the liquid phase. A study of enantiodiscrimination between *N*-acetyl-L-cysteine and proline is given in Chapter 2 including a model based on DFT for the interaction responsible for enantiodiscrimination.

Part IV includes one chapter on the oxidation of 2-propanol over Pd/Al_2O_3 catalyst investigated by ATR-IR MES.

Finally, the appendix provides supplementary information. In Chapter A a 3D model of the ATR flow-through reactor based on FEM is presented and the calculated flow-field is discussed. Chapter B introduces the transport and adsorption model that was used to assess proline adsorption and desorption kinetics on/from the L-glutathione SAM (see Part III, Chapter 1). The simulation of surface spectra based on the calculated transition dipole moments is presented in Chapter C. This method was used to derive the orientation of *N*-acetyl-L-cysteine adsorbed on gold (see Part II, Chapter 3).

Part I

Introduction

Chapter 1

General Introduction

1.1 Self-Assembled Monolayers

The formation of monolayers by self-assembly [Ulman, 1996, 1991] of surfactant molecules at surfaces is one example of the general phenomena of self-assembly. In nature, self-assembly results in supramolecular organizations of interlocking components that provides very complex systems [Kuhn and Ulman, 1995]. Self-assembled monolayers (SAMs) offer unique opportunities to increase fundamental understanding of self-organization, structure–property relationships, and interfacial phenomena. The ability to tailor both head and tail groups of the constituent molecules makes SAMs excellent model systems for a fundamental understanding of phenomena affected by competing intermolecular, molecule–surface and molecule–solvent interactions. That SAMs are well-defined and easily prepared further makes them attractive for studies in physical chemistry, computational chemistry and statistical physics in two dimensions, and the crossover to three dimensions.

Beside the model character, the interest in the general area of self-assembly, and specifically in SAMs, stems from their perceived relevance to science and technology. In contrast to ultrathin films made by, for example, molecular beam epitaxy or chemical vapor deposition, SAMs are highly ordered and oriented and can incorporate a wide range of groups both in the chain and chain termina. Therefore, a variety of surfaces with specific interactions can be prepared under chemical control [Ulman et al., 1991]. Because of their stable and dense structure, SAMs have potential applications in corrosion prevention [Guo et al., 2006, Duda et al., 2005], passivation [Dassa et al., 2006, Ganesan et al., 2005, Thomas et al., 1993] and lubrication [Zuo et al., 2005, Zhang and Archer, 2003]. In addition, the biomimetic and biocompatible nature of SAMs makes their applications in chemical and biochemical sensing promising [Jelinek and Kolusheva, 2004, Petoral and Uvdal, 2002, Cotton et al., 1998].

For many years, SAMs of alkanethiols on gold and silver surfaces have been in the focus for studying fundamental aspects of SAM formation [Ostuni et al., 1999]. However, many applications of SAMs rely on the buildup of complex structures on top of functionalized SAMs [Schreiber, 2004]. This implies the presence of functional groups, besides the thiol, that are amenable to chemical modifications or that fulfill a desired recognition function. Among the latter, chiral recognition of surfaces has attracted considerable interest, for example in chromatography [Ahuja, 2000] and het-

erogeneous enantioselective catalysis [Murzin et al., 2005, Bürgi and Baiker, 2004]. The use of chiral surfactants for self-assembly is a straightforward way to impart chirality onto the underlying substrate surface and it was demonstrated that chiral SAMs can discriminate between enantiomers of a chiral compound [Bieri and Bürgi, 2006, 2005a].

Since this work deals exclusively with chiral SAMs, its properties and its role in chiral recognition, a brief (historic) review on chirality in nature is given in the next section. It will be shown that the origin of homochirality is still an issue of debate. Furthermore, the role of chiral systems in modern science and technology will be discussed with the focus on chiral surfaces and interfaces, which stimulates the development of more advanced and sophisticated experimental methods.

1.2 Chirality in Nature

The origin of homochirality, that is the preference of one-handed form of biological molecules has puzzled scientists since the chiral nature of molecules was discovered by Pasteur [1848] more than 150 years ago. On a molecular-level, homochirality represents an intrinsic property of the building blocks of life. Although most amino acids can exist in both left- and right-handed forms, life on earth is made of left-handed amino acids, almost exclusively. Similarly, many other biochemically vital molecules are handed: DNA is right-handed, and so are all the sugars we can use.

Several explanations have been put forward for the origin of homochirality on earth. The simplest one assumes a random excess of one-handedness, which is self-perpetuating and irreversible [Saghatelian et al., 2001]. Another model proposes chiral crystal surfaces to have played a decisive role for biochemical homochirality [Zaia, 2004, Hazen et al., 2001]. The discovery of an excess of L-amino acids in meteorites [Cronin and Pizzarello, 1997, Rubenstein et al., 1983] led to the hypothesis that a preference for L-amino acids existed in our solar system material before there was life on earth. Other models propose that the interaction between chiral molecules and circularly polarized light has led to the selective destruction of one enantiomer [Belavoine et al., 1974]. Even further models make a link between homochirality and the weak force [Garay and Ahlgren-Beckendorf, 1990], one of the four fundamental forces in nature. This force has a handedness (parity violation), which results in a very small energy difference between enantiomers. The list of models mentioned above is certainly not complete and no consensus is found among origin-of-homochirality researchers [Podlech, 2001].

As a consequence of the chiral nature of living systems, metabolic and regulatory processes mediated by biological systems are sensitive to stereochemistry and different responses can often be observed for the enantiomers of a chiral molecule interacting with such systems. Specifically, in order to develop new therapeutic drugs, the stereoselectivity of many biological processes has to be accounted for. In fact, very often only one enantiomer exhibits a specific therapeutic action, whereas the other has to be considered as ballast, contributing to side effects, displaying toxicity, or acting as antagonist [Aboul-Enein and Wainer, 1997, Caldwell, 1996, 1995, Wainer, 1993].

Figure 1.1: Chirality (Greek *handedness*) is an asymmetric property deeply inherent in nature. An object or a system, like our hands, is called chiral if it differs from its mirror image. Such objects then come in two forms, which are mirror images of each other and are non-superimposable by any symmetry operation. The picture shows a detail of Michelangelo's *The Creation of Adam*, a fresco on the ceiling of the Sistine Chapel at the Apostolic Palace in Vatican City.

In this context, thalidomide is a tragic reminder of the importance of chirality. In the early 1960s, this drug was prescribed to pregnant women suffering from morning sickness. While the left-handed form is a powerful tranquillizer, the right-handed form can disrupt fetal development, resulting in severe birth defects. Unfortunately, the synthesis of the drug produced a racemate, as would be expected, and the wrong enantiomer was not removed before the drug was marketed.

The scientific and economic relevance of chiral substances has stimulated processes that can selectively produce one enantiomer or that are able to separate enantiomers from a racemic mixture, as well as the molecular-level understanding of these methods. The importance of this field of research was underlined by the Nobel Prize in Chemistry in 2001 awarded to Knowles, Noyori and Sharpless for their work on chirally catalyzed hydrogenation and oxidation reactions.

The resolution of racemic compounds necessitates a chiral environment. For this purpose, chiral auxiliaries, catalysts or selectors have to be developed. The formation of the corresponding diastereomeric species implies an energy difference between them which finally allows enantioseparation [Atkinson, 1995]. In this context, chiral surfaces and interfaces have received considerable interest in recent years because of their application in heterogeneous enantioselective catalysis [Bürgi and Baiker, 2004, Baiker and Blaser, 1997] and their importance in separation [Ahuja, 2000] and sensing [McKendry et al., 1998, Bodenhöfer et al., 1997] of enantiomers. It has, for example, been shown that the enantiomers of glucose are electrooxidized at different rates on intrinsically chiral Pt(643) electrodes [Attard, 2001]. It has also been reported that (R)-3-methylcyclohexanone desorbs enantiospecifically from the two enantiomeric forms of the chiral Cu(643) surface [Horvath and Gellman, 2002] and that desorption occurs from the chiral kink sites [Horvath et al., 2004].

1.3 Probing Chiral Interfaces: A Real Challenge

Despite the numerous reports on enantiodiscrimination at chiral surfaces, not much molecular-level information is available on the relevant intermolecular interactions between surface (selector) and analyte molecule (selectand). This is because most of the applied experimental methods merely quantify enantiodiscrimination, or in other words, give a value for the difference in Gibbs free energy between the relevant diastereomeric complexes, without allowing direct molecular-level insight.

For example, in chromatographic methodologies, one of the most utilized techniques in enantioseparation, the separation factors are derived from different retention times [Maier et al., 2001, Francotte, 1997a,b, 1994, Dingenen and Kinkel, 1994]. Experimental methods like quartz crystal microbalance (QCM) measure enantiospecificity *via* a mass change [Nakanishi et al., 2004, Huang et al., 2003, Nakanishi et al., 2002, Paolesse et al., 2002] and optical techniques detect a change in the thickness of the adsorbed layer [Bodenhöfer et al., 1997]. Even further methods, such as atomic force microscopy (AFM), rely on force measurements between the surface and the modified probe tip [McKendry et al., 1998]. Another approach makes use of soluble model systems in order to investigate the relevant intermolecular interactions by applying bulk techniques [Maier et al., 2002].

A technique to probe enantiodiscrimination at interfaces should ideally combine (surface) sensitivity with selectivity for the chiral information. Whereas the former criterion is met by many powerful surface science tools [O'Conner et al., 2003], the latter is an attribute of chiroptical techniques like circular dichroism [Pagliari et al., 2004, Alder et al., 1973], vibrational circular dichroism [Nafie, 1997] or Raman optical activity [Hug et al., 1975]. The combination of both attributes mentioned above is a real challenge. Nonlinear optical techniques may turn out to be a powerful tool in probing chiral interfaces [Ji et al., 2006, Ji and Shen, 2006, Hicks and Petralli-Mallow, 1999].

Infrared (IR) spectroscopy is a well-established tool for the investigation of interfaces and it has been used to probe enantiospecific interactions at chiral surfaces [Horvath et al., 2004, Gellman et al., 2001]. However, conventional IR spectroscopy is non-specific. Thus the adsorption of a chiral molecule on a chiral surface may result in very similar spectra for the two enantiomers, the interesting differences being overlaid by much stronger signals due to non-specific interactions. In order to overcome these problems, attenuated total reflection infrared ATR [Harrick, 1967] was recently combined with modulation excitation spectroscopy, MES [Bürgi and Baiker, 2002, Baurecht and Fringeli, 2001]. MES selectively highlights the periodically changing signals stimulated by an external parameter. For example, by periodically changing the absolute configuration of the analyte molecule (selectand) enantiospecific interactions can be spotted, as was demonstrated for interactions taking place at chiral stationary phases [Wirz et al., 2004, 2003] and chiral SAMs [Bieri and Bürgi, 2006, 2005a, see Part III].

Chapter 2

Experimental and Theoretical Methods

2.1 Attenuated Total Reflection Infrared Spectroscopy

2.1.1 The Principle of Total Internal Reflection

A beam propagation in an optically dense medium with refractive index n_1 undergoes total reflection at the interface of an optically rare medium (n_2) when the angle of incidence exceeds the critical angle θ_c (see Figure 2.1 on the next page).

Newton's experiments showed [Newton, 1952], and it follows from Maxwell's equations [Born and Wolf, 1979], that an electromagnetic wave propagates through the optical interface and generates an evanescent field in the rare medium. The amplitude of the evanescent electric field falls off exponentially with distance z from the surface, *i.e.*

$$E = E_0 \, e^{-z/d_\mathrm{p}} \tag{2.1}$$

The depth of penetration d_p, defined as the distance required for the electric field amplitude to fall to e^{-1} of its value at the surface is given by

$$d_\mathrm{p} = \frac{\lambda_1}{2\pi\sqrt{\left(\sin^2\theta - n_{21}^2\right)}} \tag{2.2}$$

where $\lambda_1 = \lambda \, n_1^{-1}$ is the wavelength in the denser medium and $n_{21} = n_2 \, n_1^{-1}$ is the ratio of the refractive indices of the rarer and denser medium. It is important to note that the depth of penetration depends on the optical constants of the interface, the angle of incidence θ and also on the wavelength λ of the electric field. In the infrared d_p is about one micron.

2.1.2 Attenuated Total Reflection Spectroscopy

In 1967 Harrick [Harrick, 1967] showed that the principle of total internal reflection can be used for spectroscopy. If the rare medium (n_2) is absorbing, the evanescent electric field will be attenuated due to absorption and less intensity is reflected, resulting in an *attenuated* total reflection (ATR).

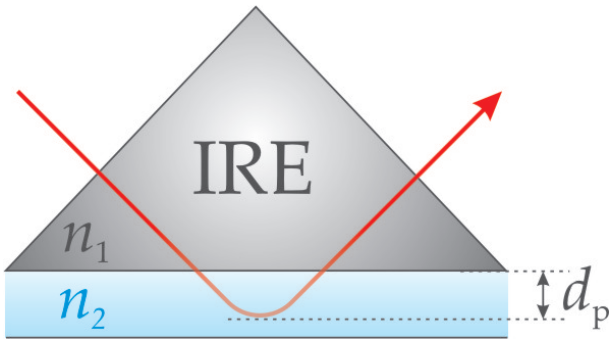

Figure 2.1: Schematic representation of path of a ray of light for total internal reflection. The internally reflected light propagates within the internal reflection element (IRE, n_1) and penetrates a fraction of wavelength (d_p) beyond the reflecting surface into the rare medium (n_2).

A schematic representation of the basic ATR-IR experimental setup is given in Figure 2.2. A beam emitted from a light source (left side) is coupled into a so-called internal reflection element (IRE, n_1). For the IR, materials like ZnSe ($n_1 = 2.3$), Si ($n_1 = 3.4$) and Ge ($n_1 = 4.0$) are commonly used as IREs. On the way to the detector the IR beam is undergoing multiple internal reflections (typically about 30) which significantly increase the signal-to-noise ratio. At each total internal reflection an evanescent field is being formed which is schematically indicated in the figure. Due to the evanescent nature of the field only a small volume is being probed at the interface, which makes the ATR-IR technique surface sensitive and a powerful tool for the investigation of solid–liquid interfaces [Bürgi and Baiker, 2006].

ATR-IR was used as the main experimental method in this work to investigate *in situ* the self-assembly of L-glutathione, *N*-acetyl-L-cysteine and D-penicillamine on gold. The technique yielded molecular-level insight into the kinetics of adsorption, the (average) orientation of molecules within the monolayer and structural changes during self-assembly. Results and discussion of these investigations are presented in Part II.

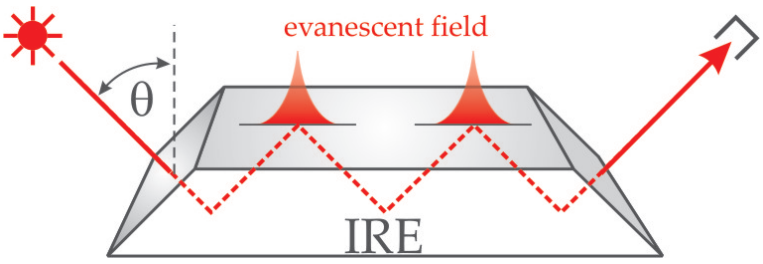

Figure 2.2: A beam, emitted from a source depicted on the left, is coupled into an IRE and undergoes multiple internal reflections until it is focused on a detector (depicted on the right). At each total internal reflection an evanescent electric field is being formed that penetrates into the rare medium. The depth of penetration depends on the optical constants of the interface, the wavelength of radiation and the angle of incidence.

2.2 Modulation Excitation Spectroscopy

2.2.1 Introduction

Conventional IR spectroscopy is non-specific. All species that are probed by the IR beam and that have IR active vibrations will give rise to signals in the spectrum, whether the species are involved or not in the process under investigation. A conventional approach to partly overcome this problem is difference spectroscopy [Mäntele, 1996]. However, in order to further extract important information, *e.g.* the kinetics of surface reactions, more sophisticated techniques such as time-dependent stimulation may be applied, provided that the system under observation responds to an external parameter, *e.g.* concentration of reactive species, pH, temperature, and so on. Practically, there are two methods for external stimulation: the relaxation technique or parameter jump [Strehlow and Knoche, 1977] and the modulation technique or parameter modulation [Fringeli et al., 2000]. A prerequisite of the latter technique is a reversible system response to a periodic stimulation.

Figure 2.3 shows the principle of modulation excitation spectroscopy (MES). The sample is periodically stimulated by an external parameter at the stimulation frequency ω (the stimulation is represented as a green sinusoidal line). The periodic system response (reversibility provided) due to the stimulation is shown as red line in the figure.

2.2.2 The Theory of Phase-Sensitive Detection

If a system is disturbed periodically by an external parameter, all the species in the system addressed by the stimulation will also change periodically at the same frequency as the stimulation or harmonics thereof [Baurecht and Fringeli, 2001]. As is indicated in Figure 2.3, there may be a phase lag ϕ between the stimulation and system response. A phase lag is observed when the time constant of a process giving rise to a signal is on the same order as the time constant $T = 2\pi\,\omega^{-1}$ of the stimulation. After

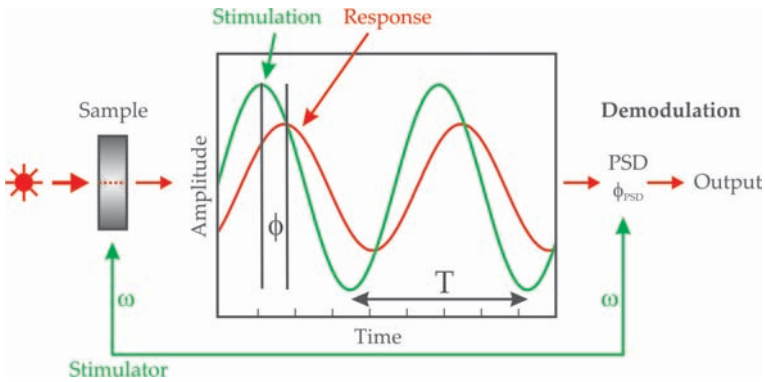

Figure 2.3: Schematic representation of the modulation excitation spectroscopy (MES) principle. The system (sample) is periodically stimulated at frequency ω by an external parameter of interest (like *e.g.* temperature, pH, concentration, absolute configuration, and so on...). The periodic sample response is sensed by IR spectroscopy and may exhibit frequency-dependent amplitude and phase lag ϕ. Selective detection of the periodic sample responses due to the stimulation is performed by phase-sensitive detection (PSD). See text for more details.

reaching a new quasi-stationary state at the beginning of the modulation, the system is oscillating at frequency ω around this state. The resulting absorbance variations $A(\tilde{\nu}, t)$ are followed by measuring spectra at different times during the modulation period T. The set of time-resolved spectra $A(\tilde{\nu}, t)$ is then transformed by means of a digital phase-sensitive detection (PSD), according to Equation 2.3, to a set of phase-resolved spectra.

$$A_k^{\phi_k^{\mathrm{PSD}}}(\tilde{\nu}) = \frac{2}{T}\int_0^T A(\tilde{\nu}, t)\ \sin(k\omega t + \phi_k^{\mathrm{PSD}})\,\mathrm{d}t \tag{2.3}$$

where $k = 1, 2, 3, \ldots$ determines the demodulation frequency, *i.e.* fundamental, first harmonic, and so on, T is the modulation period, $\tilde{\nu}$ denotes the wavenumber, ω the stimulation frequency and ϕ_k^{PSD} the demodulation phase angle. With a set of time-resolved spectra, Equation 2.3 can be evaluated for different phase angles ϕ_k^{PSD} resulting in a series of phase-resolved spectra $A_k^{\phi_k\mathrm{PSD}}$. Equation 2.3 is closely related to a Fourier analysis [Fourier, 1878]. According to the Fourier theorem every periodic function $f(t)$ can be expressed as a Fourier series in the form

$$f(t) = a_0 + \sum_{k=1}^{\infty} a_k\ \cos(k\omega t)\ + \sum_{k=1}^{\infty} b_k\ \sin(k\omega t) \tag{2.4}$$

where a_k and b_k, respectively, are the orthogonal cosine and sine Fourier coefficients, respectively, and the integer k is the frequency multiplier, *i.e.* fundamental, first harmonic, and so on. Now the Fourier series represented by Equation 2.4 can also be expressed as a sine series with an additional phase angle ϕ_k according to

$$f(t) = a_0\ +\ \sum_{k=1}^{\infty} c_k\ \sin(k\omega t + \phi_k) \tag{2.5}$$

with $c_k = \sqrt{a_k^2\ +\ b_k^2}$ and $\tan\phi_k = a_k\, b_k^{-1}$. The Fourier coefficients of the periodic function described by Equation 2.5 are given by

$$a_0 = \frac{1}{T}\int_0^T f(t)\,\mathrm{d}t \tag{2.6}$$

$$c_k = \frac{2}{T}\int_0^T f(t)\ \sin(k\omega t + \phi_k)\,\mathrm{d}t \tag{2.7}$$

By replacing $f(t)$ with $A(\tilde{\nu}, t)$ and ϕ_k with ϕ_k^{PSD} Equation 2.7 yields the demodulation transformation given in Equation 2.3. In other words, a demodulated spectrum represents the Fourier coefficient of the time varying signal $A(\tilde{\nu}, t)$ for a given frequency (usually fundamental, $k = 1$) and a given user defined phase lag ϕ_k^{PSD}.

This theoretical section is concluded by stating the main benefits of MES. The signals arising in demodulated spectra are exclusively related to the stimulation of the external parameter, *i.e.* MES selectively highlights the species that are affected by the external parameter. Furthermore, demodulated spectra are of much higher quality with a better signal-to-noise ratio (about one order of magnitude compared

to conventional time-resolved spectra). The kinetic information of the investigated system is contained in the frequency dependent amplitude of the response and the phase lag between stimulation and response (see Figure 2.3 on page 9). Consequently, species with different kinetics can be separated by setting the demodulation phase angle ϕ_k^{PSD} accordingly. An excellent and exhaustive quantitative discussion of MES is found in Baurecht and Fringeli [2001] and more information is given elsewhere [Urakawa et al., 2006b,c,a, Bürgi and Baiker, 2002, Fringeli et al., 2000].

2.2.3 Applications of Modulation Excitation Spectroscopy

In order to use the benefits of MES for ATR-IR, a special home-built flow-through cell was designed [Urakawa et al., 2003].

Figure 2.4 shows the basic experimental setup for ATR-IR in combination with MES. The flow-through reactor has two inlet tubes leading to the interior of the cell and coinciding directly above the surface of the IRE. Each of the two inlet tubes is connected through a Teflon valve with a bubble tank, containing the appropriate solution. By means of a peristaltic pump, situated behind the cell, each of the solutions can be introduced and continuous flow over the IRE surface is established. Typical stimulation experiments are modulations of temperature [Baurecht et al., 2002, Müller et al., 1996], pressure, electric field, light flux [Müller et al., 1996], concentration [Bürgi and Baiker, 2002] and pH [Bieri and Bürgi, 2005b, Fringeli et al., 2000].

In order to probe chiral interfaces and enantiodiscrimination, absolute configuration modulation was applied [Bieri and Bürgi, 2006, 2005a, Wirz et al., 2004, 2003], which consists of periodically flowing the two enantiomers of the chiral probe molecule (separately stored in bubble tanks I and II, see Figure 2.4) over the chiral interface. This approach has the advantage that signals due to unspecific interactions, *i.e.* inter-

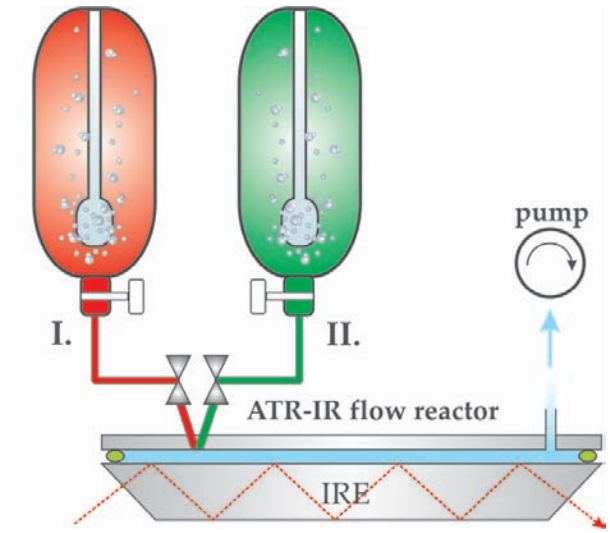

Figure 2.4: Flow-through cell specially designed for MES. The cell has two inlet tubes leading to the interior of the cell and coinciding directly above the surface of the IRE. Each of the two inlet tubes is connected through a Teflon valve with a bubble tank, containing the appropriate solution. By means of a peristaltic pump, situated behind the cell, each of the solutions can be introduced and continuous flow over the IRE surface is established.

actions with achiral sites, are efficiently suppressed. The latter may completely hide the relevant spectral features arising from enantiodiscriminating interactions. Results and discussion of enantiodiscrimination probed by ATR-IR MES is presented in Part III.

2.3 Quartz Crystal Microbalance

2.3.1 The Quartz Crystal Resonator

A quartz crystal microbalance (QCM) resonator is commonly configured with electrodes on both sides of a thin disk of AT-cut quartz (Figure 2.5). Due to the piezoelectric properties and crystalline orientation of the quartz, the application of a voltage between these results in a shear deformation of the crystal. The quartz crystal typically resonates at resonant frequency that is determined by the crystal thickness.

The Butterworth–Van Dyke, BVD [Henderson, 1992] equivalent electric circuit model (see Figure 2.6 on the facing page) is often used to represent the electrical behavior of an unperturbed crystal resonator near series resonance. The model has also been successful in predicting the frequency shifts and losses of an AT-cut quartz crystal in QCM applications.

The BVD electrical model consists of two arms. The motional arm has three components:

1. L_{m} (inductor) corresponds to the inertial component of the oscillation, which is related to the mass displaced during the vibration.

2. C_{m} (capacitor) corresponds to the stored energy in the oscillation and is related to the elasticity of the quartz and the surrounding medium.

3. R_{m} (resistor) corresponds to the dissipation of the oscillation energy from mounting structures and from the medium in contact with the crystal (*i.e.* losses induced *via* viscous coupling to a liquid).

Figure 2.5: AT-cut 1 in. standard QCM sensor crystals. The surface is a chrome/gold composite with an optically clear finish (about 50 nm average surface roughness). The crystal on the left shows the contact surface while the one on the right shows the sensor surface in contact with a gas or liquid.

Figure 2.6: Butterworth–Van Dyke equivalent electric circuit model for the unperturbed quartz crystal microbalance. A static capacitance C_0 is in parallel with a motional arm; L_m, C_m, R_m.

Sauerbrey [1959] was the first to recognize the potential usefulness of a quartz crystal resonator and demonstrated the extremely sensitive nature of these devices towards mass changes at the surface of quartz electrodes. The results of his pioneering work are embodied in the Sauerbrey equation, which relates the mass change per unit area at the QCM electrode surface to the observed change in oscillation frequency of the crystal:

$$\Delta f = -c_f \cdot \Delta m, \quad \text{with} \tag{2.8}$$

$$c_f = \frac{2 f_0^2}{\sqrt{\rho_\mathrm{Q} \mu_\mathrm{Q}}} \tag{2.9}$$

In Equation 2.8, Δf is the observed frequency shift and Δm the change in mass per unit area. The mass sensitivity constant c_f defined by 2.9 is a property of the crystal where f_0 denotes the series resonant frequency, ρ_Q the density and μ_Q the shear modulus of quartz, respectively. For example, c_f is 17.7 ng cm^{-2} for a 5 MHz AT-cut crystal.

It has to be emphasized that Equation 2.8 with the linear relationship between the observed frequency shift and the mass uptake of the sensor surface due to adsorption is only strictly applicable to uniform and rigid thin-film deposits [Buttry, 1991].

2.3.2 Liquid Contact Measurements

For many years it was believed that excessive viscous loading would prohibit the use of the QCM in liquids. However, it was shown by Nomura and Okuhara [1982] that operation in liquids is indeed possible, and that the response of the QCM is still extremely sensitive to mass changes at the crystal–liquid interface.

When the QCM comes in contact with a liquid there is a decrease in resonant frequency that is dependent upon the viscosity and the density of the liquid. A quantitative understanding of the resonator behavior is a prerequisite for proper interpretation of experimental results of liquid contact measurements. A physical model

introduced by Kanazawa and Gordon II [1985] treats the quartz as a totally lossless elastic solid and the liquid as a purely viscous medium. The frequency shift arises from coupling the oscillation of the crystal, involving a standing shear wave, with a damped propagated shear wave in the liquid (Figure 2.7). In this model, the frequency shift due to viscous coupling is given by

$$\Delta f_{\text{visc}} = -f_0^{3/2} \sqrt{\frac{\rho_{\text{L}} \eta_{\text{L}}}{\pi \rho_{\text{Q}} \mu_{\text{Q}}}} \tag{2.10}$$

where ρ_{L} and η_{L} denote the density and viscosity of the liquid in contact with the QCM crystal surface. The expression assumes a continuity of displacement at the interface, continuity of shear stresses at the interface, a perfectly insulating liquid contacting the surface and an ideally smooth surface.

In liquid contact measurements, the resonant frequency is obviously affected by both mass uptake (Equation 2.8 on the previous page) and liquid loading (Equation 2.10) and measurement of the resonant frequency alone cannot distinguish changes in surface mass and solution properties. As a consequence, measurement of shifts in series resistance ΔR (recall the meaning of R_{m} in the BVD model in Section 2.3.1 on page 12) are used as independent indicators of viscous loading at the crystal–liquid interface. Viscous coupling of the liquid medium to the oscillating crystal surface results not only in a decrease in resonant frequency Δf but *also* in damping of the resonant oscillation—the viscous loss is manifested as shift in series resistance ΔR. Thus, Δf and ΔR measurements both serve as indicators of mass loading and viscosity at the crystal–liquid interface of the QCM resonator during chemical and electrochemical depositions in solution [Martin et al., 1997].

As an example related to this work, the self-assembly of molecules at the crystal–liquid surface typically results in frequency shifts in the order of some Hz and shifts in series resistance are usually not manifested (provided that small bulk concentrations,

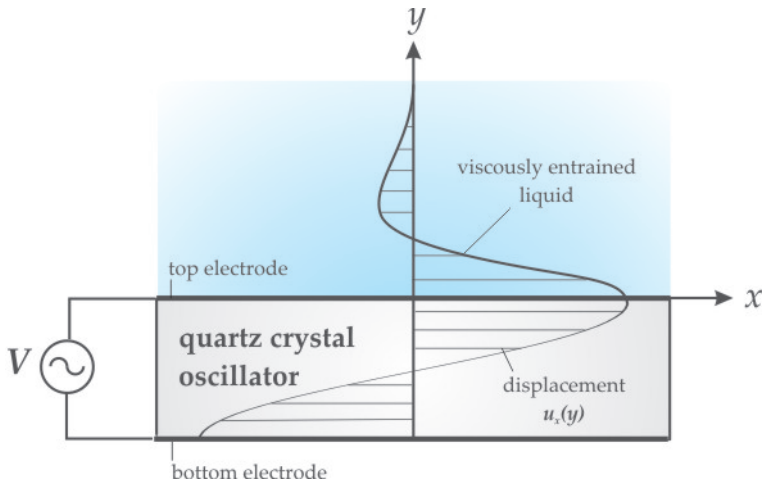

Figure 2.7: Cross-sectional view of a smooth QCM resonator with the upper surface in contact with a liquid. The shear displacement (shown at maximum displacement) generates laminar flow in the contacting liquid.

typically < 1 mM, are used and that the crystal was previously in contact with the liquid for baseline stabilization). This indicates that SAMs define rigid films in contact with the crystal surface (see Part II, Chapters 2, 3 and 4).

2.3.3 Experimental Setup for Liquid Contact Measurements

For liquid contact measurements the QCM is operated with an axial flow cell (Stanford Research Systems) providing high sensitivity and well defined flow conditions. In the axial flow cell with a volume of about 150 μL the sample flows radially outward from the input port at the center of the cell to the exit channel at the edge of the cell (see QCM flow cell in Figure 2.8 on the following page). The sample solution is injected perpendicularly with respect to the flat surface of the QCM crystal which results in a stagnating flow field [Dabros and van de Ven, 1987, 1983] at the center of the crystal surface.

In order to implement the lowest noise flow setup, the system fully relies on gravity and is operated in open flow mode (Siphon principle). Small flow rates $< 0.1\,\mathrm{mL\,s^{-1}}$ are commonly used. In the present configuration up to six sample solutions can be stored in separate tanks and injected into the axial flow cell *via* a 6-way selection valve (Upchurch Scientific). However, only two tanks are typically used for investigations of SAMs.

In liquid contact measurements, the dominant source of error in frequency drift originates from the temperature dependence of the viscosity of the liquid. For example, the series resonant frequency of a 5 MHz AT-cut crystal in water will increase by about 8 Hz/°C. In order to minimize thermal fluctuations, the QCM is operated in a temperature controlled room and with a thermal shielding protecting the axial flow cell (see Figure 2.8 on the next page).

2.4 Polarization-Modulation Infrared Reflection-Absorption Spectroscopy

2.4.1 Introduction

In the 1960s [Greenler, 1966, Francis and Ellison, 1959], infrared reflection-absorption spectroscopy, often noted as IRRAS, IRAS or RAIRS, has been recognized as one of the most surface-sensitive methods for the investigation of surface structures, chemical states of adsorbates, and their interactions [Hayden, 1987]. The technique further benefits from the so-called surface selection rule [Pearce and Sheppard, 1976] which provides information about the orientation of adsorbed species on a surface (see also Appendix, Section C.2 on page 133). However, conventional IRRA spectroscopy has the disadvantage that bulk species (here *bulk* is defined as the phase where light is radiated from and reflected out at the interface) give rise to large background signals which interfere with information from surface species. Therefore, IRRAS is conveniently applied under ultra-high vacuum (UHV) conditions.

The IRRAS technique was significantly advanced by the use of a photoelastic modulator, PEM [Hipps and Crosby, 1979]. The main advantage of polarization-modulation infrared reflection-absorption spectroscopy (PM-IRRAS) is the compensation of bulk phase absorption. This allows measurements under ambient conditions.

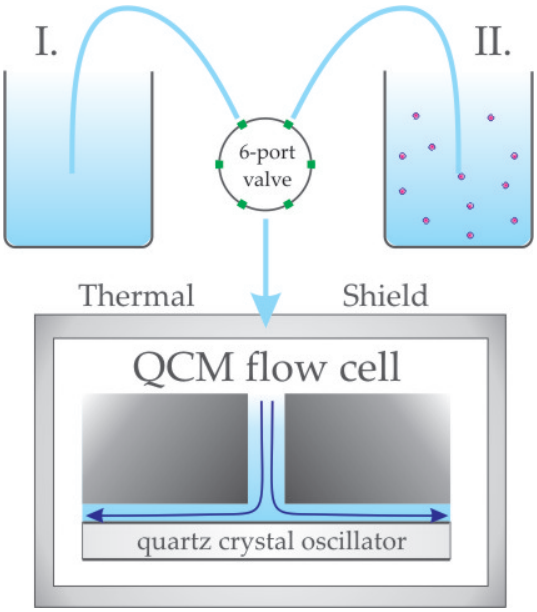

Figure 2.8: Experimental setup for QCM liquid contact measurements. In the present configuration up to six sample solutions can be stored in separate tanks and injected into the axial flow cell *via* a 6-way selection valve. As shown, two tanks are typically used for the investigation of SAMs (tank I. contains solvent and II. the surfactant solution). In order to minimize thermal fluctuations, the QCM flow cell is protected by a thermal shielding. Note that the sample solution flows radially outward from the input port at the center of the cell to the exit channel at the edge of the cell.

Surface-sensitivity is further enhanced and a surface spectrum can be measured within a short time compared to conventional IRRAS. PM-IRRAS allows the investigation of surface structures and species residing at the solid–gas [Goodman, 2003, Barner et al., 1991, Green et al., 1991], liquid–gas [Islam and Kato, 2004, Blaudez et al., 1993] and even solid–liquid interfaces [Zamlynny et al., 2003, Kunimatsu et al., 1985, Seki et al., 1985]. Most recently, the technique was combined with modulation excitation (see Section 2.2 on page 9) to monitor *in situ* surface and gas species and surface properties [Urakawa et al., 2006b,c,a].

2.4.2 The Principle of PM-IRRAS

Unpolarized light can mathematically be separated into two orthogonal components of the electric field, the *p*- and *s*-polarizations. In case of *p*-polarization, the electric field vector is oscillating parallel to the plane of incidence (see Figure 2.9 on the facing page, top). Similarly, the *s*-polarized light has the oscillation of the electric field perpendicular to the plane of incidence.

When a light beam is reflected from a surface, a phase shift occurs between the incident and reflected light which depends on the polarization. According to the Fresnel equations [McIntyre and Aspnes, 1971], the phase shift is about 180° for all angles of incidence ϕ when *s*-polarized light is reflected off a metallic surface. As a consequence, destructive interference occurs and there is no net electric field near the surface (Figure 2.9, bottom). In contrast, little phase shift occurs for the parallel component, *p*, except under extremely grazing conditions ($\phi > 80°$). As a result, there

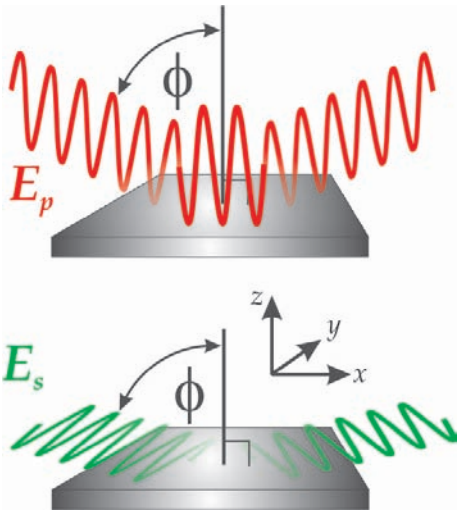

Figure 2.9: The principle of polarization-modulation infrared reflection-absorption spectroscopy (PM-IRRAS). A photoelastic modulator (PEM) modulates the electric field between *p*- and *s*-polarization. When a light beam is reflected from a metallic surface, the *p*-polarized component is enhanced near the surface (top picture). The *s*- component, on the other hand suffers destructive interference and there is no net field near the surface (bottom). For external reflection measurements angles near grazing incidence (typically between 80 and 85°) are used due to the large *z*-component of the electric field at the surface.

is an enhancement of the electric field for *p*-polarization near the metallic surface which is maximized near grazing angle due to the large *z*-component of the electric field.

PM-IRRAS uses both *p*- and *s*-polarizations. A PEM alternately generates the two polarizations at high frequencies, typically between about 50 and 100 kHz and the reflectivities are detected for both polarizations (R_p and R_s, where $R_{p,s} \propto |E_{p,s}|^2$). A PM-IRRAS spectrum is then, in principle, measured by taking the ratio of ΔR and R according to

$$\frac{\Delta R}{R} = \frac{|R_p - R_s|}{R_p + R_s} \tag{2.11}$$

where $\Delta R = |R_p - R_s|$ is the reflectivity difference of the *p*- and *s*-component and $R = R_p + R_s$ the sum of the reflectivities. Clearly, the difference ΔR between the reflectivities yields the surface species information and the ratio between the difference and sum reflectivity $\Delta R\, R^{-1}$ is used to compensate the bulk phase absorbance, hence yielding a PM-IRRA surface spectrum. In reality, the polarization modulation introduced by the PEM, optical components located in the setup and sensitivity enhancement by the lock-in amplifier result in more complicated differential and sum spectra which is given by the following expression [Buffeteau et al., 2000, 1991]

$$\frac{\Delta R}{R} = \frac{g \cdot |(\gamma R_p - R_s) \cdot J_2(\phi_0)|}{(\gamma R_p + R_s) \pm (\gamma R_p - R_s) \cdot J_0(\phi_0)} \tag{2.12}$$

where g is a constant accounting for different gain and filtering during the two-channel electronic processing; $\gamma = C_p\, C_s^{-1}$ is a factor taking the polarization effects by the optoelectronic components into account, where C_p and C_s are different overall responses

of the optoelectronic setup for the p- and s-polarizations; and $J_0(\phi_0)$ and $J_2(\phi_0)$ are zero- and second-order Bessel functions of the maximum dephasing ϕ_0 introduced by the PEM. The plus and minus signs in the equation correspond to cases where p- and s-polarization is used before the PEM, respectively.

In this work, PM-IRRAS was used complementarily to ATR-IR for analyzing the structure of SAMs *ex situ*. After immersion of the substrate in the surfactant solution, the sample was dried and measured under ambient conditions. Beside different measurement condition compared to ATR-IR, the main advantage of *ex situ* PM-IRRAS is the analysis of SAMs after several hours or days of self-assembly. In ATR-IR long-term analysis is often hampered by incomplete background compensation, which results in a contamination of interesting signals. Studies of PM-IRRAS are found in Part II, Chapters 1 and 3.

2.5 Density Functional Theory

Traditional methods in electronic structure theory, in particular Hartree–Fock (HF) theory and its descendants [Szabo and Ostlund, 1996], are based on the complicated many-electron wave function. In order to obtain all information that can be known about a molecular system such as the energy and the molecular properties, one has to solve the non-relativistic, time-independent Schrödinger equation [Schrödinger, 1926] within the Born–Oppenheimer approximation [Born and Oppenheimer, 1927] which assumes that the motions of electrons and nuclei can be treated separately:

$$\hat{H}\psi = E\psi \tag{2.13}$$

where ψ is the electronic wave function and $\hat{H}$ is the electronic Hamiltonian of the form

$$\hat{H} = \hat{T} + \hat{V}_{Ne} + \hat{V}_{ee} \tag{2.14}$$

The purely electronic Hamiltonian (2.14) is the sum of electron kinetic energy terms, electron–nuclear attractions, and electron–electron repulsions. The calculation of the many-body wave function of a system of interacting electrons is a formidable task which can only be carried out for systems with a few tens of electrons and is meaningful only for such systems [Kohn, 1999].

2.5.1 The Hohenberg–Kohn Theorem

Since the electron–electron interaction is known (Coulomb potential), the Hamilton operator of a quantum-mechanical many-electron system is completely determined once the external potential $v_{\text{ext}}(\boldsymbol{r})$ is specified in which the electrons move. From a very fundamental point of view the problem is therefore solved, leaving only the "technical detail" of actually computing the solution of the Schrödinger equation. The theorem of Hohenberg and Kohn, HK [Hohenberg and Kohn, 1964], which is the foundation of density functional theory (DFT), focuses on the relationship between $v_{\text{ext}}(\boldsymbol{r})$ and the electronic density $\rho_0(\boldsymbol{r})$ of the ground state. The theorem states that there exists a one-to-one mapping between $v_{\text{ext}}(\boldsymbol{r})$ and $\rho_0(\boldsymbol{r})$. In order to fully specify an electronic system, it is therefore equivalent to determine either $v_{\text{ext}}(\boldsymbol{r})$ or $\rho_0(\boldsymbol{r})$.

The Hohenberg–Kohn Theorem

i.) For a non-degenerate ground state $|\psi\rangle$ of the system the external potential $v_{\text{ext}}(\boldsymbol{r})$ is determined, within an additive constant, as a functional of the electronic density $\rho(\boldsymbol{r})$.

ii.) Given an external potential $v_{\text{ext}}(\boldsymbol{r})$, the correct ground-state density $\rho(\boldsymbol{r})$ minimizes the ground-state energy E_0, which is a functional uniquely determined by $\rho(\boldsymbol{r})$. It can be shown that

$$E_0 \leq E_v[\,\tilde{\rho}(\boldsymbol{r})] \tag{2.15}$$

where $\tilde{\rho}(\boldsymbol{r})$ is any trial density fulfilling $\tilde{\rho}(\boldsymbol{r}) \geq 0$ and $\int \mathrm{d}^3 r\, \tilde{\rho}(\boldsymbol{r}) = N$, N being the number of electrons in the system. The subscript v emphasizes the dependence of E_0 on the external potential $v_{\text{ext}}(\boldsymbol{r})$.

The theorem guarantees the existence of an energy functional $E_v[\,\rho]$ that reaches its minimum for the correct density $\rho(\boldsymbol{r})$ yet gives no explicit prescription for its construction. In order to determine $E_v[\,\rho]$, it is useful to separate the various known contributions to the total energy, like $T_s[\rho]$, the kinetic energy of a noninteracting electron gas, $E_{\text{ext}}[\rho]$, the classical Coulomb energy of the electrons moving in the external potential $v_{\text{ext}}(\boldsymbol{r})$, and $E_{\text{Coul}}[\rho]$, the classical energy due to the mutual Coulomb interaction of the electrons:

$$E[\,\rho(\boldsymbol{r})] = T_s[\,\rho(\boldsymbol{r})] + E_{\text{ext}}[\,\rho(\boldsymbol{r})] + E_{\text{Coul}}[\,\rho(\boldsymbol{r})] + E_{\text{xc}}[\,\rho(\boldsymbol{r})] \tag{2.16}$$

The last term $E_{\text{xc}}[\,\rho(\boldsymbol{r})]$ contains the quantum mechanical exchange and correlation energy and, in principle, the difference between the true kinetic energy, $T[\,\rho(\boldsymbol{r})]$, and $T_s[\,\rho(\boldsymbol{r})]$, the kinetic energy of the gas of noninteracting Kohn–Sham (KS) electrons. Since this difference is very small it is often neglected.

2.5.2 The Kohn–Sham Equations

Due to the second part of the HK theorem, namely that the total energy is minimized by the true ground-state density, the variational principle can now be applied. With the standard functional derivatives and the additional definition of the so-called exchange–correlation potential, the functional derivative of the exchange–correlation energy E_{xc}

$$v_{\text{xc}}(\boldsymbol{r}) \equiv \frac{\delta E_{\text{xc}}[\,\tilde{\rho}(\boldsymbol{r})]}{\delta \tilde{\rho}(\boldsymbol{r})} \tag{2.17}$$

the following set of equations can be derived [Kohn and Sham, 1965]:

$$\left[-\frac{\hbar^2}{2m}\nabla^2 + v_{\text{eff}}(\boldsymbol{r})\right] \phi_i(\boldsymbol{r}) = \epsilon_i\, \phi_i(\boldsymbol{r}) \tag{2.18}$$

where the effective potential is a functional of the electronic density

$$v_{\text{eff}}(\boldsymbol{r}) = v_{\text{eff}}[\rho(\boldsymbol{r})] = v_{\text{ext}}(\boldsymbol{r}) + e^2 \int \mathrm{d}^3 r' \frac{\rho(\boldsymbol{r'})}{|\boldsymbol{r} - \boldsymbol{r'}|} + v_{\text{xc}}[\rho(\boldsymbol{r})] \tag{2.19}$$

The required electron density is generated from one-electron wave functions as

$$\rho(\boldsymbol{r}) = \sum_{i=1}^{N} |\phi_i(\boldsymbol{r})|^2 \tag{2.20}$$

The set of equations (2.18) to (2.20) are the famous KS equations. The electron density which minimizes the energy functional is found by a self-consistent solution of the set of KS equations. The result is formally exact, but in practice the exchange–correlation energy E_{xc} is unknown and an appropriate approximation is required.

In this work, the DFT approach was used for structure optimization and vibrational analysis of molecules. For the functional for the exchange–correlation energy E_{xc}, the hybrid functional B3PW91 [Becke, 1993, Perdew et al., 1992] was used exclusively due to its very high accuracy, especially in vibrational frequency calculations. In appropriate situations solvent effects were accounted for by using a polarizable continuum model, PCM [Cancès et al., 1997].

References

H. Y. Aboul-Enein and I. W. Wainer. *The Impact of Stereochemistry on Drug Development and Use*. Wiley, New York, 1997.

S. Ahuja. *Chiral Separations by Chromatography*. Oxford University Press, Washington, DC, 2000.

A. J. Alder, N. J. Greenfield, and G. D. Fasman. Circular Dichroism and Optical Rotatory Dispersion of Proteins and Polypeptides. *Meth. Enzymology*, 27:675, 1973.

R. S. Atkinson. *Stereoselective Synthesis*. John Wiley & Sons, New York, 1995.

G. A. Attard. Electrochemical Studies of Enantioselectivity at Chiral Metal Surfaces. *J. Phys. Chem. B*, 105(16):3158–3167, 2001.

A. Baiker and H. U. Blaser. Enantioselective Catalysts and Reactions. In G. Ertl, H. Knözinger, and J. Weitkamp, editors, *Handbook of Heterogeneous Catalysis*, volume 5, pages 2422–2436. VCH Publishers, Weinheim, 1997.

B. J. Barner, M. J. Green, E. I. Saez, and R. M. Corn. Polarization Modulation Fourier Transform Infrared Reflectance Measurements of Thin Films and Monolayers at Metal Surfaces Utilizing Real-Time Sampling Electronics. *Anal. Chem.*, 63(1): 55–60, 1991.

D. Baurecht and U. P. Fringeli. Quantitative Modulated Excitation Fourier Transform Infrared Spectroscopy. *Rev. Sci. Instr.*, 72(10):3782–3792, 2001.

D. Baurecht, I. Porth, and U. P. Fringeli. A New Method of Phase Sensitive Detection in Modulation Spectroscopy Applied to Temperature Induced Folding and Unfolding of RNase A. *Vib. Spectr.*, 30:85–92, 2002.

A. D. Becke. Density-functional Thermochemistry. III. The Role of Exact Exchange. *J. Chem. Phys.*, 98(7):5648–5652, 1993.

G. Belavoine, A. Moradpour, and H. B. Kagan. Preparation of Chiral Compounds with High Optical Purity by Irradiation with Circularly Polarized Light. *J. Am. Chem. Soc.*, 96:5152–5158, 1974.

M. Bieri and T. Bürgi. Probing Enantiospecific Interactions between Proline and an L-Glutathione Self-Assembled Monolayer by Modulation Excitation ATR-IR Spectroscopy. *J. Phys. Chem. B*, 109(20):10243–10250, 2005a.

M. Bieri and T. Bürgi. L-Glutathione Chemisorption on Gold and Acid/Base Induced Structural Changes: A PM-IRRAS and Time-Resolved in Situ ATR-IR Spectroscopic Study. *Langmuir*, 21(4):1354–1363, 2005b.

M. Bieri and T. Bürgi. Enantiodiscrimination between an *N*-Acetyl-L-cysteine SAM and Proline: An In Situ Spectroscopic and Computational Study. *ChemPhysChem*, 7(2):514–523, 2006.

D. Blaudez, T. Buffeteau, J. C. Cornut, B. Desbat, N. Escafre, M. Pezolet, and J. M. Turlet. Polarization-Modulated FT-IR Spectroscopy of a Spread Monolayer at the Air/Water Interface. *Appl. Spectrosc.*, 47(7):869–874, 1993.

K. Bodenhöfer, A. Hierlemann, J. Seemann, G. Gauglitz, B. Koppenhoefer, and W. Göpel. Chiral Discrimination Using Piezoelectric and Optical Gas Sensors. *Nature*, 387:577–580, 1997.

M. Born and R. Oppenheimer. Quantum Theory of Molecules. *Ann. Phys. Berlin*, 84: 457–484, 1927.

M. Born and E. Wolf. *Principles of Optics*. Pergamon, 3rd edition, 1979.

T. Bürgi and A. Baiker. In Situ Infrared Spectroscopy of Catalytic Solid–Liquid Interfaces Using Phase-Sensitive Detection: Enantioselective Hydrogenation of a Pyrone over Pd/TiO_2. *J. Phys. Chem. B*, 106:10649–10658, 2002.

T. Bürgi and A. Baiker. Heterogeneous Enantioselective Hydrogenation over Cinchona Alkaloid Modified Platinum: Mechanistic Insights into a Complex Reaction. *Acc. Chem. Res.*, 37(11):909–917, 2004.

T. Bürgi and A. Baiker. Attenuated Total Reflection Infrared Spectroscopy of Solid Catalysts Functioning in the Presence of Liquid-Phase Reactants. *Adv. Catal.*, 50: 228–283, 2006.

T. Buffeteau, B. Desbat, and J. M. Turlet. Polarization Modulation FT-IR Spectroscopy of Surfaces and Ultra-Thin Films: Experimental Procedure and Quantitative Analysis. *Appl. Spectrosc.*, 45(3):380–389, 1991.

T. Buffeteau, B. Desbat, D. Blaudez, and J. M. Turlet. Calibration Procedure to Derive IRRAS Spectra from PM-IRRAS Spectra. *Appl. Spectrosc.*, 54(11):1646–1650, 2000.

D. Buttry. Applications of the QCM to Electrochemistry. In A. Bard, editor, *A Series of Advances in Electroanalytical Chemistry*, pages 23–33. Marcel Dekker, 1991.

J. Caldwell. Stereochemical Determinants of the Nature and Consequences of Drug Metabolism. *J. Chromatogr. A*, 694(1):39–48, 1995.

J. Caldwell. Importance of Stereospecific Bioanalytical Monitoring in Drug Development. *J. Chromatogr. A*, 719(1):3–13, 1996.

M. T. Cancès, B. Mennucci, and J. Tomasi. A New Integral Equation Formalism for the Polarizable Continuum Model: Theoretical Background and Applications to Isotropic and Anisotropic Dielectrics. *J. Chem. Phys.*, 107(8):3032–3041, 1997.

C. Cotton, A. Glidle, G. Beamson, and G. Cooper. Dynamics of the Formation of Mixed Alkanethiol Monolayers: Applications in Structuring Biointerfacial Arrangements. *Langmuir*, 14(18):5139–5146, 1998.

J. T. Cronin and S. Pizzarello. Enantiomeric Excess in Meteoritic Amino Acids. *Science*, 275:951–955, 1997.

T. Dabros and T. G. M. van de Ven. A Direct Method for Studying Particle Deposition onto Solid Surfaces. *Coll. Polymer Sci.*, 261:694–707, 1983.

T. Dabros and T. G. M. van de Ven. Deposition of Latex Particles on Glass Surfaces in an Impinging Jet. *Phys.Chem. Hydrodyn.*, 8:161–172, 1987.

O. Dassa, V. Sidorov, Y. Paz, and D. Ritter. Coating and Passivation of InP-InGaAs Devices by Organic Self-Assembled Monolayers. *J. Electrochem. Soc.*, 153(1):G91–G97, 2006.

J. Dingenen and J. N. Kinkel. Preparative Chromatographic Resolution of Racemates on Chiral Stationary Phases on Laboratory and Production Scales by Closed-Loop Recycling Chromatography. *J. Chromatogr. A*, 666:627–650, 1994.

Y. Duda, R. Govea-Rueda, M. Galicia, H. I. Beltran, and L. S. Zamudio-Rivera. Corrosion Inhibitors: Design, Performance, and Computer Simulations. *J. Phys. Chem. B*, 109(47):22674–22684, 2005.

J. Fourier. *The Analytical Theory of Heat.* Cambridge University Press, 1878.

S. A. Francis and A. H. Ellison. Infrared Spectra of Monolayers on Metal Mirrors. *J. Opt. Soc. Am.*, 49:131–138, 1959.

E. R. Francotte. Contribution of Preparative Chromatographic Resolution to the Investigation of Chiral Phenomena. *J. Chromatogr. A*, 666(1-2):565–601, 1994.

E. R. Francotte. In S. Ahuja, editor, *Chiral Separations, Applications and Technology*, page 349. American Chemical Society, Washington, DC, 1997a.

E. R. Francotte. Enantioselective Chromatography. An Essential and Versatile Tool for the Analytical and Preparative Separation of Enantiomers. *Chimia*, 51(10): 717–725, 1997b.

U. P. Fringeli, D. Baurecht, and H. H. Günthard. Infrared and Raman Spectroscopy of Biological Materials. In H. U. Gremlich and B. Yan, editors, *Infrared and Raman Spectroscopy of Biological Materials*, pages 143–192. Dekker, New York/Basel, 2000.

P. G. Ganesan, A. Kumar, and G. Ramanath. Surface Oxide Reduction and Bilayer Molecular Assembly of a Thiol-Terminated Organosilane on Cu. *Appl. Phys. Lett.*, 87(1):011905/1–011905/3, 2005.

A. S. Garay and J. A. Ahlgren-Beckendorf. Differential Interaction of Chiral Beta-Particles with Enantiomers. *Nature*, 346:451–453, 1990.

A. J. Gellman, J. D. Horvath, and M. T. Buelow. Chiral Single Crystal Surface Chemistry. *J. Mol. Catal A: Chemical*, 167(1-2):3–11, 2001.

D. W. Goodman. Model Catalysts: From Imagining to Imaging a Working Surface. *J. Catal.*, 216(1-2):213–222, 2003.

M. J. Green, B. J. Barner, and R. M. Corn. Real-Time Sampling Electronics for Double Modulation Experiments with Fourier Transform Infrared Spectrometers. *Rev. Sci. Instrum.*, 62(6):1426–1430, 1991.

R. G. Greenler. Infrared Study of Adsorbed Molecules on Metal Surfaces by Reflection Techniques. *J. Chem. Phys.*, 44(1):310–315, 1966.

W. J. Guo, S. H. Chen, B. D. Huang, H. Y. Ma, and X. G. Yang. Protection of Self-Assembled Monolayers Formed from Triethyl Phosphate and Mixed Self-Assembled Monolayers from Triethyl Phosphate and Cetyltrimethyl Ammonium Bromide for Copper against Corrosion. *Electrochimica Acta*, 52(1):108–113, 2006.

N. J. Harrick. *Internal Reflection Spectroscopy.* Interscience Publishers, New York, 1967.

B. E. Hayden. Vibrational Spectroscopy of Molecules on Surfaces. In J. T. J. Yates and T. E. Madey, editors, *Vibrational Spectroscopy of Molecules on Surfaces.* Plenum Press, New York, 1987.

R. M. Hazen, T. R. Filley, and G. A. Goodfriend. Selective Adsorption of L- and D-Amino Acids on Calcite: Implications for Biochemical Homochirality. *Proc. Nat. Acad. Sci. USA*, 98(10):5487–5490, 2001.

J. Henderson. *Electronic Devices: Concepts and Applications*, volume 1. Prentice Hall, 1992.

J. M. Hicks and T. Petralli-Mallow. Nonlinear Optics of Chiral Surface Systems. *Appl. Phys. B—Lasers and Optics*, 68(3):589–593, 1999.

K. W. Hipps and G. A. Crosby. Applications of the Photoelastic Modulator to Polarization Spectroscopy. *J. Phys. Chem.*, 83(5):555–562, 1979.

P. Hohenberg and W. Kohn. Inhomogeneous Electron Gas. *Phys. Rev. B*, 136:B864, 1964.

J. D. Horvath and A. J. Gellman. Enantiospecific Desorption of Chiral Compounds from Chiral Cu(643) and Achiral Cu(111) Surfaces. *J. Am. Chem. Soc.*, 124(10): 2384–2392, 2002.

J. D. Horvath, A. Koritnik, P. Kamakoti, D. S. Sholl, and A. J. Gellman. Enantioselective Separation on a Naturally Chiral Surface. *J. Am. Chem. Soc.*, 126(45): 14988–14994, 2004.

J. Huang, V. M. Egan, H. Guo, J.-Y. Yoon, A. L. Briseno, I. E. Rauda, R. L. Garrell, C. M. Knobler, F. Zhou, and B. Kaner. Enantioselective Discrimination of D- and L-Phenylalanine by Chiral Polyaniline Thin Films. *Adv. Mater.*, 15(14):1158–1161, 2003.

W. Hug, S. Kint, G. F. Bailey, and J. R. Scherer. Raman Circular Intensity Difference Spectroscopy. The Spectra of (-)-Alpha-Pinene and (+)-Alpha-Phenylethylamine. *J. Am. Chem. Soc.*, 97:5589–5590, 1975.

M. N. Islam and T. Kato. Faceted Structures in Langmuir Monolayers of Diethylene Glycol Mono-*n*-octadecyl Ether at the Air–Water Interface. *Langmuir*, 20:10872–10877, 2004.

R. Jelinek and S. Kolusheva. Carbohydrate Biosensors. *Chem. Rev.*, 104(12):5987–6015, 2004.

N. Ji and Y.-R. Shen. A Novel Spectroscopic Probe for Molecular Chirality. *Chirality*, 18(3):146–158, 2006.

N. Ji, K. Zhang, H. Yang, and Y.-R. Shen. Three-Dimensional Chiral Imaging by Sum-Frequency Generation. *J. Am. Chem. Soc.*, 128(11):3482–3483, 2006.

K. K. Kanazawa and J. Gordon II. Frequency of a Quartz Microbalance in Contact with Liquid. *Anal. Chem.*, 57:1770–1771, 1985.

W. Kohn. Nobel Lecture: Electronic Structure of Matter-Wave Functions and Density Functionals. *Rev. Mod. Phys.*, 71(5):1253–1266, 1999.

W. Kohn and L. J. Sham. Self-Consistent Equations Including Exchange and Correlation Effects. *Phys. Rev. A*, 140:A1133, 1965.

H. Kuhn and A. Ulman. Supramolecular Assemblies: Vision and Strategy. In *Thin Films*. Academic Press, New York, 1995.

K. Kunimatsu, H. Seki, W. G. Golden, J. G. Gordon, and M. R. Philpott. Electrode/Electrolyte Interphase Study Using Polarization Modulated FTIR Reflection-Absorption Spectroscopy. *Surf. Sci.*, 158(1-3):596–608, 1985.

N. M. Maier, P. Franco, and W. Lindner. Separation of Enantiomers: Needs, Challenges, Perspectives. *J. Chromatogr. A*, 906:3–33, 2001.

N. M. Maier, S. Schefzick, G. M. Lombardo, M. Feliz, K. Rissanen, W. Lindner, and K. B. Lipkowitz. Elucidation of the Chiral Recognition Mechanism of Cinchona Alkaloid Carbamate-Type Receptors for 3,5-Dinitrobenzoyl Amino Acids. *J. Am. Chem. Soc.*, 124:8611–8629, 2002.

S. J. Martin, J. J. Spates, K. O. Wessendorf, T. W. Schneider, and R. J. Huber. Resonator/Oscillator Response to Liquid Loading. *Anal. Chem.*, 69(11):2050–2054, 1997.

J. D. E. McIntyre and D. E. Aspnes. Differential Reflection Spectroscopy of Very Thin Surface Films. *Surf. Sci.*, 24(2):417–434, 1971.

R. McKendry, M. E. Theoclitou, T. Rayment, and C. Abell. Chiral Discrimination by Chemical Force Microscopy. *Nature*, 391:566–568, 1998.

M. Müller, R. Buchet, and U. P. Fringeli. 2D-FTIR ATR Spectroscopy of Thermo-Induced Periodic Secondary Structural Changes of Poly-(L)-Lysine: A Cross-Correlation Analysis of Phase-Resolved Temperature Modulation Spectra. *J. Phys. Chem.*, 100(25):10810–10825, 1996.

W. Mäntele. *Biophysical Techniques in Photosynthesis*. Kluwer Academic, Dordrecht, The Netherlands, 1996.

D. Murzin, P. Maki-Arvela, E. Toukoniitty, and T. Salmi. Asymmetric Heterogeneous Catalysis: Science and Engineering. *Catal. Rev.—Sci. Eng.*, 47(2):175–256, 2005.

L. A. Nafie. Infrared and Raman Optical Activity: Theoretical and Experimental Aspects. *Annu. Rev. Phys. Chem.*, 48:357–386, 1997.

T. Nakanishi, N. Yamakawa, T. Asahi, T. Osaka, B. Ohtani, and K. Uosaki. Enantioselecive Adsorption of Phenylalanine on Self-Assembled Monolayers of 1,1'-Binaphthalenne-2,2'-Dithiol on Gold. *J. Am. Chem. Soc.*, 124(5):740–741, 2002.

T. Nakanishi, N. Yamakawa, T. Asahi, N. Shibata, B. Ohtani, and T. Osaka. Chiral Discrimination between Thalidomide Enantiomers Using a Solid Surface with Two-Dimensional Chirality. *Chirality*, 16:S36–S39, 2004.

I. Newton. *Opticks*. Dover Publications, Book III, New York, 2nd edition, 1952.

T. Nomura and M. Okuhara. Frequency Shifts of Piezoelectric Quartz Crystals Immersed in Organic Liquids. *Anal. Chim. Acta*, 142:281–284, 1982.

D. J. O'Conner, B. A. Sexton, and R. S. C. Smart. *Surface Analysis Methods in Materials Science, Springer Series in Surface Sciences, Second Edition*, volume 23. Springer Verlag, Berlin, 2003.

E. Ostuni, L. Yan, and G. M. Whitesides. The Interaction of Proteins and Cells with Self-Assembled Monolayers of Alkanethiolates on Gold and Silver. *Colloids Surf. B Biointerfaces*, 15(1):3–30, 1999.

S. Pagliari, R. Corradini, G. Galaverna, S. Sforza, A. Dossena, M. Montalti, L. Prodi, N. Zaccheroni, and R. Marchelli. Enantioselective Fluorescence Sensing of Amino Acids by Modified Cyclodextrins: Role of the Cavity and Sensing Mechanism. *Chem. Eur. J.*, 10:2749–2758, 2004.

R. Paolesse, D. Monti, L. La Monica, M. Venanzi, A. Froiio, S. Nardis, C. Di Natale, E. Martinelli, and A. D'Amico. Preparation and Self-Assembly of Chiral Porphyrin Diads on the Gold Electrodes of Quartz Crystal Microbalances: A Novel Potential Approach to the Development of Enantioselective Chemical Sensors. *Chem. Eur. J.*, 8(11):2476–2483, 2002.

L. Pasteur. Recherches sur les relations qui peuvent exister entre la forme cristalline et la composition chimique, et le sens de la polarisation rotatoire. *Ann. Chim. Phys.*, 24:442–459, 1848.

H. A. Pearce and N. Sheppard. Possible Importance of a "Metal-Surface Selection Rule" in the Interpretation of the Infrared Spectra of Molecules Adsorbed on Particulate Metals; Infrared Spectra from Ethylene Chemisorbed on Silica-Supported Metal Catalysts. *Surf. Sci.*, 59(1):205–217, 1976.

J. P. Perdew, J. A. Chevary, S. H. Vosko, K. A. Jackson, M. R. Pederson, D. J. Singh, and C. Fiolhais. Atoms, Molecules, Solids, and Surfaces: Applications of the Generalized Gradient Approximation for Exchange and Correlation. *Phys. Rev. B*, 46(11):6671–6687, 1992.

R. M. Petoral and K. Uvdal. Arg-Cys and Arg-Cysteamine Adsorbed on Gold and the G-Protein-Adsorbate Interaction. *Colloids and Surf. B Biointerfaces*, 25:335–346, 2002.

J. Podlech. Origin of Organic Molecules and Biomolecular Homochirality. *Cell. and Mol. Life Sci.*, 58:44–60, 2001.

E. Rubenstein, W. A. Bonner, H. P. Noyes, and G. S. Brown. Supernovae and Life. *Nature*, 306(10):118, 1983.

A. Saghatelian, Y. Yokobayashi, K. Soltani, and M. R. Ghadiri. A Chiroselective Peptide Replicator. *Nature*, 409(6822):797–801, 2001.

G. Sauerbrey. The Use of Quartz Oscillators for Weighing Thin Layers and for Microweighing. *Z. Phys.*, 155:206–222, 1959.

E. Schrödinger. Quantisierung als Eigenwertproblem. *Ann. Phys. Berlin*, 79:361–376, 1926.

F. Schreiber. Self-Assembled Monolayers: From "Simple" Model Systems to Biofunctionalized Interfaces. *J. Phys.: Condens. Matter*, 16:R881–R900, 2004.

H. Seki, K. Kunimatsu, and W. G. Golden. A Thin-Layer Electrochemical Cell for Infrared Spectroscopic Measurements of the Electrode/Electrolyte Interface. *Appl. Spectrosc.*, 39(3):437–443, 1985.

H. Strehlow and W. Knoche. *Fundamentals of Chemical Relaxation*, volume 10. Verlag Chemie, Weinheim, 1977.

A. Szabo and N. S. Ostlund. *Modern Quantum Chemistry: Introduction to Advanced Electronic Structure Theory.* Dover Publications, 1996.

R. C. Thomas, J. E. Houston, T. A. Michalske, and R. M. Crooks. The Mechanical Response of Gold Substrates Passivated by Self-Assembling Monolayer Films. *Science*, 259(5103):1883–1885, 1993.

A. Ulman. *An Introduction to Ultrathin Organic Films: From Langmuir–Blodgett to Self-Assembly.* Academic Press, 1991.

A. Ulman. Formation and Structure of Self-Assembled Monolayers. *Chem. Rev.*, 96: 1533–1554, 1996.

A. Ulman, S. D. Evans, Y. Shnidman, R. Sharma, J. E. Eilers, and J. C. Chang. Concentration-Driven Surface Transition in the Wetting of Mixed Alkanethiol Monolayers on Gold. *J. Am. Chem. Soc.*, 113(5):1499–1506, 1991.

A. Urakawa, R. Wirz, T. Bürgi, and A. Baiker. ATR-IR Flow-Through Cell for Concentration Modulation Excitation Spectroscopy: Diffusion Experiments and Simulations. *J. Phys. Chem. B*, 107(47):13061–13068, 2003.

A. Urakawa, T. Bürgi, and A. Baiker. Modulation Excitation PM-IRRAS: A New Possibility for Simultaneous Monitoring of Surface and Gas Species and Surface Properties. *Chimia*, 60(4):231–233, 2006a.

A. Urakawa, T. Bürgi, and A. Baiker. Kinetic Analysis Using Square-Wave Stimulation in Modulation Excitation Spectroscopy: Mixing Property of a Flow-Through PM-IRRAS Cell. *Chem. Phys.*, 324(2-3):653–658, 2006b.

A. Urakawa, T. Bürgi, H.-P. Schläpfer, and A. Baiker. Simultaneous In Situ Monitoring of Surface and Gas Species and Surface Properties by Modulation Excitation Polarization-Modulation Infrared Reflection-Absorption Spectroscopy: CO Oxidation over Pt Film. *J. Chem. Phys.*, 124:054717(1–11), 2006c.

I. W. Wainer. *Drug Stereochemistry: Analytical Methods and Pharmacology: Second Edition, Revised and Expanded.* Marcel Dekker, New York, 1993.

R. Wirz, T. Bürgi, and A. Baiker. Probing Enantiospecific Interactions at Chiral Solid–Liquid Interfaces by Absolute Configuration Modulation Excitation Infrared Spectroscopy. *Langmuir*, 19:785–792, 2003.

R. Wirz, T. Bürgi, W. Lindner, and A. Baiker. Absolute Configuration Modulation Attenuated Total Reflection IR Spectroscopy: An in Situ Method for Probing Chiral Recognition in Liquid Chromatography. *Anal. Chem.*, 76(18):5319–5330, 2004.

D. A. M. Zaia. A Review of Adsorption of Amino Acids on Minerals: Was it Important for the Origin of Life? *Amino Acids*, 27(1):113–118, 2004.

V. Zamlynny, I. Zawisza, and J. Lipkowski. PM FTIRRAS Studies of Potential-Controlled Transformations of a Monolayer and a Bilayer of 4-Pentadecylpyridine, a Model Surfactant, Adsorbed on a Au(111) Electrode Surface. *Langmuir*, 19(1): 132–145, 2003.

Q. Zhang and L. A. Archer. Boundary Lubrication and Surface Mobility of Mixed Alkylsilane Self-Assembled Monolayers. *J. Phys. Chem. B*, 107(47):13123–13132, 2003.

L. Zuo, Y. Xiong, X. Xie, and X. Xiao. Enhanced Lubricity in Mixed Alkanethiol Monolayers. *J. Phys. Chem. B*, 109(48):22971–22975, 2005.

Part II

Adsorption and Self-Assembly

Preface

This part includes studies on the adsorption and self-assembly of chiral surfactants from the liquid phase ethanol (EtOH) on gold surfaces. As prime technique ATR-IR was used to probe the solid–liquid interface *in situ* which provided information on structure and orientation of adsorbed molecules. Complementarily, quartz crystal microbalance (QCM) was used to study mass uptake and kinetics of adsorption and polarization-modulation infrared reflection-absorption spectroscopy (PM-IRRAS) was used to study the structure of adsorbate layers *ex situ*.
Constituent surfactants used for adsorption and self-assembly studies were L-glutathione (GSH), *N*-acetyl-L-cysteine (NAC) and D-penicillamine (PEN). GSH is a tripeptide (γ-glu-cys-gly) and has various physiological functions. It is the most abundant non-protein thiol in mammalian cells. It has, furthermore, the most complex structure among the surfactants used in this work for adsorption studies. This complexity is reflected in the kinetics of adsorption and significant structural changes that take place during self-assembly. NAC may be viewed as the anchoring part of GSH and it has less degree of freedom than the latter. Due to its simpler structure, NAC was amenable to orientation analysis at low surface coverage, where intermolecular interaction is negligible. PEN is an amino acid related to cysteine (β,β-dimethylcysteine) and valine (β-mercaptovaline). PEN has three functional groups and ATR-IR indicated that all of them (*i.e.* thiol, carboxylate, and amine) interact with the surface, thus explaining PEN's superior properties as chelating agent.

Chapters 1 and 2 are dedicated to the adsorption of GSH on gold. For the study presented in Chapter 1, ATR-IR was further combined with modulation excitation spectroscopy (MES) in order to investigate the structure of the SAM. It was shown that the molecules are firmly anchored on the gold surface *via* the thiol group of the cys part. However, ATR-IR in combination with MES gave evidence that a large fraction of molecules within the SAM undergoes significant reversible structural changes upon acid–base stimuli (pH modulation). These structural changes are mainly induced by alternately protonating and deprotonating the carboxylic acid group at the gly moiety, which involves surface interaction. Analysis of the kinetics of protonation/deprotonation further showed significant different regimes—the glu moiety is readily (de)protonated while the process at the gly moiety, due to surface interaction, is considerably slower.

Chapter 2 focuses on the kinetics of adsorption and structural changes within the SAM during self-assembly by using both *in situ* ATR-IR and QCM. Different IR signals of adsorbed GSH show significantly different behavior with time, which reveals that their increase is not related to adsorption (mass uptake) alone. This indicates that structural transformations take place during the formation of the SAM. The

complexity of the self-assembly process was confirmed by QCM measurements, which showed initial fast mass uptake followed by a considerably slower regime.

An adsorption study of NAC on gold is presented in Chapter 3. ATR-IR spectra recorded at low surface coverage were used for orientation analysis. The surface spectrum showed significant differences to spectra of randomly oriented NAC recorded in liquid phase. Based on a novel approach, fully relying on density functional theory (DFT), the calculated transition dipole moments of NAC were used to simulate the experimental surface spectrum and the method was successfully applied to derive the orientation of NAC adsorbed on gold. Besides, ATR-IR revealed significant structural changes of NAC during self-assembly on gold.

Chapter 4 deals with the formation of a PEN SAM on gold. It was found that part of the molecules deprotonate at the amine group which is assisted by surface interaction. Furthermore, spectroscopic results indicate a three-point interaction of PEN with the surface, involving the thiol, carboxylate and amine functional groups. It was also shown that (in contrast to GSH and NAC) PEN has strong affinity for multilayer growth. A second, physisorbed layer was independently confirmed by ATR-IR and QCM.

Chapter 1

L-Glutathione Chemisorption on Gold and Acid/Base Induced Structural Changes: A PM-IRRAS and Time-Resolved *in Situ* ATR-IR Spectroscopic Study

Marco Bieri and Thomas Bürgi

Published in Langmuir, Volume 21(4), pp. 1354–1363, doi: 10.1021/la047735s, 2005.

1354 *Langmuir* **2005,** *21,* 1354−1363

L-Glutathione Chemisorption on Gold and Acid/Base Induced Structural Changes: A PM-IRRAS and Time-Resolved in Situ ATR-IR Spectroscopic Study

Marco Bieri and Thomas Bürgi*

Institut de Chimie, Faculté des Sciences, Université de Neuchâtel, Rue Emile-Argand 11, 2007 Neuchâtel, Switzerland

Received September 10, 2004. In Final Form: November 19, 2004

Adsorption of the tripeptide L-glutathione (*γ-glu-cys-gly*) on gold surfaces was investigated by polarization modulation infrared reflection absorption spectroscopy (PM-IRRAS) and attenuated total reflection (ATR) infrared spectroscopy. PM-IRRAS was used to study ex situ the adsorbate layer prepared from aqueous solutions at different pH, whereas ATR-IR was applied to study in situ adsorption from ethanol in the presence and absence of acid and base. ATR-IR was furthermore combined with modulation spectroscopy in order to investigate the reversible changes within the adsorbate layer induced by acid and base stimuli, respectively. The molecule is firmly anchored on the gold surface via the thiol group of the cys part. However, the ATR-IR spectra in ethanol indicate a further interaction with the gold surface via the carboxylic acid group of the gly part of the molecule, which deprotonates upon adsorption. Hydrochloric acid readily protonates the two acid groups of the adsorbed molecule. During subsequent ethanol flow the acid groups deprotonate again, a process which proceeds in two distinct steps: a fast step associated with the deprotonation of the acid in the glu part of the molecule and a considerably slower step associated with deprotonation of the acid in the gly moiety. The latter process is assisted by the interaction of the corresponding acid group with the surface. The spectra furthermore indicate a rearrangement of the hydrogen bonding network within the adsorbate layer upon deprotonation. Depending on the protonation state during adsorption of L-glutathione, the response toward identical protonation−deprotonation stimuli is significantly different. This is explained by the ionic state-dependent shape of the molecule, as supported by density functional theory calculations. The different shapes of the individual molecules during layer formation thus influence the structure of the adsorbate layer.

Introduction

The formation of self-assembled monolayers (SAMs) of molecules on solid surfaces has extensively been studied in recent years.[1] In particular SAMs of thiol-containing molecules on gold and silver surfaces are important systems for understanding fundamental aspects of SAM formation.[2] These systems have interesting potential for applications in various surface-related technologies, for example in sensing of biomolecules.[3,4] An important case for applications related to biology are SAMs of cysteine (cysteamine) or cysteine-containing molecules.[4−7]

The present work deals with L-glutathione (*γ*-glu-cys-gly, GSH, Chart 1) adsorption on gold surfaces. GSH is a natural reducing molecule and ubiquitous. In fact, it is the most abundant nonprotein thiol in mammalian cells[8] found in millimolar concentration. The molecule has a multitude of physiological functions,[9] such as redox-buffering, detoxification, and antioxidant activity. Furthermore, GSH is cheap, which makes it an attractive candidate for surface and electrode modification[10−23] and the synthesis of monolayer-protected nanoparticles.[24−26] Glutathione-modified gold surfaces were for example used

Chart 1. Structure of l-Glutathione (*γ*-glu-cys-gly, GSH) and Some Different Possible Ionic Forms

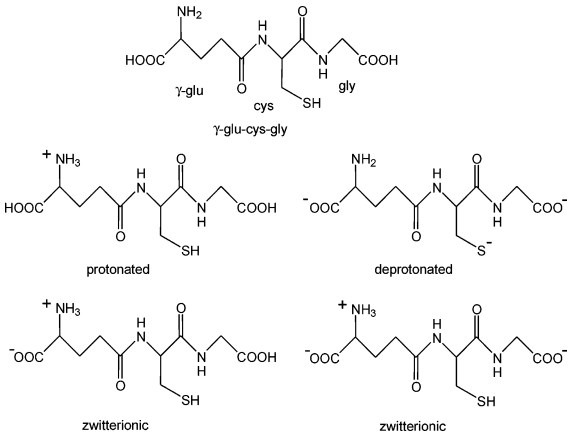

* To whom correspondence should be addressed. Telephone: ++41 32 718 24 12. Fax: ++41 32 718 25 11. E-mail: thomas.burgi@unine.ch.

(1) Ulman, A. *Chem. Rev.* **1996**, *96*, 1533.
(2) Ostuni, E.; Yan, L.; Whitesides, G. M. *Colloids Surf., B* **1999**, *15*, 3.
(3) Cotton, C.; Glidle, A.; Beamson, G.; Cooper, G. *Langmuir* **1998**, *14*, 5139.
(4) Petoral, R. M.; Uvdal, K. *Colloids Surf., B* **2002**, *25*, 335.
(5) Zhang, J.; Chi, Q.; Nielsen, J. U.; Friis, E. P.; Andersen, J. E. T.; Ulstrup, J. *Langmuir* **2000**, *16*, 7229.
(6) Felice, R. D.; Selloni, A.; Molinari, E. *J. Phys. Chem. B* **2003**, *107*, 1151.
(7) Kühnle, A.; Linderoth, T. R.; Hammer, B.; Besenbacher, F. *Nature* **2002**, *415*, 891.
(8) Bray, T. M.; Taylor, C. G. *Can. J. Physiol. Pharmacol.* **1993**, *71*, 746.
(9) Sies, H. *Free Radical Biol. Med.* **1999**, *27*, 916.
(10) Takehara, K.; Aihara, M.; Ueda, N. *Electroanalysis* **1994**, *6*, 1083.
(11) McCormick, H.; McMillan, R.; Merrett, K.; Bensebaa, F.; Deslandes, Y.; Dubé, M. A.; Sheardown, H. *Colloids Surf., B* **2002**, *26*, 351.
(12) Damrongchai, N.; Yun, K.; Kobatake, E.; Aizawa, M. *J. Biotechnol.* **1997**, *55*, 125.
(13) Kanagaraja, S.; Alaeddine, S.; Eriksson, C.; Lausmaa, J.; Tengvall, P.; Wennerberg, A.; Nygren, H. *J. Biomed. Mater. Res.* **1999**, *46*, 582.
(14) Fang, C.; Zhou, X. *Electroanalysis* **2001**, *13*, 949.

10.1021/la047735s CCC: $30.25
Published on Web 01/15/2005

for specific protein binding.[12,13] Copper(II) and lanthanide(III) ions were found to bind strongly to glutathione-modified gold electrodes.[20,22,23] The affinity for the ions was assigned to the carboxylic acid groups and depended on pH.[22] On the basis of voltammetry and electrochemical quartz crystal microbalance (EQCM) investigations, it was furthermore proposed that during the redox process of Cu^{2+}/Cu^{+} the glutathione monolayer could rearrange.[22]

Electrochemical investigations of glutathine-modified gold electrodes revealed interesting "ion-gating" properties.[10,19] Interaction of rare earth metal ions, transition metal ions, neurotransmitters, and a cationic drug with the glutathione monolayer leads to opening of ion gates in the glutathione film, as revealed by redox ion probes.[19] On the basis of investigations using electrochemical quartz crystal microbalance (EQCM),[19] it was proposed that interaction of metal ions with adsorbed glutathione leads to a conformational change of the latter. More specific information on the structure of and proposed conformational changes within the glutathione layer on gold requires techniques that can provide structural insight. To date, such information is virtually missing for the glutathione−gold system.

In this contribution infrared vibrational spectroscopic techniques were applied to study glutathione layers and structural changes within these layers induced by admitting acid and base. Specifically we used polarization modulation infrared reflection absorption spectroscopy (PM-IRRAS)[27] to characterize the monolayers ex situ and attenuated total reflection (ATR-IR)[28] infrared spectroscopy as an in situ method. With the former we characterized in ambient air glutathione layers that were adsorbed on gold surfaces from aqueous solutions at different pH. The latter method was used to study in situ glutathione adsorption on gold from ethanol solution in a flow-through cell.[29] The ATR-IR method has been shown to yield detailed structural information of even relatively complex molecules on metal surfaces.[30] We have furthermore applied modulation excitation spectroscopy[31,32] in order to follow changes within the glutathione layer induced by periodically admitting acid and base, respectively. Modulation excitation spectroscopy leads to enhanced signal-to-noise ratio[32−34] and helps disentangling complex spectra of overlapping bands,[35] a situation that is anticipated for such complex molecules as glutathione.

Experimental Section

Materials. L-Glutathione reduced (GSH, Sigma-Aldrich Inc., ≥98%) was used as received. As solvents served ethanol (Merck p.a.) and water (osmosed and distilled, aqua pure, Merck). Solutions were treated with nitrogen gas (99.995%, CarbaGas) to remove dissolved oxygen.

PM-IRRAS Analyses: Sample Preparation. A cover glass for microscopy (Milian SA) with a size of 24 mm × 40 mm was used as a substrate. A thin gold layer with a thickness of about 100 nm was deposited on the substrate with a sputtering machine (Balzers Union SCD 030; sputtering rate, 0.5 Å/s). Before immersion in GSH solutions the Au surface of the PM-IRRAS sample was plasma-cleaned (PlasmaPrep2, GALA Instrumente) under a flow of air during 5 min. GSH solutions were prepared from distilled water, resulting in about pH 5. HCl (37% p.a., CARLO ERBA reagents) and NaOH pellets (p.a., CARLO ERBA reagents) were used to adjust the solution to about pH 1 and 12, respectively. The corresponding GSH concentrations in the solutions were 7 mM (neutral), 13 mM (basic) and 16 mM (acid). Adsorption from solutions of lower concentrations (by about 1 order of magnitude) led to the same PM-IRRAS spectra. After immersion in the solutions for 12 h the gold sample was rinsed thoroughly with a GSH-free solution of the same pH and dried by nitrogen gas. It has been reported previously that assembly of GSH on gold takes several hours.[12] Analogous experiments were also performed with an Au(111) single crystal (15 mm × 1 mm, MaTeck). The latter was treated with piranha solution (H_2SO_4:H_2O_2 (30%), 3:1) and rinsed with water immediately before immersion in GSH solution. PM-IRRAS spectra obtained from the Au single crystal and the sputtered films were in good agreement.

Safety note: Piranha solution is extremely aggressive and should be handled with care!

PM-IRRAS Spectroscopy and Data Acquisition. The gold sample was mounted on an attachment for PM-IRRAS measurements within the compartment of a Bruker PMA 50, connected to an external beam port of a Bruker tensor 27 Fourier transform infrared (FT-IR) spectrometer. After reflection at an angle of incidence of 80° the light was focused on a liquid nitrogen-cooled photovoltaic MCT detector in the PMA 50 cabinet. Polarization was modulated with a photoelastic modulator (Hinds, PEM 90) at a frequency of 50 kHz. Demodulation was performed with a lock-in amplifier (Stanford Research, SR830 DSP). All spectra were recorded during a sample scan time of 15 min at 4 cm^{-1} resolution. Resulting PM-IRRAS reflectance spectra were calculated with the bare gold substrate as the reference.

In Situ ATR-IR Analyses: Sample Preparation. A diamond paste with a grain size of 0.25 μm was used to polish the Ge internal reflection element (IRE). After rinsing the IRE copiously with ethanol, the surface was plasma-cleaned during 5 min. A thin gold layer with a thickness of about 2 nm was then sputtered onto the IRE. For each experiment, a fresh gold layer was used. Control experiments without gold on the Ge IRE revealed no GSH adsorption, as indicated by the absence of significant bands in the course of several-hours exposure to GSH solution.

ATR-IR Spectroscopy and Data Acquisition. ATR-IR infrared spectra were measured on a Bruker EQUINOX 55 FT-IR spectrometer with a nitrogen-cooled narrow-band MCT detector. A home-built liquid flow-through cell with a total volume of 0.077 mL and a gap of 250 μm between the IRE and the polished steel surface was used to record the ATR-IR spectra at a resolution of 4 cm^{-1}. The flow-through cell can be heated or cooled, but all measurements reported here were performed at room temperature. The ATR-IR cell is described in more detail elsewhere.[29,32]

Modulation Experiments. Ethanol served as solvent for ATR-IR measurements. Before each experiment the solvent was saturated with nitrogen gas (CarbaGas, 99.995%) and was allowed to flow first over the IRE until no variation in the spectrum could be detected. The corresponding spectrum, recorded by co-adding 200 interferograms, served as the reference for all subsequent measurements. GSH at typical concentrations of about 0.35 mM was then introduced at a flow rate of 0.18

(15) Fang, C.; Zhou, X. *Electroanalysis* **2002**, *14*, 711.
(16) Wang, J.; Gründler, P. *Electroanalysis* **2003**, *15*, 1756.
(17) Zhao, F.; Zeng, B.; Pang, D. *Electroanalysis* **2003**, *15*, 1060.
(18) Zhou, A.; Xie, Q.; Wu, Y.; Cai, Y.; Nie, L.; Yao, S. *J. Colloid Interface Sci.* **2000**, *229*, 12.
(19) Hepel, M.; Tewksbury, E. *J. Electroanal. Chem.* **2003**, *552*, 291.
(20) Zeng, B.; Ding, X.; Zhao, F. *Electroanalysis* **2002**, *14*, 651.
(21) Wang, J.; Zeng, B.; Fang, C.; X., Z. *Electroanalysis* **2000**, *12*, 763.
(22) Fang, C.; Zhou, X. *Electroanalysis* **2003**, *15*, 1632.
(23) Aihara, M.; Tanaka, F.; Miyazaki, Y.; Takehara, K. *Anal. Lett.* **2002**, *35*, 759.
(24) Schaaff, T. G.; Knight, G.; Shafigullin, M. N.; Borkman, R. F.; Whetten, R. L. *J. Phys. Chem. B* **1998**, *102*, 10643.
(25) Schaaff, T. G.; Whetten, R. L. *J. Phys. Chem. B* **2000**, *104*, 2630.
(26) Negishi, Y.; Takasugi, Y.; Sato, S.; Yao, H.; Kimura, K.; Tsukuda, T. *J. Am. Chem. Soc.* **2004**, *126*, 6518.
(27) Buffeteau, T.; Desbat, B.; Turlet, J. M. *Appl. Spectrosc.* **1991**, *45*, 380.
(28) Harrick, N. J. *Internal Reflection Spectroscopy*; Interscience: New York, 1967.
(29) Urakawa, A.; Wirz, R.; Bürgi, T.; Baiker, A. *J. Phys. Chem. B* **2003**, *107*, 13061.
(30) Ferri, D.; Bürgi, T. *J. Am. Chem. Soc.* **2001**, *123*, 12074.
(31) Baurecht, D.; Porth, I.; Fringeli, U. P. *Vib. Spectrosc.* **2002**, *30*, 85.
(32) Bürgi, T.; Baiker, A. *J. Phys. Chem. B* **2002**, *106*, 10649.
(33) Wirz, R.; Bürgi, T.; Baiker, A. *Langmuir* **2003**, *19*, 785.
(34) Bürgi, T.; Bieri, M. *J. Phys. Chem. B* **2004**, *108*, 13364.
(35) Muller, M.; Buchet, R.; Fringeli, U. P. *J. Phys. Chem.* **1996**, *100*, 10810.

mL/min, and the adsorption process was followed in situ. Note that at this concentration the signal contribution from the dissolved molecules is negligible. After about 4 h the static ATR-IR spectrum was recorded. Modulation was then started by periodically varying the "pH" by pumping alternately ethanol and a solution of HCl and NaOH, respectively, in ethanol over the sample (approximate concentrations are 0.013 mM for HCl and 0.18 mM for NaOH in ethanol). In the following we will refer to pH modulation for experiments where the concentration of acid and base was periodically changed in ethanol. The solutions were saturated with N_2 and stored in separate glass bubble tanks. A typical modulation experiment consisted of two initial "dummy loops" to allow the system to reach a new quasi stationary state followed by averaging over six measurement loops. During one measurement period (loop, flow of ethanol followed by an equally long flow of HCl and NaOH, respectively, in ethanol) 60 infrared spectra were recorded at 80 kHz sampling rate using the rapid scan acquisition mode of the FT-IR spectrometer. For each spectrum several interferograms were averaged. By changing the number of interferograms per spectrum and loop (6, 10, 30, and 40) different modulation periods $T = 72.4$, 120.7, 362.4, and 483.2 s could be achieved. Time-resolved infrared spectra were then demodulated by means of digital phase-sensitive detection (PSD) according to eq 1:

$$A_k^{\phi_k^{\mathrm{PSD}}}(\tilde{\nu}) = \frac{2}{T}\int_0^T A(\tilde{\nu},t)\,\sin(k\omega t + \phi_k^{\mathrm{PSD}})\,\mathrm{d}t \qquad (1)$$

where $k = 1, 2, 3, \ldots$ determines the demodulation frequency, i.e., fundamental, first harmonic, and so on, $\tilde{\nu}$ denotes the wavenumber, ω is the stimulation frequency, T represents the modulation period, and ϕ_k^{PSD} is the demodulation phase angle. With a set of time-resolved spectra $A(\tilde{\nu},t)$ eq 1 can be evaluated for different phase angles ϕ_k^{PSD}, resulting in a series of phase -resolved spectra $A_k^{\phi_k^{\mathrm{PSD}}}$. A description in more detail of the modulation technique applied here can be found elsewhere.[32,36] Adsorption experiments described above were carried out with GSH in the three ionic forms, i.e., zwitterionic, cationic, and anionic. Subsequent pH modulation experiments were neutral−acidic and neutral−basic for the zwitterionic form, neutral−acidic for the cationic form, and neutral−basic for the anionic form.

DFT Calculations of L-Glutathione. To better understand the structure of the different ionic forms of GSH (zwitterionic, cationic, and anionic), we have performed density functional theory (DFT) calculations using the hybrid functional B3PW91[37,38] with a 6-31G basis set.[39] GAUSSIAN03 was used for all calculations.[40] The conformational space of the molecule was probed using a Born−Oppenheimer molecular dynamics (BOMD)[41] with a semiempirical method (AM1).[42] For every ionic form five conformations with low energies were chosen as the starting geometries for structure optimization performed by DFT calculations. DFT calculations resulted generally in Y-shape conformations for zwitterionic and cationic GSH and T-shape conformations for anionic GSH.

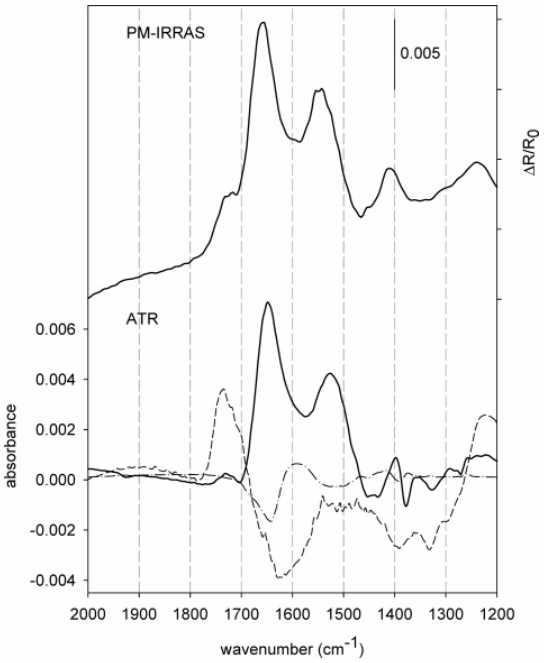

Figure 1. PM-IRRAS and ATR-IR spectra of zwitterionic GSH adsorbed on Au from neutral solution (about pH 5). PM-IRRAS spectrum (top) was recorded after sample immersion in distilled water for 12 h. Ethanol solution was used for an adsorption process of GSH on a gold-coated Ge IRE. After about 4 h of adsorption the static ATR-IR spectrum was recorded (bold solid line, bottom). Demodulated, phase-resolved spectra for a neutral−acidic (dashed line) and a neutral−basic (point−dashed line) modulation experiment are presented at the same scale as the static spectrum. During the modulation experiment (T = 483.2 s) acidic (basic) and neutral solutions were allowed to flow alternately over the GSH sample (flow rate = 0.18 mL/min) and 60 infrared spectra were recorded at 80 kHz sampling rate.

Results

GSH has four relevant possibilities for acid dissociation.[43] The corresponding pK values are (determined at 25 °C and ionic strength of 0.2−0.55 M):[44] 2.05 (−COOH of glu), 3.40 (−COOH of gly), 8.72 (−SH), and 9.49 ($-NH_3^+$). Some possible ionic forms are shown in Chart 1. In ethanol solution the zwitterionic form (Chart 1, bottom left) prevails (see below).

PM-IRRAS and ATR-IR spectra of zwitterionic GSH on Au together with demodulated spectra of two modulation experiments are displayed in Figure 1. The PM-IRRAS (Figure 1, top) and the ATR-IR spectrum (Figure 1, bottom, bold solid line) resemble each other surprisingly well, bearing in mind that measurement conditions and sample preparation are rather different (see Experimental Section). Strong bands are observed in the ATR-IR spectrum at 1649 and 1527 cm^{-1} (1658 and 1547 cm^{-1} for PM-IRRAS) and less intense signals at around 1397 and 1731 cm^{-1} (1410 and 1725 cm^{-1}). The latter is less prominent in the ATR-IR spectrum. Demodulated (phase-resolved) spectra are depicted (at the same scale) as the dashed line for the

(36) Baurecht, D.; Fringeli, U. P. *Rev. Sci. Instrum.* **2001**, *72*, 3782.
(37) Becke, A. D. *J. Chem. Phys.* **1993**, *98*, 5648.
(38) Perdew, J. P.; Chevary, J. A.; Vosko, S. H.; Jackson, K. A.; Pederson, M. R.; Singh, D. J.; Fiolhais, C. *Phys. Rev. B* **1992**, *46*, 6671.
(39) Ditchfield, R.; Hehre, W. J.; Pople, J. A. *J. Chem. Phys.* **1971**, *54*, 724.
(40) Frisch, M. J.; Trucks, G. W.; Schlegel, H. B.; Scuseria, G. E.; Robb, M. A.; Cheeseman, J. R.; Montgomery, J. A.; Vreven, T.; Kudin, K. N.; Burant, J. C.; Millam, J. M.; Iyengar, S. S.; Tomasi, J.; Barone, V.; Mennucci, B.; Cossi, M.; Scalmani, G.; Rega, N.; Petersson, G. A.; Nakatsuji, H.; Hada, M.; Ehara, M.; Toyota, K.; Fukuda, R.; Hasegawa, J.; Ishida, M.; Nakajima, T.; Honda, Y.; Kitao, O.; Nakai, H.; Klene, M.; Li, X.; Knox, J. E.; Hratchian, H. P.; Cross, J. B.; Adamo, C.; Jaramillo, J.; Gomperts, R.; Stratmann, R. E.; Yazyev, O.; Austin, A. J.; Cammi, R.; Pomelli, C.; Ochterski, J. W.; Ayala, P. Y.; Morokuma, K.; Voth, G. A.; Salvador, P.; Dannenberg, J. J.; Zakrzewski, V. G.; Dapprich, S.; Daniels, A. D.; Strain, M. C.; Farkas, O.; Malick, D. K.; Rabuck, A. D.; Raghavachari, K.; Foresman, J. B.; Ortiz, J. V.; Cui, Q.; Baboul, A. G.; Clifford, S.; Cioslowski, J.; Stefanov, B. B.; Liu, G.; Liashenko, A.; Piskorz, P.; Komaromi, I.; Martin, R. L.; Fox, D. J.; Keith, T.; Al-Laham, M. A.; Peng, C. Y.; Nanayakkara, A.; Challacombe, M.; Gill, P. M. W.; Johnson, B.; Chen, W.; Wong, M. W.; Gonzalez, C.; Pople, J. A. *GAUSSIAN03*, Rev. B.05 ed.; Gaussian, Inc.: Wallingford, CT, 2003.
(41) Helgaker, T.; Eggerud, E.; Jensen, H. J. A. *Chem. Phys. Lett.* **1990**, *173*, 145.
(42) Dewar, M.; Thiel, W. *J. Am. Chem. Soc.* **1977**, *99*, 4499.
(43) Huckerby, T. N.; Tudor, A. J.; Dawber, J. G. *J. Chem. Soc., Perkin Trans. 2* **1985**, 759.
(44) Rabenstein, D. L. *J. Am. Chem. Soc.* **1973**, *95*, 2797.

neutral−acidic and the point−dashed line for the neutral−basic modulation experiment. The demodulation phase angle ϕ_k^{PSD} (eq 1) was chosen such that the amplitude $A_{k^{\phi_k^{PSD}}}$ was at the maximum. Only bands that are periodically changing with time due to the stimulation (pH modulation) show up in these spectra. The spectrum for the neutral−acidic experiment reveals strong positive bands at 1734 and 1230 cm^{-1} and a negative band of similar intensity at 1625 cm^{-1}. Further less intense signals are observed at 1390 and 1330 cm^{-1}. During the first half-period of the modulation experiment, ethanol was flowed over the sample and the signal at 1734 cm^{-1} was observed to decrease simultaneously. At the beginning of the second half-period HCl in ethanol was introduced accompanied by a decrease of the band at 1625 cm^{-1} and a simultaneous increase of the signal at 1734 cm^{-1}. Thus, the two bands mentioned reveal amplitudes of different sign in the demodulated spectrum. Note that for demodulation angles ϕ_k^{PSD} differing by 180° the resulting demodulated spectra are identical but for the sign of all absorption bands. An in-flow of NaOH solution over the sample during the first half-period resulted in a rising of the band at around 1593 cm^{-1}—when switched to neutral solution, this signal became weaker, while the one around 1643 cm^{-1} increased. In the static absorption spectrum (solid line) the signal at 1595 cm^{-1} is hidden. Detection of overlapping or hidden bands is thus a useful attribute of phase-sensitive detection. Furthermore phase-resolved spectra represent high-quality difference spectra. For the described pH modulation experiments the spectra reveal the difference between different ionic forms after adsorption of the molecule in the zwitterionic state. As can be seen from the amplitudes of these phase-resolved spectra, the intensity of the corresponding bands (1625 and 1725 cm^{-1}) changes significantly with respect to the static signals.

PM-IRRAS and ATR-IR spectra of GSH adsorbed in cationic form (from ethanol + HCl) are displayed in Figure 2. Again good agreement between the two spectra is apparent. Compared to the spectrum of zwitterionic GSH depicted in Figure 1, the signal above 1700 cm^{-1} is clearly more pronounced. On the other hand in the cationic case the band at about 1650 cm^{-1} is less pronounced compared to the one at 1535 cm^{-1}. The demodulated spectrum of the neutral−acidic modulation experiment (dashed line) reveals a positive signal at 1735 cm^{-1} and a negative one around 1620 cm^{-1} which is not visible in the static spectrum. Note that the demodulated spectrum is assigned its own ordinate on the right side (absorbance PSD, phase sensitive detection). The modulation experiment (neutral−acidic) was performed in a way analogous to the one described for GSH adsorbed in zwitterionic form. However, the amplitude of the bands relative to the static spectrum is about four times smaller compared to the analogous experiment with the GSH layer adsorbed in zwitterionic form (from ethanol).

PM-IRRAS and ATR-IR spectra of GSH adsorbed in anionic form are depicted in Figure 3. Both spectra reveal bands around 1600 cm^{-1} (1595 cm^{-1} in ATR-IR and 1608 cm^{-1} in PM-IRRAS) and about 1400 cm^{-1} (1404 and 1408 cm^{-1}). Signals at 1643 and 1542 cm^{-1} in the ATR-IR spectrum are less pronounced and appear as a shoulder on the prominent band at 1595 cm^{-1}. The modulation experiment neutral−basic (dashed line) bears again some resemblance to the corresponding experiment described for GSH adsorbed in zwitterionic form (Figure 1) but also exhibits significant differences in the 1650 and 1400 cm^{-1} spectral regions. The small amplitudes with respect to the static adsorption spectrum (note the ordinate on the right side) are a further difference with respect to the analogous experiment for the zwitterionic GSH.

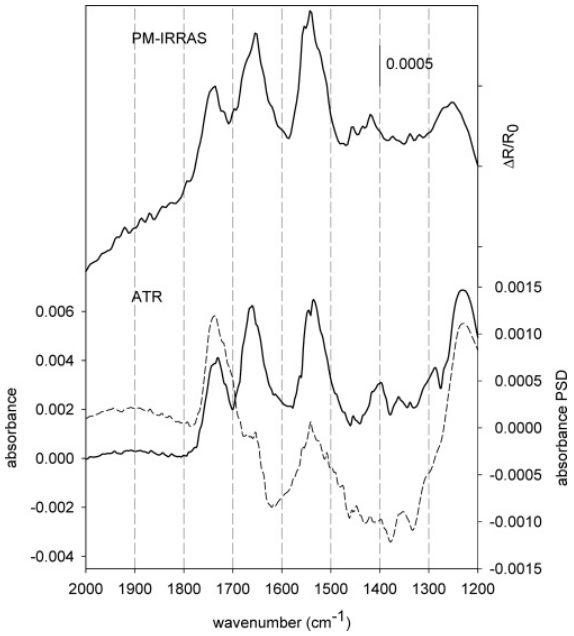

Figure 2. PM-IRRAS and ATR-IR spectra of cationic GSH adsorbed on Au from acidic solution (about pH 1). The PM-IRRAS spectrum (top) was recorded after 12 h of sample immersion in acidic distilled water. The ATR-IR spectrum (bold solid line, bottom) was recorded after about 4 h of adsorption from ethanol + HCl solution. A demodulated, phase-resolved spectrum (dashed line) is presented together with the static spectrum. The corresponding modulation experiment ($T = 483.2$ s) consisted of an alternate flow of neutral and acidic solutions (flow rate = 0.18 mL/min) over the cationic GSH sample. Note that the demodulated spectrum has a different ordinate (absorbance PSD).

All the described modulation experiments reveal that (at least partial) interconversion between ionic forms is a reversible process regardless of the ionic form GSH was adsorbed on Au. Reversibility further holds for different modulation periods applied; i.e., T = 72.4, 120.7, 362.4, and 483.2 s. We should also mention that the signals were well-reproducible in consecutive modulation experiments and experiments performed on different samples on different days.

The time dependence of the ATR-IR signals at 1650 cm^{-1} (upper curve) and 1725 cm^{-1} (lower curve) within a modulation period of the neutral−acidic stimulation experiment is depicted in Figure 4. GSH was adsorbed in zwitterionic form. The experiment reveals two regimes with different deprotonation kinetics. The first regime (I) is a fast process starting at $t = 0$ when ethanol replaces the acidic solution. After around 50 s a slower process is observed with a linear decrease with time of the intensity at 1725 cm^{-1}. This slow process is not completed at the end of the first half-period (at $t = 241.6$ s) of the modulation experiment.

Difference spectra for the two regimes described above are depicted in Figure 5. The solid line is the difference between spectra no. 7 ($t = 50$ s) and no. 1 ($t = 0$ s) of regime I, and the dashed line is the difference between spectra no. 30 ($t = T/2 = 241.6$ s) and no. 7 ($t = 50$ s) of regime II. The difference spectra of the two regions are significantly different. It appears that in the difference spectrum of regime II the positive signal between 1500 and 1600

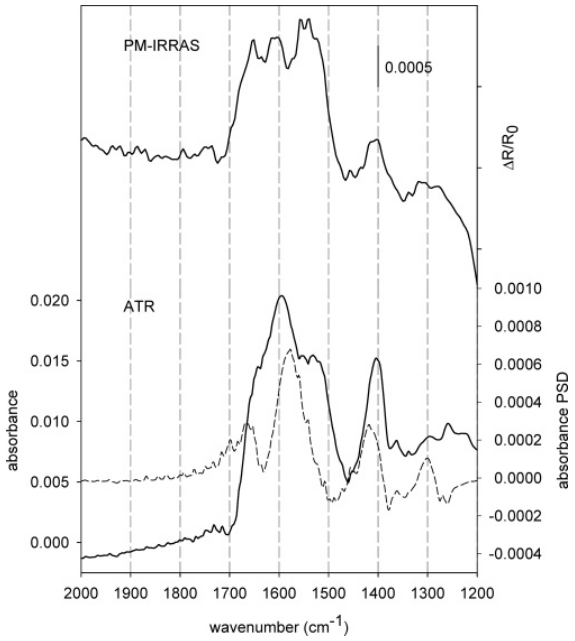

Figure 3. PM-IRRAS and ATR-IR spectra of anionic GSH on Au adsorbed from basic solution (about pH 12). After 12 h of sample immersion the PM-IRRAS spectrum (top) was recorded. The ATR-IR spectrum (bold solid line, bottom) was recorded after 4 h of adsorption. A demodulated, phase-resolved spectrum (dashed line) is presented together with the static adsorption spectrum. During the corresponding modulation experiment (T = 483.2 s) neutral and basic solutions were allowed to flow alternately over the anionic GSH sample at a flow rate of 0.18 mL/min. The ordinate on the right side (absorbance PSD) refers to the phase-resolved spectrum.

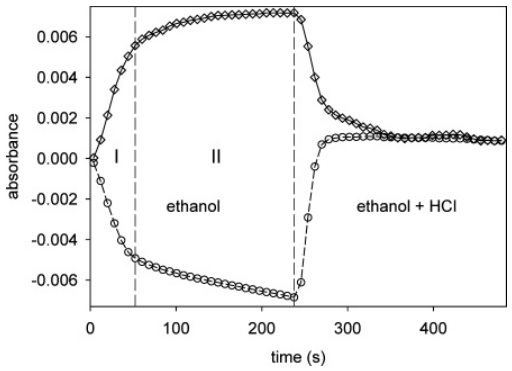

Figure 4. Absorbance of signals at 1650 (upper curve) and 1725 cm^{-1} (lower curve) as a function of time for a modulation experiment (T = 483.2 s). GSH was adsorbed on a gold-coated Ge IRE in zwitterionic form from ethanol solution. An alternate flow of ethanol, followed by a flow of ethanol + HCl of equal time was admitted to the GSH sample during a modulation experiment. The time dependence of the two signals reveals two regimes with different deprotonation kinetics.

cm^{-1} becomes more prominent with respect to regime I. In this spectral region, at 1527 cm^{-1} precisely, there is a prominent band in the static ATR-IR spectrum (see Figure 1). The positive signals at about 1400 and 1330 cm^{-1} have different relative intensity in the difference spectra of the two regimes. Furthermore, in regime I the relative intensity of the 1220 cm^{-1} with respect to the 1735 cm^{-1} band is much larger than in regime II.

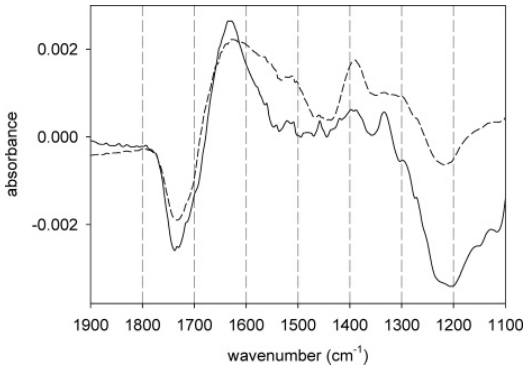

Figure 5. Difference spectra representing changes within the two regimes with different deprotonation kinetics (see text for details). Both spectra are calculated for the first half-period of a modulation experiment when ethanol was flowed over the zwitterionic GSH sample, after a flow of HCl in ethanol. The difference between spectra no. 7 (t = 50 s) and no. 1 (t = 0 s) in Figure 4 is depicted as a solid line for regime I and as a dashed line for regime II, corresponding to the difference between spectra no. 30 (t = T/2) and no. 7.

Discussion

General Discussion. PM-IRRAS and in situ ATR-IR spectra of GSH on Au are in surprisingly good agreement with each other for the corresponding adsorption condition, i.e., for neutral, acidic, and basic solution (see Figures 1−3). Besides the two measurement techniques applied, sample preparation differed considerably by the use of substrate, solvent (water for PM-IRRAS and ethanol for ATR-IR measurements), and sample immersion time (4 h for ATR-IR and 12 h for PM-IRRAS) as well as measurement conditions (in air for PM-IRRAS and liquid phase for ATR-IR). In this respect it is important to note that the selection rule for ATR-IR spectroscopy on metal films[45,46] was found to be the same as the well-established selection rule for external reflection off metal surfaces.[47] Upon careful inspection differences between PM-IRRAS and ATR-IR spectra are, however, observable, which may be due to different ionic states and/or different interactions within the chemisorbed layer under the vastly different measurement conditions.

The reversible switching between the different ionic forms of GSH adsorbed on Au stimulated by periodic admission of acid and base, respectively, made it possible to follow the induced spectral changes using in situ ATR-IR combined with modulation spectroscopy. When identical modulation experiments were performed with GSH layers prepared by adsorption of different ionic forms of GSH (in the absence and presence of HCl and NaOH, respectively), the resulting spectra were similar. Careful inspection of these spectra, however, revealed some spectral differences. Furthermore, the relative size of the static and modulated signal differed significantly, depending on adsorption condition; i.e., the intensity which changed due to the pH modulation was much less in case in which GSH was adsorbed in cationic and anionic form, respectively (see Figures 1−3). This could be due to a smaller fraction of adsorbed molecules that are reversibly protonated−deprotonated, or due to slower protonation−deprotonation kinetics. In the pH modulation experiments

(45) Osawa, M.; Ataka, K.-I.; Yoshii, K.; Yotsuyanagi, T. *J. Electron. Spectrosc. Relat. Phenom.* **1993**, *64/65*, 371.
(46) Hutter, E.; Assiongbon, K. A.; Fendler, J. H.; Roy, D. *J. Phys. Chem. B* **2003**, *107*, 7812.
(47) Greenler, R. G. *J. Chem. Phys.* **1966**, *44*, 310.

(dashed and point−dashed spectra in Figures 1−3) the corresponding stimulation was identical. Still the system response was different, depending on the ionic state of GSH during initial adsorption. In the modulation experiments only the reversibly changing species are observed. If adsorption of zwitterionic GSH and subsequent protonation of this layer by flowing dissolved HCl would lead to a layer that is completely identical to the one formed from direct adsorption of protonated (cationic) GSH and visa versa, then protonation−deprotonation modulation experiments (HCl in ethanol versus ethanol) would result in identical spectra, independent of the initial state of adsorption. The experiments show that this is not the case. We conclude that adsorption of GSH in the corresponding ionic form leads to adsorbate layers, which cannot be interconverted into completely identical layers to one other by simply changing the ionic form of the adsorbate. The system "remembers" adsorption conditions.

The DFT calculations performed for different ionic forms of GSH resulted in characteristic shapes, i.e., a Y-shape for zwitterionic and cationic and a T-shape for the anionic form (see Figure 6). These shapes were found to be a general feature for the corresponding ionic form, regardless of the fact that several structures with similar energy were located for each form. It is likely that the shape of the molecule during the adsorption process is decisive for the structure of the resulting adsorbate layer. This may thus explain the observation that the system remembers the adsorption conditions as evidenced by the pH modulation experiments.

A more detailed analysis of the infrared spectra and of the in situ ATR-IR spectra in particular, allows to extract more molecular level information. However, this requires assignment of the vibrational bands, which is presented in the next section.

Assignment of Vibrational Bands. Prominent bands for adsorbed glutathione are associated with the acid, carboxylate, amide, and ammonium functional groups. The following assignment is based on literature data on amino acids and peptides[48−51] and quantum chemical calculations as well as the modulation experiments. The observed band positions for the different experiments and the corresponding assignment are summarized in Table 1.

The carboxylic acid vibrations ν(−COOH) are easily spotted as a band above 1700 cm^{-1}. In the PM-IRRAS spectrum the band is found at 1741 cm^{-1} for GSH adsorbed from acidic solution (Figure 2) and at about 1725 cm^{-1} for GSH adsorbed from neutral solution (Figure 1). The latter value corresponds well with reported spectra of GSH in H_2O and D_2O.[51] In the corresponding ATR-IR experiments the bands are found at 1736 and 1731 cm^{-1}, respectively. The frequency shift of the band associated with the ν(−COOH) vibrations observed in both types of experiments (ATR-IR and PM-IRRAS) may be due to different interactions of these groups under different conditions and/or different extents of dissociation of the two acid groups. The band shifts to lower wavenumbers as part of the acid groups are dissociated. Under such conditions the ν(−COOH) vibration of the weaker acid is observed predominantly. This is in full agreement with the calculated infrared spectra of protonated GSH, which consistently yield lower frequencies of ν(−COOH) for the gly

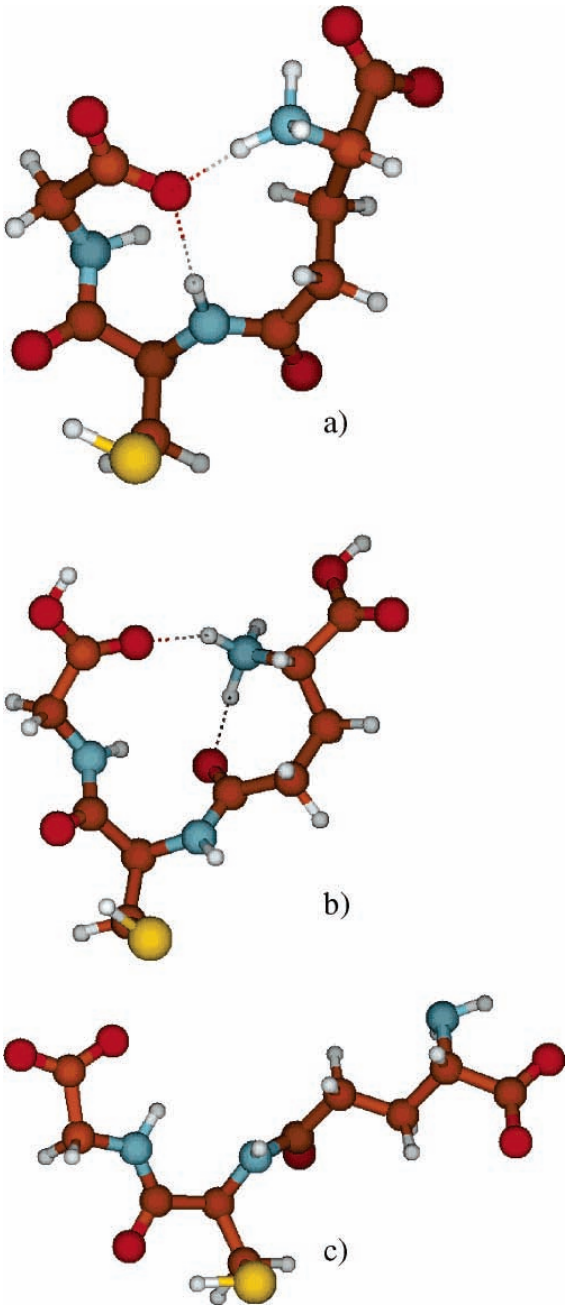

Figure 6. Pictorial representations of optimized structures of GSH as found by density functional theory calculations (see text for details): (a) Y-shaped structure of GSH zwitterionic; (b) Y-shaped structure of GSH cationic; (c) T-shaped structure of GSH anionic.

part of the molecule in all conformations found. The frequency difference of ν(COOH) associated with the two carboxylic acid groups is caused by the nearby NH_3^+ group in the glu part. It is known that local electric fields (local environment) can affect the frequency of the ν(−COOH) vibration.[49,50] The band associated with the two ν(−COOH) vibrations has asymmetric shape and exhibits (at least) two components. This is seen best in the demodulated spectra of the modulation experiment, where alternately

(48) Pearson, J. F.; Slifkin, M. A. *Spectrochim. Acta* **1972**, *28A*, 2408.
(49) Wright, W. W.; Vanderkooi, J. M. *Biospectroscopy* **1997**, *3*, 458.
(50) Dioumaev, A. K.; Braiman, M. S. *J. Am. Chem. Soc.* **1995**, *117*, 10572.
(51) Picquart, M.; Grajcar, L.; Baron, M. H.; Abedinzadeh, Z. *Biospectroscopy* **1999**, *5*, 328.

Table 1. Observed Vibrational Bands in the Static and Phase-resolved Spectra Depicted in Figures 1-3 and 5 and Corresponding Assignment. pH Modulation Experiments (Neutral − Acidic and Neutral − Basic) Were Performed for Layers that Were Prepared from Zwitterionic, Cationic and Anionic GSH

static signals						ATR-IR phase-resolved signals					
GSH zwitterionic		GSH cationic		GSH anionic		GSH zwitterionic		GSH cationic	GSH anionic	
PM-IRRAS	ATR-IR	PM-IRRAS	ATR-IR	PM-IRRAS	ATR-IR	assignment	neutral−acidic	neutral−basic	neutral−acidic	neutral-basic	assignment
1725	1731	1741	1736			ν(−COOH)	1734		1735		ν(−COOH)
1658	1649	1660	1662	1653	1643	amide I	1625		1620		ν_{as}(−COO$^-$)
				1608	1595	ν_{as}(−COO$^-$)	1575		1575		ν_{as}(−COO$^-$)
1547	1527	1543	1537	1550	1542	amide II	1390		1380		ν_s(−COO$^-$)
		1420	1410			δ_s(−CH$_2$) scissoring	1330		1330		ρ_w(−CH$_2$) wagging
1410	1397			1408	1404	ν_s(−COO$^-$)	1230−1250		1230		δ(−COH) bending + ν(CO) stretching
1230		1230	1230			δ(−COH) bending + ν(CO) stretching				1655	amide I
								1643			shift of ν_{as}(−COO$^-$)
										1632	ν_{as}(−COO$^-$), amide I
								1593			shift of ν_{as}(−COO$^-$)
										1578	ν_{as}(−COO$^-$)
								1520		1490	δ_s(−NH$_3^+$)
										1410	ν_s(−COO$^-$)
										1300	

ethanol and ethanol + HCl was flowed over the sample (Figures 1 and 2). In the PM-IRRAS and the static ATR-IR spectra of the protonated species (Figure 2) the two components are difficult to distinguish, due to the lower quality of the static spectra.

A feature arising together with the ν(−COOH) band is the broad intense signal at about 1230−1250 cm^{-1}. We assign this band to a C−O−H bending mode with possibly some C−O stretching character.[48] This band disappears in deuterated amino acids,[48] and its broadness furthermore supports the assignment. The calculations for the protonated GSH predict a very intense C−O−H band at somewhat lower energy. Alternatively, amide III vibrations fall in this spectral region. However, these vibrations are usually considerably weaker than the amide I vibrations,[52] which is also confirmed by the calculations.

The most prominent bands of GSH adsorbed from neutral or acidic solution both in the PM-IRRAS and in the ATR-IR experiments around 1660 and 1540 cm^{-1} are mostly due to amide I and amide II vibrations, respectively. The band maxima shift slightly upon changing conditions. For example in the ATR-IR the amide II band shifts from 1527 cm^{-1} in the spectrum of GSH adsorbed from ethanol to 1537 cm^{-1} in the spectrum of GSH adsorbed from ethanol + HCl. The observed band shifts are due to different interactions (intra- or intermolecular) of the amide groups and possibly overlap with $-COO^-$ and $-NH_3^+$ vibrations.

In the deprotonated state the carboxylic acid groups give rise to asymmetric and symmetric stretching vibrations expected at 1550−1620 cm^{-1} (ν_{as}(−COO$^-$)) and 1300−1420 cm^{-1} (ν_s(−COO$^-$)), respectively.[49,52] The former bands are prone to overlap with amide and $-NH_3^+$ vibrations. The static ATR-IR spectrum of GSH adsorbed on Au from ethanol (Figure 1) is dominated by the amide bands at 1649 and 1527 cm^{-1}. Between these bands there is considerable intensity. A qualitatively similar situation is found for the PM-IRRAS experiment (Figure 1, top) of GSH adsorbed from neutral aqueous solution. In the ATR-IR and PM-IRRAS spectra of protonated GSH (Figure 2) the intensity between the amide I and amide II bands is much weaker and in the corresponding spectra of deprotonated GSH (Figure 3) much stronger. The ν_{as}(−COO$^-$) signals are therefore found between the prominent amide I and amide II bands. The demodulated spectra of protonation−deprotonation experiments (Figures 1, 2, and 5) allow a more precise assignment of the ν_{as}(−COO$^-$) vibrations to an asymmetric band with maximum at 1620 cm^{-1} and a shoulder at 1575 cm^{-1}. With respect to the ν_s(−COO$^-$) modes, there is a band around 1410 cm^{-1} in the static ATR-IR and PM-IRRAS spectra. This band is most prominent in the ATR-IR spectrum (at 1404 cm^{-1}) of GSH that was adsorbed from ethanol + NaOH solution and can therefore be assigned to ν_s(−COO$^-$) vibrations. However, the ATR-IR and PM-IRRAS spectra in Figure 2 exhibit some intensity around 1420 cm^{-1}, even when the acid groups are protonated, which can be assigned to CH_2 scissoring modes. In the phase-resolved spectra of the protonation−deprotonation modulation experiments (Figures 1, 2, and 5) there are clear bands at 1390 and 1330 cm^{-1}. The former is due to a ν_s(−COO$^-$) vibration, whereas the latter can be assigned to CH_2 wagging modes.[48] In the calculations the CH_2 vibrations in this frequency range loose and gain intensity, respectively, upon protonation and deprotonation, respectively, of the acid groups.

(52) Bellamy, L. J. *The Infrared Spectra of Complex Molecules*; Chapman and Hall−Wiley: London−New York, 1975.

Signals due to the $-NH_3^+$ group are expected around 1600 cm^{-1} for the weak deformation vibration ($\delta_{as}(-NH_3^+)$) and for the stronger symmetric deformation at 1500−1550 cm^{-1} ($\delta_s(-NH_3^+)$).[48] Assignment of these bands is hampered by their generally low intensity and overlap with stronger bands. The best indications for these bands stem from the modulation experiments where the adsorbed GSH was alternately exposed to ethanol and ethanol + NaOH, which is expected to cause interconversion between $-NH_3^+$ and NH_2 groups. Demodulated spectra for such experiments are shown in Figures 1 and 3 for GSH adsorbed from ethanol and ethanol + NaOH, respectively. In these spectra there is a broad relatively weak band visible around 1520 cm^{-1} (negative in Figure 1), which can be assigned to the symmetric $-NH_3^+$ deformation $\delta_s(-NH_3^+)$. This band is negative in Figure 1 because the $-NH_3^+$ group is deprotonated upon admission of NaOH, resulting in NH_2. The latter group should exhibit a scissoring mode around 1590−1650 cm^{-1},[52] which may however be too weak to be observed.[48] Indeed a broad band at about 1590 cm^{-1} arises upon deprotonation of the $-NH_3^+$ group (Figures 1 and 3). However, we prefer another assignment of this band: Upon deprotonation of the $-NH_3^+$ group the prominent $\nu_{as}(COO^-)$ mode of the close COO^-- group is expected to shift considerably to lower wavenumbers due to the loss of electron withdrawal.[48,52,53] Therefore the negative and positive bands, respectively, at 1643 and 1590 cm^{-1}, respectively, in Figure 1 are assigned to a frequency shift of $\nu_{as}(COO^-)$ to lower wavenumbers upon deprotonation of the $-NH_3^+$ group. A frequency shift or change in intensity of the amide I band possibly also contributes to this feature in the demodulated spectra.

GSH on Au Adsorbed from Ethanol. In the in situ ATR-IR spectrum of GSH adsorbed on Au from ethanol (Figure 1) the ν(COOH) vibration at 1731 cm^{-1} has very low intensity. In ethanol carboxylic acids are not dissociated in the absence of a base. Hence, in ethanol GSH exists in zwitterionic form, with deprotonated acid (COO^-) and protonated amine ($-NH_3^+$) group on the glu part and an acid group (COOH) on the gly part of the molecule (Chart 1, bottom left). The presence of a strong ν(COOH) signal was also confirmed for GSH dissolved in ethanol-d_6 (Supporting Information). Unless there are further interactions to be considered, dissociation of the acid is not expected upon adsorption through the thiol group of the molecule. For example, the adsorption of 3-mercaptopropionic acid from ethanol on Au films, as investigated by in situ surface-enhanced infrared absorption spectroscopy, revealed a ν(COOH) band above 1700 cm^{-1}.[54] Carboxylate vibrations were not observed, thus showing that the carboxylic acid group of the adsorbed molecule is fully protonated in ethanol.[54] The very low intensity of the band at 1731 cm^{-1} in Figure 1 associated with carboxylic acid groups is therefore surprising. This could be explained by the presence of a highly ordered GSH layer bearing acid groups with the C=O bond oriented almost perfectly parallel to the Au surface. This would result in a dynamic dipole moment associated with this vibration parallel to the surface and, according to the metal surface selection rule,[55] in very weak intensity. We consider this as unlikely. We suggest that a large fraction of GSH molecules is also deprotonated at the gly moiety upon adsorption, which strongly indicates interaction of the latter acid group with the Au surface. Interaction of acid groups with gold surfaces has been reported before. For the adsorption of thioctic acid on Au from ethanol a mixture of carboxyl and carboxylate was found by ex situ reflection absorption infrared spectroscopy.[56] This work also showed that thioctic acid adsorption from ethanol leads to disordered adsorbate layers.

Adsorption of molecules containing both thiol and carboxylic acid functional groups on Au is determined by the former.[54,56] Whether the latter can also interact with the Au surface depends on the distance between the two functional groups and the flexibility of the molecule. For GSH there are six single bonds between the thiol and acid group of the gly part, which guarantees high flexibility and thus allows the acid group to interact with the Au surface.

The periodic admission of ethanol and HCl in ethanol to the GSH adsorbed from ethanol (demodulated spectra in Figure 1, bottom) leads to significant and reversible changes induced by protonation−deprotonation. The plot of the intensity of the ν(COOH) vibration as a function of time within the modulation experiment in Figure 4 shows that protonation is fast. On the other hand, deprotonation clearly proceeds in two steps, a fast (regime I) and a considerably slower one (regime II). Within about 200 s the second deprotonation process is not completed. Figure 5 reveals significantly different spectral changes within the two regimes. From a chemical point of view the stronger carboxylic acid on the glu part is expected to deprotonate first. This is supported by two observations: Figure 5 shows that the ν(COOH) signal has a more pronounced intensity at higher wavenumbers for the faster deprotonation (regime I), as expected for the glu part of the molecule. Similarly, the appearing asymmetric carboxylate vibration $\nu_{as}(COO^-)$ is found at higher wavenumber for the faster deprotonation, again indicating that the latter is associated with the glu part of the molecule.[49] It is furthermore apparent from Figure 5 that the relative intensity of the bands at 1735 and 1230 cm^{-1} is different for the two regimes. Both vibrations are associated with the acid groups (ν(COOH) and δ(COH)). The two vibrations usually exhibit different directions of the dynamic dipole moment. Their different relative intensity in the two regimes thus indicates that in the protonated state the two acid groups adopt significantly different orientation with respect to the surface.

On the basis of the observations made for the modulation experiments just discussed, and the nature of GSH on Au when adsorbed from ethanol as discussed above, we can propose the following processes during the modulation experiment: Upon admitting HCl the carboxylic acid groups are both protonated fast. For the gly part of the molecule this means that the interaction between the carboxylate and the surface is lost upon protonation. The DFT calculations show that for the protonated case the molecule tends to adopt a Y shape, stabilized by intramolecular hydrogen bonding between the two arms of the molecule. Upon flowing again ethanol the acid group of the glu part is deprotonated first. In a slower step the second carboxylic acid group is deprotonated upon readsorption on the surface. This view is further supported by the observation that a considerably more intense $\nu_s(COO^-)$ mode at 1390 cm^{-1} is observed for the slower regime. A strong $\nu_s(COO^-)$ mode is usually observed for carboxylate groups adsorbed on metal surfaces.[57] Another

(53) Roddick-Lanzilotta, A. D.; McQuillan, A. J. *J. Colloid Interface Sci.* **1999**, *217*, 194.
(54) Imae, T.; Torii, H. *J. Phys. Chem. B* **2000**, *104*, 9218.
(55) Francis, S. A.; Ellison, A. H. *J. Opt. Soc. Am.* **1959**, *49*, 131.
(56) Willey, T. M.; Vance, A. L.; Bostedt, C.; vanBuuren, T.; Meulenberg, R. W.; Terminello, L. J.; Fadley, C. S. *Langmuir* **2004**, *20*, 4939.
(57) Ortega Lorenzo, M.; Haq, S.; Bertrams, T.; Murray, P.; Raval, R.; Baddeley, C. J. *J. Phys. Chem. B* **1999**, *103*, 10661.

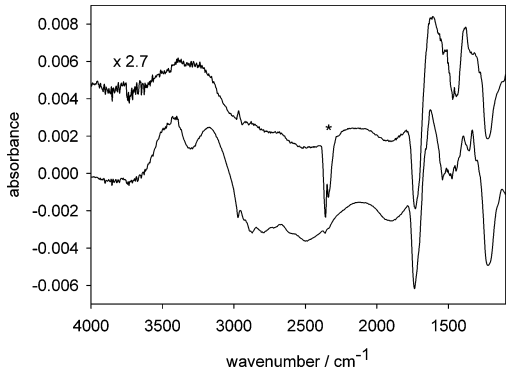

Figure 7. Difference spectra (overview) representing changes within the two regimes with different deprotonation kinetics (see text for details). Both spectra are calculated for the first half-period of a modulation experiment when ethanol was flowed over the zwitterionic GSH sample, after a flow of HCl in ethanol. The difference spectrum represents the changes between t = 50 and 0 s (bottom) and $t = T/2 = 241.3$ s and $t = 50$ s (top). The top spectrum was scaled in order to have comparable intensity. The asterisk indicates uncompensated absorption from atmospheric CO_2.

difference between the spectra of the two regimes (Figure 5) is the presence (absence) of a CH_2 band at 1330 cm^{-1} for the faster (slower) regime, which may be due to a reorientation of the molecule upon deprotonation. A rearrangement induced by the deprotonation is also indicated by the N−H and O−H stretching vibrations. Figure 7 shows overview difference spectra for the two deprotonation regimes. Prominent broad bands are observed at 2500 and 2800 cm^{-1} (negative) and 3200 and 3400 cm^{-1} (positive). The 2500 cm^{-1} band is characteristic for N^+−H groups involved as donor in hydrogen bonding.[58,59] The band at 2800 cm^{-1} may be due to an acid group involved as donor in a hydrogen bond. On the other hand the broad bands above 3000 cm^{-1} fall in the typical range of amide A (N−H stretching vibration) and amide B band (Fermi resonance-enhanced overtone of the amide II band).[60,61] The appearance of these bands clearly shows that the hydrogen-bonding network within the adsorbate layer changes considerably upon protonation−deprotonation. On the basis of the (gas-phase) calculations a rearrangement of the hydrogen bonding interactions upon changing the ionic state of the molecule is not surprising (Figure 6). These calculations only consider an isolated molecule. Intermolecular hydrogen-bonding interactions between adjacent molecules in the adsorbate layer are also feasible and were evidenced for other thiols bearing amide groups.[60−63] The exact structure of the hydrogen-bonded network within the GSH layer and whether the hydrogen bonding is intra- and/or intermolecular remain open at the present stage.

GSH Adsorbed from Ethanol + HCl. When adsorbing GSH in the presence of HCl, i.e., in the protonated form, the amplitude of the response in the modulation experiments (ethanol−(ethanol + HCl)) is comparably weak (Figure 2). A considerable fraction of acid groups are not deprotonated within half the modulation period upon flowing ethanol, in contrast to the behavior of the layer when adsorbed from ethanol. Since deprotonation of part of the carboxylic acid groups is assisted by interaction with the Au surface, as discussed above, this observation indicates that interaction between acid groups and the Au surface is inhibited or put in other words that the deprotonation is displaced to lower pH for a GSH layer adsorbed from ethanol + HCl. The DFT calculations show that for the protonated case the molecule adopts a Y shape. Within a densely packed layer of Y-shaped molecules there may not be enough free space available for the acid group

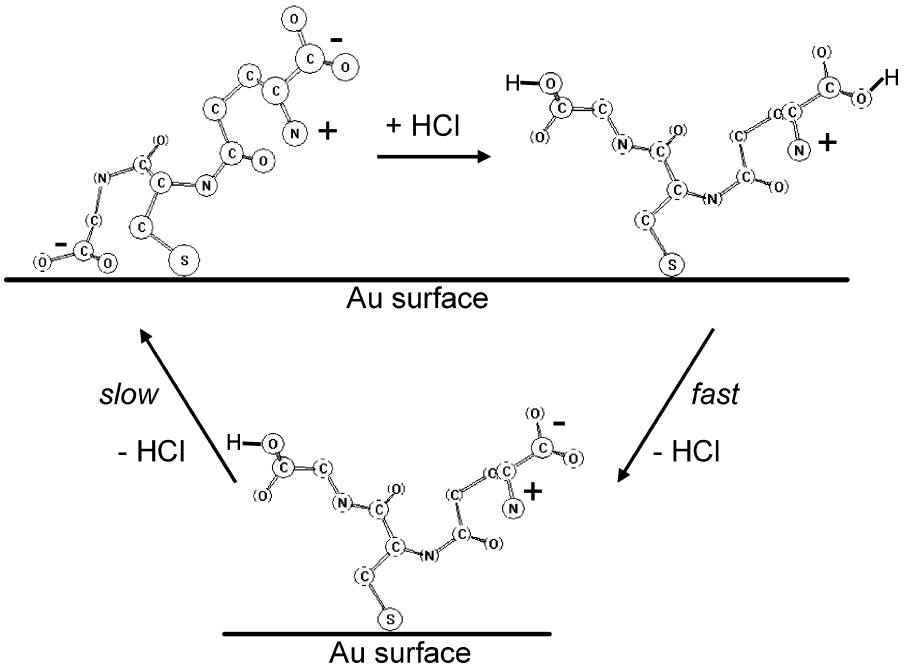

Figure 8. Pictorial representation of the processes occurring during protonation and deprotonation of L-glutathione on gold. The deprotonation in ethanol proceeds in two steps with distinctly different kinetics. The slow deprotonation of the carboxylic acid of the gly moiety is accompanied by adsorption of the carboxylate on the gold surface. During protonation−deprotonation a considerable rearrangement of the hydrogen-bonding network (inter- and/or intramolecular) takes place.

to interact with the Au surface and deprotonate. Comparison between the demodulated spectra for the ethanol−(ethanol + HCl) modulation experiments for the two layers, adsorbed from ethanol (Figure 1) and adsorbed from ethanol + HCl (Figure 2) show considerable similarities but also significant differences. One important difference in these spectra supporting the above view is a considerably broader and more intense $\nu_s(COO^-)$ mode at 1390 cm^{-1} for the layer adsorbed from ethanol. Also the intensity of the 1230 cm^{-1} band relative to the one at 1735 cm^{-1} is larger for the layer formed from protonated GSH. On the basis of the discussion above (Figure 5) this indicates that the gly part of GSH does not strongly respond to the protonation−deprotonation stimulation for the layer adsorbed from ethanol + HCl. Another significant difference is the region around 1660 cm^{-1}. Whereas for the layer adsorbed from ethanol + HCl there is no strong signal in this spectral region (plateau between the positive 1735 cm^{-1} and the negative 1620 cm^{-1} band), a signal can be observed for the layer adsorbed from ethanol. This spectral region is associated with the amide I bands. The different response of this spectral region for the two layers thus indicates different reorientation of GSH upon applying identical stimulation (protonation−deprotonation). Figure 8 schematically summarizes the interpretation based on the ATR-IR spectra and pH modulation experiments discussed above.

Conclusions

In situ ATR-IR combined with modulation excitation spectroscopy turned out to be a powerful combination for the investigation of reversible changes within L-glutatione layers on gold induced by protonation−deprotonation stimuli. The results show that the ionic state during adsorption influences the structure of the adsorbate layer. Whereas the adsorbed molecules can be protonated and deprotonated, respectively, by admitting acid and base, respectively, in ethanol, the response toward periodic protonation−deprotonation depends both qualitatively and quantitatively on the ionic state during adsorption. This is rationalized, supported by DFT calculations, by the different molecular shape of the different ionic forms. When L-glutathione is adsorbed from ethanol, the spectra indicate a second anchoring apart from the strong the thiol−gold linkage, via the acid function of the gly part of the molecule. The latter is deprotonated upon interaction with the gold surface. The in situ ATR-IR experiments furthermore indicate a reorientation of the molecule upon protonation−deprotonation and a concomitant rearrangement of the hydrogen-bonding network within the adsorbed layer. These findings bear some similarity with electrochemical investigations of L-glutathione-modified electrodes exposed to metal ions.[10,19] On the basis of such investigations it was proposed that in the absence of ions in water the molecule forms a T shape with the two arms (glu and gly parts) of glutathione far apart from each other. In this conformation access of redox ion probes to the electrode surface is inhibited. In the presence of a metal ion the carboxylate groups of the two arms interact with the metal ion and hence form a Y shape with the two arms of the molecule approaching each other. This opens up the electrode surface and thus allows redox reactions to occur. Our findings support the idea that L-glutathione on gold exhibits structural changes addressable by external stimuli like pH or ion concentration.

Acknowledgment. Financial support from the Swiss National Science Foundation and the grants of computer time from the Swiss National Supercomputing Centre (CSCS) Manno are gratefully acknowledged. Use of sputtering facilities at the Swiss Center for Electronics and Microtechnology in Neuchâtel (CSEM) is kindly acknowledged.

Supporting Information Available: Transmission infrared spectrum of L-glutathione in ethanol-d_6 (spectral region around 1700 cm^{-1}). This material is available free of charge via the Internet at http://pubs.acs.org.

LA047735S

(58) Bonalumi, N.; Bürgi, T.; Baiker, A. *J. Am. Chem. Soc.* **2003**, *125*, 13342.
(59) Matsuda, Y.; Ebata, T.; Mikami, N. *J. Chem. Phys.* **1999**, *110*, 8397.
(60) Templeton, A. C.; Chen, S.; Gross, S. M.; Murray, R. W. *Langmuir* **1999**, *15*, 66.
(61) Sabapathy, R. C.; Bhattacharyya, S.; Leavy, M. C.; Cleland, W. E.; Hussey, C. L. *Langmuir* **1998**, *14*, 124.
(62) Clegg, R. S.; Reed, S. M.; Hutchinson, J. E. *J. Am. Chem. Soc.* **1998**, *120*, 2486.
(63) Clegg, R. S.; Hutchinson, J. E. *Langmuir* **1996**, *12*, 5239.

Chapter 2

Adsorption Kinetics of L-Glutathione on Gold and Structural Changes during Self-Assembly: An *in Situ* ATR-IR and QCM Study

Marco Bieri and Thomas Bürgi

Published in Phys. Chem. Chem. Phys., Volume 8(4), pp. 513–520, doi: 10.1039/b511146c, 2006.

PAPER www.rsc.org/pccp | Physical Chemistry Chemical Physics

Adsorption kinetics of L-glutathione on gold and structural changes during self-assembly: an *in situ* ATR-IR and QCM study

Marco Bieri and Thomas Bürgi*

Received 4th August 2005, Accepted 14th November 2005
First published as an Advance Article on the web 29th November 2005
DOI: 10.1039/b511146c

The adsorption of L-glutathione (γ-Glu-Cys-Gly) from ethanol on gold surfaces was studied *in situ* by both attenuated total reflection infrared (ATR-IR) spectroscopy and using a quartz crystal microbalance (QCM). The molecule is firmly anchored to the gold surface through the thiol group. Different IR signals of adsorbed L-glutathione, notably the amide I and ν(–COOH), show significantly different behavior with time, which reveals that their increase is not related to adsorption (mass uptake) alone. This indicates that structural transformations take place during the formation of the self-assembled monolayer (SAM). In particular, the intensity of the acid signal increases quickly only within the first couple of minutes. The complexity of the self-assembling process is confirmed by QCM measurements, which show fast mass uptake within about 100 s followed by a considerably slower regime. The structural change superimposed on the mass uptake is, based on the *in situ* time-resolved ATR-IR measurements, assigned to the interaction of the acid group of the Gly moiety with the surface. The latter group is protonated in ethanol but deprotonates upon interaction with the gold surface. The protonation–deprotonation equilibrium is sensitive to external stimuli, such as the presence of dissolved L-glutathione molecules. The interaction of the acid group with the surface and concomitant deprotonation proceeds *via* two distinguishable steps, the first being a reorientation of the molecule, followed by the deprotonation.

Introduction

Self-assembled monolayers (SAMs) have been extensively studied in recent years[1–3] due to their potential applications in various branches of surface technology, such as passivation, lubrication, surface engineering, development of (bio-)sensors[4] and biocompatibility. The self-assembly of alkanethiols on gold surfaces was the focus of many studies due to the model character of this system. However, even for these simple models relatively complex adsorption behavior was found, deviating from Langmuir adsorption. Despite the fact that some central assumptions of the Langmuir model are not met (no intermolecular interactions, the adsorption probability only determined by the available free sites), deviations are expected due to the rich phase diagram of these systems.[5] At very low coverage the adsorbed molecules lay flat on the surface, whereas at high coverage a standing structure is formed with the individual molecules tilted with respect to the surface. At intermediate coverage still more phases were found. Therefore, as coverage increases, the system crosses phase boundaries. The different phases have their own energy landscape and thus adsorption kinetics can be heavily affected when crossing phase boundaries.[3] For more complicated thiols with additional functional groups the phase diagram (in temperature and coverage) is not expected to become simpler. Indeed, rather complex phase diagrams were found for relatively small molecules such as tartaric acid adsorbed on metal surfaces.[6]

An important class of SAMs is those composed of polypeptides containing cysteine. These molecules contain other functional groups besides thiol which may also interact with the surface[7] and give rise to intra- and intermolecular interactions. This has important consequences on the properties of the corresponding SAM but is also likely to be important for the self-assembling process itself. In this contribution we focus on the self-assembly of L-glutathione (GSH, γ-Glu-Cys-Gly, Scheme 1) on gold. GSH has various physiological functions and is the most abundant non-protein thiol in mammalian cells.[8] GSH-modified gold surfaces were considered for specific protein binding.[9] Furthermore, GSH SAMs on gold electrodes exhibited "ion gating" when interacting with rare earth metal ions, transition metal ions, neurotransmitters and a cationic drug. Interaction with these analytes opened up free electrode surface as revealed by redox ion probes.[10,11]The adsorbed molecules also respond with significant structural changes towards acid–base stimuli.[12] It was found that the acid group

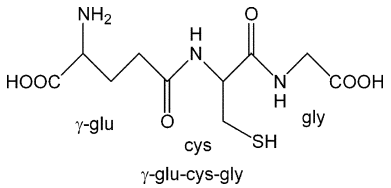

γ-glu-cys-gly

Scheme 1 Structure of L-glutathione (GSH, γ-Glu-Cys-Gly).

Université de Neuchâtel, Institut de Chimie, Rue Emile-Argand 11, 2007 Neuchâtel, Switzerland. E-mail: thomas.burgi@unine.ch; Fax: ++41 32 718 25 11; Tel: ++41 32 718 24 12

of the Gly can interact with the gold surface.[12] In the following it will be shown by using a combination of *in situ* attenuated total reflection infrared (ATR-IR) spectroscopy[13] and quartz crystal microbalance (QCM) measurements [14] that the relative complexity of GSH with its flexible structure and presence of ionizable functional groups is reflected in its self-assembly and adsorption kinetics. The ATR-IR spectra shed light onto the structural changes which are at the origin of the complex adsorption behavior.

Experimental

Chemicals

L-glutathione (γ-Glu-Cys-Gly, GSH, Sigma Aldrich Inc., ≥ 98%) was used as received. Ethanol (EtOH, Merck p.a.) served as the solvent for both the ATR-IR and QCM measurements reported here.

In situ ATR-IR spectroscopy

Sample preparation. ATR-IR measurements were performed using a Ge internal reflection element (IRE, 50 mm × 20 mm × 2 mm, Komlas). The IRE was first polished with a 0.25 μm grain size diamond paste (Buehler, Metadi II) and rinsed copiously with EtOH before the surface was plasma cleaned under a flow of air for 5 min. In the next step, a gold layer with a thickness of about 2 nm was sputtered onto the IRE. It should be noted that sputtering of such thin films does not result in uniformly flat gold surfaces but rather islands or particles (see for example ref. 15). A freshly prepared IRE was used for each ATR-IR experiment. In control experiments using a bare Ge IRE the absence of prominent GSH signals revealed no GSH adsorption during several hours of exposure to GSH solution.

Data acquisition. A Bruker EQUINOX 55 FT-IR spectrometer equipped with a nitrogen cooled narrow band MCT detector was used for ATR-IR measurements. The spectral resolution used for all experiments was 4 cm^{-1}. The Ge IRE was mounted on a home-built liquid flow-through cell (0.077 mL volume) with a gap of 250 μm between the IRE and the polished steel surface. The flow-through cell can be heated or cooled but all measurements reported here were performed at room temperature. More detailed descriptions of the flow-through cell can be found elsewhere.[16,17]

ATR-IR experiments. The solvent (EtOH) and GSH solution (typically 0.33 mM for ATR-IR experiments) were stored in separate bubble tanks. Before starting an experiment both the solvent and GSH solution were saturated with nitrogen gas (CarbaGas, 99.995%). An experiment started with a flow of EtOH over the gold coated Ge IRE until no variation in the spectrum could be detected (about 5 min). Then a spectrum was recorded by co-adding 200 interferograms which served as a reference for all subsequent measurements. Two types of ATR-IR experiments were carried out: in the first experiment GSH was flowed (flow rate = 0.18 mL min^{-1}) over the gold coated Ge IRE for more than 4 h and the spectral changes were followed. Spectra were recorded by co-adding 200 interferograms at a 40 kHz sampling rate resulting in time intervals of 42 s between subsequent spectra. The time-dependence of the bands in the ATR-IR spectra yields information on the velocity of adsorption and structural changes occurring during the GSH self-assembling process. The second type of ATR-IR experiment is identical to that described above, except that adsorption of GSH was stopped after some time by replacing the flow of GSH solution with solvent (EtOH). This abrupt stop of GSH supply may have an impact on the GSH SAM structure; possible scenarios are the desorption of adsorbed molecules or restructuring of the adsorbate layer. To adequately follow the changes in the spectra the rapid scan acquisition mode of the FT-IR spectrometer was used resulting in time intervals down to 20 s. Note that with the use of small GSH concentrations (0.33 mM) contributions from bulk molecules can be neglected, as was verified in control experiments with the bare Ge IRE.

Quartz crystal microbalance

Instrumentation. QCM measurements were performed with a QCM200 model (Stanford Research Systems) with a 5 MHz (nominal) crystal oscillator. The sensor crystals (5 MHz, AT cut, 1 in diameter, Stanford Research Systems) are a chrome–gold composite with an optically clear surface finish (about 50 nm average surface roughness). The QCM is operated with an axial flow cell (Stanford Research Systems) providing high sensitivity and well defined flow conditions. In the axial flow cell of about 150 μL volume, the sample flows radially outward from the input port at the center of the cell to the exit channel at the edge of the cell. The sample solution is injected perpendicularly with respect to the flat surface of the QCM crystal. The stagnation point is located at the center of the crystal, overlapping the area of highest sensitivity of the flat QCM oscillator. Information about the hydrodynamics associated with stagnation point flow can be found elsewhere.[18,19] In order to implement the lowest noise flow setup the system is operated in open flow mode (siphon principle) and small flow rates of <0.1 mL min^{-1} are used. Sample solutions were stored in separate vessels and injected into the axial flow cell *via* a 6-way selection valve (Upchurch Scientific).

Sample preparation. Quartz crystal sensors were immersed in a modified piranha solution (1 : 2 H_2O_2(30%) : H_2SO_4) at 120 °C for 9 min. The crystals were then copiously rinsed with Milli-Q water for 5 min and dried in a stream of argon.

Safety note: Piranha solution is extremely aggressive and should be handled with care!

QCM measurements. Individual GSH adsorption measurements began with a flow of solvent (EtOH) over the QCM crystal surface. After a stable frequency baseline was reached (after about 1 h) GSH in solution (0.33 mM) was injected into the axial flow cell. Frequency measurements were performed with a 10 s gate time providing a frequency resolution of 0.01 Hz. The frequency shift was fitted to adsorption models within the Langmuir frame as detailed in the Appendix.

Results

The time-dependence of two prominent GSH signals obtained by ATR-IR measurements is depicted in Fig. 1. A detailed

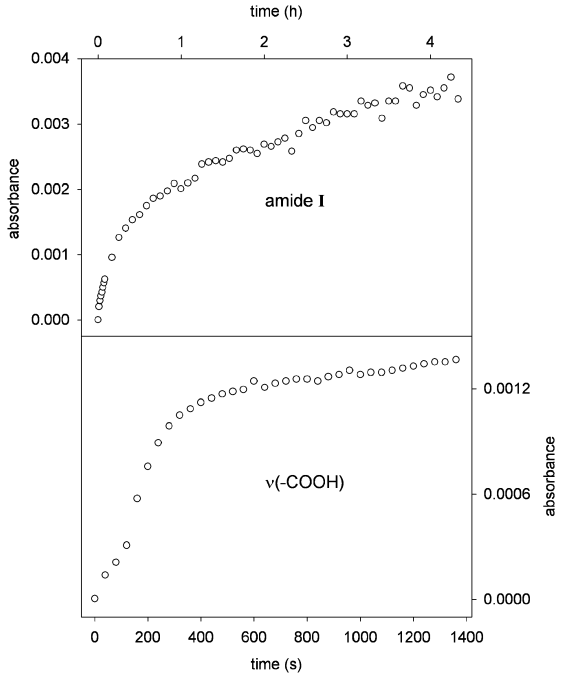

Fig. 1 Time-dependence of two prominent GSH signals obtained by ATR-IR when flowing (flow rate = 0.5 mL min^{-1}) GSH in solution (0.33 mM) over the gold coated Ge IRE. The absorbance as a function of time for the amide I signal and the ν(–COOH) signal is depicted in the upper and lower halves of this figure, respectively. Note that the two signals refer to the same GSH self-assembly process and each of the two signals is assigned a different time axis with the one for the amide I signal depicted above the upper graph.

assignment of the GSH infrared signals can be found elsewhere[12] but a summary of the most prominent bands is listed in Table 1. The absorbance as a function of time of the amide I signal at 1649 cm^{-1} is depicted in the upper half of Fig. 1 whereas the ν(–COOH) signal at 1731 cm^{-1} is displayed in the lower half. Due to their completely different behavior with time the signals are assigned a different time axis. The amide I signal shows a slow increase in intensity over a long time. In contrast, the intensity of the ν(–COOH) signal reveals a completely different behavior and almost stagnates in less than 1400 s. The completely different shape of the two curves in Fig. 1 shows that the ATR-IR spectrum is not only changing quantitatively but also qualitatively. Therefore, not only a bare mass uptake is observed in the ATR-IR experiment. The behavior shown in Fig. 1 points to other processes occurring simultaneously to adsorption and which affect the adsorbate spectrum qualitatively. This points to some structural changes during the self-assembly process, as will be discussed later.

Table 1 Observed vibrational bands of GSH depicted in the spectra in Fig. 4 and 5

GSH (zwitterionic)/cm^{-1}	Assignment
1731	ν(–COOH)
1649	Amide I
1600	ν_{as}(–COO^-)
1527	Amide II
1397	ν_s(–COO^-)
1230	δ(–C–O–H) bending + ν(–C–O) stretching

Diffusion can significantly influence the observed adsorption behavior at small bulk concentrations and/or high adsorption rates. In a non-stagnant liquid the thickness of the diffusion layer depends on the flow velocity. For two flow velocities $v_1 > v_2$ the thickness l of the diffusion layer becomes larger for smaller velocities, *i.e.* $l_2 > l_1$.[20] In order to estimate the influence of diffusion, experiments were repeated using flow rates of 0.18, 0.5, 1.0 and 1.25 mL min^{-1}. In further experiments GSH bulk concentrations of down to 0.04 mM were used, but in all these experiments the shape of the curves in Fig. 1 was not affected. It is therefore concluded that diffusion of GSH bulk molecules through the stagnant layer to the gold surface does not influence the adsorption behavior in our system.

The result of GSH adsorption on gold (solid line) as investigated by QCM is depicted in Fig. 2. Also given (dashed line) is a fit to a simple Langmuir (1L) model (see eqn (3) of the Appendix). Obviously, the shift in resonant frequency with time does not follow simple Langmuir (1L) kinetics. A more complex process with three different kinetic regimes is apparent. At the beginning of GSH adsorption, a sharp linear decrease in frequency is observed. This initial process is replaced after about 200 s by a slower, almost linear shift in resonant frequency. Finally, after about 1000 s, the onset of a very slow process is visible. This final step of the GSH adsorption process is still proceeding after 4000 s and a further shift (decrease) in frequency may fall below the detection limit. According to the Sauerbrey relation[14], assuming a mass sensitivity constant of 17.7 ng cm^{-2} Hz^{-1}, a frequency shift of 8.5 Hz (about saturation coverage) corresponds to 4.9×10^{-10} mol GSH cm^{-2}. This value should however only be taken as rough estimate considering the difficulty of determining absolute coverage by QCM in the liquid phase.[21] It should

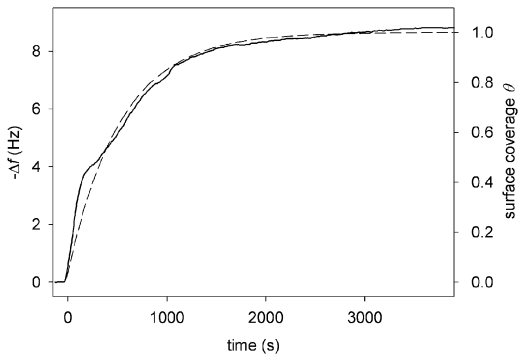

Fig. 2 The shift in resonance frequency upon GSH (0.33 mM) adsorption on gold as a function of time investigated by QCM (solid line). The flow rate was adjusted to 0.1 mL min^{-1} and the onset of GSH adsorption was taken as time zero. A Langmuir model (1L, see Appendix) was used to fit the data (dashed line).

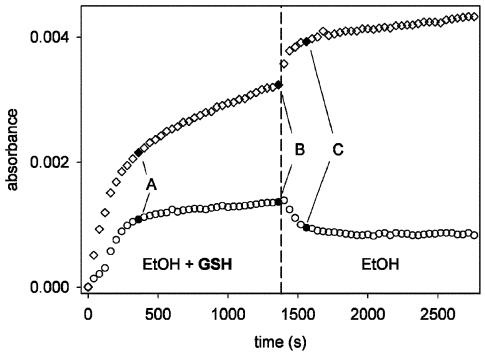

Fig. 3 The absorbance as a function of time for the amide I signal (diamonds) and the ν(–COOH) signal (circles). On the left-hand side, indicated by "EtOH + GSH", GSH in solution was flowed (flow rate = 0.5 mL min^{-1}) over the gold coated Ge IRE and replaced after 1380 s by an inflow of EtOH as indicated by "EtOH" on the right-hand side of this figure. Black circles and diamonds labelled with the letters A, B and C represent selected spectra which are displayed in Fig. 4 and 5.

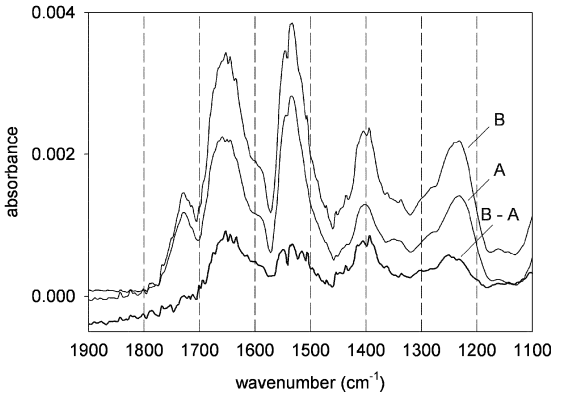

Fig. 4 GSH ATR-IR spectra recorded while flowing GSH in solution (0.33 mM, flow rate = 0.5 mL min^{-1}) over the gold coated Ge IRE. The spectrum labelled (A) was recorded 360 s after initial GSH self-assembly on gold (note that this spectrum refers to the first black circle/diamond indicated by A in Fig. 3). The spectrum (B) was recorded after 1360 s, just before the inflow of EtOH over the GSH SAM set in (see also Fig. 3). The corresponding difference spectrum B – A is also shown.

be noted that the described overall shape of the frequency shift curve was reproducible.

As already mentioned in the Experimental, an abrupt stop of GSH supply may have an impact on the GSH SAM structure. The spectral response to this stimulation is depicted in Fig. 3 where the absorbance as a function of time is displayed both for the amide I signal (represented as diamonds, upper plot) and the ν(–COOH) signal (circles, lower plot). For the left-hand side of Fig. 3, indicated by "EtOH + GSH", GSH in solution (0.33 mM) was flowed at 0.5 mL min^{-1} over the gold coated Ge IRE and GSH self-assembly took place. After 1380 s the supply of GSH molecules was stopped by flowing neat solvent (EtOH) at the same flow rate (0.5 mL min^{-1}) over the GSH SAM (right-hand side of Fig. 3, indicated by "EtOH"). The observed response of the amide I signals to EtOH flow over the GSH SAM is the opposite of that seen for ν(–COOH), as shown in the right-hand side of Fig. 3, which shows that the spectral changes can not be explained simply by desorption of weakly bound (physisorbed) molecules. This was further confirmed by analogous QCM experiments, which did not show a positive frequency shift upon flowing neat EtOH, as would be expected for desorption. Note that the response to the stimulation is occurring quickly. At about 120 s after the inflow of EtOH the ν(–COOH) signal has collapsed and reached a steady level whereas the amide I signal increases further, although at a slower rate. Careful inspection of the time-dependence of the two signals shows that the amide I signal increases slightly before the ν(–COOH) signal starts to decrease. In summary, Fig. 3, together with the result from the analogous QCM experiment, indicate that a reorganization within the adsorbate layer takes place upon flowing solvent, as will be discussed in detail later, and that desorption of weakly bound (physisorbed) molecules is only of minor importance for the observed spectral changes.

In order to gain more insight into the structural changes during adsorption and the flow of neat solvent, as indicated by the signals in Fig. 3, selected spectra (labelled by letters in Fig. 3) are depicted in Fig. 4 and 5, respectively. The first GSH spectrum shown was recorded 360 s after the inflow of GSH solution over the gold coated Ge IRE. This spectrum, labelled

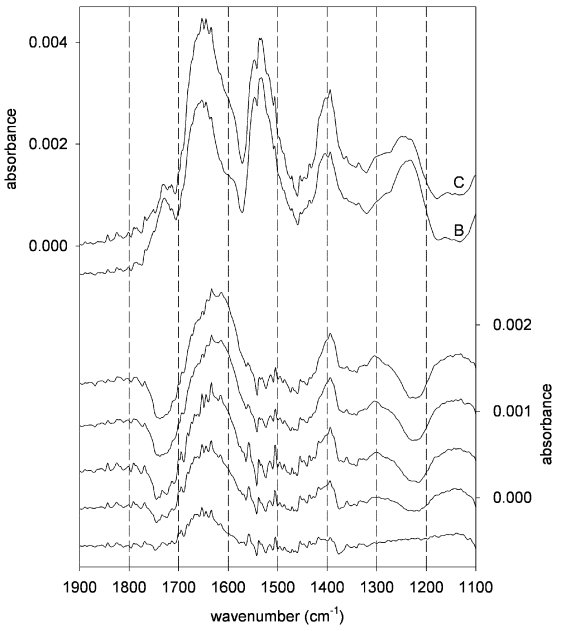

Fig. 5 The GSH absorption spectrum recorded before the EtOH inflow (flow rate = 0.5 mL min^{-1}) over the GSH SAM (B) is depicted in the upper half (note that this spectrum is identical to the one displayed in Fig 4). The spectrum recorded 200 s after the EtOH inflow (C) (third black circle/diamond C in Fig. 3) is also shown in the upper half. In the lower half a set of time-resolved difference spectra is shown which were obtained by subtracting the spectrum recorded at 1360 s (spectrum (B) in the upper half of this figure) from the five subsequent spectra. Time increases in intervals of 40 s from bottom to top.

(A) in Fig. 4, represents the adsorbate layer at the end of the initial fast adsorption process. In order of increasing intensity, three prominent GSH bands are visible at 1731 (ν(–COOH)), 1649 (amide I) and 1527 cm^{-1} (amide II). Less intense signals are apparent at 1397 (ν_s(–COO^-)) and 1230 cm^{-1} (δ(–C–O–H) bending + ν(–C–O) stretching). Spectrum (B) in Fig. 4 was recorded after 1360 s of GSH adsorption on the gold coated Ge IRE. The GSH coverage is now very large, *i.e.* adsorption is almost complete. All of the prominent GSH bands have gained intensity with the exception of the ν(–COOH) signal at 1731 cm^{-1}. The difference between the spectra recorded at 1360 (B) and 360 s (A) (see Fig. 3) is displayed in Fig. 4 (labelled B − A). Note that this difference spectrum reveals the changes associated with the final stages of SAM formation. Obviously, the ν(–COOH) signal at 1731 cm^{-1} is hardly apparent in the difference spectrum. All the other prominent GSH bands gained intensity, especially the amide I band at 1649 cm^{-1}.

The spectral response to solvent flow over the GSH adsorbate layer is depicted in Fig. 5. The spectrum recorded after 1360 s of GSH adsorption (B) is displayed in the upper half of Fig. 5 (the same spectrum is depicted in Fig. 4). It represents the final spectrum recorded before GSH in solution was replaced by EtOH. The second spectrum depicted in the upper half of Fig. 5 (C) was recorded 200 s after the EtOH inflow (see also Fig. 3). As can be expected from the time-dependence in Fig. 3 the ν(–COOH) signal at 1731 cm^{-1} has lost intensity and the amide I signal clearly appears more intense. Furthermore, the asymmetric band mainly associated with the amide I vibration has broadened in the region of 1600 cm^{-1}. In addition, the intensity of the band at about 1400 cm^{-1} has increased considerably compared to the two prominent GSH signals at 1527 and 1230 cm^{-1}. Difference spectra are shown in the lower half of Fig. 5 that were obtained by subtracting the spectrum recorded before GSH was replaced by EtOH (trace (B) in the upper half of Fig. 5) from the five subsequent spectra (the last spectrum in this set is labelled (C) in the upper half of Fig. 5). Time increases in intervals of 40 s (bottom to top), providing a temporal evolution of the processes occurring within the adsorbate layer. At 40 s after the onset of EtOH flow over the GSH SAM the amide I signal at 1649 cm^{-1} is clearly visible. Another small signal may be located at 1397 cm^{-1}. Obviously, the ν(–COOH) signal at 1731 cm^{-1} does not appear in this spectrum. Note that this behavior also emerges from Fig. 3, which shows that the amide I signal increases slightly before the ν(–COOH) signal starts to decrease. In the second difference spectrum (referring to 80 s after switching to EtOH flow over the GSH SAM) a negative band at 1731 cm^{-1} is visible due to a decrease in intensity of the ν(–COOH) signal. Simultaneously, the band at 1230 cm^{-1} associated with a carboxylic acid group (δ(–C–O–H) + ν(–C–O)) decreases as well. The amide I signal has gained further intensity, with a shoulder appearing at about 1600 cm^{-1}, which we assign to ν_{as}(–COO^-). The band at 1397 cm^{-1}, assignable to ν_s(−COO^-), is more pronounced as well. In the three subsequent difference spectra the discussed signals gain and lose intensity, respectively. Notably, the amide I band shifts to slightly lower wavenumbers which is due to the increase of the shoulder at 1600 cm^{-1}, assignable to ν_{as}(−COO^-). In summary, the set of time-resolved difference spectra reveals that upon flowing EtOH over the GSH SAM, processes with distinctly different kinetics take place, which are most apparent from the amide I and ν(–COOH) signals.

Discussion

The intensity of a signal in ATR-IR depends not only on the concentration or coverage of a surfaces species, but also on the transition dipole moment vector associated with the corresponding vibration and on the angle between the transition dipole moment vector and the electric field vector,[22,23] the latter being polarized perpendicular to metal surfaces.[24] Processes that affect these parameters thus influence the (relative) intensity of vibrational bands. The magnitude (and orientation) of the transition dipole moment of a vibration can be influenced by a change of the chemical entity (conformational changes, protonation/deprotonation *etc.*), whereas a change of the orientation of an adsorbed molecule will affect the angle between the transition dipole moment and the electric field. Fig. 1 reveals that the amide I and ν(–COOH) vibrational bands grow at different rates during adsorption and self-assembling of GSH on gold. The different time-dependence of the GSH ATR-IR signals thus strongly indicates structural changes within the adsorbate layer during self-assembly and shows that the ATR-IR signals do not only reflect mass uptake in this case. Using the benefits of a flow-through cell by changing the flow conditions and using considerably different GSH concentrations, it was further elucidated that the ATR-IR signals were not affected by diffusion effects.

As the ATR-IR signals measured during adsorption do not only represent the mass uptake, a second method, QCM, was used to shed some more light on the adsorption kinetics. Note that QCM was previously used to study the adsorption kinetics of thiols on gold.[21,25] The change (*i.e.* decrease) in resonant frequency depends on mass loading according to the Sauerbrey equation.[14] In liquid contact measurements, however, frequency changes may be affected by other factors. During SAM formation, the energy of the interaction of the surface with the solvent is changing.[25] In addition, viscous coupling of the liquid medium to the oscillating crystal surface results not only in a decrease in the resonant frequency but also in a damping of the resonant oscillation—the viscous loss is manifested as an increase in the resonance resistance R of the QCM resonator.[26] However, the measured frequency change during adsorption caused by these different processes is still assumed to be a direct result of the formation of the GSH SAM.[21] Because of the use of small GSH concentrations (0.33 mM) we assume that viscosity effects have a negligible influence on frequency measurements. The validity of this assumption was confirmed by the absence of a sharp increase in resonance resistance during the GSH self-assembling process.

The QCM data provide a complex picture of the GSH self-assembling process as is obvious by the different kinetic regimes. From Fig. 2 it emerges that the adsorption is fast up to a relative coverage of about 0.4 (assuming that the frequency shift is proportional to mass uptake and described by the 1L model). It is likely that at this point the adsorbed

molecules start to interact with each other. One possible explanation for the abrupt change in slope of the adsorption curve is a crossing of a phase boundary at this point. The structural changes during the self-assembly process as indicated by ATR-IR are thus further confirmed by the QCM measurements, which show a rather complex frequency shift with different slopes due to GSH adsorption. In other words, both the ATR-IR and QCM measurements coherently indicate structural changes within the adsorbate layer during self-assembly.

In principle, both the ATR-IR and QCM measurements are sensitive to the presence of physisorbed GSH at the SAM interface. However, two observations indicate that both the ATR-IR and QCM signals are dominated by chemisorbed species: First, the inflow of EtOH over the GSH modified QCM sensor crystals did not reveal a positive frequency shift as would be expected in case of the desorption of a weakly bound physisorbed species. Second, in the ATR-IR experiment the signals are expected to decrease upon desorption of physisorbed species. As is visible from Fig. 3 the amide I band is increasing upon switching to neat solvent (whereas the ν(–COOH) band decreases). This shows that upon changing to neat solvent structural changes within the adsorbate layer dominate the ATR-IR spectra over desorption of weakly bound (physisorbed) species.

The nature of the structural changes during self-assembly is addressed in the following. In order to extract information at the molecular level from the ATR-IR spectra, an assignment of the vibrational bands is required. A detailed discussion can be found elsewhere[12] and a summary of the most prominent bands observed in Fig. 4 and 5 is given in Table 1. In EtOH GSH exists in zwitterionic form with the acid group on the Glu moiety deprotonated and the one on the Gly protonated. Note that the stronger acid at the Glu protonates the amine (also at the Glu, see Scheme 1). We have recently shown that within a GSH SAM on gold a fraction of the adsorbed molecules are also deprotonated at the acid group of the Gly moiety.[12] This deprotonation is assisted by the interaction of the carboxylate group with the gold surface.

The ATR-IR signals revealing deprotonation/protonation of the acid groups are the ν(–COOH), $\nu_{as}(-COO^-)$ and $\nu_s(-COO^-)$ signals at 1731, about 1600 and 1397 cm^{-1}, respectively. The ν(–COOH) signal is most informative since it is associated with the protonated acid group of the Gly[12] and the corresponding band is well isolated in the spectrum. The carboxylate ($-COO^-$) bands are partly overlapped by other signals and furthermore associated with both the Gly and the Glu of the adsorbed GSH.

During the adsorption process the ν(–COOH) signal at 1731 cm^{-1} increases quickly until about 300 s before changing to a much more slowly increasing rate (Fig. 1 and 3). QCM and ATR-IR measurements reveal that after 300 s the surface is not yet fully covered. This shows that at relatively high coverage (*i.e.* after 300 s of adsorption) the increase of protonated acid groups on the surface through adsorption is compensated by a decrease through deprotonation. The protonated and deprotonated states at the acid group of the Gly co-exist on the surface in a dynamic equilibrium which can be shifted by changing the stability of one of the two states involved in the equilibrium. During the adsorption, at increasing coverage, intermolecular interactions may have an influence on the protonated (not surface bound)–deprotonated (surface bound) equilibrium of adsorbed molecules, thereby shifting the latter towards a new value. The ν(–COOH) signal in Fig. 1 indicates such a behavior. At high coverage the equilibrium shifts towards the deprotonated state, possibly due to intermolecular interactions.

The equilibrium between the protonated and deprotonated state of the acid group of the Gly moiety can also be shifted by the presence of dissolved GSH molecules. One possible reason is the stabilization of the protonated state due to hydrogen bonding of the protonated carboxylic acid group (a hydrogen bond donor) with dissolved molecules. Upon flowing EtOH, *i.e.* upon removing dissolved GSH, the ν(–COOH) signal collapses quickly (Fig. 3, circles) and simultaneously the bands associated with carboxylate vibrations, *i.e.* the $\nu_{as}(-COO^-)$ at 1600 cm^{-1} and the $\nu_s(-COO^-)$ at 1397 cm^{-1}, respectively, increase, as the time-resolved difference spectra in Fig. 5 reveal. Broad bands were also observed above 3000 cm^{-1} (not shown) upon flowing EtOH, which could partly be due to the O–H of the acid group but also due to the (reorientation of the) N–H groups or due to EtOH. The presence of dissolved GSH shifts the equilibrium towards the protonated state, whereas the presence of neat EtOH shifts the equilibrium towards the deprotonated state. It should be noted that readmission of GSH in solution shifts the equilibrium back towards the protonated state. Fig. 3 also shows that the amide I signal (diamonds, upper plot) keeps increasing in the absence of GSH, although at a considerably slower rate. This increase, which can not be due to adsorption, indicates that further slow structural changes proceed in the absence of GSH in solution, which do not affect the ν(–COOH) signal, since the latter stays constant.

The spectra recorded during the switching from GSH solution to neat EtOH solvent (Fig. 5) change not only quantitatively, but also qualitatively, showing that processes with different kinetics are responsible for the observed spectral changes. In particular, the amide I band at 1649 cm^{-1} starts to increase first (lower spectrum of Fig. 5). Only after some time, due to a deprotonation, the ν(–COOH) band at 1731 cm^{-1} loses intensity, *i.e.* becomes negative in the difference spectra in Fig. 5 and the carboxylate bands become positive. This means that before the deprotonation another process occurs, which leads to an increase of the amide I signal. Such a sudden increase of the amide I band intensity can be induced by a reorientation of the amide group(s) of adsorbed GSH. This reorientation is characterized by an alignment of the corresponding transition dipole moment to be more parallel to the electric field, the latter being oriented perpendicular to the surface. Such an alignment would result in a stronger ATR signal. Note that due to the metal surface selection rule[24] only the component of the transition dipole moment normal to the metal surface gives rise to IR intensity.

Based on the spectral features just discussed and relying on former findings on the GSH–gold system,[12] which revealed that the acid group of the Glu moiety of GSH is deprotonated, whereas part of the GSH molecules are protonated at the Gly part of the molecule, we propose that a large fraction of GSH

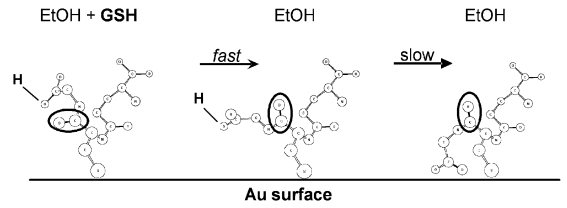

Fig. 6 Pictorial representation of the suggested structural change that a large fraction of the adsorbed GSH molecules undergoes by removing dissolved GSH from the SAM interface. The initial state is depicted on the left. In a fast step the reorganization of the Gly part of the molecule changes the orientation of the strong amide I transition dipole moment (compared to that depicted on the left) as can be seen in the intermediate picture. Note that at this stage a large fraction of the acid groups of the Gly moiety is still protonated. In the subsequent slower step the Gly acid groups are deprotonated by interaction with the gold surface (right).

molecules within the SAM undergo the following structural changes by admitting EtOH, *i.e.* removing dissolved GSH from the SAM interface (see Fig. 6): In an initial fast step the interfacial interactions between the acid groups of the Gly part of the adsorbed GSH molecules and dissolved GSH molecules are lost by the removal of the latter. This loss in interaction induces reorganization to a new energetically favorable state. As discussed above, this state is found upon deprotonation of the corresponding acid group by interaction with the Au surface. This new state is reached in two steps with distinctly different kinetics. In a first step, a reorientation of the Gly part of the molecule (see Fig. 6, centre) takes place. This increases the alignment of the strong amide I transition dipole moment with the electric field, the latter being perpendicular to the surface (compared to the initial state represented by Fig. 6, left), leading to the observed increase of the amide I signal. In the following second step the Gly acid groups now interact with the Au surface and deprotonate as depicted in Fig. 6, right. The involved deprotonation thus becomes visible in the absorbance spectra as the decreasing ν(–COOH) band at 1731 cm^{-1}. At this point it should be noted that GSH involves two amide groups (the Gly and Glu of the molecule). Though structural changes are likely to occur in the Glu part of the molecule as well, we assume that the major contribution to the increase in the amide I signal while flowing EtOH over the GSH SAM is attributable to the amide group of the Gly arm of the molecule since this arm finally interacts with the gold surface *via* the carboxylate.[12] In contrast, during the adsorption process the slow increase of the amide I band at 1649 cm^{-1} is not specifically attributable to the Gly or Glu moieties.

Conclusions

Both the ATR-IR and QCM results show that GSH adsorption on gold is a complex process involving distinctly different kinetic regimes depending on surface coverage. This leads to mass uptake curves in the QCM experiments that are far from being smooth as would be the case for simple Langmuir adsorption. In ATR-IR this behavior is reflected by the different time-dependence of the bands in the spectra, notably the amide I and ν(–COOH) bands. The latter band increases significantly only in the beginning of adsorption, when QCM reveals very fast mass uptake and remains almost constant in intensity afterwards. In contrast, the amide I signal keeps increasing at appreciable rate for a much longer time. Experiments performed at different flow rates and concentrations clearly show that adsorption is not diffusion-limited under the applied conditions. The spectroscopic results point to a structural change within the adsorbate layer, which is overlaid by the adsorption process. The clear distinction of several kinetic regimes observed by both of the applied techniques strongly indicates that the structure of the adsorbate layer is coverage dependent, leading to crossings of phase boundaries of the phase diagram as coverage is increasing during adsorption. A dominant role for the relevant structural changes is played by the acid group of the Gly moiety of GSH, which is protonated when dissolved in ethanol, but partly deprotonated when adsorbed, assisted by the interaction of the corresponding carboxylate group with the surface. The deprotonated state becomes more favored at coverages where intermolecular interactions cannot be neglected. It is further evident from the experimental results that the equilibrium between protonated and deprotonated states is easily shifted by external stimuli, such as the presence of dissolved GSH. Upon removal of dissolved GSH the relaxation of the system towards the new equilibrium state is fast, but proceeds in at least two distinct steps with different kinetics. Based on the ATR-IR measurements a model for the structural change is provided.

Appendix

The QCM data was fit to the well known first order Langmuir model (1L), which assumes that the surface reaction rate is proportional to the number of available sites for adsorption according to

$$\frac{d\theta}{dt} = k_{ads}c(1-\theta) - k_{des}\theta \qquad (1)$$

where θ denotes the fractional surface coverage, c is the bulk concentration of dissolved molecules and k_{ads} and k_{des} are the rate constants for adsorption and desorption, respectively. Integrating eqn (1) with respect to time t gives the following analytical expression for $\theta(t)$:

$$\theta(t) = \left(1 + \frac{k_{des}}{k_{ads}}\frac{1}{c}\right)^{-1}\{1 - \exp(-(k_{ads}c + k_{des})t)\} \qquad (2)$$

Assuming $k_{des} \approx 0$ for thiol adsorption eqn (2) further simplifies to

$$\theta(t) = 1 - \exp(-k_{ads,1L}ct) \qquad (3)$$

In order to fit the QCM data, eqn (3) was modified according to

$$A(t) = A_\infty\{1 - \exp(-k_{ads,1L}ct^b)\} \qquad (4)$$

where the exponent $b = 1$ for the 1L adsorption model. $A(t)$ is the measured signal, *i.e.* frequency shift for QCM. In eqn (4) the factor A_∞ and rate constant $k_{ads,1L}$ are fittable parameters. Note that for $t \to \infty$ $A(t) \to A_\infty$ and the ratio $A(t)/A_\infty \leq 1$ thus represents the fractional surface coverage $\theta(t)$.

Acknowledgements

Financial support from the Swiss National Science Foundation is gratefully acknowledged. The use of the sputtering facilities at the Swiss Center for Electronics and Microtechnology in Neuchâtel (CSEM) is acknowledged.

References

1 C. D. Bain and G. M. Whitesides, *Science*, 1988, **240**, 62.
2 A. Ulman, *Chem. Rev.*, 1996, **96**, 1533.
3 F. Schreiber, *J. Phys.: Condens. Matter*, 2004, **16**, R881.
4 R. Jelinek and S. Kolusheva, *Chem. Rev.*, 2004, **104**, 5987.
5 G. E. Poirier, *Langmuir*, 1999, **15**, 1167.
6 M. O. Lorenzo, C. J. Baddeley, C. Muryn and R. Raval, *Nature*, 2000, **404**, 376.
7 E. M. Marti, C. Methivier and C. M. Pradier, *Langmuir*, 2004, **20**, 10223.
8 H. Sies, *Free Radical Biol. Med.*, 1999, **27**, 916.
9 S. Kanagaraja, S. Alaeddine, C. Eriksson, J. Lausmaa, P. Tengvall, A. Wennerberg and H. Nygren, *J. Biomed. Mater. Res.*, 1999, **46**, 582.
10 M. Hepel and E. Tewksbury, *J. Electroanal. Chem.*, 2003, **552**, 291.
11 K. Takehara, M. Aihara and N. Ueda, *Electroanalysis*, 1994, **6**, 1083.
12 M. Bieri and T. Bürgi, *Langmuir*, 2005, **21**, 1354.
13 N. J. Harrick, *Internal Reflection Spectroscopy*, Interscience Publishers, New York, 1967.
14 G. Sauerbrey, *Z. Phys.*, 1959, **155**, 206.
15 B. El Roustom, G. Foti and C. Comninellis, *Electrochem. Commun.*, 2005, **7**, 398.
16 A. Urakawa, R. Wirz, T. Bürgi and A. Baiker, *J. Phys. Chem. B*, 2003, **107**, 13061.
17 T. Bürgi and A. Baiker, *J. Phys. Chem. B*, 2002, **106**, 10649.
18 T. Dabros and T. G. M. van de Ven, *Phys. Chem. Hydrodyn.*, 1987, **8**, 161.
19 T. Dabros and T. G. M. van de Ven, *Colloid Polym. Sci.*, 1983, **261**, 694.
20 U. P. Fringeli, D. Baurecht and H. H. Günthard, in *Infrared and Raman Spectroscopy of Biological Materials*, ed. H. U. Gremlich and B. Yan, Marcel Dekker, Inc,, New York, 2000.
21 W. Pan, C. J. Durning and N. J. Turro, *Langmuir*, 1996, **12**, 4469.
22 H. Shinohara, T. Kasahara, K. Kadokura, Y. Uryu and K. Itoh, *J. Phys. Chem. B*, 2004, **108**, 3584.
23 S. C. Street and A. J. Gellman, *J. Chem. Phys.*, 1996, **105**, 7158.
24 M. Osawa, K.-I. Ataka, K. Yoshii and T. Yotsuyanagi, *J. Electron Spectrosc. Relat. Phenom.*, 1993, **64/65**, 371.
25 D. S. Karpovich and G. J. Blanchard, *Langmuir*, 1994, **10**, 3315.
26 K. K. Kanazawa and J. Gordon II, *Anal. Chem.*, 1985, **57**, 1770.

Chapter 3

Adsorption Kinetics, Orientation, and Self-Assembling of *N*-Acetyl-L-cysteine on Gold: A Combined ATR-IR, PM-IRRAS, and QCM Study

Marco Bieri and Thomas Bürgi

Published in J. Phys. Chem. B, Volume 109(47), pp. 22476–22485, doi: 10.1021/jp052409m, 2005.

22476 *J. Phys. Chem. B* **2005,** *109,* 22476−22485

Adsorption Kinetics, Orientation, and Self-Assembling of *N*-Acetyl-L-cysteine on Gold: A Combined ATR-IR, PM-IRRAS, and QCM Study

Marco Bieri and Thomas Bürgi*

Institut de Chimie, Université de Neuchâtel, Rue Emile-Argand 11, 2007- Neuchâtel, Switzerland

Received: May 9, 2005; In Final Form: August 6, 2005

The adsorption of *N*-acetyl-L-cysteine from ethanol solution on gold has been studied by in situ attenuated total reflection infrared (ATR-IR) spectroscopy, polarization modulation infrared reflection absorption spectroscopy, and a quartz crystal microbalance. After an initial fast adsorption, in situ ATR-IR revealed two considerably slower processes, besides further adsorption. The appearance of carboxylate bands and the partial disappearance of the carboxylic acid bands demonstrated that part of the molecules on the surface underwent deprotonation. In addition, the C═O stretching vibration of the carboxylic acid group shifted to lower and the amide II band to higher wavenumbers, indicating hydrogen-bonding interactions within the adsorbate layer. Based on the initial ATR-IR spectrum, which did not reveal deprotonation, the orientation of the molecule within the adsorbate layer was determined. For this, density functional theory was used to calculate the transition dipole moment vectors of the vibrational modes of *N*-acetyl-L-cysteine. The projections of the latter onto the *z*-axis of the fixed surface coordinate system were used to determine relative band intensities for different orientations of the molecule. The analysis revealed that the amide group is tilted with respect to and points away from the surface, whereas the carboxylic acid is in proximity to the surface, which is also supported by a shift of the C−O−H bending mode. This position of the acid group favors its deprotonation assisted by the gold surface and easily enables intermolecular interactions. Periodic acid stimuli revealed reversible protonation/deprotonation of part of the adsorbed molecules. However, only non-hydrogen-bonded carboxylic acid groups showed a response toward the acid stimuli.

Introduction

Self-assembled monolayers (SAMs) have been studied extensively in recent years,[1] due to their large potential for applications in surface-based technologies such as the sensing of biomolecules.[2,3] The gold alkanethiol system served as a prototype to study self-assembling phenomena. However, many applications of SAMs rely on the buildup of complex structures on top of functionalized SAMs.[4] This implies the presence of functional groups, besides the thiol, that fulfill a desired recognition function or that are amenable to chemical modifications. These functional groups influence or even dominate the self-assembling through intermolecular interactions and interactions with the surface. An important group, particularly for biochemical applications, are SAMs of cysteine[5−7] or cysteine-containing molecules, such as, for example, glutathione (γ-Glu−Cys−Gly).[8−13] Cysteine adsorption on gold surfaces is influenced by intermolecular interactions involving the carboxylic acid groups, as revealed by scanning tunneling microscopy (STM).[14] Glutathione, a tripeptide containing cysteine, contains two carboxylic acid groups. It was shown recently by in situ infrared spectroscopy that at least one of these carboxylic acid groups forms an additional anchor to the gold surface, besides the strong gold−sulfur bond. Upon interaction with the surface, part of the carboxylic acid groups deprotonates. Although quite detailed molecular level information could be obtained on the adsorbed layer, the multitude of functional groups of the glutathione molecule complicated much deeper insight.

N-Acetyl-L-cysteine (NAC, Figure 1) is much simpler in this respect, containing only one amide and carboxylic acid group,

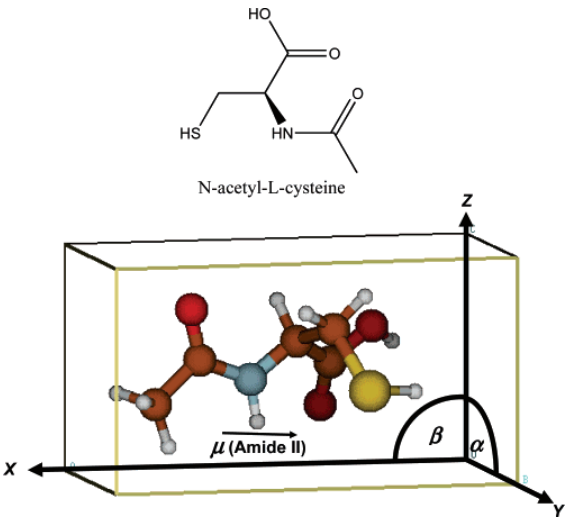

Figure 1. Structure of *N*-acetyl-L-cysteine (NAC, top) and pictorial representation of the optimized structure of NAC (bottom) as found by density functional theory calculations using a polarizable continuum model (see text for details). The molecular coordinate system is depicted as a box around the molecule with its axes parallel to the principal axes of inertia of the molecule. The fixed surface coordinate system (*x*,*y*,*z*) with the *x*−*y* plane defining the surface plane and *z* the surface normal has the same orientation as the molecular coordinate system for the reference orientation of the molecule. The molecular coordinate system is allowed to rotate around the angles α (*x*-axis) and β (*y*-axis), respectively, providing different orientations of the molecule with respect to the surface coordinate system. The orientation of the amide II transition dipole moment is also given.

* Corresponding author. Tel.: ++41 32 718 24 12. Fax: ++41 32 718 25 11. E-mail: thomas.burgi@unine.ch.

10.1021/jp052409m CCC: $30.25
Published on Web 11/01/2005

besides the thiol. Gold electrodes modified with NAC showed excellent sensitivity and selectivity for Cu(II) determination,[15] similar to glutathione-modified gold electrodes.[16] Also, NAC was used to confine proteins to gold electrodes via electrostatic attraction[17,18] or covalent bonding using condensing agent 1-ethyl-3-(3,3-dimethylaminopropyl)carbodiimide.[19]

In this contribution, we report on the self-assembling of NAC on gold, as investigated mainly by attenuated total reflection infrared (ATR-IR) spectroscopy.[20] After a fast initial adsorption, which leads to an adsorbate layer with a well-defined infrared spectrum, two subsequent processes are identified besides the slow increase in coverage. The infrared spectra give evidence for a slow deprotonation of part of the molecules and for intermolecular interactions involving the (protonated) carboxylic acid groups and the N−H of the amide. The orientation of the molecule within the adsorbate layer is determined from a comparison of band intensities of dissolved (randomly oriented) and adsorbed (oriented) molecules. Furthermore, the response of the *N*-acetyl-L-cysteine SAM toward concentration and acid stimuli is investigated.

Experimental Section

Chemicals. NAC (Figure 1, Sigma-Aldrich Inc., >99%) was used as received. Ethanol (EtOH, Merck p.a.) served as solvent for all ATR-IR, polarization modulation infrared reflection absorption spectroscopy (PM-IRRAS), and quartz crystal microbalance (QCM) measurements reported here. Before each ATR-IR measurement, solutions were treated with nitrogen gas (99.995%, CarbaGas) to remove dissolved oxygen.

In Situ ATR-IR Spectroscopy. *Sample Preparation.* Ge internal reflection elements (IRE; 50 mm × 20 mm × 2 mm, Komlas) were used for ATR-IR experiments. The IREs were first polished with a 0.25-μm-grain size diamond paste (Buehler, Metadi II) and afterward rinsed copiously with EtOH before the surface was plasma cleaned under a flow of air for 5 min (PlasmaPrep 2, Gala Instrumente). In a subsequent step, a gold layer with a thickness of ∼2 nm was sputtered onto the Ge-IRE (Balzers Union SCD 030). For each experiment, a fresh gold layer was prepared. Control experiments with a bare Ge-IRE revealed no NAC adsorption during several hours of exposure to a corresponding solution.

Data Acquisition. ATR-IR measurements were performed with a Bruker Equinox 55 FT-IR spectrometer equipped with a liquid nitrogen-cooled narrow-band MCT detector. A home-built liquid flow-through cell with a volume of 0.077 mL and a gap of 265 μm between the IRE and the polished steel surface was used to record ATR-IR spectra at room temperature (T = 298 K) with a resolution of 4 cm^{-1}. More detailed information about the ATR-IR cell can be found elsewhere.[21,22]

Modulation Experiments. A typical modulation experiment started with a flow of solvent (EtOH) over the gold-coated Ge-IRE until no variation in the spectrum could be detected (after ∼5 min). The corresponding spectrum, recorded by coadding 200 interferograms, served as reference for all subsequent measurements. Then a solution of NAC (0.6 mM) was allowed to flow at 0.18 mL/min over the gold-coated Ge-IRE. The adsorption and self-assembling process of NAC was followed in situ for 4 h by recording spectra in time intervals of 5 min. In a subsequent step, two kinds of modulation experiments were performed with the *N*-acetyl-L-cysteine SAM: (i) concentration modulation and (ii) "pH" modulation. In both modulation experiments, the flow of EtOH was replaced by an equally long flow of NAC in EtOH (0.6 mM, modulation experiment i) and HCl in EtOH (∼0.013 mM, modulation experiment ii), respectively. The modulation experiments finally resulted in a set of time-resolved spectra, which were then transformed by means of a digital phase-sensitive detection (PSD), according to eq 1, to a set of phase-resolved spectra.

$$A_k^{\phi_k^{\mathrm{PSD}}}(\tilde{\nu}) = \frac{2}{T}\int_0^T A(\tilde{\nu},t)\,\sin(k\omega t + \phi_k^{\mathrm{PSD}})\,\mathrm{d}t \qquad (1)$$

where k = 1, 2, 3, ..., determines the demodulation frequency, i.e., fundamental, first harmonic, and so on, T is the modulation period, $\tilde{\nu}$ denotes the wavenumber, ω is the stimulation frequency, and ϕ_k^{PSD} is the demodulation phase angle. With a set of time-resolved spectra $A(\tilde{\nu},t)$, eq 1 can be evaluated for different phase angles ϕ_k^{PSD} resulting in a series of phase-resolved spectra $A_k^{\phi_k^{\mathrm{PSD}}}$. Only spectra demodulated at the fundamental frequency (k = 1) are reported here. A more detailed description of the modulation technique can be found elsewhere.[13,22,23]

PM-IRRAS Spectroscopy. *Sample Preparation.* A cover glass for microscopy (Milian SA, 24 mm × 40 mm) served as substrate. After rinsing the surface copiously with EtOH, the substrate was plasma cleaned under a flow of air during 5 min. A thin gold layer with a thickness of ∼100 nm was then sputtered onto the substrate (Balzers Union SCD 030, sputtering rate ∼0.5 Å/s). Before the immersion in solutions of NAC (typical concentrations of NAC for PM-IRRAS measurements were ∼7 mM), the Au surface was again plasma cleaned. After immersion in the solutions for 24 h, the gold sample was rinsed copiously with EtOH and dried in a stream of argon.

Data Acquisition. A Bruker PMA 50 connected to the external beam port of a Bruker Tensor 27 FT-IR spectrometer was used for PM-IRRAS experiments. The gold sample was mounted on an attachment for PM-IRRAS measurements within the PMA 50 compartment. After reflection at an angle of incidence of 85°, the IR beam was focused on a liquid nitrogen-cooled photovoltaic MCT detector in the PMA 50 cabinet. A photoelastic modulator (Hinds, PEM 90) was used to modulate the polarization of the light at a frequency of 50 kHz. Demodulation was performed with a lock-in amplifier (Stanford Research Systems, SR830 DSP). All spectra were recorded using a sample scan time of 15 min at 4-cm^{-1} spectral resolution. The final PM-IRRAS reflectance spectra were calculated using the bare gold substrate as the reference.

Quartz Crystal Microbalance Analyses. *Instrumentation.* Experiments were performed using a QCM 200 microbalance (Stanford Research Systems) with a 5-MHz (nominal) crystal oscillator. The sensors (5 MHz, AT cut, 1 in. in diameter, Stanford Research Systems) are a quartz/chrome/gold composite with an optically clear surface finish (∼50 nm average surface roughness). To provide well-defined flow conditions and high sensitivity, the QCM is equipped with an axial flow cell (Stanford Research Systems) with a volume of ∼150 μL. The sample solution is injected perpendicularly with respect to the surface of the QCM crystal and flows radially outward from the input port of the cell to the exit channel at the edge of the cell. The stagnation point is located at the center of the crystal, overlapping the area of highest sensitivity of the flat QCM oscillator. The resulting stagnant point flow field is described in more detail elsewhere.[24,25]

To reduce noise induced by the flowing liquid the system is operated in open flow mode (siphon principle) and small flow rates < 0.1 mL/min are used. Solvent and sample solutions are stored in separate vessels and can be injected into the axial flow cell via a 6-way selection valve (Upchurch Scientific).

Sample Preparation. Before each QCM experiment, the quartz crystal sensors were immersed in a modified piranha

solution (1:2 H_2O_2(30%)/H_2SO_4, heated at 120 °C) during 5 min. The crystals were then thoroughly rinsed with Milli-Q water for 5 min and dried in a stream of argon.

Safety note: Piranha solution is extremely aggressive and should be handled with care!

QCM Measurements. Each of the QCM measurements started with a flow of solvent (EtOH) over the QCM crystal surface. After a stable frequency baseline was reached (after ∼1 h), NAC in solution (0.6 mM) was injected into the axial flow cell and the frequency response during the adsorption process was followed in situ with a 10-s gate time, resulting in a final frequency resolution of 0.01 Hz.

Density Functional Theory (DFT) Calculations of NAC. To better understand the structure of NAC and to assign the measured vibrational spectrum, DFT calculations were performed using the hybrid functional B3PW91[26,27] with a 6-31G basis set.[28] To account for solvent (EtOH) effects, a polarizable continuum model[29] was used and all calculations were performed with NAC in neutral form, as this prevails in EtOH. The calculations were performed on GAUSSIAN03.[30] The conformation with lowest energy that was found is depicted in Figure 1. A characteristic of this lowest energy conformation is a hydrogen bond between the amide and the carboxylic acid group.

Simulation of Infrared Spectra of Adsorbed Molecules. The determination of the orientation of a molecule on a surface relies on the fact that the intensity of a vibrational band depends on the angle between the corresponding transition dipole moment vector and the electric field vector. For metals, the electric field is polarized perpendicular to the surface, which leads to the metal surface selection rule.[31] The latter states that only vibrations associated with a transition dipole moment vector component perpendicular to the surface can be observed. This rule is generally applied for external reflection, but its validity for internal reflection has been demonstrated.[32,33] To simulate the influence of orientation on the infrared spectra, the transition dipole moment vector for each normal mode has to be determined in the (arbitrary defined) molecular coordinate system. For symmetric molecules, the direction of some transition dipole moment vectors can be determined by symmetry considerations.[34] Since NAC is not symmetric, the determination of the transition dipole moment vectors fully relies on quantum chemical calculations. After complete structure optimization, a normal-mode analysis was performed, yielding the transition dipole moment vectors for every normal mode of vibration. The vectors are represented in the molecular coordinate system with the coordinate axes pointing along the principal axes of inertia of the molecule. For simplicity, in the reference orientation, the molecular coordinate system coincides with the fixed surface coordinate system (x,y,z) with the x−y-plane defining the surface plane and the z-axis the surface normal. The coordinate systems are defined in Figure 1 for the reference orientation as a box around the molecule.

To simulate the impact of different orientations on the spectra, the molecular coordinate system was rotated around the x- and y-axis, respectively, of the surface coordinate system, by the rotation angles α and β, respectively. Mathematically, the rotation around α, followed by rotation around β is represented by the orthogonal transformation matrix

$$\mathbf{R}_{\alpha\beta} = \begin{pmatrix} \cos(\beta) & \sin(\beta)\sin(\alpha) & \sin(\beta)\cos(\alpha) \\ 0 & \cos(\alpha) & -\sin(\alpha) \\ -\sin(\beta) & \cos(\beta)\sin(\alpha) & \cos(\beta)\cos(\alpha) \end{pmatrix} \quad (2)$$

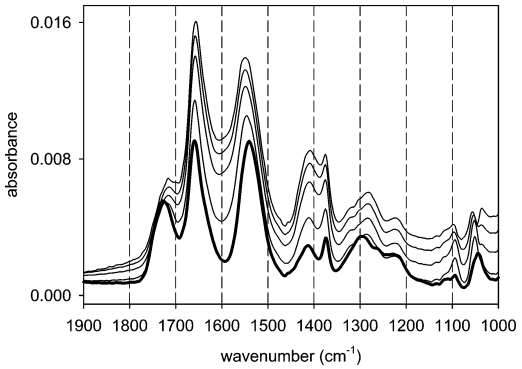

Figure 2. Time-resolved ATR-IR spectra recorded in situ during the NAC self-assembling process on the gold-coated Ge-IRE. The boldface solid line refers to the first spectrum recorded 43 s after the inflow of dissolved NAC (0.6 mM) at 0.18 mL/min. Subsequent spectra are recorded in a time interval of ∼12 min.

Due to the metal surface selection rule, only the z-component of the transition dipole moment μ_z contributes to the intensity of a vibrational band. Note that μ_z depends on the rotation angles α and β.

By using a normalized Lorentzian band shape (half-width at half maximum $\gamma = 1$ cm^{-1}), the spectra for different molecule orientations were calculated according to[35]

$$I(\nu) = \sum_{i=1}^{N} {\mu_{z,i}}^2 \frac{\gamma}{\pi} \frac{1}{(\nu - \nu_{\mathrm{calc},i})^2 + \gamma^2} \quad (3)$$

where N is the total number of normal modes and $\nu_{\mathrm{calc},i}$ is the calculated frequency of mode i.

Results and Discussion

Orientation of *N*-Acetyl-L-cysteine within the Adsorbate Layer. The ATR-IR spectra recorded during the self-assembling of NAC on the gold-coated Ge-IRE are depicted in Figure 2. The set of ATR-IR spectra represents the first hour of adsorption with a time interval of ∼12 min between subsequent spectra. Obviously, significant differences in the spectra emerge during the self-assembling process, indicating structural changes within the adsorbate layer as will be discussed in detail below. The initial spectrum recorded 42 s after the inflow of NAC (0.6 mM) over the gold-coated Ge-IRE is depicted as the boldface solid line in Figure 2. This spectrum serves as the reference for the initial state of the NAC on the surface, reflecting mainly the gold−NAC interaction. At higher coverage, intermolecular interactions between adsorbed molecules become increasingly important.

To assess the orientation of NAC adsorbed on the Au surface, an ATR-IR spectrum of the dissolved or liquid sample is needed. This allows a comparison with the calculated spectrum and yields experimental values for relative band intensities of the randomly oriented molecule. For this purpose, an EtOH versus EtOH + NAC modulation experiment was performed over the bare Ge-IRE. The measured phase-resolved spectrum is depicted in the lower half in Figure 3. The most prominent NAC bands are visible at 1729, 1665, and 1551 cm^{-1}, respectively, together with less intense signals at 1375, 1221, and 1043 cm^{-1}. The calculated IR spectrum of NAC is presented in the upper half in Figure 3. The calculated IR spectrum reveals intense signals at 1729, 1655, and 1494 cm^{-1} with less intense signals at 1353, 1136, and 1100 cm^{-1}. The overall agreement between the

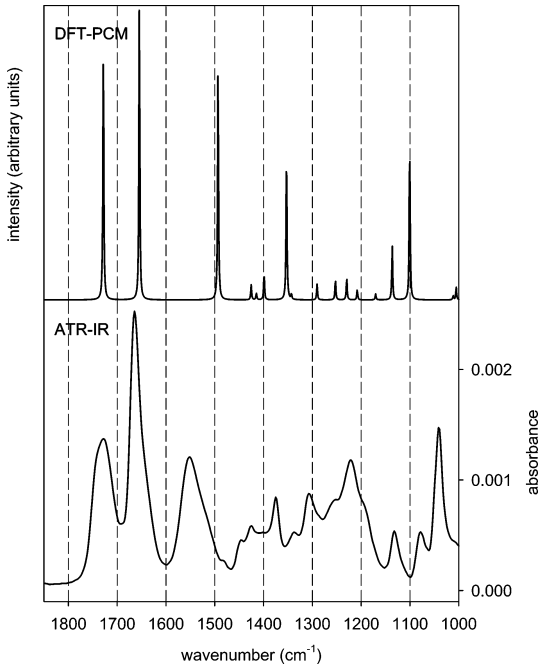

Figure 3. Top: Calculated IR spectrum of NAC. The spectrum was obtained by convoluting the calculated IR intensities with a Lorentzian band shape (half-width at half maximum, 1 cm^{-1}). The optimized structure of NAC found by DFT calculations (see text for details) is shown in Figure 1. Bottom: Demodulated ATR-IR spectrum of NAC dissolved in EtOH. The spectrum was obtained from an EtOH vs EtOH + NAC (0.03 M, flow rate 0.5 mL/min) modulation experiment using a modulation period $T = 120.4$ s.

TABLE 1: Observed Vibrational Frequencies (in Wavenumbers/cm^{-1}) of NAC Dissolved in EtOH and Adsorbed on Gold[a]

label[b]	dissolved NAC	adsorbed NAC	calculated	assignment
A	1729	1727	1729	ν(−COOH)
B	1665	1661	1655	amide I
		1590		ν_{as}(−COO^-)
C	1551	1539/1560 (shifted)	1494	amide II
		1400		ν_s(−COO^-)
D	1375	1375	1353	methyl + δ(−CH_2) + δ(−COH) + ν(−CO)
	1221	1294		δ(−COH) bending
		1130	1136	δ(−COH) bending + δ(−CH_2) twisting + ν(−CN) stretching
E	1040	1042	1100	δ(−COH) bending + δ(−CH_2) twisting + ν(−CN) stretching

[a] Experimental ATR-IR spectra of dissolved NAC and adsorbed on gold are displayed in Figure 4. The calculated NAC vibrations are also given (see text for details). The calculated spectrum is presented in the upper half in Figure 3 and in Figure 6. [b] Label used to denote characteristic bands in the calculated spectra in Figures 5 and 6.

experimental and calculated spectra is good enough to allow an assignment of the most prominent NAC bands, which is given in Table 1.

The spectrum of dissolved NAC (as presented in the lower half in Figure 3) is compared to the spectrum of the adsorbed species in Figure 4 (the same spectrum as in Figure 2, solid line). As is obvious, significant differences in intensity of the prominent bands are visible, which strongly implies the presence

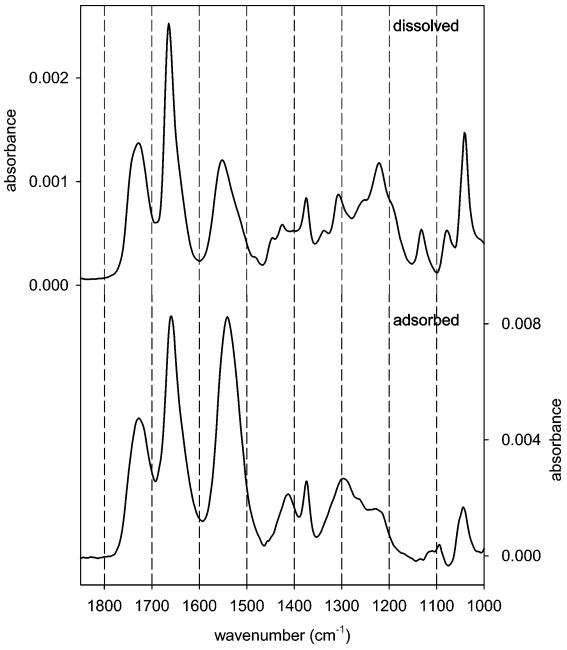

Figure 4. Top: ATR-IR spectrum of dissolved NAC obtained from a modulation experiment (see also Figure 3, bottom). The spectrum corresponds to randomly oriented molecules. Bottom: ATR-IR spectrum of NAC adsorbed on the gold-coated Ge-IRE (the same spectrum is depicted as the boldface solid line in Figure 2) recorded 43 s after the inflow of EtOH + NAC (0.6 mM) at 0.18 mL/min. Note that this spectrum corresponds to oriented molecules adsorbed on the surface.

of an oriented adsorbate layer on the gold surface. Specifically, the intensity ratios of the amide I (1665 cm^{-1})/amide II (1551 cm^{-1}) and amide II (1551 cm^{-1})/methyl (1375 cm^{-1}) bands change significantly upon adsorption of NAC on gold. Other changes in band intensity between random orientation and surface orientation are visible for the band at 1045 cm^{-1}, which loses intensity upon adsorption, and the spectral region between 1300 and 1200 cm^{-1}. Apart from the described changes in relative band intensity, the frequency of most vibrational bands does not change much (see Table 1), which indicates that the structure of the dissolved and adsorbed molecule is similar.

An experimentally accessible parameter directly related to the orientation is the intensity ratio of two vibrational bands for random (solution) and surface orientation, as expressed by the following equation:[34,36]

$$R_{exp} = \frac{(I^s_m/I^s_n)}{(I^r_m/I^r_n)} \quad (4)$$

where $I_{m,n}$ denotes the measured integrated intensity of vibrational bands m and n, respectively, and the superscripts s and r, respectively, refer to surface and randomly oriented (dissolved) species, respectively. The determination of the orientation, as described in the following, relies on the comparison between experimental and calculated R values. The goal is to find a corresponding value R_{calc}, analogously defined as R_{exp} in eq 4, for the calculated IR (randomly oriented molecules) and simulated ATR-IR (oriented molecules) spectra, using the orientation angles α and β as adjustable parameters. In principle, two values of R_{exp} (i.e., two pairs of vibrations) are sufficient to determine the orientation angles α and β. However, the amide I/amide II, amide I/ν(−COOH) and amide II/methyl pairs of

TABLE 2: Calculated Angles in Degrees between Transition Dipole Moment Vectors for Prominent Normal Modes of Vibration of NAC

	ν(−COOH)	amide I	amide II	methyl
ν(−COOH)	0	47.8	76.3	107.7
amide I		0	117.6	75.9
amide II			0	159.9
methyl				0

modes were considered. The amide I, amide II, and methyl vibrational bands of NAC are located within the *N*-acetyl part of the molecule, which is rather rigid and therefore serves as a pointer for the orientation analysis. It should be noted here that NAC, similar to *N*-acetyl-L-cysteine-*N*-methylamide,[37] is likely not completely rigid, at least in the liquid phase. However, the presence of a pointer fragment with well-defined transition dipole moments, for which the orientation on the surface can be well assessed, together with the assumption that the sulfur interacts with the gold surface, gives rather detailed information on the orientation of the whole molecule. It should also be noted that the angles that result from this analysis give an average value for the adsorbate layer. Furthermore, the described analysis assumes that the magnitudes of the transition dipole moment vectors μ are the same in solution and in the monolayer.

In the reference orientation (Figure 1), the well-defined amide II transition dipole moment vector is oriented almost parallel to the $x-y$ surface plane. The orientation of other prominent dipole moment vectors, i.e., the angles they define with respect to each other is helpful for the orientation analysis and calculated values are thus listed in Table 2.

The effect of different orientation angles α and β on the calculated spectra is illustrated in Figure 5 for different orientation angles α in the upper half and β in the lower half, respectively. Note that, while rotating around one orientation angle, the other was fixed at 0°. The reference orientation is the one depicted in Figure 1 with the corresponding angles $\alpha = \beta = 0°$. For clarity, subsequent spectra are shifted to lower wavenumbers and capital letters indicate prominent calculated vibrational bands of NAC (see Table 1). The simulated spectra for different orientation angles α (upper half in Figure 5) reveal significant changes for the ν(−COOH) (A) and amide I (B) band. Less important changes are visible in the mode labeled E, which has δ(−COH) bending, $\delta(-CH_2)$ twisting, and ν(−CN) stretching character. As is obvious, the prominent amide II band (C) hardly appears in the simulated spectra for any orientation angle α, for $\beta = 0°$, because its transition dipole moment is almost parallel to the $x-y$ plane of the surface coordinate system in this orientation (see Figure 1) and parallel to the long axis of the molecule. This finding, together with the experimental spectrum (Figure 4, lower part), strongly indicates that the long axis of the molecule is not oriented parallel to the surface. Changing the orientation angle β (lower half in Figure 5) has a clear impact on the intensity of the amide II band (C). The latter continuously gains intensity with decreasing orientation angle β, for $\alpha = 0°$, reaching a maximum when the long axis of the molecule is almost parallel to the surface normal z. Note that the methyl band (D) increases together with the amide II band since the two corresponding transition dipole moment vectors are oriented almost antiparallel with respect to each other (159.9°, see Table 2).

By changing the rotation angles α and β in order to adjust R_{calc} to R_{exp}, an optimum agreement was found for $\alpha = -72.5°$ and $\beta = -37.5°$. The corresponding simulated ATR-IR spectrum together with the calculated IR spectrum (random orientation) is displayed in Figure 6. The prominent vibrational bands

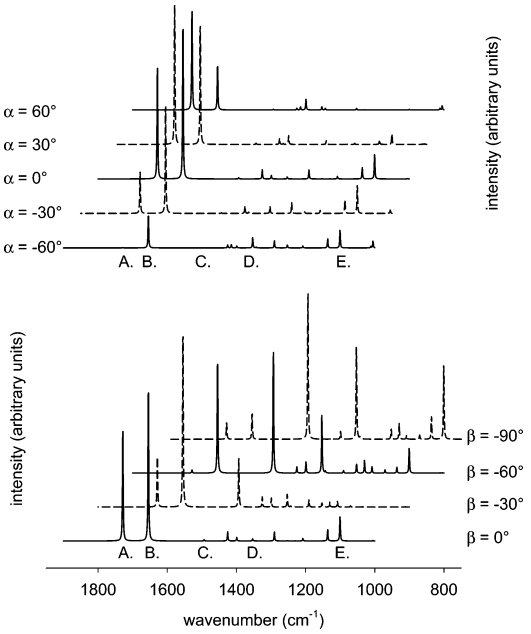

Figure 5. Simulated infrared spectra of NAC for different orientations of the molecule with respect to the metal surface (see Figure 1 for the reference orientation of the molecular and fixed surface coordinate system). Rotations were performed around the *x*- and *y*-axis corresponding to the orientation angles α and β. Note that while one orientation angle was changed, the other was fixed at 0° (see text for calculation method). Capital letters denote prominent vibrational bands of NAC as listed in Table 1.

are again labeled with capital letters as summarized in Table 1. The changes in the relative ATR-IR intensities of the ν(−COOH), amide I, and amide II bands upon adsorption, as evident from the experimental spectra in Figure 4, are well reproduced by the simulations. Note that absolute peak heights are somewhat misleading when comparing the simulated (Figure 6) and experimental spectra (Figure 4), since the simulations assume a fixed line width, whereas not all the bands have the same widths in the experimental spectrum. This is important when comparing the relative intensity of the amide I and amide II bands. The intensity ratio of the amide II/methyl vibrational bands increased upon adsorption, which is in good agreement with the experimental results (see Figure 4), yet the amount of the increase is overestimated in the simulations. This overestimation for the amide II/methyl modes may be explained by the coupling of the methyl mode to the δ(−COH) bending mode as it emerges from the normal-mode analysis. This mode is likely to be affected by the interactions of the OH group with the surface (see below), which are not considered in the applied analysis. Larger deviations are also visible for the mode E calculated at 1100 cm^{-1}, which is clearly more pronounced in the experimental ATR-IR surface spectrum. The calculations revealed that the latter mode has δ(−COH) bending, $\delta(-CH_2)$ twisting, and ν(−CN) stretching character and may thus also be affected by interactions of the C−O−H group with the surface. Noteworthy is the band at 1136 cm^{-1}, which contains most of all CH_2 twisting, but also COH bending character, according to the normal-mode analysis. Both in the experimental and in the simulated spectra, this band is observed for the randomly oriented sample but is basically absent for the oriented molecule.

Based on the simulations discussed above, we suggest an (average) orientation of NAC adsorbed on gold as is schemati-

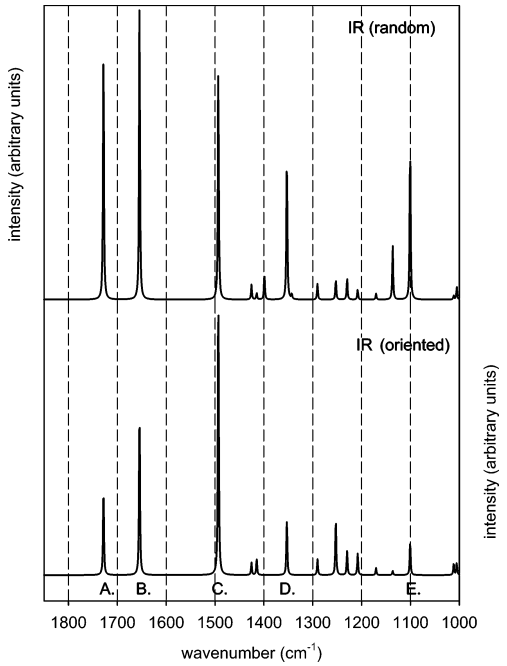

Figure 6. Comparison between calculated spectra of NAC for random orientation (top) and oriented on the gold surface (bottom). The latter spectrum was calculated for the orientation angles $\alpha = -72.5°$ and $\beta = -37.5°$ that were found to best describe the experimentally obtained spectra (compare to the ATR-IR spectra depicted in Figure 4). Prominent vibrational bands of NAC are indicated with capital letters as summarized in Table 1.

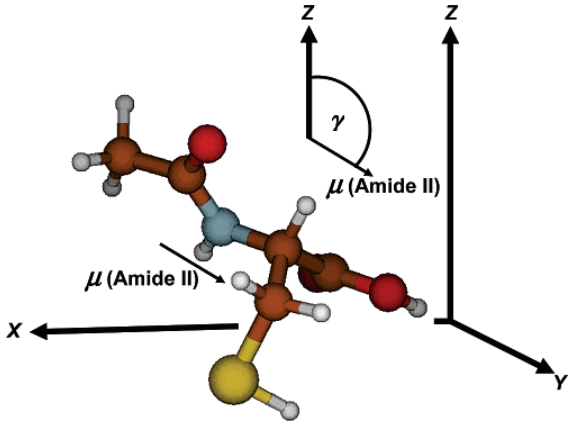

Figure 7. Orientation of NAC on the gold surface (*x*-*y* plane) emerging from the orientation analysis. The corresponding IR spectrum is depicted in Figure 6, bottom. The orientation of the molecule is indicated by the angle $\gamma = 127.5°$ between the surface normal *z* and the amide II transition dipole moment vector (see inset). Note that the amide I transition dipole moment vector is oriented nearly parallel to the C═O bond.

cally depicted in Figure 7. The pointer for the orientation of the molecule, the amide II transition dipole moment vector, now defines an angle $\gamma = 127.5°$ (i.e., a complementary angle of 52.5°) with respect to the surface normal *z* (see inset in Figure 7). It has to be pointed out that the value of γ should be regarded as an estimate rather than a precise value, considering the assumptions inherent in the simulations. However, a characteristic of the elaborated orientation is the considerable tilt of the

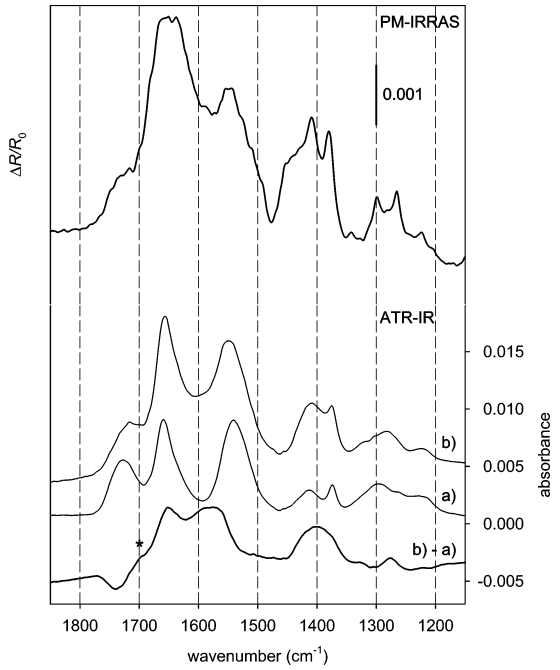

Figure 8. Top: PM-IRRAS spectrum recorded ex situ after sample immersion in a solution of NAC (7 mM) in EtOH for 24 h. Bottom: ATR-IR spectra obtained during the flow of EtOH + NAC (0.6 mM) over the gold-coated Ge-IRE. Spectrum a, recorded 43 s after admitting NAC, is representative for the adsorbate layer at the beginning of the self-assembling process, whereas spectrum b, recorded after 1 h, reveals structural changes within the adsorbate layer during the self-assembling process. To emphasize the structural changes a difference spectrum (b) − (a) is also presented as boldface solid line. The asterisk specifically denotes the ν(−COOH) band shift to lower frequencies.

N-acetyl (pointer) group with respect to the surface, which is clearly supported by the simulations. In addition, in this orientation, the carboxylic acid group of the molecule is in proximity to the surface, which implies interactions between carboxylic acid group and gold surface, as is indicated by the shift of the δ(−COH) band. The latter is found at 1221 cm^{-1} in solution and at 1294 cm^{-1} (broadened) on the surface (compare the spectra in Figure 4).[38] Hence, it shifts to higher wavenumbers upon adsorption. Note again that the proposed structure describes the initial stage of self-assembly.

Structural Changes within the *N*-Acetyl-L-cysteine Monolayer during Self-Assembling. The time-resolved ATR-IR spectra recorded during the self-assembling process of NAC on gold (Figure 2) reveal significant changes. Notably these are the shift of the ν(−COOH) band at 1727 cm^{-1} to lower wavenumbers, the growing intensity between the amide I and amide II bands, and the increasing band around 1400 cm^{-1}. To emphasize these structural changes during the self-assembling process, the first and the last recorded spectra ($\Delta T = 1$ h, Figure 2) are again displayed in the lower half in Figure 8, labeled (a) and (b), respectively, together with the corresponding difference spectrum (b) − (a). Clearly, the ν(−COOH) band shifts to lower frequency as evidenced by the negative band in the difference spectrum at 1740 cm^{-1} and the positive shoulder (indicated with an asterisk) at ∼1700 cm^{-1}. This indicates that the C═O of the acid group is involved in an interaction. On the other hand, a broad intense feature around 1600 cm^{-1} with peaks at 1651, 1590, and 1560 cm^{-1} is apparent. The former peak is due to the gain in intensity of the amide I band which is also obvious

from the two spectra a and b. The band at 1590 cm^{-1} can be assigned to the $\nu_{as}(-COO^-)$ vibration, whereas the band at 1560 cm^{-1} is consistent with an amide II mode, shifted due to hydrogen bonding.[39] In addition, two other positive bands appear in the difference spectrum, a broad intense signal at 1400 cm^{-1} and a less intense one at 1277 cm^{-1}. The former band is assigned to the $\nu_s(-COO^-)$ whereas the latter may be the $\delta(-COH)$ bending mode. In the upper half in Figure 8, a PM-IRRAS spectrum is shown recorded ex situ after 24 h of NAC self-assembling on a gold surface. The overall agreement to the ATR-IR spectrum recorded in situ after 1 h of self-assembling (trace b) is good; however, there are also significant differences. The amide I band has broadened significantly, and the amide II band at 1579 cm^{-1} appears as a small peak out of the pronounced $\nu_{as}(-COO^-)$ band. Additionally, the $\nu_s(-COO^-)$ band at 1400 cm^{-1} has further gained intensity with respect to the amide II band.

The spectral changes during self-assembly, as discussed above, give evidence for two kinds of slow structural changes within the adsorbate layer, besides further adsorption (increasing coverage). The shift of the $\nu(-COOH)$ band at 1727 cm^{-1} to lower wavenumbers indicates hydrogen bonding within the adsorbate layer. A feasible interaction is the hydrogen bonding between carboxylic acid groups of adjacent adsorbed molecules, i.e., dimerization as is found for carboxylic acids in solution.[40] Dimerization of cysteine adsorbed on Au(110) via hydrogen bonding between carboxylic acid groups was proposed based on STM investigations.[14] Another possibility would be the interaction between amide and acid groups of adjacent molecules. The upward shift of the amide II band during the self-assembling would be consistent with such an interpretation, as the amide II vibrations shift to higher frequency upon hydrogen bonding involving the N−H part.[39,41] A shift of the amide II band may also be expected as a consequence of protonation/deprotonation of the carboxylic acid. The DFT calculations, however, show that when the acid is deprotonated the amide II vibration shifts to lower wavenumbers, in contrast to observation. Note that the orientation of the molecule in Figure 7 emerging from the orientation analysis is compatible with the proposed interaction modes since the position and orientation of the acid group easily allows for intermolecular interactions.

Another process occurring on the surface during self-assembling is the deprotonation of the acid group, which is evident from the increase of the $\nu_{as}(-COO^-)$ band at 1590 cm^{-1} and the $\nu_s(-COO^-)$ band at 1400 cm^{-1}, respectively. In EtOH, NAC prevails in neutral form with the carboxylic acid groups being protonated, as is evident from the solution spectrum (Figure 4, top). The observed deprotonation is assisted by the interaction of the acid groups with the Au surface, which acts as a proton acceptor. The observed deprotonation process of NAC thus requires the vicinity of the acid group to the gold surface. In other words, the proposed initial orientation of the molecules on the surface (Figure 7) is favorable for both processes observed during self-assembling, namely, deprotonation and intermolecular hydrogen bonding. As emerges from the differences between the PM-IRRAS spectrum (upper half in Figure 8) recorded ex situ after 24 h of self-assembling and the ATR-IR spectrum (trace b) recorded in situ after 1 h of self-assembling, the structural changes discussed above seem to continue for a long time. ATR-IR experiments where the flow of NAC was replaced by a flow of neat ethanol after 1 min also revealed the slow deprotonation, showing that the latter process is independent of further supply of NAC (increasing coverage).

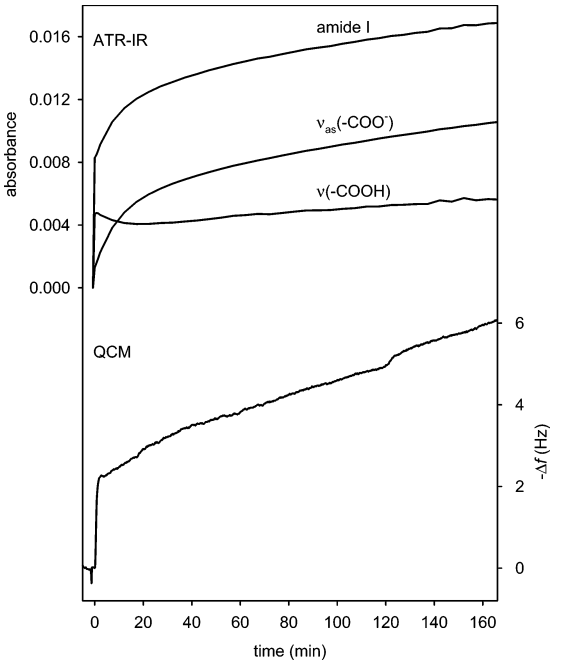

Figure 9. Top: Time dependence of selected prominent NAC bands obtained by ATR-IR when flowing NAC in solution (0.6 mM) over the gold-coated Ge-IRE (flow rate 0.18 mL/min). Bottom: Shift in resonant frequency recorded in situ during the adsorption of NAC (0.6 mM) on the QCM sensor crystals.

To learn more about the kinetics of the self-assembling process and the structural changes, the absorbance as a function of time of selected NAC vibrational bands is depicted in the upper half in Figure 9. A fast initial increase of the amide I signal is replaced by a considerably slower, almost linear increase after ∼90 min. In contrast, the $\nu(-COOH)$ signal behaves completely different with time. Shortly after the onset of the self-assembling process, the signal decreases in order to increase smoothly and almost linearly with time after ∼30 min. The frequency shift as a function of time recorded during the adsorption of NAC on the surface of the QCM crystal is shown in the lower half in Figure 9. The frequency shifts rapidly and almost linearly with time during the initial step of self-assembling. After the abrupt onset, a distinctly slower shift in resonant frequency with time is observed. We should mention that the shape of the frequency shift curve was well reproducible on different days with different QCM sensor crystals. The slow-frequency shift was found to continue for hours and was after some time indistinguishable from overlapped baseline drifts.

In Figure 9, the response to the adsorption and self-assembling of NAC on gold is presented for two different measurement techniques, i.e., ATR-IR and QCM. For the former, the increase in intensity of a signal is not related to the net mass uptake only. Structural changes in a SAM, such as reorientation, intermolecular interactions, or protonation/deprotonation of adsorbed molecules may also affect the transition dipole moments (magnitude and orientation) and thus influence the intensity of vibrational bands. The shift in resonant frequency of a QCM resonator, on the other hand, depends on mass loading according to the Sauerbrey equation.[42] In liquid environment, however, frequency changes are influenced by the energy dissipation at the interface, which may be changing during SAM formation.[43] In addition, viscous coupling of the oscillating crystal surface to the liquid medium results not only in a

decrease in the resonant frequency but also in a damping of the resonant oscillation. The latter viscous loss is manifested as an increase in resonance resistance of the QCM resonator.[44] However, besides the different complex processes occurring simultaneously, as indicated by the ATR-IR experiments, the measured shift in resonant frequency is still assumed to be a direct result of the self-assembling. This assumption was further confirmed by the absence of a sharp increase in resonance resistance during the SAM formation. According to the Sauerbrey relation[42] (with a mass sensitivity constant of 17.7 ng cm^{-2} Hz^{-1}), a frequency shift of 6 Hz, reached at ∼2.5 h of adsorption, corresponds to a total mass uptake of 106.2 ng/cm^2, which is equivalent to 3.9×10^{14} NAC molecules/cm^2 (neglecting trapped solvent molecules). This is less than one NAC molecule per three Au surface atoms. STM work on cysteine SAMs on gold showed that one molecule occupies three gold surface atoms.[45] Therefore, the QCM analysis indicates that there are no multilayers present under the applied conditions. However, it is noted that the numbers given above should be taken as an estimate due to the difficulties of quantitative QCM measurements in liquid phase, as just outlined.

Both ATR-IR and QCM provide a rather complex picture of the SAM formation. Within the NAC adsorbate layer, structural changes are mainly induced by three different processes, namely, the adsorption, i.e., bare mass uptake, the deprotonation of the acid group upon interaction with the Au surface, and the changes in the hydrogen-bonding network. The initial fast increase in intensity of the amide I and the ν(−COOH) signal is mainly attributable to adsorption of molecules on the surface. The initial fast mass uptake is also reflected in the sharp shift in resonant frequency of the QCM sensor crystals. At later stages of self-assembly, i.e., at higher surface coverage, the different processes occurring simultaneously on the surface are more difficult to separate. What concerns the amide I signal the slight, almost linear increase in intensity after some time, is likely not only due to the adsorption process (mass uptake). In an experiment where the flow of NAC was replaced by neat ethanol, the amide I band continued to slightly increase, concomitant to the deprotonation process. This indicates a reorientation of the amide group when the molecule is deprotonated. In the case of the ν_{as}(−COO$^-$) signal, the increase in intensity is primarily attributable to the formation of the deprotonated species on the surface. The ν(−COOH) signal at 1727 cm^{-1}, which refers to the non-hydrogen-bonded species, shows the most complex behavior. The decrease in intensity of this signal shortly after the onset the self-assembling process reveals that the hydrogen-bonding or deprotonation processes dominate over the adsorption, which in turn would result in an increase in intensity.

Induced Structural Changes within the *N*-Acetyl-L-cysteine Self-Assembled Monolayer. Structural changes within the adsorbate layer upon concentration and acid stimuli were probed by modulation excitation ATR-IR spectroscopy (see Experimental Section). It was shown in a previous work that the structure of the molecules within the adsorbate layer can reversibly be changed by alternately flowing EtOH and EtOH + HCl over a glutathione SAM (acid stimuli).[13] In addition, the presence of dissolved species at the SAM interface may have an impact on the structure of the latter. In Figure 10, we present the results of the modulation experiments described above. For clarity, a static spectrum of NAC recorded after 1 h of self-assembling on gold is displayed as a boldface solid line, trace a) in Figure 10. The curve labeled (b) refers to a phase-resolved (PSD) spectrum of the EtOH versus EtOH + NAC (0.6 mM) modulation experiment, scaled by a factor of 20. In

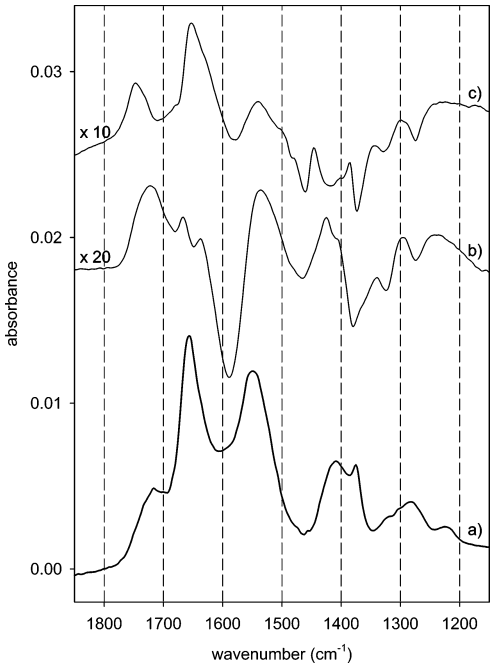

Figure 10. Static ATR-IR spectrum recorded 1 h after the inflow (0.18 mL/min) of NAC in solution over the gold-coated Ge-IRE (trace a). A demodulated, i.e., phase-resolved spectrum for a concentration modulation experiment (T = 483.2 s) is represented by trace b. In this experiment, EtOH and NAC dissolved in EtOH was allowed to flow (at 0.18 mL/min) alternately over the NAC SAM. Trace c refers to a demodulated spectrum of a "pH" modulation experiment (T = 120.7 s) upon flowing alternately EtOH and EtOH + HCl (∼0.013 mM) at 0.5 mL/min over the SAM.

this experiment, dissolved NAC and neat solvent (EtOH) were flowed alternately over the SAM (after 2 h of self-assembling). The experiment was repeated with different modulation periods, i.e., T = 72.4, 120.7, 362.4, 483.2, and 604 s, respectively. The presented PSD spectrum (trace b) refers to a modulation period T = 483.2 s and was obtained by evaluating eq 1 for a set of 60 time-resolved spectra. Only bands that are periodically changing with time due to the stimulation (concentration modulation) show up in this spectrum. During the first half-period of the modulation experiment, EtOH was flowed over the SAM and the signal at 1722 cm^{-1} was observed to decrease. At the beginning of the second half-period, NAC in EtOH was introduced accompanied by a decrease of the band at 1590 cm^{-1} and a simultaneous increase of the signal at 1722 cm^{-1}. The two bands mentioned thus reveal amplitudes of different sign in the PSD spectrum. Note that the signals are relatively small compared to the static spectrum (scale factor 20), indicating that only a small fraction of molecules contributes to the spectral response.

The appearance of the band at 1590 cm^{-1} may indicate a reversible protonation-deprotonation of the acid groups of part of the molecules within the adsorbate layer, stimulated by the concentration modulation. In addition, the ν(−COOH) band at 1722 cm^{-1} gives evidence that primarily the hydrogen-bonded species respond toward the stimulation. Possibly this signal is partly due to weakly bound (physisorbed) molecules. Physisorbed molecules were also evident for cysteine SAMs.[46] The demodulated spectrum, however, cannot only be explained by the appearance/disappearance of physisorbed species at the interface. The presence of weakly bound NAC leads to structural

changes within the SAM. A similar observation was already reported for glutathione (γ-Glu−Cys−Gly) SAMs.[13] These structural changes, besides protonation/deprotonation, are indicated for example by the band at 1535 cm^{-1}, which falls in the amide II region. The latter band, together with (part of) the band of opposite sign at 1590 cm^{-1} may arise due to a shift of the amide II vibration, induced by a change in the hydrogen-bonding network. The following process may thus explain the observations during concentration modulation (although we note that other interpretations of the spectral changes may be possible): In the absence of physisorbed molecules (in ethanol), the carboxylic acids are involved in intermolecular hydrogen bonding, involving the N−H of the amide group. Upon admitting NAC, the physisorbed molecules compete for these intermolecular interactions among chemisorbed molecules, by acid dimer formation. Thus, the hydrogen bond involving the N−H group is broken (causing the shift of the amide II signal) and new hydrogen-bonding interactions (acid dimer formation) involving the acid groups of one chemisorbed and one physisorbed molecule are established (causing the band at 1722 cm^{-1}).

Trace c in Figure 10 shows a PSD spectrum of the EtOH versus EtOH + HCl modulation experiment ("pH" modulation, $T = 120.7$ s). During the first half-period (inflow of EtOH over the SAM), the signal at 1747 cm^{-1} was observed to decrease with the band at 1581 cm^{-1} increasing simultaneously. The behavior of the bands was opposite during the second half-period of the modulation experiment (inflow of HCl in ethanol). The spectra thus indicate a protonation/deprotonation of the acid group of adsorbed NAC within the adsorbate layer. Interestingly, the position of the ν(−COOH) signal (1747 cm^{-1}) shows that mainly the not hydrogen-bonded species respond to the acid stimuli. The appearance of a pronounced amide I signal at 1653 cm^{-1} in the demodulated spectra indicates a reorientation of the amide group upon protonation/deprotonation of the carboxylic acid group. Again, the overall signals in the demodulated spectra are relatively small compared to the signals in the static ATR-IR spectrum (note the scale factor 10), indicating that only a fraction of the molecules are involved in the observed process.

Comparison between *N*-Acetyl-L-cysteine and Glutathione. At this point, it is interesting to compare the behavior of NAC and glutathione (γ-Glu−Cys−Gly).[13] Both molecules contain cysteine as the main anchoring part to the gold surface. In both cases, the (partial) deprotonation of a carboxylic acid group is observed during self-assembling. Both molecules respond toward acid stimuli and toward the presence of physisorbed molecules with structural changes. For both systems, the carboxylic acid groups seem to have a significant effect on SAM formation, through both intermolecular interactions (in the case of glutathione possibly also intramolecular interactions) and interactions with the gold surface. A significant difference between the two systems is the kinetic of SAM formation as evidenced by QCM measurements. Glutathione also shows the initial fast frequency change. However, afterward, the frequency changes further for ∼30 min, before reaching an almost constant value, in contrast to the observation made for NAC. A further important difference between the two systems concerns the ionic state-dependent conformation observed for glutathione but not for NAC. DFT calculations (neglecting the surface) have shown that the conformation of glutathione changes drastically upon changing the ionic state.[13] This is related to the observed "ion gating" phenomena for glutathione SAMs.[10] In contrast, our calculation for NAC (neglecting the surface) does not reveal strong conformational changes upon protonation/deprotonation. The relative simple structure of NAC, compared to glutathione, furthermore allows the determination of its orientation on the surface, which is much more difficult for glutathione.

Conclusions

The self-assembling of NAC on gold was studied by IR spectroscopy and QCM. Both the kinetics of the self-assembling and the resulting structure of the adsorbate layer are quite complex. QCM and in situ IR spectroscopy reveal very fast initial adsorption from ethanol, followed, after ∼1 min, by a considerably slower mass uptake. After the initial adsorption step, two processes are observed simultaneously to the further slow increase in coverage. On one hand, a fraction of the molecules undergo deprotonation of the carboxylic acid group, the gold surface serving as the proton acceptor. On the other hand, frequency shifts of the ν(−COOH) and amide II bands indicate hydrogen-bonding interactions within the SAM, possibly between the acid and the amide groups of adjacent molecules.

The spectrum recorded after the initial fast adsorption, which does not indicate deprotonation, was used to determine the orientation of the molecule. The analysis was based on transition dipole moment vectors determined by density functional theory and the fact that only the projection of the transition dipole moment vectors on the metal surface normal gives rise to IR intensity for the adsorbed molecules. The orientation analysis showed that the amide group is tilted with respect to the surface. In such an orientation, and assuming that the sulfur binds to the gold, the carboxylic acid group is in proximity to the surface. This is furthermore supported by a shift of the C−O−H bending vibration upon adsorption. This initial adsorption orientation favors both the deprotonation of the carboxylic acid and intermolecular interactions, as observed in the later stage of self-assembling.

Concentration and acid stimuli lead to spectral responses attributable to a reversible protonation/deprotonation of the acid groups of the molecules. However, even for the stimulation with a strong acid (HCl), only a fraction of the adsorbed molecules responded to the stimulation. Also, the two stimuli addressed different molecules on the surface, as is obvious from the different positions of the ν(−COOH) signals in the two corresponding modulation experiments. The physisorption of NAC at the SAM leads to a considerable rearrangement of the hydrogen-bonding network within the SAM, as the physisorbed molecules compete for intermolecular interactions among chemisorbed species. Both concentration and acid stimuli lead to reorientation of the adsorbed molecules, driven by the primarily induced responses (protonation/deprotonation, change of intermolecular interactions).

Acknowledgment. Financial support by the Swiss National Science Foundation and grants of computer time from the Swiss National Supercomputer Centre (CSCS) are kindly acknowledged. Use of sputtering facilities at the Swiss Center for Electronics and Microtechnology (CSEM) in Neuchâtel is kindly acknowledged.

References and Notes

(1) Ulman, A. *Chem. Rev.* **1996**, *96*, 1533.

(2) Cotton, C.; Glidle, A.; Beamson, G.; Cooper, G. *Langmuir* **1998**, *14*, 5139.

(3) Boozer, C.; Ladd, J.; Chen, S. F.; Homola, J.; Jiang, S. Y. *Anal. Chem.* **2004**, *76*, 6967.

(4) Schreiber, F. *J. Phys.: Condens. Matter* **2004**, *16*, R881.

(5) Di Felice, R.; Selloni, A.; Molinari, E. J. *J. Phys. Chem. B* **2003**, *107*, 1151.
(6) Zhang, J.; Chi, Q.; Nielsen, J. U.; Friis, E. P.; Andersen, J. E. T.; Ulstrup, J. *Langmuir* **2000**, *16*, 7229.
(7) Dakkouri, A. S.; Kolb, D. M.; EdelsteinShima, R.; Mandler, D. *Langmuir* **1996**, *12*, 2849.
(8) Takehara, K.; Aihara, M.; Ueda, N. *Electroanalysis* **1994**, *6*, 1083.
(9) Zhou, A.; Xie, Q.; Wu, Y.; Cai, Y.; Nie, L.; Yao, S. *J. Colloid Interface Sci.* **2000**, *229*, 12.
(10) Hepel, M.; Tewksbury, E. *J. Electroanal. Chem.* **2003**, *552*, 291.
(11) Fang, C.; Zhou, X. *Electroanalysis* **2003**, *15*, 1632.
(12) Bieri, M.; Bürgi, T. *J. Phys. Chem. B* **2005**, *109*, 10243.
(13) Bieri, M.; Bürgi, T. *Langmuir* **2005**, *21*, 1354.
(14) Kühnle, A.; Linderoth, T. R.; Hammer, B.; Besenbacher, F. *Nature* **2002**, *415*, 891.
(15) Zheng, B. Z.; Ding, X. G.; Zhao, F. Q.; Yang, Y. X. *Anal. Lett.* **2002**, *35*, 2245.
(16) Aihara, M.; Tanaka, F.; Miyazaki, Y.; Takehara, K. *Anal. Lett.* **2002**, *35*, 759.
(17) Gaigalas, A. K.; Ruzgas, T. J. *J. Electroanal. Chem.* **1999**, *465*, 96.
(18) Ruzgas, T.; Wong, L.; Gaigalas, A. K.; Vilker, V. L. *Langmuir* **1998**, *14*, 7298.
(19) Cooper, J. M.; Greenough, K. R.; McNeil, C. J. *J. Electroanal. Chem.* **1993**, *347*, 267.
(20) Harrick, N. J. *Internal Reflection Spectroscopy*; Interscience Publishers: New York, 1967.
(21) Urakawa, A.; Wirz, R.; Bürgi, T.; Baiker, A. *J. Phys. Chem. B* **2003**, *107*, 13061.
(22) Bürgi, T.; Baiker, A. *J. Phys. Chem. B* **2002**, *106*, 10649.
(23) Baurecht, D.; Fringeli, U. P. *Rev. Sci. Instrum.* **2001**, *72*, 3782.
(24) Dabros, T.; van de Ven, T. G. M. *Colloid Polym. Sci.* **1983**, *261*, 694.
(25) Dabros, T.; van de Ven, T. G. M. *Phys. Chem. Hydrodyn.* **1987**, *8*, 161.
(26) Becke, A. D. *J. Chem. Phys.* **1993**, *98*, 5648.
(27) Perdew, J. P.; Chevary, J. A.; Vosko, S. H.; Jackson, K. A.; Pederson, M. R.; Singh, D. J.; Fiolhais, C. *Phys. Rev. B* **1992**, *46*, 6671.
(28) Ditchfield, R.; Hehre, W. J.; Pople, J. A. *J. Chem. Phys.* **1971**, *54*, 724.
(29) Cancès, M. T.; Mennucci, B.; Tomasi, J. *J. Chem. Phys.* **1997**, *107*, 3032.
(30) Frisch, M. J.; Trucks, G. W.; Schlegel, H. B.; Scuseria, G. E.; Robb, M. A.; Cheeseman, J. R.; Montgomery, J. A.; Vreven, T.; Kudin, K. N.; Burant, J. C.; Millam, J. M.; Iyengar, S. S.; Tomasi, J.; Barone, V.; Mennucci, B.; Cossi, M.; Scalmani, G.; Rega, N.; Petersson, G. A.; Nakatsuji, H.; Hada, M.; Ehara, M.; Toyota, K.; Fukuda, R.; Hasegawa, J.; Ishida, M.; Nakajima, T.; Honda, Y.; Kitao, O.; Nakai, H.; Klene, M.; Li, X.; Knox, J. E.; Hratchian, H. P.; Cross, J. B.; Adamo, C.; Jaramillo, J.; Gomperts, R.; Stratmann, R. E.; Yazyev, O.; Austin, A. J.; Cammi, R.; Pomelli, C.; Ochterski, J. W.; Ayala, P. Y.; Morokuma, K.; Voth, G. A.; Salvador, P.; Dannenberg, J. J.; Zakrzewski, V. G.; Dapprich, S.; Daniels, A. D.; Strain, M. C.; Farkas, O.; Malick, D. K.; Rabuck, A. D.; Raghavachari, K.; Foresman, J. B.; Ortiz, J. V.; Cui, Q.; Baboul, A. G.; Clifford, S.; Cioslowski, J.; Stefanov, B. B.; Liu, G.; Liashenko, A.; Piskorz, P.; Komaromi, I.; Martin, R. L.; Fox, D. J.; Keith, T.; Al-Laham, M. A.; Peng, C. Y.; Nanayakkara, A.; Challacombe, M.; Gill, P. M. W.; Johnson, B.; Chen, W.; Wong, M. W.; Gonzalez, C.; Pople, J. A. *GAUSSIAN03*; Rev. C.01 ed.; Gaussian, Inc.: Wallingford, CT, 2003.
(31) Greenler, R. G. *J. Chem. Phys.* **1966**, *44*, 310.
(32) Osawa, M.; Ataka, K.-I.; Yoshii, K.; Yotsuyanagi, T. *J. Electron Spectrosc. Relat. Phenom.* **1993**, *64/65*, 371.
(33) Hutter, E.; Assiongbon, K. A.; Fendler, J. H.; Roy, D. *J. Phys. Chem. B* **2003**, *107*, 7812.
(34) Street, S. C.; Gellman, A. J. *J. Phys. Chem. B* **1997**, *101*, 1389.
(35) Shinohara, H.; Kasahara, T.; Kadokura, K.; Uryu, Y.; Itoh, K. *J. Phys. Chem. B* **2004**, *108*, 3584.
(36) Street, S. C.; Gellman, A. J. *J. Chem. Phys.* **1996**, *105*, 7158.
(37) Bombasaro, J. A.; Zamora, M. A.; Baldoni, H. A.; Enriz, R. D. *J. Phys. Chem. A* **2005**, *109*, 874.
(38) Pearson, J. F.; Slifkin, M. A. *Spectrochim. Acta* **1972**, *28A*, 2408.
(39) Clegg, R. S.; Hutchinson, J. E. *Langmuir* **1996**, *12*, 5239.
(40) Ferri, D.; Bürgi, T.; Baiker, A. *J. Chem. Soc., Perkin Trans. 2* **1999**, 1305.
(41) Wirz, R.; Bürgi, T.; Baiker, A. *Langmuir* **2003**, *19*, 785.
(42) Sauerbrey, G. *Z. Phys.* **1959**, *155*, 206.
(43) Karpovich, D. S.; Blanchard, G. J. *Langmuir* **1994**, *10*, 3315.
(44) Kanazawa, K. K.; Gordon, J., II. *Anal. Chem.* **1985**, *57*, 1770.
(45) Dodero, G.; De Michieli, L.; Cavalleri, O.; Rolandi, R.; Oliveri, L.; Daccà, A.; Parodi, R. *Colloids Surf., A* **2000**, *175*, 121.
(46) Marti, E. M.; Methivier, C.; Pradier, C. M. *Langmuir* **2004**, *20*, 10223.

Chapter 4

D-Penicillamine Adsorption on Gold: An *in Situ* ATR-IR Spectroscopic and QCM Study

Marco Bieri and Thomas Bürgi

Published in Langmuir, Volume 22(20), pp. 8379–8386, doi: 10.1021/la061454y, 2006.

Langmuir **2006,** *22,* 8379−8386

D-Penicillamine Adsorption on Gold: An in Situ ATR-IR Spectroscopic and QCM Study

Marco Bieri and Thomas Bürgi*

Faculté des Sciences, Institut de Microtechnique, Université de Neuchâtel, Rue Emile Argand 11, Bâtiment G, 2009-Neuchâtel, Switzerland

Received May 23, 2006. In Final Form: July 14, 2006

The adsorption of penicillamine from ethanol on gold was studied in situ by attenuated total reflection infrared (ATR-IR) and quartz crystal microbalance (QCM) experiments. Both ATR-IR and QCM reveal a fast mass uptake. In ethanol, the molecule adopts a zwitterionic form. Upon adsorption, part of the molecules deprotonate at the amine group, which is a relatively slow process that goes along with a strong shift of the $\nu_{as}(COO^-)$ mode. Both ATR-IR and QCM confirm a physisorbed layer. ATR-IR furthermore shows that the latter consists of zwitterionic molecules only, whereas both zwitterionic and anionic species are found in the chemisorbed layer. The infrared spectra of the physisorbed and chemisorbed layers are rather different, and the molecules within both layers seem to be oriented with respect to the surface. The ATR-IR spectra furthermore indicate that all three functional groups of penicillamine (i.e., thiol, carboxylate, and amine) interact with the surface, and density functional theory calculations support this finding. QCM also shows that the molecule uses considerably more space on the surface than molecules of similar size, which supports a three-point interaction. The latter leads to a strong anchoring of the molecule to the metal, which may explain the exceptional capability of penicillamine to bind metals.

Introduction

Self-assembled monolayers (SAMs) have been studied extensively in recent years[1−3] due to their potential applications in various branches of surface technology, such as passivation, lubrication, surface engineering, development of (bio)sensors,[4] and biocompatibility. SAMs based on chemisorption of alkanethiols on metal surfaces have been a focus of interest due to their stability and the model character of these systems. However, many applications rely on the buildup of complex structures on top of functionalized SAMs.[3] The presence of additional functional groups, in addition to the thiol, therefore greatly enhances the application potential of these systems, but may also increase the complexity of the self-assembly process due to additional intermolecular interactions and interactions with the surface. For example, the adsorption of cysteine-containing molecules on gold surfaces is enhanced by intermolecular interactions involving the carboxylic acid groups, as revealed by scanning tunneling microscopy.[5] It was furthermore shown that carboxylic acid groups also form an anchor to the gold surface, in addition to the strong gold−sulfur bond.[6−8]

D-Penicillamine (PEN; Scheme 1) is an amino acid related to cysteine (β,β-dimethylcysteine) and valine (β-mercaptovaline). PEN is a strong chelating agent and reacts with the majority of heavy metal ions, particularly with those with an affinity for sulfur.[9] This outstanding metal-binding capability is reflected in the pharmaceutical importance of PEN. However, only the D-enantiomer may be useful because the L-enantiomer is toxic.

Scheme 1. Structures of PEN enantiomers

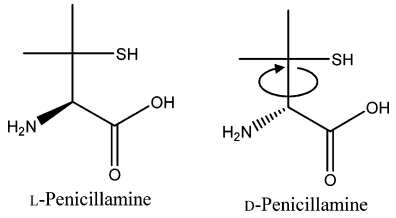

L-Penicillamine D-Penicillamine

In Wilson's disease, a rare genetic disorder of copper metabolism, the main therapeutic treatment relies on PEN's strong binding to accumulated copper and its elimination through urine.[10−12] Chelate formation is also the basis for the elimination of other heavy metals such as, for example, mercury and lead compounds.

In this contribution, we report on the self-assembly of PEN on gold from ethanol solution, as investigated mainly by in situ attenuated total reflection infrared (ATR-IR) spectroscopy. The infrared spectra give evidence for amine−surface interactions concomitant with a deprotonation of the amine functional group. Additionally, significant shifts of the carboxylate vibrational modes also give evidence for COO^-−surface interactions. Adding the strong sulfur−gold bond, this implies a three-point interaction between PEN and the gold surface involving the thiol, amine, and carboxylate functional groups. ATR-IR spectra further suggest the presence of a considerable physisorbed layer on top of the chemisorbed adsorbate layer. Evidence for physisorption is further provided by quartz crystal microbalance (QCM) measurements.

Experimental Section

Materials. PEN (Scheme 1; Sigma-Aldrich Inc., ≥99%) was used without further purification. Ethanol (EtOH, Merck p.a.) was used as solvent for ATR-IR and QCM measurements reported here. Ethanol-d_6 (d_6-EtOD, Cambridge Isotope Laboratories Inc., 99%

* Corresponding author. Telephone: ++41 32 718 24 12. Fax: ++41 32 718 25 11. E-mail: thomas.burgi@unine.ch.

(1) Bain, C. D.; Whitesides, G. M. *Science* **1988**, *240*, 62.
(2) Ulman, A. *Chem. Rev.* **1996**, *96*, 1533.
(3) Schreiber, F. *J. Phys.: Condens. Matter* **2004**, *16*, R881.
(4) Jelinek, R.; Kolusheva, S. *Chem. Rev.* **2004**, *104*, 5987.
(5) Kühnle, A.; Linderoth, T. R.; Hammer, B.; Besenbacher, F. *Nature* **2002**, *415*, 891.
(6) Marti, E. M.; Methivier, C.; Pradier, C. M. *Langmuir* **2004**, *20*, 10223.
(7) Bieri, M.; Bürgi, T. *Langmuir* **2005**, *21*, 1354.
(8) Bieri, M.; Bürgi, T. *J. Phys. Chem. B* **2005**, *109*, 22476.
(9) McAuliffe, C. A.; Murray, S. G. *Inorg. Chim. Acta* **1972**, *6*, 103.
(10) Peisach, J.; Blumberg, W. E. *Mol. Pharmacol.* **1969**, *5*, 200.
(11) Yeh, S. J.; Leu, M. L.; Strickland, G. T. *J. Lab. Clin. Med.* **1971**, *77*, 438.
(12) Tu, J. B.; Blackwell, R. Q.; Watten, R. H. *Metabolism* **1965**, *14*, 653.

10.1021/la061454y CCC: $33.50
Published on Web 08/25/2006

anhydrous) was used to record PEN transmission spectra and for selected adsorption experiments.

In Situ ATR-IR Spectroscopy. Sample Preparation. For ATR-IR spectroscopy, 50 mm × 20 mm × 2 mm Ge trapezoids (Komlas) with an angle of incidence of 45° were used as internal reflection elements (IREs). For PEN adsorption experiments, the IREs were first polished with a 0.25-μm grain size diamond paste (Buehler, Metadi II) and afterward rinsed copiously with EtOH before the surface was cleaned in an air plasma (PlasmaPrep 2, Gala Instrumente) for 5 min. Next, a thin gold layer with a thickness of about 2 nm was sputtered (Balzers Union SCD 030) onto the Ge IRE surface. It should be noted that sputtering of such thin films does not result in uniformly flat gold surfaces but rather islands or particles (see, for example, ref 13). For each PEN adsorption experiment a fresh gold layer was prepared. Control experiments with a bare Ge IRE revealed no PEN adsorption during several hours of exposure to a corresponding solution.

Data Acquisition. For ATR-IR measurements a Bruker Equinox 55 Fourier transform infrared (FT-IR) spectrometer with a liquid nitrogen-cooled narrow-band mercury cadmium telluride detector was used. For in situ ATR-IR analyses, a home-built liquid flow-through cell was used with a volume of 0.077 mL and a gap of 265 μm between the IRE and the steel surface. All ATR-IR spectra presented here were recorded at room temperature (298 K) with 4 cm^{-1} resolution at 40 kHz sampling rate. More detailed information about the ATR-IR cell can be found elsewhere.[14,15]

PEN Adsorption and Modulation Experiments. Before starting a (modulation) ATR-IR experiment, solvent and sample solution were treated with nitrogen gas (99.995%, CarbaGas) to remove dissolved oxygen. Solvent (EtOH) was then allowed to flow first over the gold-coated Ge IRE until no variations in the spectrum could be detected (typically after about 5 min). The corresponding spectrum, recorded by co-adding 200 interferograms, served as the reference for all subsequent measurements. Then PEN dissolved in EtOH (PEN concentrations for all ATR-IR measurements reported here were 0.6 mM) was flowed at 0.18 mL/min over the gold-coated Ge IRE, and the adsorption and self-assembly, respectively, were followed in situ up to 2 h by recording spectra in intervals of 43 s.

In addition to the investigation of the PEN adsorption process, acid/base stimuli of the adsorbate layer were performed. For this purpose, EtOH was first flowed copiously over the adsorbate layer before acidic EtOH (0.013 mM HCl in EtOH) and basic EtOH (0.18 mM NaOH in EtOH) were introduced into the flow-through cell. Acid/base stimuli may change the ionic form of chemisorbed molecules and thus lead to shifts and/or appearance of new vibrational bands, which furthermore assists in the assignment of vibrational bands.

To further investigate the structure of the PEN adsorbate layer, notably to elucidate the presence of a physisorbed layer, concentration modulation experiments were performed. For these experiments, performed after PEN chemisorption, the flow of EtOH was periodically replaced by an equal long flow of PEN (0.6 mM) dissolved in EtOH. For concentration modulation experiments, a period of $T = 120.7$ s (co-addition of 10 interferograms per spectrum, 60 spectra per modulation period) was used. Modulation experiments result in sets of time-resolved spectra that were transformed by means of a digital phase-sensitive detection (PSD) according to eq 1:

$$A_k^{\phi_k^{\mathrm{PSD}}}(\tilde{\nu}) = \frac{2}{T}\int_0^T A(\tilde{\nu},t)\,\sin(k\omega t + \phi_k^{\mathrm{PSD}})\,\mathrm{d}t \qquad (1)$$

where $k = 1, 2, 3,...$ determines the demodulation frequency (i.e., fundamental, first harmonic, and so on), T is the modulation period, $\tilde{\nu}$ denotes the wavenumber, ω is the stimulation frequency, and ϕ_k^{PSD} is the demodulation phase angle. By evaluating eq 1 for different demodulation phase angles ϕ_k^{PSD}, a set of time-resolved spectra $A(\tilde{\nu},t)$ can be transformed into a series of phase-resolved spectra $A_k^{\phi_k^{\mathrm{PSD}}}$. It should be noted that only spectra demodulated at the fundamental frequency ($k = 1$) are reported here. More information about the modulation technique can be found elsewhere.[7,15,16]

Quartz Crystal Microbalance Analyses. Instrumentation and Setup. The model used for QCM measurements was a QCM 200 from Stanford Research Systems with a 5 MHz (nominal) crystal oscillator, which allowed simultaneous measurement of resonant frequency and resistance. The QCM sensors (5 MHz, AT cut, 1 in. in diameter) were a quartz/chrome/gold composite with an optically clear surface finish (about 50 nm average surface roughness). Well-defined flow conditions and high sensitivity over the QCM sensor surface were established by using an axial flow cell with a volume of about 150 μL (Stanford Research Systems). The sample solution was injected perpendicularly with respect to the QCM sensor surface and flowed radially outward from the input port to the exit channel at the edge of the axial flow-cell chamber. The design of the axial flow cell provided a stagnant flow field with the stagnant point coinciding with the center of the QCM sensor and overlapping the area of highest sensitivity of the QCM crystal oscillator. More information about the stagnant flow field can be found elsewhere.[17,18]

To minimize noise induced by the flowing liquid, the system was operated in open-flow mode, that is, completely relied on gravity (siphon principle). Small flow rates <0.1 mL were used. Solvent and sample solutions were stored in separated vessels and could be introduced into the axial flow cell by means of a six-port selection valve (Upchurch Scientific).

Sample Preparation. Before each QCM experiment, the sensor crystals were immersed into a modified piranha solution (1:2 H_2O_2(30%)/H_2SO_4, heated at 120 °C) for 5 min and afterward rinsed copiously with Milli-Q water and EtOH in succession.

Safety note: Piranha solution is extremely aggressive and should be handled with care!

QCM Measurements. Individual PEN adsorption experiments started with a flow of EtOH over the QCM sensor crystal surface. After a stable frequency baseline was reached (typically about 1 h after injection), PEN (0.6 mM) was injected into the axial flow cell and the adsorption process was followed in situ by recording the shifts in QCM resonant frequency and resistance, respectively, using a gate time of 10 s, resulting in 0.01 Hz frequency and 0.001 Ω resistance resolution, respectively.

Density Functional Theory Calculations of Penicillamine. To better understand the structure of PEN and to assign the observed vibrational spectrum, density functional theory (DFT) calculations were performed with Gaussian 03[19] using the hybrid functional B3PW91[20,21] with a 6-31G basis set.[22] Solvent effects (EtOH) were accounted for by using a polarizable continuum model[23] for both structure optimization and normal modes analyses. The calculations were performed for PEN in zwitterionic form, as this prevails in

(13) El Roustom, B.; Foti, G.; Comninellis, C. *Electrochem. Commun.* **2005**, *7*, 398.
(14) Urakawa, A.; Wirz, R.; Bürgi, T.; Baiker, A. *J. Phys. Chem. B* **2003**, *107*, 13061.
(15) Bürgi, T.; Baiker, A. *J. Phys. Chem. B* **2002**, *106*, 10649.
(16) Baurecht, D.; Fringeli, U. P. *Rev. Sci. Instrum.* **2001**, *72*, 3782.
(17) Dabros, T.; van de Ven, T. G. M. *Colloid Polym. Sci.* **1983**, *261*, 694.
(18) Dabros, T.; van de Ven, T. G. M. *Phys. Chem. Hydrodyn.* **1987**, *8*, 161.
(19) Frisch, M. J.; Trucks, G. W.; Schlegel, H. B.; Scuseria, G. E.; Robb, M. A.; Cheeseman, J. R.; Montgomery, J. A.; Vreven, T.; Kudin, K. N.; Burant, J. C.; Millam, J. M.; Iyengar, S. S.; Tomasi, J.; Barone, V.; Mennucci, B.; Cossi, M.; Scalmani, G.; Rega, N.; Petersson, G. A.; Nakatsuji, H.; Hada, M.; Ehara, M.; Toyota, K.; Fukuda, R.; Hasegawa, J.; Ishida, H.; Nakajima, T.; Honda, Y.; Kitao, O.; Nakai, H.; Klene, M.; Li, X.; Knox, J. E.; Hratchian, H. P.; Cross, J. B.; Adamo, C.; Jaramillo, J.; Gomperts, R.; Stratmann, R. E.; Yazyev, O.; Austin, A. J.; Cammi, R.; Pomelli, C.; Ochterski, J.; Ayala, P. Y.; Morokuma, K.; Voth, G. A.; Salvador, P.; Dannenberg, J. J.; Zakrzewski, V. G.; Dapprich, S.; Daniels, A. D.; Strain, M. C.; Farkas, O.; Malick, D. K.; Rabuck, A. D.; Raghavachari, K.; Foresman, J. B.; Ortiz, J. V.; Cui, Q.; Baboul, A. G.; Clifford, S.; Cioslowski, J.; Stefanov, B. B.; Liu, G.; Liashenko, A.; Piskorz, P.; Komaromi, I.; Martin, R. L.; Fox, D. J.; Keith, T.; Al-Laham, M. A.; Peng, C. Y.; Nanayakkara, A.; Challacombe, M.; Gill, P. M. W.; Johnson, B.; Chen, W.; Wong, M. W.; Gonzalez, C.; Pople, J. A. *Gaussian 03*, revision C.01; Gaussian, Inc.: Wallingford, CT, 2003.
(20) Becke, A. D. *J. Chem. Phys.* **1993**, *98*, 5648.
(21) Perdew, J. P.; Chevary, J. A.; Vosko, S. H.; Jackson, K. A.; Pederson, M. R.; Singh, D. J.; Fiolhais, C. *Phys. Rev. B* **1992**, *46*, 6671.
(22) Ditchfield, R.; Hehre, W. J.; Pople, J. A. *J. Chem. Phys.* **1971**, *54*, 724.
(23) Cancès, M. T.; Mennucci, B.; Tomasi, J. *J. Chem. Phys.* **1997**, *107*, 3032.

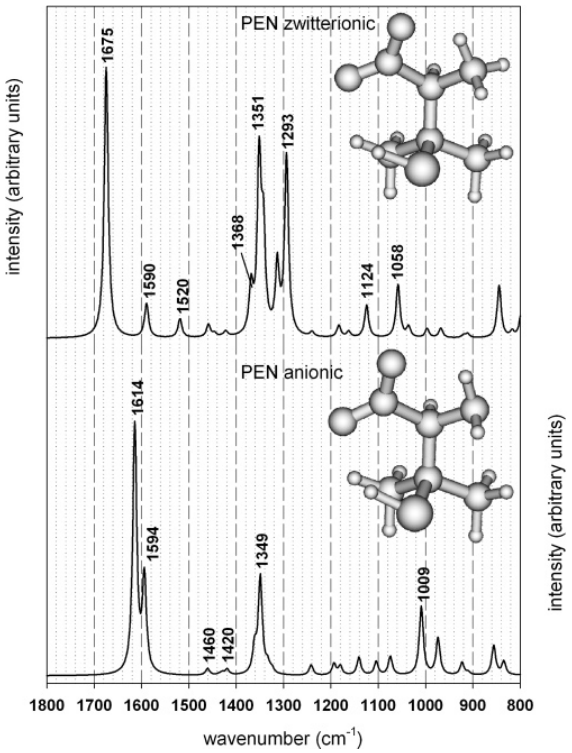

Figure 1. Calculated IR spectra of PEN in zwitterionic (top) and anionic forms (bottom). Spectra were obtained by convoluting the calculated IR intensities with a Lorentzian band shape (half width at half-maximum = 5 cm^{-1}). Corresponding conformations are displayed as insets, and selected prominent vibrational bands are labeled (a summary of the observed vibrational bands is also given in Table 1).

EtOH and in anionic (i.e., deprotonated) form for reasons that will be discussed later. The interaction between the positively charged NH_3^+ group and the negatively charged COO^- is dominated by electrostatics, and a hydrogen bond is being formed between the two functional groups. The molecule furthermore has some rotational degree of freedom around the C−C bond highlighted by a turning arrow in Scheme 1 (right side). The differences in energy between the corresponding conformers were found to be smaller than 1.5 kcal/mol. The conformations with lowest energy that were finally used are displayed as insets in Figure 1 together with the corresponding calculated spectra (top: PEN zwitterionic, bottom: PEN anionic).

The adsorption of anionic PEN on an Au_{19} cluster was studied using Gaussian 03.[19] For the gold atoms, an effective core potential was used. The calculations were performed using the B3PW91[20,21] functional and a LanL2DZ basis set[24] for Au and a 6-31G(d,p) basis set[22] for all other atoms. The geometry of the gold cluster was kept fixed during optimization of the adsorbed PEN with interatomic distances between the gold atoms of 2.884 Å.

Results and Discussion

Calculated IR Spectra of PEN. Figure 1 shows calculated spectra for the lowest energy conformers for both zwitterionic and anionic PEN (see insets). The spectra of both PEN ionic forms are dominated by the strong carboxylate vibrations ($\nu_{as}(-COO^-)$ and $\nu_s(-COO^-)$). The former of the two significantly shifts from 1675 (zwitterionic form, top in Figure 1) to 1614 cm^{-1} (anionic form, bottom) upon deprotonation of the

(24) Hay, P. J.; Wadt, W. R. *J. Chem. Phys.* **1985**, *82*, 270.

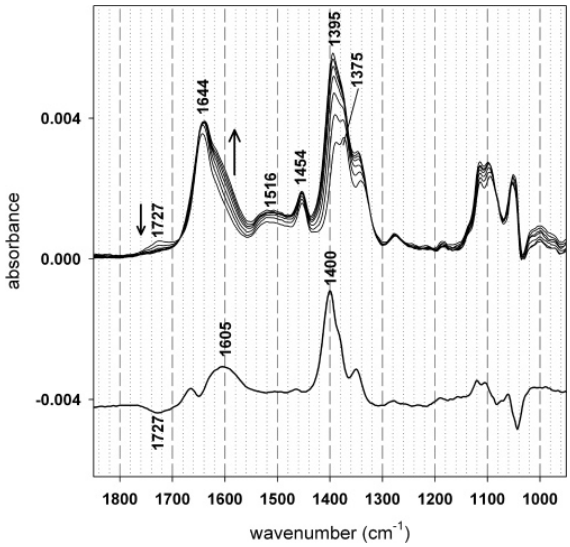

Figure 2. (Top) Set of time-resolved ATR-IR spectra recorded during the first 15 min of PEN adsorption on the gold-coated Ge IRE. Spectra were recorded in intervals of about 2 min. (Bottom) Difference spectrum between the spectrum recorded after 15 min and the one recorded at the beginning (after about 2 min) of adsorption. Prominent vibrational bands used for discussion are labeled in the figure and summarized in Table 1.

NH_3^+ group. The zwitterionic form furthermore has two $\delta_{as}(-NH_3^+)$ modes at 1590 and 1520 cm^{-1}, respectively. The spectral region between 1400 and 1250 cm^{-1} is rather complex for the zwitterionic species with coupling between the $\delta_{as}(-NH_3^+)$, $\nu_s(-COO^-)$, $\delta_s(-CH_3)$, and $\delta(-CH)$ modes. For the anionic case, the $\nu_s(-COO^-)$ mode is coupled to $\delta_s(-CH_3)$ and $\delta(-CH)$ vibrations.

Structural Changes within the PEN Adsorbate Layer during Adsorption on Gold. On top in Figure 2 a set of time-resolved spectra is presented that were recorded during adsorption of PEN from EtOH onto the gold-coated Ge IRE. This set represents the initial 15 min of adsorption, and the spectra were recorded in intervals of about 2 min. Prominent vibrational bands used for the discussion are labeled in the figure and summarized in Table 1. As is obvious, the spectra change significantly during the first 15 min of adsorption, which is further reflected in the corresponding difference spectrum displayed at the bottom in Figure 2. In addition to bare mass uptake during adsorption, these spectral differences indicate structural changes within the adsorbate layer that will be discussed in the following sections.

The set of spectra, recorded during PEN adsorption, first show a strong signal at 1644 cm^{-1} with a shoulder appearing with time (indicated by an arrow pointing upward). This shoulder is clearly visible as a broad band at 1605 cm^{-1} in the difference spectrum. The set of spectra further shows a rather weak band at 1516 cm^{-1}, followed by a sharp signal at 1454 cm^{-1}. The most intense bands are visible between about 1400 and 1300 cm^{-1}. Some of these are growing at different rates with time (e.g., compare the signals at 1395 and 1375 cm^{-1}) but are also undergoing small shifts (e.g., the band at 1395 cm^{-1} is shifting about 7 cm^{-1} to higher wavenumbers). In this spectral region, an intense and sharp signal is appearing at 1400 cm^{-1} in the difference spectrum. Other signals referring to PEN adsorbed on gold are visible in the region between about 1120 and 1050 cm^{-1}. In EtOH, PEN prevails in zwitterionic form (pK_a = 1.90, 7.92, and 10.69, respectively[25]) with the carboxylate (COO^-) moiety being

8382 *Langmuir, Vol. 22, No. 20, 2006* *Bieri and Bürgi*

Table 1. Observed Vibrational Frequencies (in wavenumbers/cm^{-1}) of PEN Adsorbed on Gold as Displayed in Figures 2 and 3[a]

observed zwitterionic	observed anionic	calculated zwitterionic	calculated anionic	assignment
1644/1639		1675		$\nu_{as}(-COO^-) + \delta_{as}(-NH_3^+)$
	1613/1605		1614	$\nu_{as}(-COO^-) + \delta(-NH_2)$
			1594	$\delta(-NH_2)$
1516		1590 and 1520		$\delta_{as}(-NH_3^+)$
			1460 and 1420	$\delta_{as}(-CH_3)$
1454		1368		$\delta_{as}(-CH_3)$
		1351		$\delta_s(-NH_3^+) + \delta_s(-CH_3)$
	1400		1349	$\nu_s(-COO^-) + \delta_s(-CH_3) + \delta(-CH)$
		1293		$\nu_s(-COO^-) + \delta(-CH) + \delta_s(-NH_3^+)$
		1124		$\rho(-CH_3) + \rho(-NH_3^+)$
		1058		$\rho(-NH_3^+) + \delta(-CH)$
			1009	$\rho(-NH_2) + \rho(-CH_3)$

[a] For the sake of completeness, the calculated frequencies are also included for the conformations shown as insets in Figure 1 (top: PEN zwitterionic, bottom: PEN anionic). See Experimental Section for details concerning the calculation method. Note that for mixed vibrations the order of appearance of modes indicates its relative contribution.

deprotonated and the amine moiety being protonated (NH_3^+). This form is also indicated for adsorbed PEN from the spectra in Figure 2 by the $\nu_{as}(-COO^-)$ mode appearing at 1644 cm^{-1}, the $\nu_s(-COO^-)$ vibrational band appearing at about 1400 cm^{-1}, and the broad band at 1516 cm^{-1}, which we assign to the (NH_3^+) mode. The latter assignment is further supported by DFT calculations that predict two $\delta_{as}(-NH_3^+)$ modes at 1590 and 1520 cm^{-1}, respectively (see Figure 1, top).

The signals at 1605 and 1400 cm^{-1}, respectively, in the difference spectrum (Figure 2, bottom) also belong to $\nu_{as}(-COO^-)$ and $\nu_s(-COO^-)$ vibrational modes, respectively. The $\nu_{as}(-COO^-)$ mode is considerably shifted to lower wavenumbers in the difference spectrum. This is consistent with a deprotonation of the NH_3^+ group. The DFT calculations predict a strong shift of the $\nu_{as}(-COO^-)$ mode upon deprotonation of the NH_3^+ group (Figure 1). Furthermore, the calculations reveal a rather strong coupling between the carboxylate and amine vibrational modes for both the zwitterionic and anionic species. In summary, the band at 1644 cm^{-1} in Figure 2, top, is related to the $\nu_{as}(-COO^-)$ mode of the zwitterionic species and the growing shoulder at about 1605 cm^{-1} shows the formation of the anionic species.

The observed deprotonation can be attributed to neither dissolved nor physisorbed molecules as there is no proton acceptor in the liquid phase or in a physisorbed adsorbate layer. We therefore conclude that deprotonation is related to chemisorbed zwitterionic molecules on the Au surface and that the observed deprotonation process is assisted by the interaction of the amine groups with the Au surface, which acts as a proton acceptor.

The weak band at 1727 cm^{-1}, which is assigned to the $\nu(-COOH)$ vibrational mode, shows that a very small fraction of adsorbed molecules is initially protonated at the carboxylate moiety. This could be related to the deprotonation of the NH_3^+ group at the surface, which liberates a proton. The protonation of the carboxylic acid group is, however, only an intermediate state. After some time, the band completely vanishes, which shows the complete deprotonation of the carboxylic acid and which indicates carboxylate surface interactions.

Both the zwitterionic and anionic species contribute to the set of ATR-IR spectra displayed on top in Figure 2. The anionic form is unambiguously related to chemisorbed molecules on the Au surface. In the case of the zwitterionic form, however, the spectra in Figure 2 do not allow discrimination between chemisorbed and possibly physisorbed species. It should also be noted that due to the small concentrations used here (0.6 mM) dissolved PEN from the bulk solution is not visible by ATR-IR. The issue of physisorption will be discussed in the next section.

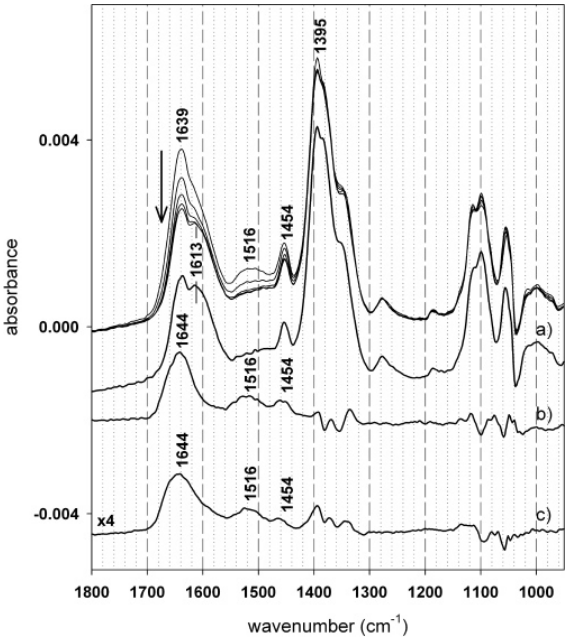

Figure 3. (Top) Set of time-resolved ATR-IR spectra recorded while flowing EtOH (at 0.5 mL/min) for about 10 min over the PEN adsorbate layer. Spectra were recorded in intervals of about 1.5 min. For the sake of clarity, the last spectrum of this set is shifted and labeled with a). (b) A difference spectrum. It represents the difference between the spectrum recorded at the beginning and the one recorded at the end of EtOH flow over the PEN adsorbate layer. (c) A demodulated (i.e., phase-resolved) spectrum of a concentration modulation experiment. In this modulation experiment, EtOH and PEN (0.6 mM) dissolved in EtOH were periodically flowed at 0.5 mL/min over the adsorbate layer using a modulation period of $T =$ 120.7 s.

Physisorption of PEN on the Chemisorbed Adsorbate Layer. In Situ ATR-IR Spectroscopic Analysis. On top in Figure 3, a set of time-resolved spectra is presented that were recorded while flowing EtOH for about 10 min over the PEN adsorbate layer. The temporal interval between subsequent spectra is about 1.5 min. For clarity, the last spectrum recorded in this set is shifted and labeled a). Significant spectral changes become apparent that are emphasized in the corresponding difference spectrum (spectrum b). A rapid decrease of the band at 1639 cm^{-1} (indicated by an arrow pointing downward) is observed.

(25) Sóvágó, I. Metal Ion Complexes with Sulfhydryl-Containing Peptides. In *Handbook of Metal−Ligand Interactions in Biological Fluids. Bioinorganic Chemistry*; Berthon, G., Ed.; Marcel Dekker: New York, 1995; p 657.

The latter signal is slightly shifted to higher wavenumbers in the difference spectrum. In addition, the broad signal at about 1516 cm^{-1} and the one at 1454 cm^{-1} also decrease while rinsing the PEN adsorbate layer with EtOH. In contrast, the intense bands between about 1400 and 1300 cm^{-1} and between about 1120 and 1050 cm^{-1}, respectively, give rise to only weak signals in the difference spectrum. On the basis of the discussion in the preceding section, we associated the spectral changes observed during rinsing only with the zwitterionic species. This is confirmed by the simultaneous decrease of the $\nu_{as}(-COO^-)$ vibrational band at 1639 cm^{-1} and the ($-NH_3^+$) band at 1516 cm^{-1}. In a long-term experiment, the adsorbate layer was rinsed for more than 1 h with EtOH, but the decrease of the $\nu_{as}(-COO^-)$ band referring to the zwitterionic species was found to stagnate after about 30 min. This strongly indicates that two different species are present within the chemisorbed adsorbate layer, notably zwitterionic and anionic molecules.

To further investigate the reversibility of the process, a concentration modulation experiment was performed after formation of a chemisorbed layer. In this modulation experiment, EtOH and PEN dissolved in EtOH were periodically flowed (at 0.5 mL/min) over the adsorbate layer, using a modulation period of $T = 120.7$ s. A corresponding demodulated (phase resolved) spectrum is displayed at the bottom in Figure 3, scaled by a factor 4 and labeled c). It should be noted that only signals that are periodically changing with time due to the stimulation appear in this spectrum. Obviously, the phase-resolved spectrum (label c) is in excellent agreement with the difference spectrum (label b), which underlines the reversibility of the process. Both the difference and phase-resolved spectra thus reveal zwitterionic species, which can be explained in two ways: (i) Structural changes, that is, a deprotonation (via amine ($-NH_3^+$)−surface interactions) of chemisorbed zwitterionic PEN molecules or (ii) the presence of a significant second layer of physisorbed (zwitterionic) PEN molecules on the chemisorbed adsorbate layer. Of these two possibilities, the first one is less plausible, since the deprotonation of the NH_3^+ group of the zwitterionic form should result in the formation of the anionic species at the surface, which is, however, not observed in the difference spectra. We therefore prefer the second possibility and suggest the presence of a physisorbed layer. Furthermore, PSD spectra showed a weak broad band at about 2550 cm^{-1} (not shown) that we assign to the thiol vibration $\nu(-SH)$, which is a strong indication for weakly bound, physisorbed molecules. To further confirm the presence of a physisorbed layer, QCM measurements were performed.

In Situ QCM Analysis. The shift in resonant frequency of a QCM resonator depends on mass loading, according to the Sauerbrey equation.[26] In liquid environment, frequency changes are further influenced by the energy dissipation at the interface, which may change during adsorption.[27] In addition, viscous coupling of the oscillating crystal surface to the liquid medium results not only in a decrease in resonant frequency but also in a damping of the resonant oscillation. The latter viscous loss is manifested as an increase in resonant resistance of the QCM resonator.[28] Despite the different processes occurring simultaneously during adsorption, the shift in resonant frequency is still assumed to be a direct result of the self-assembly.

Figure 4 summarizes the QCM response, that is, the shift in resonant frequency (bold solid line) and resistance (thin solid line) during PEN adsorption on the QCM sensor crystal. As can be seen, the inflow and adsorption of PEN on the crystal oscillator

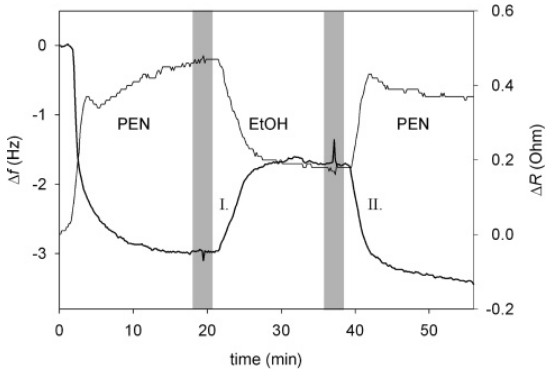

Figure 4. QCM response of PEN (0.6 mM) adsorption from EtOH on gold-coated sensor crystals. The shift in resonant frequency is depicted as bold solid line, and the corresponding frequency axis is shown on the left side. The shift in resonant resistance is shown as thin solid line with the corresponding axis displayed on the right side. The gray regions indicate small disturbances in liquid flow (seen as spikes is the frequency curve) introduced when switching between solutions.

result in a rapid decrease in resonant frequency of about 2.8 Hz that stagnates after about 20 min. In addition, a small increase in resonant resistance of about 0.4 Ω is also observable. Rinsing with EtOH is manifested as an increase in resonant frequency of about 1.2 Hz and a decrease in resonant resistance of about 0.3 Ω (this region is indicated by "EtOH" in the figure). Finally, new inflow of PEN solution again results in a decrease in resonant frequency and an increase in resonant resistance, respectively. The spikes in the frequency curve that are indicated by the gray areas are induced by small disturbances in liquid flow when switching between solutions.

The shift in resonant frequency shows that PEN adsorption on gold is a very rapid process, in agreement with the ATR-IR experiments and results reported on modification of gold electrodes by PEN as investigated by cyclic voltammetry.[29] The initial frequency shift of 2.8 Hz is related not only to chemisorption but also to physisorption, which is clearly evident in the increase of resonant frequency of about 1.2 Hz when flowing EtOH over the adsorbate layer. The desorption of physisorbed molecules (regime I, Figure 4) is followed by readsorption (regime II) when again flowing PEN solution over the chemisorbed adsorbate layer.

The shift in resonant resistance is rather small but still significant. As already stated earlier, this indicates a damping of the resonant oscillation. This viscous loss could be due to a slightly different viscosity of the PEN solution compared to pure EtOH. This is, however, very unlikely, since the PEN concentration used here (about 0.6 mM) is very small. Careful inspection further shows that the shift in resonant resistance has the same shape as the frequency shift, that is, different rates are observed for the PEN adsorption (regime I) and desorption (regime II) regime, which is not explainable by viscosity effects of the liquid. In addition, glutathione (GSH)[30] and *N*-acetyl-L-cysteine (NAC)[8] adsorption experiments with QCM using equal concentrations did not reveal a significant response in resonant resistance. This strongly indicates that the PEN and GSH/NAC adsorbate layers differ qualitatively. In the case of PEN, the physisorption of weaker bound molecules on the chemisorbed adsorbate layer produces an additional viscous film that contributes to a damping of the resonant oscillation. The shift in resonant resistance (in

(26) Sauerbrey, G. *Z. Phys.* **1959**, *155*, 206.
(27) Karpovich, D. S.; Blanchard, G. J. *Langmuir* **1994**, *10*, 3315.
(28) Kanazawa, K. K.; Gordon, J., II. *Anal. Chem.* **1985**, *57*, 1770.
(29) Profumo, A.; Merli, D.; Pesavento, M. *Anal. Chim. Acta* **2006**, *557*, 45.
(30) Bieri, M.; Bürgi, T. *Phys. Chem. Chem. Phys.* **2006**, *8*, 513.

addition to the frequency shift) is therefore another indication of the presence of a physisorbed layer. The frequency shift associated with the chemisorbed layer is 1.6 Hz (2.8 Hz attributed to chemisorption plus physisorption minus 1.2 Hz for physisorption). Assuming a rigid chemisorbed layer, the Sauerbrey relation[26] (with a mass sensitivity constant of 17.7 ng cm^{-2}) corresponds to a mass uptake of 28.3 ng cm^{-2}, which is equivalent to 1.2×10^{14} molecules cm^{-2} (neglecting trapped solvent molecules). The numbers should be taken as an estimate due to the difficulties of quantitative QCM measurements in liquid phase, as outlined earlier. For the physisorbed layer, a quantitative determination based on the Sauerbrey relation is inadequate since the latter does not hold for viscous films.

QCM clearly confirms the presence of a second, physisorbed layer, as was already suggested by ATR-IR spectroscopy. This is a behavior significantly different from glutathione and *N*-acetyl-L-cysteine SAMs, where no evidence for a physisorbed layer was found under similar conditions.[8,30]

Orientation of Molecules within the Chemisorbed and Physisorbed Layers. The determination of the orientation of a molecule on a surface relies on the fact that the intensity of a vibrational band depends on the angle between the corresponding transition dipole moment vector and the electric field vector. For metals, the electric field is polarized perpendicular to the surface, which leads to the metal surface selection rule.[31] The latter states that only vibrations associated with a transition dipole moment vector component perpendicular to the surface can be observed. This rule is generally applied to external reflection, but its validity for internal reflection has been demonstrated.[32,33] The metal surface selection rule is further valid for metal islands or metal particle films, as demonstrated in ref 32, since locally the electric field remains polarized perpendicularly even on curved surfaces.

A straightforward approach to assess the (average) orientation of molecules adsorbed on a (metal) surface is to compare the intensity ratio of two vibrational bands of random (solution) and surface orientation.[8,34,35] To follow this strategy for PEN, more experimental efforts were needed since the solubility of PEN in EtOH is very poor[36] and therefore ATR-IR spectra of the dissolved (i.e., random oriented) species could not be obtained. To measure a transmission spectrum, the molecule was dissolved in deuterated ethanol (d_6-EtOD) since normal ethanol has strong vibrational bands in the region of 1400 cm^{-1} that would hide prominent PEN signals. It should be noted that in d_6-EtOD the protons at the amine nitrogen are exchanged by deuterium (ND_2 and ND_3^+). This proton exchange, however, does not affect the discussion on the orientation of adsorbed molecules. Figure 5 shows on top a transmission spectrum of PEN dissolved in d_6-EtOD and at the bottom a spectrum of PEN adsorbed on the gold-coated Ge IRE from d_6-EtOD. Again, the latter spectrum is a superposition of zwitterionic and anionic species. Comparison of the intensity ratio of the prominent bands at 1600 and 1400 cm^{-1} between the liquid phase (i.e., random orientation) and the surface shows significant differences. Specifically, the $\nu_{as}(-COO^-)$ band is more pronounced in solution compared to the $\nu_s(-COO^-)$ signal at about 1400 cm^{-1}. This is also supported by DFT calculations that were performed by including ethanol solvent effects (spectrum not shown). On the surface, however, the intensity ratio is reversed,

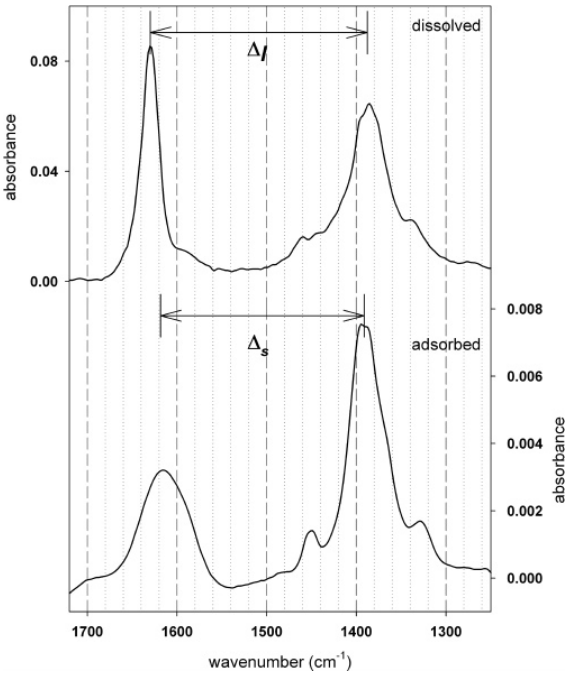

Figure 5. (Top) Transmission spectrum of PEN dissolved in ethanol-d_6 (d_6-EtOD). For this experiment, a saturated PEN solution was used. (Bottom) Spectrum of PEN adsorbed on the gold-coated Ge IRE from d_6-EtOD and after being rinsed a couple of minutes with solvent (d_6-EtOD). For the adsorption experiment, a concentration of 0.6 mM was used. Δ_l and Δ_s, respectively, indicate the difference between the band positions of the asymmetric and symmetric carboxylate stretching modes for the liquid phase and adsorbed species, respectively. For more information, see text.

that is, the $\nu_s(-COO^-)$ band is stronger than the asymmetric mode, which suggests an oriented chemisorbed adsorbate layer. Note that the deuteration experiments support the band assignment. In particular, the labeled species adsorbed on the surface (see Figure 5, spectrum at the bottom) shows a rather broad band with two components of the $\nu_{as}(-COO^-)$ carboxylate vibration arising from the zwitterionic and anionic species. Also, bands associated with amine vibrations are not apparent in the region between 1550 and 1450 cm^{-1} since the deuterated modes shift down in frequency.

The carboxylate functional group with the corresponding vibrational modes $\nu_{as}(-COO^-)$ and $\nu_s(-COO^-)$ is an attractive candidate for orientation analysis since the two associated transition dipole moments (i) lie in the COO plane and (ii) are mutually orthogonal. This feature can be used for elucidation if the COO^- plane is tilted with respect to the surface and if the two oxygen atoms are equidistant from the surface.[6,37,38] However, this strategy may be complicated by the coupling of other modes with the carboxylate vibrations. In fact, in the case of PEN, DFT calculations predict a coupling between the carboxylate and amine modes for both the zwitterionic and anionic species (see Table 1). Since the vibrational analysis yields the components of transition dipole moment vectors for each normal mode of vibration, the vector dot product can be used to calculate the angle between them. Using this method, we found that the angles between the symmetric and asymmetric carboxylate transition

(31) Greenler, R. G. *J. Chem. Phys.* **1966**, *44*, 310.
(32) Osawa, M.; Ataka, K.-I.; Yoshii, K.; Yotsuyanagi, T. *J. Electron Spectrosc. Relat. Phenom.* **1993**, *64/65*, 371.
(33) Hutter, E.; Assiongbon, K. A.; Fendler, J. H.; Roy, D. *J. Phys. Chem. B* **2003**, *107*, 7812.
(34) Street, S. C.; Gellman, A. J. *J. Chem. Phys.* **1996**, *105*, 7158.
(35) Street, S. C.; Gellman, A. J. *J. Phys. Chem. B* **1997**, *101*, 1389.
(36) Weigert, W. M.; Offermanns, H.; Scherberich, P. *Angew. Chem., Int. Ed.* **1975**, *14*, 330.
(37) Humblot, V.; Methivier, C.; Pradier, C. M. *Langmuir* **2006**, *22*, 3089.
(38) Lorenzo, M. O.; Haq, S.; Bertrams, T.; Murray, P.; Raval, R.; Baddeley, C. J. *J. Phys. Chem. B* **1999**, *103*, 10661.

dipole moments were 140.0° and 79.8°, respectively, for the zwitterionic form and for the anionic form, respectively, of normal PEN. Particularly, the value for the zwitterionic species is far from the 90° expected in the case of uncoupled modes. Upon deuteration, this value changes to 98.1°, which shows that in this case the carboxylate vibrations are much less coupled to other modes, due to the shift to lower wavenumbers of the N−D vibrations. The vicinity of the amine group thus affects the angle between the carboxylate transition dipole moments, especially in the case of the zwitterionic form of normal PEN. However, even in the latter case the strong intensity of the $\nu_s(-COO^-)$ vibrational band at 1395 cm^{-1} compared to the intensities of the $\nu_{as}(-COO^-)$ band at 1644 cm^{-1} (zwitterionic species) and 1605 cm^{-1} (anionic species) is an indication of a considerable tilt of the carboxylate functional group and interaction of both oxygen atoms with the surface. This is in agreement with the spectra of the deuterated species in Figure 5, for which the carboxylate modes are relatively pure. These spectra show an enhancement of the $\nu_s(-COO^-)$ mode upon adsorption. Even further support stems from the frequency difference between the asymmetric and symmetric carboxylate stretching modes, which allows the discrimination between mono- and bidentate/bridging geometry.[39,40] The $\Delta_l = 240$ cm^{-1} in liquid phase is decreasing to $\Delta_s = 225$ cm^{-1} for the adsorbed species (i.e., $\Delta_l > \Delta_s$) (see Figure 5). This indicates bidentate or bridging adsorption rather than monodentate geometry.

It is important to note that the intensity ratio of the carboxylate vibrational modes is not constraining information for a carboxylate−surface interaction. However, the shift of the $\nu_{as}(-COO^-)$ band (of both the zwitterionic and anionic species) at about 1625 cm^{-1} in solution (top in Figure 5) to lower wavenumbers at about 1618 cm^{-1} (bottom in Figure 5) on the surface indicates a carboxylate−surface interaction. Another indication of carboxylate−surface interaction is the observed deprotonation of the small fraction of molecules that is protonated at the carboxylate moiety (see Figure 2). The deprotonation is likely assisted by surface interaction, as there is no proton acceptor in the bulk for deprotonation. In fact, carboxylate interactions have been reported for various systems; for example, cysteine adsorption on copper[6] and adsorption of L-glutathione[7,30] and *N*-acetyl-L-cysteine[8] on gold and, most importantly, PEN adsorption on silver colloids.[41]

An additional carboxylate−surface interaction would suggest that PEN is anchored to the gold surface via three different functional groups, notably the thiol, amine, and carboxylate, which is also suggested by the DFT calculations of PEN adsorption on an Au_{19} cluster as depicted in Figure 6. In this adsorption mode, the thiol is bridged between two gold atoms and both the amine and carboxylate are involved in surface interaction. In a surface-enhanced Raman scattering study of PEN adsorption on silver colloids, Otero and co-workers[41] also suggest a three-point interaction of the molecule with the surface. Further indirect support is also provided by the QCM results, which reveal 1.2×10^{14} molecules cm^{-2} for the chemisorbed PEN layer. QCM measurements of NAC adsorption on gold (at equal concentration) were manifested as a shift of 6 Hz, which corresponds to 3.9×10^{14} molecules cm^{-2}.[8] The PEN coverage is thus less than half compared to the NAC coverage (i.e., PEN uses more surface space). Bearing in mind that the two molecules are of comparable size (PEN is even slightly smaller than NAC), this result supports an interaction via three functional groups for PEN.

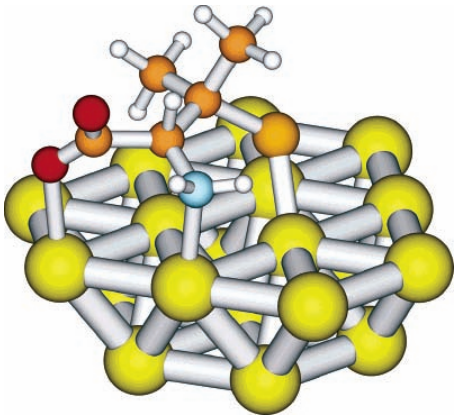

Figure 6. Calculated adsorption mode of PEN on an Au_{19} cluster. In this conformation, the thiol is bridged between two gold atoms and the amine and carboxylate are involved in surface interaction.

Significant spectral differences are visible between the chemisorbed and physisorbed layer, as can be seen by comparing spectra a and b/c in Figure 3. Specifically, the strong band in the region of about 1400 cm^{-1} is not apparent in the spectrum referring to the physisorbed layer (spectra b or c). The physisorbed layer consists of zwitterionic molecules only, whereas the chemisorbed layer consists of both zwitterionic and anionic species. Therefore, it could, for example, be concluded that the spectral difference is reducible to the chemisorbed anionic species. This would indicate that the anionic species within the chemisorbed layer is oriented differently compared to the zwitterionic species and that only the anionic species significantly contributes to the strong bands in the region of 1400 cm^{-1}. We regard these arguments as unlikely. Another explanation could be that the zwitterionic and anionic molecules have about the same orientation in the adsorbate layer but that the mutual orientation between the transition dipole moments of the $\nu_s(-COO^-)$ vibrational modes is considerably different for the different ionic forms. DFT studies do not support this hypothesis since they predict an angle of 14.9° between the transition dipole moments of the symmetric carboxylate modes of the zwitterionic and anionic forms, which seems not large enough to explain the observed difference. We finally prefer the interpretation that (i) the orientation of zwitterionic and anionic molecules within the chemisorbed layer is similar and that (ii) the orientation of molecules within the chemisorbed and physisorbed layers is considerably different. The differences in orientation are explainable by different interactions within the layers. In the case of the chemisorbed layer, the structure of adsorbed molecules is determined by surface interactions, whereas the orientation of physisorbed molecules is determined by intermolecular interactions with the chemisorbed layer.

Acid/Base Stimuli of Chemisorbed PEN Molecules on Gold. On the basis of the ATR-IR spectroscopic results discussed earlier, it was found that zwitterionic and anionic molecules coexist in the chemisorbed PEN adsorbate layer. To confirm these statements, acid/base stimuli were performed by flowing acidic and basic EtOH over the chemisorbed layer. Due to these stimulations, structural changes in the form of protonation/deprotonation of chemisorbed molecules can be expected, which further assisted in the assignment of vibrational bands.

The spectrum on top in Figure 7 (line a) represents the PEN chemisorbed layer after rinsing copiously with EtOH for about

(39) Deacon, G. B.; Phillips, M. J. *Coord. Chem. Rev.* **1980**, *33*, 227.
(40) Mehrota, R. C.; Bohra, R. Vibrational Spectra. In *Metal Carboxylates*; Academic Press: New York, 1983; p 48.
(41) López-Ramírez, M. R.; Arenas, J. F.; Otero, J. C.; Castro, J. L. *J. Raman Spectrosc.* **2004**, *35*, 390.

8386 *Langmuir, Vol. 22, No. 20, 2006* *Bieri and Bürgi*

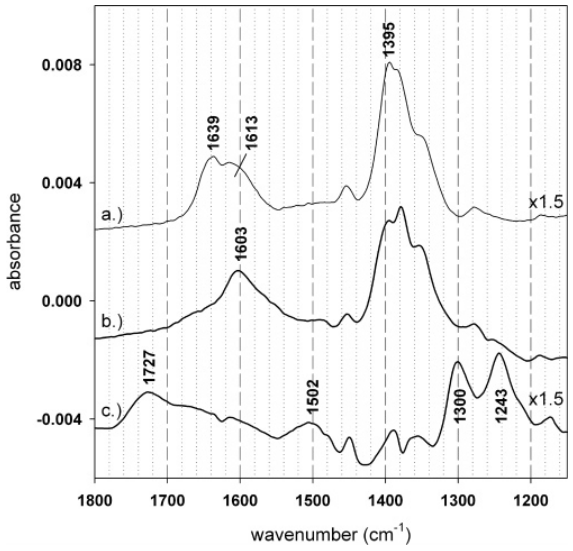

Figure 7. (a) PEN adsorbed on the gold-coated Ge IRE and after being rinsed with EtOH for about 30 min to remove physisorbed molecules. (b) Recorded after flowing basic EtOH (0.18 mM NaOH) over the chemisorbed PEN adsorbate layer. (c) Obtained after flowing acidic EtOH (0.013 mM HCl) over the chemisorbed layer.

30 min to remove physisorbed molecules. The chemisorbed layer consists, as already discussed, of zwitterionic and anionic molecules.

An inflow of basic EtOH (0.18 mM NaOH in EtOH) has significant effects on the vibrational spectrum as can be seen in spectrum b in Figure 6. Apparently, the $\nu_{as}(-COO^-)$ vibration at 1639 cm^{-1}, associated with zwitterionic chemisorbed PEN, is disappearing while the band at 1613 cm^{-1}, related to the $\nu_{as}(-COO^-)$ mode of the anionic species, is increasing in intensity. Minor spectral changes are further apparent in the region between 1400 and 1300 cm^{-1}. A flow of basic EtOH over the chemisorbed adsorbate layer is thus clearly manifested as a deprotonation of chemisorbed zwitterionic molecules within the layer.

An acidic stimulation of the PEN chemisorbed layer has strong impact on the structure of the latter, as can be verified by spectrum c in Figure 6. The band appearing at 1727 cm^{-1} is assigned to the $\nu(-COOH)$ vibration of the protonated carboxylic acid group of PEN. In addition, two bands are visible at 1300 and 1243 cm^{-1} that we assign to the $\delta(-COH)$ bending and $\nu(-CO)$ stretching modes, respectively. Accompanied by the protonation of the COO^- group is the disappearance of the $\nu_{as}(-COO^-)$ and $\nu_s(-COO^-)$ modes at about 1600 and 1400 cm^{-1}, as can be seen in the spectrum. Another band that appears upon flowing acidic EtOH over the adsorbate layer can be spotted at about 1502 cm^{-1}, which is the $(-NH_3^+)$ vibrational mode. However, the spectrum also indicates complex structural changes and reorientations, respectively, of adsorbed molecules and not only a protonation of the carboxylic acid moieties. This is suggested by the dramatic collapse of the bands in the region between 1400 and 1300 cm^{-1}, which comprise, in addition to the $\nu_s(-COO^-)$, other (coupled) modes such as, for example, $\delta_{as}(-CH_3)$, $\delta_s(-CH_3)$, and $\delta(-CH)$, as is predicted by DFT calculations.

In summary, acid/base stimuli and concomitant protonation/deprotonation of zwitterionic and anionic molecules within the chemisorbed adsorbate layer confirm the coexistence of the two species at the surface.

Conclusions

ATR-IR and QCM experiments were used to study the adsorption of PEN on gold surfaces in situ. Both techniques reveal a chemisorbed and a physisorbed layer. The chemisorbed layer consists of both zwitterionic and anionic species, whereas the physisorbed layer is composed of zwitterionic species only. The deprotonation of the NH_3^+ group of PEN on the surface is a relatively slow process and can be followed by a significant shift of the $\nu_{as}(-COO^-)$ vibration. The IR spectra indicate that all three functional groups are involved in the interaction with the surface, which is further supported by QCM experiments, which show that the chemisorbed molecules block a comparably large surface area. Density functional theory calculations show that such an interaction is easily possible. A three-point surface interaction could explain PEN's excellent properties as chelating agent for metals and further makes it an attractive candidate for chiral surface modification.

Acknowledgment. Financial support from the Swiss National Science Foundation and the grants of computer time from the Swiss National Supercomputing Centre (CSCS) Manno are gratefully acknowledged. Use of sputtering facilities at the Swiss Center for Electronics and Microtechnology in Neuchâtel (CSEM) is kindly acknowledged.

LA061454Y

Part III

Enantiodiscrimination

Preface

The ability do discriminate between enantiomers of a chiral compound is one of the most valuable properties a chiral surface can have. In this part, results based on enantiodiscrimination between chiral self-assembled monolayers (SAMs) and an analyte molecule, probed by *in situ* ATR-IR in combination with modulation excitation spectroscopy (MES), are presented. MES highlights small spectral changes related to enantiodiscrimination and allows unique molecular-level insight into the origin of enantiodiscrimination. The two studies presented in the following have in common that the amino acid proline served as analyte molecule due to its simple and rigid structure. In order to understand and interpret the spectroscopic results related to enantiodiscriminating interactions, the structure of the adsorbed molecules in the chiral SAM should be studied first. Therefore, the investigation of the self-assembly process of L-glutathione (GSH) and *N*-acetyl-L-cysteine (NAC) on gold (see Part II) is a precursor to experiments on enantiodiscrimination.

The interaction between proline and GSH is presented in Chapter 1. It was found that adsorption and desorption kinetics of the two proline enantiomers at the chiral interface is considerably different. Applying a transport and adsorption model, based on finite element method (FEM), enabled extraction of intrinsic rate constants; fully accounting for mass transport within the ATR-IR chemical reactor. The results showed that the GSH SAM can discriminate between enantiomers, D-proline being stronger bound. Spectroscopic results further revealed that upon interaction with proline the adsorbed GSH is protonated at the gly part of the molecule, which, in the absence of proline, is bound to the gold surface as carboxylate. The observed protonation of adsorbed GSH upon interaction with proline goes along with a structural change, which seems to be crucial for enantiodiscrimination.

Enantiodiscrimination between proline and NAC is discussed in Chapter 2. Due to the rather rigid structure of NAC compared to GSH, a different mode of interaction with proline was observed. Absolute configuration modulation experiments, that is periodically flowing the proline enantiomers over the NAC SAM, and subsequent phase-sensitive detection of the spectral changes showed significant and characteristic dispersive bands. These bands arise due to very small shifts in band position and intensity depending on the enantiomer involved in interaction. By using density functional theory (DFT) calculations it was possible to reproduce the experimental spectra. The proposed model of the diastereomeric NAC–proline complexes makes electrostatic interactions responsible for enantiodiscrimination.

Chapter 1

Probing Enantiospecific Interactions between Proline and an L-Glutathione Self-Assembled Monolayer by Modulation Excitation ATR-IR Spectroscopy

Marco Bieri and Thomas Bürgi

Published in J. Phys. Chem. B, Volume 109(20), pp. 10243–10250, doi: 10.1021/jp050197n, 2005.

J. Phys. Chem. B **2005,** *109,* 10243−10250 **10243**

Probing Enantiospecific Interactions between Proline and an L-Glutathione Self-Assembled Monolayer by Modulation Excitation ATR-IR Spectroscopy

Marco Bieri and Thomas Bürgi*

Université de Neuchâtel, Institut de Chimie, Rue Emile-Argand 11, 2007- Neuchâtel, Switzerland

Received: January 11, 2005; In Final Form: March 18, 2005

The interaction of proline with self-assembled monolayers (SAMs) of L-glutathione (γ-glu-cys-gly) on gold was investigated by a combination of attenuated total reflection (ATR-IR) infrared and modulation excitation spectroscopy (MES). The latter technique makes use of phase-sensitive detection of periodically varying signals and allows discrimination between species with different kinetics such as dissolved proline and adsorbed molecules. By applying a convection−diffusion model coupled to adsorption and desorption, it was possible to extract relative adsorption and desorption rates from the experimental data for the two enantiomers of proline, fully accounting for mass transport within the flow-through cell. The results show that, in particular, the desorption kinetics is different for the two enantiomers. Therefore, the L-glutathione SAM can discriminate between enantiomers, D-proline being stronger bound. The IR spectra reveal that upon interaction with proline the adsorbed L-glutathione is protonated at the gly part of the molecule, which, in the absence of proline, is bound to the gold surface as carboxylate. The observed protonation of adsorbed L-glutathione upon interaction with proline goes along with a structural change of the former, which seems to play an important role for enantiodiscrimination.

Introduction

Chiral surfaces and interfaces have received considerable interest in recent years because of their importance in separation[1] and sensing[2,3] of enantiomers, their application in heterogeneous enantioselective catalysis[4,5] and their possibly decisive role for the origin of biochemical homochirality.[6,7] Cleavage of quartz or calcite, materials with chiral bulk structures, leads to surfaces that are naturally chiral. Similarly, cleavage of metals, which have achiral bulk structure, along certain high Miller index planes exposes naturally chiral terrace-step-king structures.[8,9] Chiral surfaces can also be created by anchoring or adsorption of a chiral molecule on a nonchiral surface.[10−15] In the latter case, the adsorption of the chiral molecule can even lead to supramolecular chiral assemblies, thus forming patterns that destroy the symmetry of the underlying surface.[11] In the absence of long-range ordering, the chirality of such surfaces is solely associated with the chirality of the adsorption complex.

The ability to differentiate between enantiomers of a chiral probe molecule is one of the most interesting properties of a chiral surface. It has, for example, been found that the enantiomers of glucose are electrooxidized at different rates on intrinsically chiral Pt(643) electrodes.[9] It has also been reported that (*R*)-3-methylcyclohexanone desorbs enantiospecifically from the two enantiomeric forms of the chiral Cu(643) surface[16] and that the enantiospecific desorption occurs from the chiral kink sites.[17] Examples of enantiodiscrimination of chirally modified surfaces are numerous and include, for example, the chiral stationary phases used in chromatography. Despite the numerous reports on enantiodiscriminating interfaces, not much molecular-level information is available on the relevant intermolecular interactions between surface (selector) and analyte molecule (selectand). This is because most of the applied experimental methods merely quantify enantiodiscrimination without giving direct molecular-level insight. For example, chromatographic methods derive separation factors from retention times. Other methods measure a mass change[18] or a change in the optical thickness due to adsorption.[2] Even further methods such as atomic force microscopy rely on force measurements between selector and selectand.[3] Other approaches make use of soluble model systems in order to investigate the relevant intermolecular interactions by applying bulk techniques.[19] However, the observed interactions in solution may still vary from the ones relevant at the corresponding interface.

An ideal method to probe enantiodiscriminating interactions at interfaces would combine (surface) sensitivity with selectivity for the chiral information. Whereas the former criterion is met by many powerful surface science tools,[20] the latter is an attribute of chiroptical techniques such as circular dichroism,[21] vibrational circular dichroism,[22] or Raman optical activity.[23] The combination of both attributes mentioned above is a real challenge. Nonlinear optical techniques may turn out to be powerful in probing chiral interfaces.[24]

Infrared spectroscopy is well-established for the study of surfaces and interfaces, and it has been used to investigate the interaction of enantiomers with chiral surfaces.[17,25] The technique has the disadvantage that nonspecific interactions also give rise to signals. Thus, the adsorption of enantiomers on a chiral surface may result in very similar spectra, the interesting differences being overlaid by much stronger signals from molecules that interact with the surface in a nonspecific manner. To overcome these problems, we have recently combined attenuated total reflection (ATR)-IR[26] with modulation excitation spectroscopy (MES)[27,28] to probe chiral discrimination at solid−liquid interfaces.[29,30] MES selectively reveals the periodically changing signals stimulated by the modulation of an external parameter. By periodically changing the absolute configuration of the probe molecule (absolute configuration modulation),

* Phone ++41 32 718 24 12. Fax ++41 32 718 25 11. E-mail: thomas.burgi@unine.ch.

10.1021/jp050197n CCC: $30.25
Published on Web 04/27/2005

10244 *J. Phys. Chem. B, Vol. 109, No. 20, 2005*

SCHEME 1: Structure of Proline (top) and L-Glutathione (GSH, bottom)

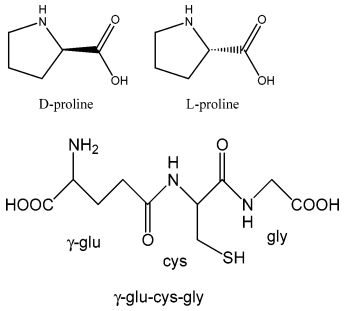

enantiospecific interactions can be spotted, as has been demonstrated for interactions taking place at chiral stationary phases.[29,30]

In the present work, we apply this strategy to investigate the interaction of proline with a chiral self-assembled monolayer (SAM) formed by adsorbing the tripeptide L-glutathione (γ-glu-cys-gly) on gold (see Scheme 1). L-Glutathione SAMs on electrodes revealed "ion gating" properties.[31,32] The interaction of cationic drugs, rare earth, and transition metal ions with the SAM leads to the opening of ion gates, as revealed by redox probes, and it has furthermore been proposed that the gating mechanism goes along with a conformational change of the adsorbed L-glutathione.[31,33] In a previous study, we reported on the reversible conformational changes within the L-glutathione SAM induced by acid and base stimuli.[34] It was furthermore shown that part of the adsorbed molecules interact with the gold surface, not only through the thiol but also through the carboxylic acid group of the gly moiety, which deprotonates upon adsorption.[34] The results presented below show that similar conformational changes are induced by the presence of the amino acid proline and that L-glutathione SAMs can differentiate between proline enantiomers.

Experimental Section

Chemicals. D- and L-Proline, respectively (Sigma-Aldrich, Inc., both >99%), were used as received. L-Glutathione (γ-glu-cys-gly, GSH, Sigma-Aldrich, Inc., ≥98%) was used without further purification. Ethanol (EtOH, Merck p.a.) was used as the solvent. Before each measurement, solutions were treated with nitrogen gas (99.995%, CarbaGas) to remove dissolved oxygen.

In situ ATR-IR Spectroscopy. *Sample Preparation.* The Ge internal reflection elements (IREs, 50 mm × 20 mm × 2 mm, 45°, Komlas) were polished with a 0.25-μm grain size diamond paste and rinsed copiously with EtOH. The surface was further plasma-cleaned under a flow of air for 5 min before a gold layer with a thickness of about 2 nm was sputtered onto the IRE. For each experiment, a fresh gold layer was used. Control experiments with the bare Ge IRE revealed no GSH adsorption as indicated by the absence of prominent GSH signals during several hours of exposure to GSH solution.

Data Acquisition. ATR-IR measurements were performed on a Bruker EQUINOX 55 FT-IR spectrometer equipped with a nitrogen-cooled narrow-band mercury cadmium telluride (MCT) detector. Spectra were recorded at a resolution of 4 cm^{-1}. A home-built liquid flow-through cell with a total volume of 0.077 mL and a gap of 250 μm between the IRE and the polished steel surface was used for ATR-IR experiments. The flow-through cell can be heated or cooled, but all measurements reported here were performed at room temperature ($T = 298$ K). The ATR-IR cell is described in more detail elsewhere.[28,35]

Modulation Experiments. EtOH was used as the solvent for all ATR-IR measurements reported here. Before each experiment, the solvent was saturated with nitrogen gas (CarbaGas, 99.995%) and was flowed over the IRE until no variation in the spectrum could be detected (about 5 min). Then, a spectrum was recorded by coadding 200 interferograms which served as reference for all subsequent measurements. Several types of experiments were carried out: A first modulation experiment was performed by flowing periodically EtOH and L-proline over the bare and gold-coated Ge-IRE. This type of experiment yields the spectrum of dissolved proline and gives information about the interaction of proline with the bare gold surface. In a further experiment, GSH at typical concentrations of 0.33 mM was flowed over a freshly prepared gold surface. The adsorption process was stopped after 20 min and 4 h, respectively. The corresponding flow rates were 0.5 mL/min for 20 min and 0.18 mL/min for 4 h adsorption time. With these freshly prepared samples, modulation experiments were performed consisting of periodically flowing EtOH and D-proline over the GSH SAM. An analogous experiment was performed with L-proline at equal concentration. Information about the interaction of the corresponding enantiomer with the GSH SAM is obtained in these experiments. Finally, an absolute configuration modulation experiment was performed (i.e., the two enantiomers were allowed to flow alternately over the GSH SAM). A modulation period started with a flow of D-proline, followed by an equally long flow of L-proline over the GSH SAM. Probing enantiospecific interactions of proline with the GSH SAM is the goal of this experiment. All of the modulation experiments reported here consisted of two initial "dummy loops" to allow the system reaching a new quasi-stationary state followed by averaging over six measurement loops (periods). During one measurement period, 60 IR spectra were recorded at an 80 kHz sampling rate using the rapid scan acquisition mode of the Fourier transform (FT)-IR spectrometer. For each spectrum, 6 (30) interferograms per modulation period were averaged, resulting in a modulation period of $T = 72.4$ (362.3) s. By a subsequent digital phase sensitive detection (PSD) according to eq 1, phase-resolved spectra are obtained from the set of time-resolved spectra.

$$A_k^{\phi_k^{\mathrm{PSD}}}(\tilde{\nu}) = \frac{2}{T}\int_0^T A(\tilde{\nu}, t)\,\sin(k\omega t + \phi_k^{\mathrm{PSD}})\,\mathrm{d}t \qquad (1)$$

where $k = 1, 2, 3, \ldots$ determines the demodulation frequency (i.e., fundamental, first harmonic, and so on), T is the modulation period, $\tilde{\nu}$ denotes the wavenumber, ω is the stimulation frequency and ϕ_k^{PSD} is the demodulation phase angle. With a set of time-resolved spectra $A(\tilde{\nu}, t)$, eq 1 can be evaluated for different phase angles ϕ_k^{PSD}'s resulting in a series of phase-resolved spectra $A_k^{\phi_k^{\mathrm{PSD}}}$. Only spectra demodulated at the fundamental frequency ($k = 1$) are reported here. A description in more detail of the modulation technique can be found elsewhere.[27,28]

DFT Calculations of L-Glutathione and Proline. To better understand the structure of GSH and proline and to assign the vibrational spectrum of proline, density functional theory (DFT) calculations were performed using the hybrid functional B3PW91[36,37] with a 6-31G basis set.[38] *GAUSSIAN 03* was used for all calculations.[39] Structures of GSH and proline are depicted in Scheme 1. A discussion of the results for the GSH DFT studies can be found elsewhere.[34] In case of proline, a

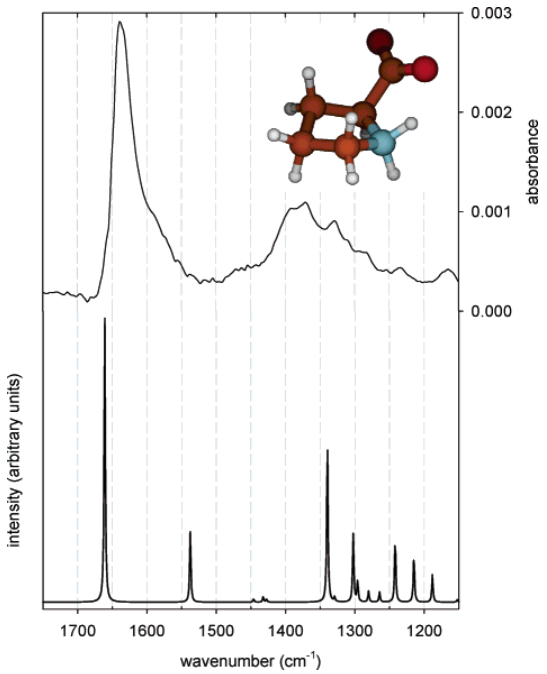

Figure 1. Top: Demodulated spectrum of EtOH vs L-proline (0.044 M at a flow rate of 0.5 mL/min) modulation experiment on the bare Ge−IRE. Bottom: Calculated IR spectrum of proline after convolution with a Lorentzian band shape (half-width at half-maximum = 1 cm^{-1}). For details concerning the calculation method, see text.

polarizable continuum model (PCM)[40] was used to include the effect of the solvent. All calculations were performed with proline in zwitterionic form, as this prevails in ethanol. The conformation with lowest energy was found to have a hydrogen bond between the carboxylate and the protonated amine (see inset in Figure 1).

Modeling Mass Transport and Surface Reactions. To evaluate adsorption and desorption kinetics in a flow-through reactor, mass transport within the bulk phase has to be considered, which can conveniently be done using numerical methods. In a previous work, it was shown that mass transport of solute molecules within the ATR-IR flow-through cell can successfully be described by convection and diffusion using a simplified two-dimensional geometry.[35] The model used in the present work further couples adsorption, surface diffusion, and desorption to the transport of species to the surface. The following assumptions are made for the transport and adsorption model: (1) laminar flow of a (2) incompressible Newtonian fluid. (3) Because of the reduced two-dimensional geometry (z denotes the direction perpendicular to the surface and x the direction of the flow within the cell), there are no concentration variations in the y direction and no velocity variations in the x or y direction. (4) Furthermore, interaction between solute molecules is neglected.

Steady-state momentum balance yields the following velocity profile which can be expressed in terms of the flow rate ϕ_V.[41]

$$v_x(z) = \frac{6\phi_V}{wh^3}(hz - z^2) \tag{2}$$

where w is the width and h the height of the simplified flow-through cell geometry.

Mass balance of solute species in the bulk is then given by the convection−diffusion equation

$$\frac{\partial c}{\partial t} = -v_x(z)\frac{\partial c}{\partial x} + D\left(\frac{\partial^2 c}{\partial x^2} + \frac{\partial^2 c}{\partial z^2}\right) \tag{3}$$

The flux of the solute species in the bulk is expressed by

$$J = v_x(z)c - D\left(\frac{\partial c}{\partial x} + \frac{\partial c}{\partial z}\right) \tag{4}$$

where c denotes the bulk concentration of the solute molecule and D is the diffusion coefficient.

On the surface boundary, the following reaction rate is defined

$$r_{\text{Surface}} = \frac{d\theta}{dt} = -k_{ads}c\theta + k_{des}c_S \tag{5}$$

In eq 5, θ is the surface concentration of active sites, c_s is the concentration of adsorbed molecules, and k_{ads} and k_{des} are the rate constants for adsorption and desorption, respectively. Note that the reaction rate expressed in eq 5 corresponds to a first-order Langmuir model. The first term on the right-hand side in eq 5, the surface concentration of active sites θ, can be written as the difference between the total number of active sites θ_0 and the surface concentration of adsorbed molecules c_s according to

$$r_{\text{Surface}} = \frac{d\theta}{dt} = -k_{ads}c(\theta_0 - c_S) + k_{des}c_S \tag{6}$$

The mass balance for the surface, including surface diffusion and the surface reaction rate as expressed in eq 6, is

$$\frac{\partial c_S}{\partial t} = D_S\frac{\partial^2 c_S}{\partial x^2} + k_{ads}c(\theta_0 - c_S) - k_{des}c_S \tag{7}$$

where D_s is the surface diffusion coefficient.

The following initial and boundary conditions were defined for the transport and adsorption model:

Initial conditions:

$$0 \le x \le L,\ 0 \le z \le h,\ c(t=0) = c_0,\ c_S(t=0) = 0 \tag{8}$$

where L denotes the length between the inlet and outlet and h the height of the cell. C_0 is the bulk concentration of the solute species.

Boundary conditions:

On the reactive surface (i.e., at $z = 0$), the boundary condition for the bulk couples the surface reaction rate with the flux of reacting species according to

$$J = v_x(z)c - D\left(\frac{\partial c}{\partial x} + \frac{\partial c}{\partial z}\right) = -k_{ads}c(\theta_0 - c_s) + k_{des}c_S \tag{9}$$

Other boundary conditions:

$$z = h,\ J = 0 \tag{10}$$

$$\text{inlet } (x = 0),\ c = c_0H(t) \tag{11}$$

$$\text{outlet } (x = L),\ J = v_x(z)\text{c} \tag{12}$$

In eq 11, the concentration modulation $H(t)$ is represented by a smoothed Heaviside function.

Simulations were performed using the finite element method (FEM) implemented in *FEMLAB*.[42] The transport and adsorption

model was solved using the real cell dimensions as $L = 36$ mm, $w = 7$ mm, and $h = 265$ μm. Furthermore, a flow rate of $\phi_V = 0.18$ mL/min and a concentration modulation ($c_0 = 4.3$ mM) frequency of 2.8 mHz were used. The total number of active sites θ_0 was assumed to be 10^{15} molecules/cm^2. The diffusion coefficient D of the solute species (proline in this case) was estimated according to the Stokes−Einstein equation

$$D = kT/(6\pi\eta a) \approx 3.7 \cdot 10^{-6}\ \mathrm{cm^2/s} \qquad (13)$$

where η is the viscosity of the solvent and a is the radius of the solute molecule approximated as a sphere. Note that the sphere radius of 5 Å of proline was derived from DFT calculations. The surface diffusion coefficient D_s was further estimated to be 3 orders of magnitude smaller than the bulk diffusion coefficient D. Finally, k_{ads} and k_{des}, respectively, are tunable parameters which were adjusted to fit the experimental curves. Note that experimentally available in an ATR-IR experiment are signals which are proportional to surface concentration c_s and bulk concentration near the surface $c(z = 0)$. In an ATR-IR experiment, the signal is integrated over the internal reflection element. To compare with the experimental data, the concentrations were therefore averaged over x.

Results

A demodulated (phase-resolved) spectrum of the EtOH versus L-proline (0.044 M at a flow rate of 0.5 mL/min) modulation experiment on the bare Ge-IRE is depicted in Figure 1 (top). The spectrum reveals a prominent peak at 1637 cm^{-1} with a shoulder at about 1570 cm^{-1}. In addition, a broad feature composed of several overlapping bands is visible in the region between 1400 and 1300 cm^{-1}. The calculated IR spectrum of proline is depicted in the bottom half of Figure 1. The spectrum was simulated by convoluting the calculated IR intensity with a Lorentzian band shape (half-width at half-maximum = 1 cm^{-1}). The calculated spectrum reveals a prominent signal at 1660 cm^{-1} and a less intense band at 1537 cm^{-1}. A series of bands falls in the region between 1350 and 1200 cm^{-1}. Besides shifts in wavenumber, the overall agreement between calculated and measured spectra of proline in EtOH is good enough to allow assignment of the most prominent bands, as given in Table 1. The assignment is in line with previous reports.[43] Table 1 also contains assignments for the most relevant bands associated with GSH adsorbed on gold as reported previously.[34]

An ATR-IR spectrum of GSH adsorbed on gold is shown in Figure 2 (trace b). A spectrum recorded while flowing L-proline (0.044 M) over the GSH SAM is also shown in Figure 2 (trace a). The most prominent signals of GSH are visible at 1658 and 1535 cm^{-1}. Less intense bands are apparent at 1725 and 1400 cm^{-1}. The most intense L-proline band is visible at 1637 cm^{-1} (compare to Figure 1). All other bands, namely the ones at 1725, 1540, and 1400 cm^{-1}, coincide well with the GSH signals already mentioned.

Figure 3 summarizes the phase-resolved spectra representing the interactions of each enantiomer (i.e., D- and L-proline, both at about 4.3 mM) with a GSH SAM after 20 min of self-assembling. The corresponding modulation experiment started with a flow of D- and L-proline, respectively, followed by an equal long flow of solvent (EtOH). Note that these spectra reveal only the signal that is periodically changing because of modulation of the proline concentration. Comparison between Figures 2 and 3 reveals important differences between the demodulated and static spectra (Figure 2a). To study the time dependence of the adsorption/desorption of proline, modulation

TABLE 1: Observed Vibrational Bands of GSH Adsorbed on Gold and Dissolved Proline (both in zwitterionic form) in EtOH[a]

GSH (zwitterionic)	proline (zwitterionic)	assignment
	static signals	
1731		ν(−COOH)
1649		amide I
1527		amide II
1397		ν_s(−COO$^-$)
	phase-resolved signals	
	1637	ν_{as}(−COO$^-$)
	1570	δ_s (−NH$_2$) scissoring (appearing as shoulder of band at 1637 cm^{-1})
	1392	ν_s(−COO$^-$) + δ (−CH)
	1370	ν_s(−COO$^-$) + δ (−CH)
	calculated signals	
	1660	ν_{as}(−COO$^-$)
	1537	δ_s (−NH$_2$) scissoring
	1340	ν_s(−COO$^-$) + δ (−CH)
	1300	ν_s(−COO$^-$) + δ (−CH)

[a] The static GSH spectrum is depicted in Figure 2b and the phase-resolved proline spectrum is displayed in Figure 1 (top). Calculated proline vibrations are also included for comparison.

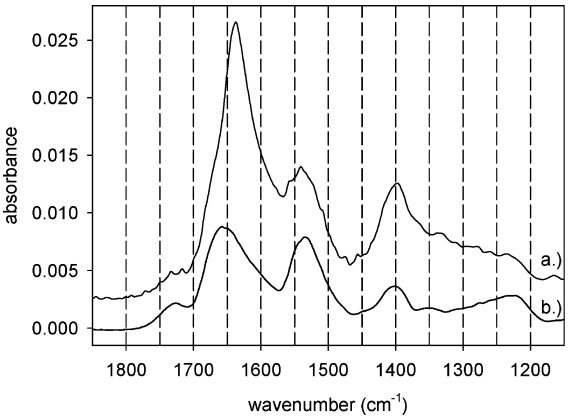

Figure 2. Static L-proline spectrum (trace a, 0.044 M) and GSH (trace b, 0.33 mM) spectrum after 5 min of adsorption. Note that the former spectrum was recorded while flowing L-proline over the GSH SAM (flow rate 0.5 mL/min) after 10 min onstream.

experiments with different modulation periods were performed, that is, $T = 72.4$ s (by coadding 6 interferograms, modulation experiment 1) and $T = 362.3$ s (by coadding 30 interferograms, modulation experiment 2). The flow rates were adjusted to the corresponding modulation periods to 0.5 mL/min ($T = 72.4$ s) and 0.18 mL/min ($T = 362.3$ s), respectively. Phase-resolved spectra of D-proline interaction with GSH SAM are depicted in the upper half of Figure 3 for modulation experiment 1 (trace b) and modulation experiment 2 (trace a), respectively. Obviously, the spectra differ considerably, indicating that the response to the described stimulation (D-proline concentration modulation) depends on the modulation frequency. This difference further reveals that species having different kinetics are observed in the spectra, such as dissolved proline and adsorbed molecules (proline and GSH). The phase-resolved spectrum of modulation experiment 1 reveals an intense asymmetric band at 1637 cm^{-1} and a broad signal in the region between 1400 and 1300 cm^{-1}. This spectrum coincides well with the spectrum of dissolved proline (Figure 1). The phase-resolved spectrum of modulation experiment 2 (trace a in Figure 3) reveals signals

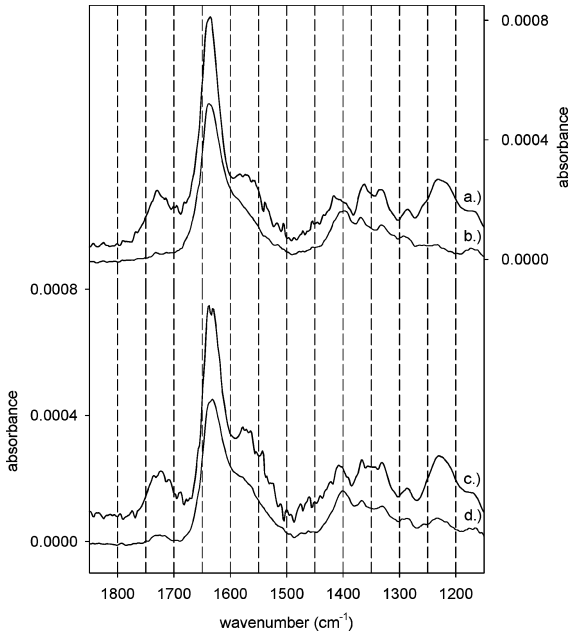

Figure 3. Phase-resolved spectra of EtOH vs D(L)-proline (both 4.3 mM) modulation experiment at different modulation frequencies (periods). Traces a and b refer to EtOH vs D-proline modulation experiment at $T = 72.4$ s (trace b) and $T = 362.3$ s (trace a) modulation periods. The same modulation experiments were performed for L-proline. Trace c refers to a modulation period of $T = 362.3$ s and trace d to $T = 72.4$ s. Note that flow rates were adjusted to the different modulation periods and amounted to 0.5 mL/min for $T = 72.4$ s and 0.18 mL/min for $T = 362.3$ s.

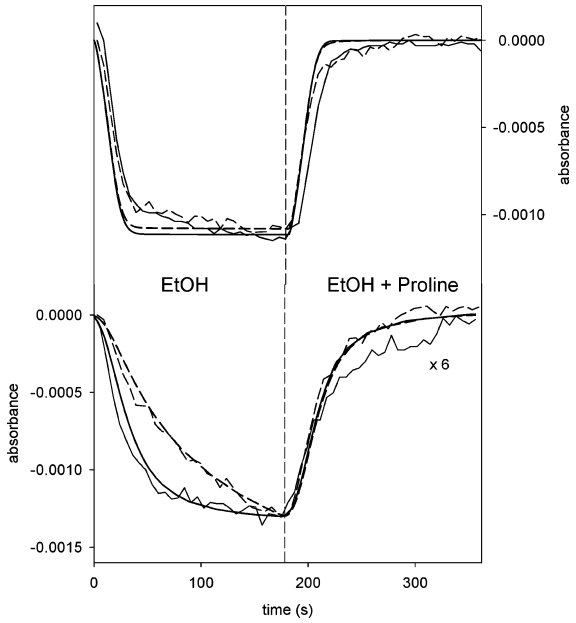

Figure 4. Time dependence of signals at 1625 (upper half in Figure 4) and 1725 cm^{-1} (lower half in Figure 4) of the corresponding EtOH vs D(L)-proline modulation experiments performed at a modulation period of $T = 362.3$ s (note that the corresponding spectra are depicted in Figure 3, traces a and c). Dashed lines refer to D-proline and solid lines to L-proline. A typical modulation period started with a flow of EtOH (at 0.18 mL/min) over the GSH SAM (after 20 min of adsorption) indicated by "EtOH" in the left part of Figure 4. During the second half-period of the modulation experiment, EtOH was replaced by an equally long flow of D(L)-proline (dissolved in EtOH) indicated by "EtOH + proline" in the right part of Figure 4. The calculated time dependence of the signals using the transport and adsorption model is depicted by bold lines. Again, dashed lines refer to D-proline and solid lines to L-proline. Note that the signals in the upper half of Figure 4 refer to changes in the concentration of dissolved proline, whereas the signals in the lower half reflect variations in the surface concentration of proline due to adsorption/desorption on/from the GSH SAM.

at 1729 and 1637 cm^{-1}, whereas the former is hardly apparent in the case of modulation experiment 1. The band at 1637 cm^{-1} further reveals a different band shape with a shoulder appearing at approximately 1570 cm^{-1}. Differences in intensity and position of the broad band in the region between 1400 and 1300 cm^{-1} are apparent; the band at 1400 cm^{-1} is shifted to 1415 cm^{-1}, and the signal at approximately 1225 cm^{-1} is clearly more intense in experiment 2.

The phase-resolved spectra of the EtOH versus L-proline modulation experiment are depicted in the lower half in Figure 3. The spectrum at the bottom (trace d) is the response to modulation experiment 1, whereas the spectrum above (trace c) corresponds to modulation experiment 2. Again, the two spectra differ significantly and in a similar manner as described above for D-proline (compare to the two spectra, traces a and b, in the upper half of Figure 3). Careful inspection yet reveals small differences between the spectra of the D- and L-proline interactions with the GSH SAM. It should be noted that the experiments with the two enantiomers were performed at different days on different samples. Also, the apparent larger noise in spectra a and c is due to a larger interference of gas-phase water in these experiments. Because the interaction of each enantiomer with the GSH SAM has been found to depend on modulation frequency, it is helpful to turn to the time dependence of selected signals in order to learn more about adsorption and desorption kinetics, respectively.

The time dependence of the signals at 1625 and 1725 cm^{-1}, respectively, for D- and L-proline, respectively, versus EtOH modulation experiment 2 ($T = 362.3$ s, coaddition of 30 interferograms) is displayed in Figure 4. Dashed lines refer to D-proline and solid lines to L-proline. In the upper half of Figure 4, the time dependence of the absorbance at 1625 cm^{-1} is displayed for D- and L-proline, respectively, revealing no large differences. The dominant contribution to this signal stems from proline in solution, and a weaker signal from proline interacting with the GSH SAM is thus probably hidden. In other words, the time dependence of the 1625 cm^{-1} signal mainly originates from changes in the concentration of dissolved proline forced by convection and diffusion. On the other hand, the time dependence of the signal at approximately 1725 cm^{-1} shows significant differences between D- and L-proline. During the first half-period of modulation experiment 2 (left part in the plot, indicated by "EtOH"), the flow of proline over the GSH SAM is replaced by EtOH, and the corresponding signals decrease with significantly different rates for the D- and L-proline experiments. Obviously, the decrease of the signal at 1725 cm^{-1} is faster for the L-proline experiment and reaches steady state, whereas for the D-proline experiment the corresponding signal is still about to decrease after the first half-period of modulation experiment 2. During the second half-period of modulation, EtOH is replaced by dissolved proline (right part in the plot, indicated by "EtOH + proline"), which leads to an increase of the signal at 1725 cm^{-1}. In the D-proline experiment, the signal increases slightly more rapidly with time, almost reaching steady state at the end of the second half-period of modulation experiment 2. As will be shown later, the signal at about 1725

cm^{-1} is likely associated with adsorbed GSH. Still, its appearance and disappearance are due to the interaction of proline with the GSH SAM and are therefore directly related to the adsorption/desorption kinetics. In summary, the signals at 1625 and 1725 cm^{-1} belong to completely different system responses. The former signal refers to changes in the concentration of dissolved proline near the interface, whereas the latter reflects the surface concentration of proline due to adsorption/desorption on/from the GSH SAM. Assuming adsorption and desorption to be first-order reactions and absorbance to be proportional to concentration (Lambert−Beer law), the time dependence of signals depicted in Figure 4 was simulated using the transport and adsorption/desorption model described in the Experimental Section. The tunable parameters k_{ads} and k_{des} were adjusted to fit the experimental curves. The result of the corresponding simulations is depicted in Figure 4 as bold lines. Again, dashed lines refer to D-proline and solid lines to L-proline.

Obviously, the simulations represent the significant differences between the responses of the bulk (upper half in Figure 4) and surface (lower half in Figure 4) well. However, deviations from experimental data are visible, which may be explained by small volumes in the ATR-IR cell (behind inlet and outlet), where the fluid is almost stagnating,[35] and slight signal drifts during measurement. In addition, larger deviations between experimental and model data are apparent in the right lower half of Figure 4. The corresponding signals are related to the adsorption of D- and L-proline, respectively. Because the applied adsorption/desorption model assumes simple Langmuir kinetics, the observed discrepancy may indicate a more complex adsorption process that is not completely captured by the model. Knowing the adsorption and desorption rate constants allows calculating $\Delta\Delta G°$ of adsorption for D- and L-proline according to

$$\Delta\Delta G^0 = -RT \ln\left(\frac{K_D}{K_L}\right) \qquad (14)$$

where $K_{D,L} = k_{ads(D,L)}/k_{des(D,L)}$ denote the corresponding equilibrium constants of D- and L-proline, respectively. Evaluating eq 14 for $T = 298$ K, we found $K_D/K_L = 7.5$, and thus, $\Delta\Delta G° \approx -5.0$ kJ mol^{-1}. In other words, the GSH SAM seems to discriminate between D- and L-proline, with the former being more strongly bound. It should be pointed out that the derived value for $\Delta\Delta G°$ should be regarded as an order-of-magnitude estimate rather than an exact value, as its derivation relies on the kinetic model outlined above. Because the GSH SAM seems to distinguish between the proline enantiomers, signals can be expected for the absolute configuration modulation experiment when the two enantiomers (at 0.045 M) are allowed to flow alternately over the GSH SAM. A phase-resolved spectrum of such an experiment is depicted in Figure 5 (trace a, scaled by a factor of 25). The phase-resolved spectrum of the enantiospecific modulation experiment reveals a negative band at 1725 cm^{-1} and a positive one at 1615 cm^{-1}. Furthermore, a broad positive band in the region between 1400 and 1250 cm^{-1} is visible and a negative band at approximately 1225 cm^{-1}. The discussed spectrum is in good agreement with the one in the middle of Figure 5 (trace b, scaled by a factor of 25), which corresponds to the EtOH versus D-proline modulation experiment discussed above. By using one of the benefits of the modulation technique, namely the separation of species with different kinetics by choosing the phase angle ϕ_k^{PSD} in eq 1 accordingly, the contribution of dissolved proline was removed by adjusting ϕ_k^{PSD} such that the signal at 1637 cm^{-1} vanished.

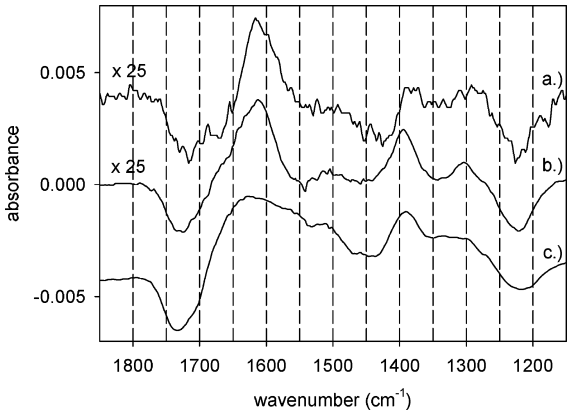

Figure 5. A demodulated ATR-IR spectrum of an absolute configuration modulation experiment (D- vs L-proline) is represented by trace a. The modulation experiment started with a flow of D-proline followed by an equally long flow of L-proline over the GSH SAM. The EtOH vs D-proline modulation experiment is displayed in trace b. The contribution from dissolved proline was minimized by choosing the demodulation phase angle accordingly. Trace c refers to an EtOH vs HCl (0.013 mM) in EtOH modulation experiment. In this kind of experiment, EtOH was allowed to flow over a GSH SAM (after 4 h of adsorption) during the first half-period and was replaced by acidic EtOH (HCl in EtOH) during the second half-period of the modulation experiment. The spectrum is a difference spectrum and represents the spectral changes during deprotonation in ethanol in the time interval between 50 and 241.6 s after switching to ethanol flow. This modulation experiment is described in more detail elsewhere.[34]

Obviously, the two spectra discussed above (traces a and b) are in good agreement with the bottom spectrum in Figure 5 (trace c). Trace c reveals an ATR-IR spectrum of another modulation experiment. In this experiment, neutral EtOH and HCl (0.013 mM) in EtOH was allowed to flow alternately over a GSH SAM after 4 h of adsorption. It was shown that GSH reversibly changes ionic form from zwitterionic to protonated state upon this stimulation. Further information about this kind of modulation experiment can be found elsewhere.[34]

Discussion

The admittance of dissolved proline to GSH self-assembled onto gold leads to characteristic signals in the ATR-IR spectra. Some of the signals arise because of dissolved proline itself, notably the prominent band at 1637 cm^{-1} ($\nu_{as}(COO^-)$). Other signals are not associated with dissolved proline, as the comparison between the spectra in Figure 1 (proline dissolved in ethanol) and Figure 3 (proline admitted to GSH SAM) shows. The latter signals are assigned to adsorbed species. A control experiment where proline was admitted to a bare gold surface revealed that the signals in Figure 3 do not arise from proline directly adsorbed on gold.

As can be seen in Figure 4, the signals from dissolved proline and the signals arising from adsorbed species have different kinetics of appearance and disappearance in the modulation experiments. As a consequence, their spectral contributions can be separated in the demodulated spectra by appropriately choosing the demodulation phase angle ϕ_k^{PSD}, as was done in Figure 5. Note that the choice of ϕ_k^{PSD} in order to remove the signals of one species from the spectra is somewhat arbitrary when all the signals associated with that species are overlapping with signals from other species. This situation may apply in the present case. We chose the demodulation phase angle ϕ_k^{PSD} such that the prominent signal at 1637 cm^{-1} vanished.

The spectra associated with the adsorbed species in Figure 5 are characterized by negative bands at 1731 cm^{-1} (ν(C═O) of COOH) and 1222 cm^{-1} (δ(C—O—H) + ν(C—O of COOH) and positive bands at 1615 cm^{-1} ($\nu_{as}(COO^-)$), 1396 cm^{-1} ($\nu_{sym}(COO^-)$), and 1303 cm^{-1}. Note that whether a band is positive or negative in a demodulated spectrum depends on the demodulation phase angle. For demodulation phase angles differing by 180°, the resulting spectra are inverted (positive bands become negative and vice versa) but otherwise identical. The spectral changes discussed above are characteristic of deprotonation/protonation of carboxylic acid groups. Figure 4 furthermore shows that the ν(C═O) signal of the acid group (COOH) increases upon admitting proline, revealing that protonation of an acid group is taking place, and deprotonation occurs upon removal of proline.

Three carboxylic acid groups are involved in the system under consideration, two on GSH and one on proline. In ethanol, proline exists in zwitterionic form, as clearly shown by the ATR-IR spectra of the dissolved species (Figure 1), hence the acid is deprotonated ($pK_a = 1.99$). GSH itself also exists in zwitterionic form in ethanol with the acid group on the glu part of the molecule deprotonated and the one on the gly part protonated.[34] However, we have shown recently that, upon adsorption of GSH onto gold, part of the molecules undergo deprotonation of the acid group of the gly moiety. This deprotonation is assisted by the interaction of the carboxylate group with the gold surface. Figure 5 shows that the demodulated spectrum obtained by modulating the proline concentration is very similar to a difference spectrum characteristic of deprotonation of the GSH sample in ethanol after admitting HCl. This strongly indicates that what is mainly seen in the demodulated spectra is the response of the GSH layer, which is partly protonated upon admission of proline and deprotonated during the subsequent ethanol flow. On the basis of previous work on GSH SAMs, we can even be more specific.[34] It was shown previously that the deprotonation of GSH in ethanol after protonation with HCl proceeds in two steps with distinctly different kinetics and spectral changes associated with them. A fast deprotonation of the glu part of the molecule is followed by a considerably slower deprotonation of the gly part. The latter step goes along with an interaction of the corresponding carboxylate group with the gold surface. Comparison shows that the spectral changes induced by the proline concentration modulation are similar to the ones observed during the deprotonation of the gly part of the molecule, in particular, the pronounced $\nu_{sym}(COO^-)$ at 1396 cm^{-1} is characteristic. The spectral changes thus indicate that, upon admitting proline, a fraction of the adsorbed GSH molecules are protonated at the gly moiety. Because proline exists as a zwitterion in ethanol (COO^- and NH_2^+) a direct proton transfer from proline to GSH seems unlikely ($pK_a(NH_2^+) = 10.60$). We therefore propose that the surface is involved in the protonation process.

As shown in a previous study, in ethanol, a fraction of GSH adsorbed on gold is protonated at the gly moiety, and another fraction is deprotonated.[34] Changing the stability of either one of the two states involved in the equilibrium between protonated and deprotonated acid groups (bound to the surface) will shift the equilibrium. We therefore propose that the presence of proline at the interface stabilizes the protonated (not surface bound) state of the gly moiety of GSH through intermolecular interactions. The differences between the spectra in Figure 5 obtained when GSH is interacting with HCl and proline, respectively, in the spectral range between 1500 and 1600 cm^{-1} may indicate such interactions.

The question that remains is why the spectra in Figure 5 mainly show the signatures of GSH, despite the fact that these changes are induced by the presence of proline at the interface. One possible explanation is based on the different sensitivity of the method for the two molecules. It has been reported that IR absorption is enhanced in the vicinity of metal and particularly gold films.[44] As one enhancement mechanism, a charge transfer has been proposed.[45] This mechanism differentiates between ions directly chemisorbed on the metal, for which a large enhancement is expected, and molecules weakly bound to the surface. This could explain why preferentially GSH signals are observed in the spectra. However, we prefer another interpretation. If the spectrum of proline interacting with the GSH SAM does not change much with respect to the spectrum of dissolved proline, as is expected in the absence of protonation/deprotonation of the molecule, then a differentiation between the two species is difficult. In this case, the contribution from the adsorbed proline is also subtracted when choosing the demodulation phase angle such that the contribution from the bulk (e.g., the strong $\nu_{as}(COO^-)$ band at 1637 cm^{-1}) vanishes. At this point, it should be noted that, even if the vibrational frequencies of adsorbed and dissolved proline are the same, the relative band intensities could change upon adsorption, because the latter depend on the orientation of the molecule on the surface. The finding that preferentially GSH signals are observed in the demodulated spectra in Figure 5 thus indicates that the proline is either not strongly oriented on the surface, which seems unlikely, or that the orientation is such that the relative intensities of the most prominent bands of the adsorbed species are similar to the ones found in solution.

The spectra do not provide much insight concerning the exact nature of the intermolecular interaction between the GSH SAM and proline. From the demodulated spectra in Figure 5 and on the basis of a previous investigation,[34] it emerges that the protonation/deprotonation of adsorbed GSH upon adsorption/desorption of proline goes along with prominent structural changes within the GSH layer. The latter change may be similar to the ion gating observed when admitting cationic drugs or metal ions to GSH SAMs.[31,32]

Finally and most importantly, the experiments reveal that the GSH SAM differentiates between D- and L-proline, the former being more strongly bound. We have found that this enantiodifferentiation depends on the structure of the GSH SAM. SAMs that were assembled for 4 h instead of only 20 min did not show appreciable signals in the absolute configuration modulation experiments. We interpret this finding with the structural changes within the GSH SAM that go along with the interaction with proline. These changes may not be possible in a SAM that was assembled for a long time. Similarly, it was observed before that the structure of the SAM strongly depends on the conditions during adsorption of GSH (i.e., presence and absence of acid and base) and that this has a significant effect on the amplitude of the response toward acid stimuli.[34]

Conclusions

L-Glutathione self-assembled on gold is found to discriminate between enantiomers of proline, with D-proline being the more strongly bound. The enantiodiscrimination was revealed by two independent types of experiments based on ATR-IR and modulation excitation spectroscopy. For the first, the adsorption/desorption kinetics of the two molecules was studied. To extract relative adsorption and desorption rates for the two enantiomers from the experimental curves, numeric simulations were performed, which couple mass transport (convection and diffusion)

with adsorption and desorption. The ATR-IR experiments revealed that, in particular, the desorption kinetics is different for the two enantiomers. The numerical simulations reproduced the measured response associated with dissolved and adsorbed species toward concentration modulation well. Absolute configuration modulation excitation experiments further confirmed enantiodiscrimination. In the latter experiment, the absolute configuration of proline was changed periodically. The signals in the demodulated spectra reveal the difference in interaction of the two enantiomers with the chiral L-glutathione SAM.

Demodulated ATR-IR spectra associated with adsorbed species strongly resemble the spectral changes observed when changing the protonation state of L-glutathione adsorbed on gold. It could furthermore be concluded that the interaction of proline with adsorbed L-glutathione leads to protonation of the gly moiety of the latter. This process is reversible in the absence of proline in solution. In the absence of dissolved proline, part of the L-glutathione is deprotonated, and the carboxylate group of the gly part of the molecule interacts with the gold surface. The protonation of L-glutathione goes along with a significant structural change.

When the L-glutathione layer was allowed to self-assemble for a long time (4 h instead of 20 min) the enantiodiscrimination was virtually lost. This is explained by the structural change of L-glutathione upon interaction with proline, which may depend on the structure of the SAM. A similar dependence of the protonation/deprotonation response on the structure of the SAM was reported earlier. This indicates that enantiodiscrimination in this system is mainly associated with defects in the L-glutathione SAM.

Acknowledgment. Financial support from the Swiss National Science Foundation and grants of computer time from the Swiss National Supercomputing Centre (CSCS) Manno are gratefully acknowledged. Use of sputtering facilities at the Swiss Center for Electronics and Microtechnology in Neuchâtel (CSEM) is kindly acknowledged.

References and Notes

(1) Ahuja, S. *Chiral separations by chromatography*; Oxford University Press: Washington, DC, 2000.
(2) Bodenhöfer, K.; Hierlemann, A.; Seemann, J.; Gauglitz, G.; Koppenhoefer, B.; Göpel, W. *Nature (London)* **1997**, *387*, 577.
(3) McKendry, R.; Theoclitou, M.-E.; Rayment, T.; Abell, C. *Nature (London)* **1998**, *391*, 566.
(4) Bürgi, T.; Baiker, A. *Acc. Chem. Res.* **2004**, *37*, 909.
(5) Baiker, A.; Blaser, H. U. Enantioselective Catalysts and Reactions. In *Handbook of Heterogeneous Catalysis*; Ertl, G., Knözinger, H., Weitkamp, J., Eds.; VCH Publishers: Weinheim, 1997; Vol. 5, p 2422.
(6) Hazen, R. M.; Filley, T. R.; Goodfriend, G. A. *Proc. Natl. Acad. Sci. U.S.A.* **2001**, *98*, 5487.
(7) Zaia, D. A. M. *Amino Acids* **2004**, *27*, 113.
(8) McFadden, C. F.; Cremer, P. S.; Gellman, A. J. *Langmuir* **1996**, *12*, 2483.
(9) Attard, G. A. *J. Phys. Chem. B* **2001**, *105*, 3158.
(10) Lorenzo, M. O.; Haq, S.; Bertrams, T.; Murray, P.; Raval, R.; Baddeley, C. J. *J. Phys. Chem. B* **1999**, *103*, 10661.
(11) Lorenzo, M. O.; Baddeley, C. J.; Muryn, C.; Raval, R. *Nature (London)* **2000**, *404*, 376.
(12) Ferri, D.; Bürgi, T. *J. Am. Chem. Soc.* **2001**, *123*, 12074.
(13) Schunack, M.; Laegsgaard, E.; Steengaard, I.; Johannsen, I.; Besenbacher, F. *Angew. Chem, Int. Ed.* **2001**, *40*, 2623.
(14) Kühnle, A.; Linderoth, T. R.; Hammer, B.; Besenbacher, F. *Nature (London)* **2002**, *415*, 891.
(15) Ernst, K.-H.; Kuster, Y.; Fasel, R.; Müller, M.; Ellerbeck, U. *Chirality* **2001**, *13*, 675.
(16) Horvath, J. D.; Gellman, A. J. *J. Am. Chem. Soc.* **2002**, *124*, 2384.
(17) Horvath, J. D.; Koritnik, A.; Kamakoti, P.; Sholl, D. S.; Gellman, A. J. *J. Am. Chem. Soc.* **2004**, *126*, 14988.
(18) Nakanishi, T.; Yamakawa, N.; Asahi, T.; Osaka, T.; Ohtani, B.; Uosaki, K. *J. Am. Chem. Soc.* **2002**, *124*, 740.
(19) Maier, N. M.; Schefzick, S.; Lombardo, G. M.; Feliz, M.; Rissanen, K.; Lindner, W.; Lipkowitz, K. B. *J. Am. Chem. Soc.* **2002**, *124*, 8611.
(20) O'Conner, D. J.; Sexton, B. A.; Smart, R. S. C. *Surface analysis methods in materials science*; Springer series in surface science; Springer-Verlag: Berlin, 1992; Vol. 23.
(21) Alder, A. J.; Greenfield, N. J.; Fasman, G. D. *Methods Enzymol.* **1973**, *27*, 675.
(22) Nafie, L. A. *Annu. Rev. Phys. Chem.* **1997**, *48*, 357.
(23) Hug, W.; Kint, S.; Bailey, G. F.; Scherer, J. R. *J. Am. Chem. Soc.* **1975**, *97*, 5589.
(24) Hicks, J. M.; Petralli-Mallow, T. *Appl. Phys. B*— **1999**, *68*, 589.
(25) Gellman, A. J.; Horvath, J. D.; Buelow, M. T. *J. Mol. Catal A: Chem.* **2001**, *167*, 3.
(26) Harrick, N. J. *Internal reflection spectroscopy*; Interscience Publishers: New York, 1967.
(27) Baurecht, D.; Fringeli, U. P. *Rev. Sci. Instr.* **2001**, *72*, 3782.
(28) Bürgi, T.; Baiker, A. *J. Phys. Chem. B* **2002**, *106*, 10649.
(29) Wirz, R.; Bürgi, T.; Baiker, A. *Langmuir* **2003**, *19*, 785.
(30) Wirz, R.; Bürgi, T.; Lindner, W.; Baiker, A. *Anal. Chem.* **2004**, *76*, 5319.
(31) Hepel, M.; Tewksbury, E. *J. Electroanal. Chem.* **2003**, *552*, 291.
(32) Takehara, K.; Aihara, M.; Ueda, N. *Electroanalysis* **1994**, *6*, 1083.
(33) Fang, C.; Zhou, X. *Electroanalysis* **2003**, *15*, 1632.
(34) Bieri, M.; Bürgi, T. *Langmuir* **2005**, *21*, 1354.
(35) Urakawa, A.; Wirz, R.; Bürgi, T.; Baiker, A. *J. Phys. Chem. B* **2003**, *107*, 13061.
(36) Becke, A. D. *J. Chem. Phys.* **1993**, *98*, 5648.
(37) Perdew, J. P.; Chevary, J. A.; Vosko, S. H.; Jackson, K. A.; Pederson, M. R.; Singh, D. J.; Fiolhais, C. *Phys. Rev. B* **1992**, *46*, 6671.
(38) Ditchfield, R.; Hehre, W. J.; Pople, J. A. *J. Chem. Phys.* **1971**, *54*, 724.
(39) Frisch, M. J.; Trucks, G. W.; Schlegel, H. B.; Scuseria, G. E.; Robb, M. A.; Cheeseman, J. R.; Montgomery, Jr., J. A.; Vreven, T.; Kudin, K. N.; Burant, J. C.; Millam, J. M.; Iyengar, S. S.; Tomasi, J.; Barone, V.; Mennucci, B.; Cossi, M.; Scalmani, G.; Rega, N.; Petersson, G. A.; Nakatsuji, H.; Hada, M.; Ehara, M.; Toyota, K.; Fukuda, R.; Hasegawa, J.; Ishida, M.; Nakajima, T.; Honda, Y.; Kitao, O.; Nakai, H.; Klene, M.; Li, X.; Knox, J. E.; Hratchian, H. P.; Cross, J. B.; Bakken, V.; Adamo, C.; Jaramillo, J.; Gomperts, R.; Stratmann, R. E.; Yazyev, O.; Austin, A. J.; Cammi, R.; Pomelli, C.; Ochterski, J. W.; Ayala, P. Y.; Morokuma, K.; Voth, G. A.; Salvador, P.; Dannenberg, J. J.; Zakrzewski, V. G.; Dapprich, S.; Daniels, A. D.; Strain, M. C.; Farkas, O.; Malick, D. K.; Rabuck, A. D.; Raghavachari, K.; Foresman, J. B.; Ortiz, J. V.; Cui, Q.; Baboul, A. G.; Clifford, S.; Cioslowski, J.; Stefanov, B. B.; Liu, G.; Liashenko, A.; Piskorz, P.; Komaromi, I.; Martin, R. L.; Fox, D. J.; Keith, T.; Al-Laham, M. A.; Peng, C. Y.; Nanayakkara, A.; Challacombe, M.; Gill, P. M. W.; Johnson, B.; Chen, W.; Wong, M. W.; Gonzalez, C.; Pople, J. A. *Gaussian 03*, Revision C.01; Gaussian, Inc., Wallingford CT, 2004.
(40) Cancès, M. T.; Mennucci, B.; Tomasi, J. *J. Chem. Phys.* **1997**, *107*, 3032.
(41) Bird, R. B.; Stewart, W. E.; Lightfoot, E. N. *Transport Phenomena*; John Wiley & Sons: New York, 1960.
(42) *FEMLAB*, v.3.0; COMSOL, Inc.: Stockholm, Sweden.
(43) Pintar, A.; Malacea, R.; Pinel, C.; Fogassy, G.; Besson, M. *Appl. Catal., A* **2004**, *264*, 1.
(44) Osawa, M.; Ataka, K.-I.; Yoshii, K.; Nishikawa, Y. *Appl. Spectrosc.* **1993**, *47*, 1497.
(45) Wadayama, T.; Sakurai, T.; Ichikawa, S.; Suëtaka, W. *Surf. Sci.* **1988**, *198*, L359.

Chapter 2

Enantiodiscrimination between an *N*-Acetyl-L-cysteine SAM and Proline: An *in Situ* Spectroscopic and Computational Study

Marco Bieri and Thomas Bürgi

Published in ChemPhysChem, Volume 7(2), pp. 514–523, doi: 10.1002/cphc.200500474, 2006.

CHEMPHYSCHEM

DOI: 10.1002/cphc.200500474

Enantiodiscrimination between an *N*-Acetyl-L-cysteine SAM and Proline: An In Situ Spectroscopic and Computational Study**

Marco Bieri and Thomas Bürgi*[a]

A combination of attenuated total reflection infrared (ATR-IR) and modulation excitation spectroscopy (MES) is used to study the enantiodiscriminating interactions between proline and a chiral, self-assembled monolayer (SAM) of N*-acetyl-*L*-cysteine on gold. The* N*-acetyl-*L*-cysteine SAM consists of a mixture of protonated and deprotonated molecules. Whereas both species are influenced by adsorbed proline, only the deprotonated molecules are involved in enantiodiscrimination. Density functional theory (DFT) calculations reveal that electrostatics dominates the interaction between the two molecules. By modulating the absolute configuration of proline over the chiral SAM, and a subsequent phase-sensitive detection of the periodically varying signals in the ATR-IR spectra, the small spectral differences between the diastereomeric complexes are spotted. The resulting difference spectrum is in qualitative agreement with the spectrum predicted by the DFT calculations.*

Introduction

Chiral surfaces and interfaces play an important role in various fields of modern technology, such as in chromatography[1] and heterogeneous enantioselective catalysis.[2,3] Despite the practical interest in chiral interfaces, the former is also more and more the subject of fundamental research.[4–22] Chiral interfaces can distinguish between enantiomers of a chiral compound,[23–25] a property which becomes increasingly important, since separation, selective production, and detection of enantiomers is a fast-growing market. At the origin of this trend is the biological homochirality on earth, which, in turn, may even have been caused by chiral surfaces.[26,27]

The rational design of the fundamental property of chiral interfaces, namely their ability to distinguish between adsorbed enantiomers, goes hand in hand with the development of powerful techniques, which can, on a molecular level, give information on the origin of enantiodiscrimination. The latter is in most cases determined by intermolecular interactions. It is therefore desirable to develop techniques that can, not only quantify enantiodifferentiation, but also shed light on its origin. Such techniques should ideally provide molecular level information and combine (surface-) sensitivity with selectivity for chiral information, a combination of criteria that is difficult to meet simultaneously. Nonlinear optical techniques may turn out to be powerful for the investigation of chiral interfaces.[28–30]

We have recently proposed a method to investigate enantiodiscrimination at chiral solid/liquid interfaces that combines attenuated total reflection infrared (ATR-IR) spectroscopy[31] with modulation excitation spectroscopy (MES).[32,33] The former allows the measurement of infrared spectra of adsorbed molecules in the presence of a solvent. The latter technique uses the periodic stimulation of the investigated system and the phase-sensitive detection (PSD) of the induced response. The PSD leads first of all to an increased sensitivity. In addition, the system under investigation can selectively be questioned by selection of the appropriate stimulation parameter. By choosing the absolute configuration of the probe molecule as the periodic stimulation, the enantiodiscriminating interactions can selectively be spotted, since the infrared spectra of the enantiomers are identical, except when they interact with a chiral environment, which is able to distinguish between them. We have demonstrated the power of the technique by investigating enantiodiscrimination at chiral stationary phases used in chromatography.[34,35]

Chiral self-assembled monolayers (SAMs) are potentially interesting for sensing applications and for separations in microsystems.[24,25,36,37] Very recently, we studied the interaction of proline with a chiral SAM of L-glutathione (GSH, γ-Glu-Cys-Gly) on gold.[38] It could be shown that the GSH SAM can discriminate well between the enantiomers of proline. Upon interaction with proline, the relatively flexible *Y*-shaped GSH molecules changed their conformation on the surface. Herein, we investigate the enantiodiscrimination of *N*-acetyl-L-cysteine (NAC, Scheme 1) SAMs on gold. NAC can be viewed as the anchoring part of GSH, and it has less conformational freedom than the latter. On the basis of the absolute configuration modulation experiments and density functional theory (DFT) calculations, a model for the interactions of proline with the chiral NAC SAM is proposed and it is furthermore shown that the interaction is significantly different from the GSH case.

[a] *M. Bieri, Prof. Dr. T. Bürgi*
Université de Neuchâtel, Institut de Chimie
Rue Emile-Argand 11, 2007 Neuchâtel (Switzerland)
Fax: (+41) 32-718-2511
E-mail: thomas.burgi@unine.ch

[**] *SAM = Self-Assembled Monolayer.*

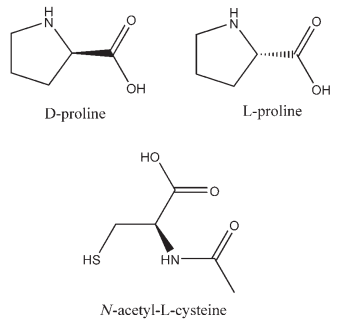

Scheme 1. Structure of proline (top) and *N*-acetyl-L-cysteine (NAC, bottom).

Results and Discussion

DFT Calculations of *N*-Acetyl-L-cysteine and Proline

For a better understanding of the structure of NAC (selector, Scheme 1), proline (selectand, Scheme 1), and their complexes, and to assign the corresponding vibrational spectra, DFT calculations were performed. The conformations with lowest energies found for proline and NAC, are displayed as insets in Figures 1 and 2, respectively. In the case of proline, the energetically most favorable conformation was found to have a hydrogen bond between the carboxylate and the protonated amine.

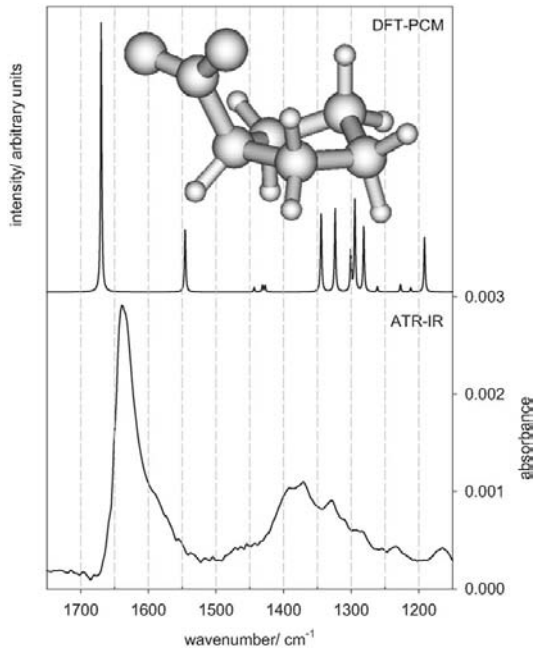

Figure 1. Top) Calculated IR spectrum of proline after convolution with a Lorentzian band shape ($\gamma = 1$ cm^{-1}). The inset shows the conformation of proline (zwitterionic) used for the spectrum calculation. For details concerning the calculation method, see text. Bottom) Experimental ATR-IR spectrum of proline dissolved in ethanol. The phase-resolved (demodulated), spectrum refers to an "L-proline versus ethanol" modulation experiment which consisted of alternately flowing L-proline (about 0.04 M) and ethanol over the bare Ge IRE at a flow rate of 0.5 mL min^{-1} (see the Experimental Section for a description of the modulation experiments). Observed and calculated vibrational bands of proline are listed in Table 1.

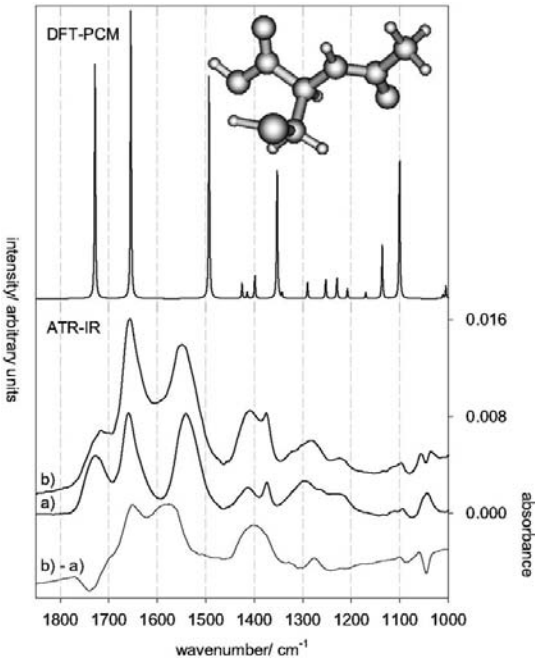

Figure 2. Top) Calculated IR spectrum of NAC. The spectrum was obtained by convoluting the calculated IR intensities with a Lorentzian band shape ($\gamma = 1$ cm^{-1}). The NAC conformation used for the calculation of the spectrum is shown in the inset. See text for details concerning the calculation method. Bottom) Experimental ATR-IR spectra of NAC adsorbed on the gold coated Ge IRE. Spectrum "a" was recorded at the start of the self-assembling process, spectrum "b" recorded about two hours afterwards. The corresponding difference spectrum is "b−a". Typical NAC concentrations were about 0.6 mM for ATR-IR experiments. Experimental and calculated vibrational frequencies of NAC are summarized in Table 1.

In this conformation, the carbon in the ring opposite to the carboxylate group points out of the ring plane in the same direction as the carboxylate (see inset in Figure 1). Another conformation with a slightly higher energy, but similar IR spectrum, has the carbon pointing in the opposite direction with respect to the carboxylate.[38] In the following, the conformation shown in Figure 1 was considered.

For NAC, a *trans* configuration within the rather rigid amide group with (weak) hydrogen bonds between the NH and the carboxylic acid, and between the SH and the carboxylic acid were found to have the lowest energy.

DFT Calculations of a *N*-Acetyl-L-cysteine–D(L)-proline Complex

The interactions between NAC and D- and L-proline, respectively, were studied with the optimized structure of anionic

NAC (see below) as the starting point. D(L)-proline was then allowed to interact with NAC at different sites involving different functional groups: proline–NH_2^+···O=C–amide–NAC, proline–NH_2^+···OOC^-–NAC and proline–COO^-···HN–amide–NAC, were used as prominent examples for interactions. However, among all these possibilities, and not surprisingly, the ionic interactions between the positively charged proline NH_2^+ group and the negatively charged NAC carboxylate COO^- turned out to dominate the interaction strength. To include ionic proline–NAC intermolecular interactions, the conformational space of the complex was further probed by using a Born–Oppenheimer molecular dynamics (BOMD) model[39] with the semi-empirical AM1 Hamiltonian.[40] The trajectory calculation was performed up to about 1.3 ps (ca. 900 steps in each trajectory). For each of the NAC–D(L)-proline complexes, three conformations with low energies of the trajectories were chosen as the starting geometries for structure optimization by DFT. All of the DFT-optimized structures revealed a relative arrangement of NAC and proline as shown in Figure 3a. This configuration is favorable from an electrostatic point of view, since the two negative charges are widely separated and at the same time opposite charges are close, as is schematically indicated in Figure 3a. With the optimized structure of the NAC–L-proline complex at hand, the same procedure was repeated for the NAC-D–proline complex, just by changing the absolute configuration of proline (see Scheme 1 for the configuration of the two enantiomers). The result of the NAC–D-proline structure optimization is displayed in Figure 3b. The analogous ionic interactions between the D-proline NH_2^+ group and the carboxylate COO^- of NAC are possible. The potential energy difference between the two chiral complexes was found to be only about 0.2 kJ mol^{-1}, with the NAC–L-proline complex being energetically more favorable. It should be noted that the structure optimization and vibrational analysis of the complexes were performed using the polarizable continuum model (PCM) model to include solvent (ethanol) effects.

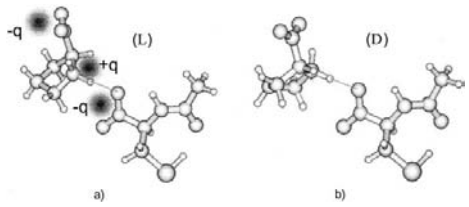

Figure 3. Pictorial representation of the optimized structures of the NAC–L-proline (a) and NAC–D-proline (b) complexes. The complex is determined by ionic proline–NH_2^+···COO^-–NAC intermolecular interactions. In (a), the partially charged groups are schematically indicated with corresponding charge clouds. For details concerning the calculation method, see text.

Characterization of the *N*-Acetyl-L-cysteine SAM (Selectand)

The lower half of Figure 2 shows the ATR-IR spectra recorded during the NAC self-assembling process on gold. Specifically, spectrum "a" was recorded at the beginning of the self-assembling process, whereas spectrum "b" was recorded about two hours afterwards. In the upper half in Figure 2, the calculated vibrational spectrum of NAC in its neutral form (see inset) is displayed, this was obtained by convoluting the calculated IR intensities with a Lorentzian band shape (half width at half maximum, $\gamma = 1$ cm^{-1}). The overall agreement between the calculated and experimentally obtained spectrum is good enough to allow an assignment of the most prominent vibrational bands, which notably are the ν(–COOH) mode at 1727 cm^{-1}, the amide I and amide II vibrations at 1661 and 1539 cm^{-1}, respectively, and the coupled methyl + δ(–CH_2) + δ(–COH) + ν(–CO) mode at 1375 cm^{-1}. The assignment is summarized in Table 1. However, considering the two ATR-IR spectra depicted in the lower half of Figure 2, significant spectral differences become apparent with time, which are emphasized in the corresponding difference spectrum labeled "b−a". The difference spectrum shows structural changes within the adsorbate layer beside bare mass uptake. The two signals at 1590 and 1400 cm^{-1} are assigned to the

Table 1. Observed vibrational bands (in wavenumbers) of NAC adsorbed on gold, and proline (zwitterionic) dissolved in ethanol.[a]

NAC	Proline	Assignment
static signals		
1727		ν(–COOH)
1661		amide I
1590		ν_{as}(–COO^-)
1539		amide II
1400		ν_s(–COO^-)
1375		methyl + δ(–CH_2) + δ(–COH) + ν(–CO)
phase-resolved signals		
	1637	ν_{as}(–COO^-)
	1570	δ_s(–NH_2) scissoring (appearing as shoulder of band at 1637 cm^{-1})
	1392	ν_s(–COO^-) + δ(–CH)
	1370	ν_s(–COO^-) + δ(–CH)
calculated signals		
1729		ν(–COOH)
	1660	ν_{as}(–COO^-)
1655		amide I
	1537	δ_s(–NH_2) scissoring
1494		amide II
1353		methyl + δ(–CH_2) + δ(–COH) + ν(–CO)
	1340	ν_s(–COO^-) + δ(–CH)
	1300	ν_s(–COO^-) + δ(–CH)

[a] The static spectrum of NAC is depicted in Figure 2 (spectrum a) and the phase-resolved proline spectrum is displayed in Figure 1 (bottom). Frequencies of calculated NAC and proline vibrations are also included for comparison.

ν_{as}(–COO$^-$) and ν_s(–COO$^-$) vibrations, respectively, which indicates a deprotonation of adsorbed NAC molecules. This deprotonation process is assisted by the interaction of the carboxylic acid group with the Au surface, which acts as a proton acceptor. In a previous work, we have derived the average orientation of NAC molecules within the adsorbate layer at the initial stage of self-assembling.[41] In this orientation analysis, based on the ratio of vibrational band intensities of randomly and oriented molecules from the bulk phase and adsorbed on the Au surface, respectively, a close proximity of the carboxylic acid group to the surface was suggested. Interaction of the carboxylic acid group with the gold surface and deprotonation was furthermore demonstrated for the adsorption of similar molecules, such as L-glutathione[42] and cysteine on gold.[43]

The spontaneous deprotonation of NAC molecules within the SAM was also observed when the adsorption was stopped after about one minute by flowing solvent (ethanol) over the sample. The spectral response clearly revealed deprotonation, which was followed in situ until no variation in the spectra could be detected (about thirty minutes). On the basis of the ratio between the integrated intensities of the carboxylic acid vibrational bands before and after the deprotonation process, we estimate that about 40% of adsorbed NAC molecules undergo a deprotonation. The spectrum recorded at the end of the deprotonation process was found to be very similar to the one shown in Figure 2, recorded two hours after the start of the self-assembling process (spectrum b). We will show later that these two NAC layers, despite the different assembling time and coverage show remarkably similar enantiodiscrimination in the absolute configuration modulation experiments, whereas in the presence of an acid, which prevents deprotonation of adsorbed NAC, the spectral response was completely different in analogous experiments. This suggests that preferentially one of the two ionic forms of NAC present on the surface is involved in the interaction with proline. As ionic interactions are expected to dominate the adsorption of zwitterionic proline under our conditions, which was further confirmed by the DFT calculations, we suggest that the deprotonated NAC on the gold surface is responsible for the observed spectral changes, upon interaction of proline with the NAC SAM, described in the following.

The Analyte Molecule Proline (Selector)

The lower half of Figure 1 shows a (demodulated) ATR-IR spectrum of L-proline in ethanol (recorded over the bare Ge internal reflection elements, IRE). The L-proline spectrum reveals a prominent peak at 1637 cm^{-1} with a shoulder at about 1570 cm^{-1}. In addition, a broad feature composed of several overlapping bands is visible in the region between 1400 and 1300 cm^{-1}. The calculated IR spectrum of proline is shown in the upper half of Figure 1. This spectrum was simulated by convoluting the calculated IR intensities with a Lorentzian band shape using $\gamma = 1$ cm^{-1}. Besides shifts in wavenumber, the overall agreement is good enough to allow an assignment of the most prominent vibrational bands. Specifically, the prominent asymmetric band at 1637 cm^{-1} can be assigned to the ν_{as}(–COO$^-$) vibration with the δ_s (–NH$_2$) scissoring mode at 1570 cm^{-1} appearing as shoulder on the former band. Other vibrational modes of proline are listed in Table 1 and were found to be in agreement with previous reports.[44]

Modulation Experiments and Enantioselective Discrimination

In the lower half of Figure 4, an ATR-IR spectrum of each of the interacting species, that is, NAC adsorbed on the gold coated Ge IRE (selector, represented by ——) and dissolved proline (selectand, represented by ——), respectively, is shown for clarity reasons. In the upper half in Figure 4, the top trace refers to a time-resolved ATR-IR spectrum, which was recorded while flowing L-proline over the NAC SAM. For this experiment, the NAC SAM was allowed to self-assemble for about two hours. This spectrum is thus a superposition of the individual NAC SAM and proline (mainly from the bulk phase) spectra. Note that the reference for this absorption spectrum was recorded before starting the NAC self-assembling. The strongest band in the spectrum at 1637 cm^{-1} is a superposition of the ν_{as}(–COO$^-$) of proline and the amide I vibration of NAC. The phase-resolved, that is, demodulated spectrum of an "L-proline

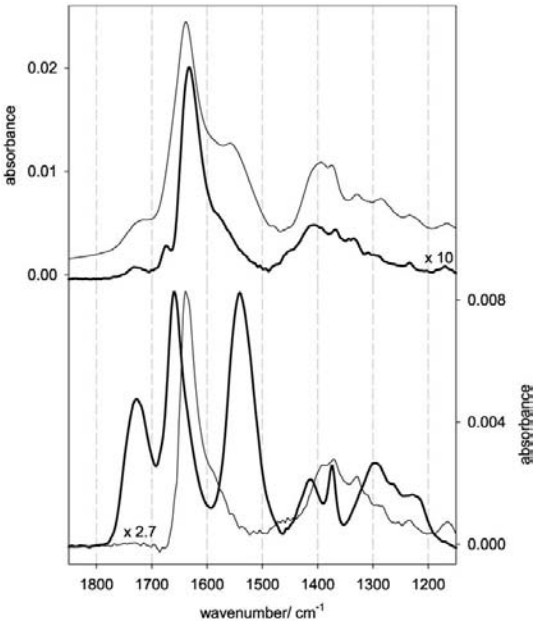

Figure 4. Bottom) ATR-IR spectra of NAC (selector) adsorbed on a gold surface (——) and proline (selectand, ——, scaled by a factor of 2.7) dissolved in ethanol. The two spectra are included for clarity, and are also presented in Figures 1 (proline) and 2 (NAC). Top) A static (time-resolved) ATR-IR spectrum (——) recorded while flowing L-proline over the NAC SAM after about two hours of self-assembling. The reference was taken before SAM formation. A demodulated (phase-resolved) spectrum (——) of an "L-proline versus ethanol" modulation experiment. In this modulation experiment (period $T = 72.4$ s, flow rate 0.5 mL min^{-1}), L-proline (0.04 M) was periodically replaced by ethanol and flowed over the NAC SAM.

versus ethanol" modulation experiment ($T = 72.4$ s, flow rate = 0.5 mL min^{-1}), performed over the NAC modified surface and scaled by a factor of ten, is depicted by —— in the upper half in Figure 4. Obviously (and not surprisingly) this spectrum is dominated by the bulk-phase proline vibrational bands (compare to the proline spectrum in the lower half in Figure 4). It should be emphasized here that only bands that are periodically changing with time owing to the stimulation (L-proline concentration modulation) show up in this demodulated spectrum. As a consequence, the contribution of adsorbed NAC is basically removed, except for periodic changes induced by the proline concentration modulation. However, besides the proline bands, other significant signals are apparent, notably the sharp small band at about 1674 cm^{-1} and a broad band at about 1732 cm^{-1}. The latter is assignable to the ν(–COOH) vibration of adsorbed NAC, whereas the former is likely due to the NAC amide I mode. Figure 4 shows that this band is shifted to higher wavenumber with respect to the bare NAC SAM. The fact that NAC vibrations show up in the demodulated spectrum and that the NAC amide I vibration has shifted, strongly suggests an interaction of proline with the NAC SAM.

The modulation technique allows species with different kinetics to be separated, by choosing the demodulation phase angle ϕ_k^{PSD} in Equation (1) (Experimental Section) accordingly. Therefore, if the dissolved and adsorbed proline have different kinetics, the contribution of the dissolved species would vanish at a certain demodulation phase angle, leaving only the spectrum of the adsorbed species. However, in the present case, the signals in the demodulated spectrum all had very similar phase behavior, that is, there was no significant phase lag between dissolved and adsorbed species. This in turn indicates that, on our time scale, dissolved and adsorbed proline are in equilibrium, and that this equilibrium is established fast. In summary, the spectral response to the L-proline concentration modulation in presence of the NAC SAM clearly indicates intermolecular interactions between selector (NAC) and selectand (proline). It should be noted that the analogous experiment with D-proline resulted in very similar spectra. In order to investigate differences in the interaction of the two proline enantiomers and the NAC SAM, absolute configuration modulation experiments were performed, which selectively highlights these differences. These experiments are discussed next.

In Figure 5 we present a series of phase-resolved spectra which refer to absolute configuration modulation experiments. In these experiments, using a modulation period of $T = 362.3$ s and a flow rate of 0.18 mL min^{-1}, the absolute configuration of proline was changed periodically by flowing the two enantiomers over the NAC SAM, starting with an inflow of D-proline. Again, it should be noted that only bands that are periodically changing with time, owing to the stimulation (absolute proline configuration modulation), show up in these spectra. These spectra thus reveal the differences in intermolecular interactions between the two proline enantiomers and the NAC SAM. The strongest features in the spectrum are positive and negative bands between 1700 and 1550 cm^{-1}, particularly at 1667 cm^{-1} (negative), 1650 cm^{-1} (positive), 1630 cm^{-1} (positive, shoulder on the 1650 cm^{-1} band), at about 1600 cm^{-1} (negative, broad) and about 1550 cm^{-1} (positive, very broad). In addition, a weaker signal is observed at about 1375 cm^{-1}.

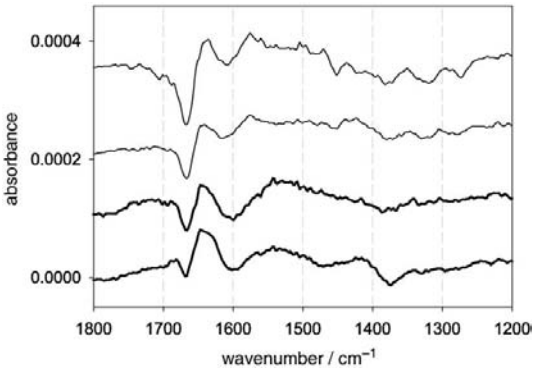

Figure 5. Demodulated spectra performed on different days using different gold-coated Ge IREs illustrating the repeatability of the absolute configuration modulation experiments (period $T = 362.3$ s, flow-rate 0.18 mL min^{-1}). Bottom) (——) D- and L-proline, (0.04 M) periodically flowed over NAC after two hours of self-assembly. Top) (——) The self-assembly of NAC on gold-coated Ge IRE was stopped after one minute, and deprotonation of adsorbed NAC molecules was followed until no spectral variation could be detected. Then D- and L-proline were allowed to flow alternately over the NAC SAM.

At this point, some general statements can be made: 1) The spectral response of the absolute configuration modulation experiments is rather complex, revealing positive and negative signals—the spectral response can therefore not be reduced to the strong adsorption of only one enantiomer, which would lead to spectra strongly resembling the proline spectrum. However, the contribution of different equilibrium coverages of the adsorbing enantiomers to the observed spectral response cannot be excluded completely, since, in general, the observed demodulated spectra are a combination of spectral differences due to enantiospecific interactions *and* coverage differences. The spectral response (positive and negative bands) still indicates that enantiospecific effects dominate over coverage effects. 2) As also mentioned in the Experimental Section, control experiments with proline and the gold-coated Ge IRE (that is, in the absence of the NAC SAM) revealed that the signals in Figure 5 are not due to proline interacting with the bare gold surface. 3) The signals due to intermolecular interactions are more than one order of magnitude smaller than the spectrum of NAC adsorbed on gold (compare to the NAC spectrum in the lower half of Figure 4). Still the signals are considerably above the noise level, which is about 5×10^{-6} in the spectral region around 1700 cm^{-1}. The strength of the signals thus suggests that the enantiodiscrimination between the NAC SAM and proline is rather weak and/or that the interaction between the SAM and proline is weak. In order to emphasize the significance of the results and reproducibility, a series of demodulated spectra is presented in Figure 5, referring to absolute configuration modulation experiments performed on different days using different gold-coated Ge IREs. Furthermore, different NAC-modified Au surfaces were probed by varying

the duration of the self- assembling process from two hours (2 h SAM) to one minute (1 min SAM). Note that in the case of the latter adsorbate layer, the subsequent deprotonation was completed about thirty minutes before modulation experiments were performed. The two spectra at the bottom in Figure 5 (——) refer to the 2 h SAM (different experiments!), whereas the two spectra depicted on top (——) refer to the 1 min SAM (again different experiments). The reproducibility of the spectral response for each of the two differently modified surfaces (2 h and 1 min SAM) is good (compare the two pairs of traces with —— and ——). But, there is also a remarkable similarity in the spectra for the 2 h and 1 min NAC SAM. This shows that the interactions responsible for the observed spectral changes are the same for the two SAMs, although the NAC coverage and also the long-range ordering, is largely different in the two cases. This, in turn, indicates that the interaction between proline and the SAM is a 1:1 type interaction, that is, an interaction between a proline molecule and one individual adsorbed NAC molecule (as opposed to an ordered "supramolecular" NAC agglomerate on the gold surface). Furthermore, in a control experiment, NAC deprotonation on the surface was inhibited by the addition of 0.013 M HCl, which was verified by the absence of corresponding carboxylate vibrational bands. A following absolute configuration modulation experiment (in the presence of HCl, 0.013 M) showed a completely different spectral response with significantly weaker signals due to the different kind of interactions (ion–dipole, dipole–dipole, etc.) in this case. Note that in these experiments, proline is protonated at the acid group.

Dispersive bands in demodulated spectra, such as the ones observed for the absolute configuration modulation experiments (Figure 5), can arise due to slight frequency shifts induced by the stimulation. In our case, this means that, owing to the different interactions between the enantiomers of proline and the chiral SAM, the spectrum of the interaction complex changes slightly. Note that no such changes, and therefore no signals, are expected in the demodulated spectra for an absolute configuration modulation experiment over a nonchiral surface.[34] The position of the dispersive bands suggests frequency shifts of the proline carboxylate $\nu_{as}(COO^-)$ (possibly also $\nu_s(COO^-)$) and NH_2 scissoring $\delta(-NH_2)$ and NAC amide and carboxylate vibrations (see corresponding spectra in the lower half of Figure 4). The demodulated spectrum of the "L-proline versus ethanol" experiment (Figure 4, top, ——) indeed shows an NAC amide I band (at 1674 cm^{-1}) that is shifted owing to interactions with proline. On the other hand, the same spectrum also reveals a small ν(COOH) band associated with protonated NAC, whereas no clear sign of such a band is visible in the demodulated spectra of the absolute configuration modulation experiments (Figure 5). This indicates that protonated NAC on the surface also interacts with proline, but that this interaction is not enantiospecific. In a more general sense, this finding shows that both enantiospecific and nonspecific interactions take place at the chiral SAM, and it indicates that it is the deprotonated NAC that is involved in the enantiospecific interaction. In order to understand the origin of the observed dispersive bands in Figure 5 better, DFT calculations on the interaction between NAC and proline have been performed, and will be discussed in the next section.

Calculated IR Spectrum of a D(L)-Proline–NAC Complex

In Figure 6 we present the calculated IR spectra of zwitterionic proline, anionic *N*-acetyl-L-cysteine, and the NAC–proline complex (see Figure 3 for the structure). The calculated spectra were obtained from the optimized structures of the corresponding conformations. All of these spectra were obtained by convoluting the corresponding calculated IR intensities with a Lorentzian band shape ($\gamma = 10$ cm^{-1}). In Figure 6, the most important vibrational bands used for the following discussion are labeled. Some of the prominent vibrational bands of proline and NAC undergo considerable frequency shifts upon complexation, as is obvious from Figure 6. Specifically, the proline $\nu_{as}(-COO^-)$ band shifts about 15 cm^{-1} to lower wavenumbers, whereas the δ_s $(-NH_2)$ scissoring vibrational band shifts about 42 cm^{-1} up in the NAC-proline complex. NAC band shifts are visible for the $\nu_{as}(-COO^-)$ and amide I bands, which results in a single, strong asymmetric band in the vibrational spectrum of the complex. Careful inspection further shows that the amide II and methyl bands slightly shift (by about 6 cm^{-1}) to higher frequencies. The calculations show that the intense band of the complex between about 1250 and 1380 cm^{-1} consists of sever-

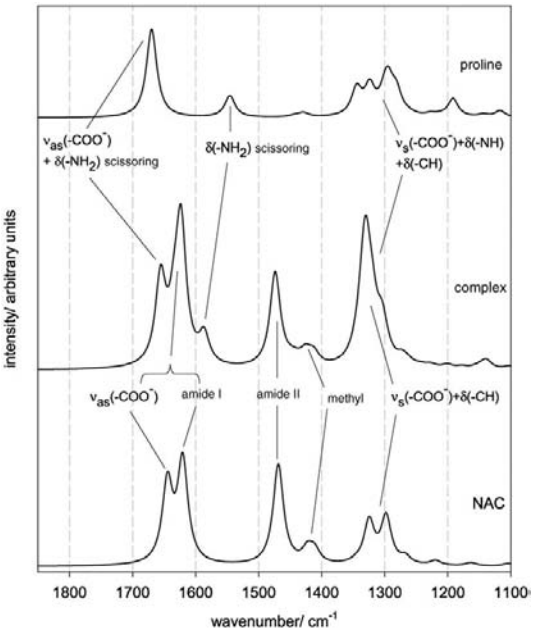

Figure 6. Calculated IR spectra of zwitterionic proline, anionic NAC, and the NAC–proline complex [IR intensities convoluted with a Lorentzian band shape ($\gamma = 10$ cm^{-1})] . The prominent vibrational bands of the corresponding species are labeled (see Table 1 for frequency calculation).

al complex vibrational modes, notably proline ν_s(–COO^-) + δ(–NH) + δ(–CH) and NAC ν_s(–COO^-) + δ(–CH).

As already mentioned above, the calculations strongly indicate that the interaction between anionic NAC and zwitterionic proline is largely determined by charge–charge interactions, that is attraction between the positive nitrogen of proline and the negative carboxylate of NAC, as well as repulsion between the negative carboxylates of proline and NAC (Figure 3). In an optimal arrangement of these charges, an additional intermolecular interaction is established, namely a proline–NH_2^+···OOC^-–NAC hydrogen bond. A direct comparison of the calculated and experimental spectra of the complex is difficult, since our experiments do not yield the direct experimental counterpart of the complex spectrum in Figure 6. What is experimentally accessible, via the proline concentration modulation over the NAC SAM (Figure 4, top, ——), is a superposition of 1) the spectrum of the complex on the surface (including changes of the NAC spectrum induced by complex formation) and 2) the spectrum of dissolved proline, the latter being considerably stronger. Still, a couple of observations support a complex structure as predicted by the DFT calculations (Figure 3): 1) The calculations predict a blue shift of the NAC amide I band upon complexation, as is observed in the experimental spectrum (band at 1674 cm^{-1} in Figure 4, top, ——). 2) The calculations predict a red shift in the proline carboxylate vibration ν_{as}(COO^-). The comparison between the ATR-IR spectrum of the dissolved proline (Figure 4, bottom, ——) and the demodulated spectrum of the "L-proline versus ethanol" modulation experiment (Figure 4, top, ——) reveals a broadening of the proline ν_{as}(COO^-) band at about 1637 cm^{-1} towards lower wavenumbers upon interaction with the NAC SAM. This shows that for the adsorbed species the ν_{as}(COO^-) has shifted to lower wavenumbers, as predicted by the calculations. 3) Upon complex formation, a rather dominant band is predicted in the spectral region of the ν_s(COO^-) bands of NAC and proline (calculated at about 1340 cm^{-1}, observed at about 1400 cm^{-1}) and that the ν_s(COO^-) bands are shifting to higher wavenumbers. The comparison between the ATR-IR spectrum of the dissolved proline (Figure 4, bottom, ——) and the demodulated spectrum of the "L-proline versus ethanol" modulation experiment (Figure 4, top, ——) indeed shows increased intensity slightly above 1400 cm^{-1}, thus supporting the calculated structure.

Finally, the absolute configuration modulation experiments (Figure 5) resulted in several dispersive bands in the spectrum due to frequency shifts, indicating that the position of the vibrational bands of the NAC–proline complex depends on the absolute configuration of proline. Note that the spectra in Figure 5, that is, the result of the absolute configuration modulation experiments, can be viewed as difference spectra between the NAC–D-proline and the NAC–L-proline complexes. The analogous difference spectrum can also be derived from the DFT calculations. The result of the vibrational analysis for the NAC–D-proline complex, denoted by "(D)" and the NAC-L-proline complex, denoted by "(L)" together with the corresponding difference spectrum (——, "L−D") is displayed in Figure 7. Note: the reason for calculating the difference spectrum in the order "(L)−(D)" and not "(D)−(L)" follows from the demodulated ATR-IR spectra of the "D versus L-proline" absolute configuration modulation experiment (starting with an inflow of D-proline) which showed maximum amplitude for demodulation phase angles ϕ_k^{PSD} around 170° (for demodulation angles differing by 180° the resulting demodulated spectra are identical, but for the sign of all absorption bands). At first glance, the calculated spectra of the (D) and (L) complex seem almost identical, but the resulting difference spectrum, scaled by a factor of five, clearly reveals significant dispersive bands that originate from slight frequency shifts of vibrational bands, notably in the region of 1560 to 1680 cm^{-1} and 1470 cm^{-1}. The former bands are related to proline ν_{as}(–COO^-) and δ_s(–NH_2) as well as NAC ν_{as}(–COO^-) and amide I bands, whereas the latter mainly originates from the NAC amide II vibrational band. The calculated frequency shifts between the bands of the NAC–D-proline and NAC–L-proline complexes are of the order of only one wavenumber for most of the important bands, and about four wavenumbers for the proline δ_s (–NH_2) scissoring mode. As can be further seen, the calculated frequency shift for the broad band between about 1250 and 1380 cm^{-1} containing complex modes is rather small. From the calculated difference spectrum in Figure 7 and the experimental counterpart, several interesting points emerge. The calculations clearly show that very small frequency shifts of the complex due to the change of the absolute configuration of proline result in significant dispersive and broad features in the corresponding difference spectrum. This means that absolute configuration modulation experiments, as performed here, are very sensitive to such small changes and are thus very sensitive to spotting small differences in diastereomeric interactions.

The dispersive bands in the region of 1650 cm^{-1} in the experimental spectrum imply a small shift in the proline ν_{as}(–COO^-) and δ_s(–NH_2) scissoring modes, as well as the NAC

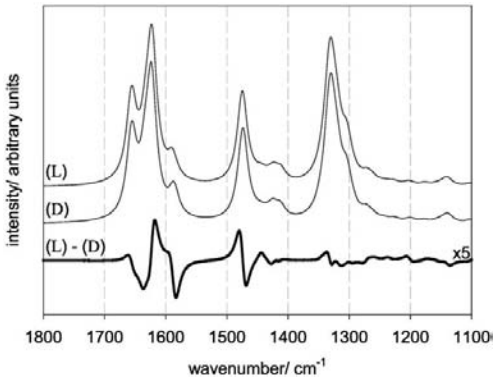

Figure 7. Top) Calculated vibrational spectra (of optimized structures from Figure 3) of NAC–D-proline ("D") and NAC–L-proline ("L") complexes [IR intensities convoluted with a Lorentzian band shape (γ = 10 cm^{-1})]. The assignment of the prominent vibrational bands is given in Figure 6. Bottom) Calculated difference (L)–(D) spectrum (——) between NAC–L-proline and NAC–D-proline complex (scaled by a factor of five). Note that the calculated difference spectrum is experimentally accessible by ATR-IR (Figure 5).

amide I mode, which is in good agreement with the calculations. Furthermore, the broad band at about 1540 cm^{-1} appearing in the experimental spectrum (Figure 5) is probably related to a shift of the NAC amide II band (see the NAC spectrum in Figure 4) which is also supported by the DFT calculations (dispersive band calculated at about 1470 cm^{-1} in Figure 7). Possibly the weak band around 1400 cm^{-1} in the experimental spectrum (Figure 5) is associated with a shift of the ν_s(–COO^-) carboxylate vibrations. A weak signal due to slight shifts of ν_s(–COO^-) is also predicted by the calculations. In summary, the calculations based on the complexes in Figure 3 are in qualitative agreement with experiment. In particular, the dispersive line pattern observed between 1550 and 1700 cm^{-1} is very well reproduced by the calculations.

It should be noted that the calculated structures in Figure 3 exhibit certain rigidity along the axis defined by the three charges (see Figure 3) due to the electrostatics. However, the complexes are certainly still rather flexible, as the interaction is basically a "one point interaction" (neglecting the surface). This flexibility is not included in the calculations, which rely on potential minima. The fact that the interaction is basically only a "one point interaction" is consistent with the very small calculated energy difference between the two diastereomeric complexes, which is also consistent with experiment. Still, even such weakly enantiodiscriminating interactions lead to detectable signals in the difference spectrum of the two diastereomeric complexes, as revealed by absolute configuration modulation.

A further interesting point is the comparison between SAMs of NAC and L-GSH with respect to enantiodiscrimination. As already mentioned in the Introduction, the GSH SAM was found to discriminate well between proline enantiomers, with D-proline being more strongly bound. The spectra furthermore indicated pronounced structural changes within the GSH SAM upon interaction with proline. In contrast, the NAC spectra revealed merely slight frequency shifts only, which indicates that the NAC conformation does not drastically change upon interaction. The reason for the better enantiodiscrimination of GSH may therefore be associated with its larger flexibility as compared to NAC.

Conclusions

The enantiodiscrimination between NAC self-assembled on gold (selector) and the analyte molecule proline (selectand, dissolved in ethanol) was probed by in situ ATR-IR MES. In particular, by modulating the absolute configuration of proline over the chiral SAM, the differences in the diastereomeric interactions between the enantiomers of the selectand and the selector can be spotted. The resulting demodulated spectra showed weak, but significant and characteristic, dispersive bands.

The ATR spectra of the NAC SAM, in the absence of proline, show that protonated and deprotonated (at the acid group) forms coexist on the surface. Whereas the protonated form is influenced by the presence of proline, only the deprotonated form leads to enantiodiscrimination. The spectral response in the absolute configuration modulation experiments was found to be very similar for SAMs that were assembled for only 1 min and SAMs that were assembled for 2 h, which points to a 1:1 interaction between proline and an adsorbed NAC molecule being responsible for the observed enantiodiscrimination rather than a supramolecular assembly of NAC molecules.

DFT calculations on the proline (zwitterionic)–NAC (anionic) complex showed that the Coulomb interaction between the charges on the two counterparts determines the structure of the complex together with a hydrogen bond between the NH_2 group of proline and the carboxylate of NAC. The vibrational analysis of the optimized structure of the complex, including solvent (ethanol) effects, revealed significant shifts in prominent vibrational bands upon interaction, notably of the amide, carboxylate, and NH_2 modes, which are consistent with the experimental observations. The calculated spectra of the two diastereomeric complexes between NAC and proline enantiomers were very similar, and the energy difference between the two complexes was only small. However, the difference spectrum still revealed significant dispersive bands, owing to slightly different band positions, of the order of only one to a few wavenumbers, for the two diastereomeric complexes. The dispersive bands in the difference spectrum were mainly related to shifts in the proline ν_{as}(–COO^-) and δ_s(–NH_2) scissoring, as well as the NAC amide vibrational bands. The calculated difference spectrum is directly comparable with the demodulated spectra obtained from an absolute configuration modulation experiment and qualitative agreement was observed. The calculations furthermore showed that the NAC–proline interaction is a "one point interaction", which explains the small energetic and spectral differences. These small differences can be spotted by absolute configuration modulation spectroscopy, since this technique selectively highlights differences and, as shown here, band shifts of the order of only one wavenumber result in significant dispersive bands in the difference spectrum between the two diastereomeric complexes.

Experimental Section

Chemicals: All the reagents, NAC (min. 99% TLC, Sigma–Aldrich Inc.), D- and L-proline (both > 99% Sigma–Aldrich, Inc.), were used as recieved. The solutions were prepared in ethanol (ethanol, Merck p.a.). Dissolved oxygen was removed by bubbling nitrogen gas (99.995%, CarbaGas) through the solutions before each ATR-IR measurement.

In Situ ATR-IR Spectroscopy: The IREs (Komlas) used for all ATR-IR experiments were 50 mm × 20 mm × 2 mm Ge trapezoids with an angle of incidence of 45°. The Ge IREs were polished with a 0.25 μm grain size diamond paste (Buehler, Metadi II) and afterwards rinsed copiously with ethanol before the surface was plasma-cleaned under a flow of air for 5 min (PlasmaPrep 2, Gala Instrumente). In a final step, a gold layer with a thickness of about 2 nm was sputtered onto the Ge IRE (Balzers Union SCD 030). For each ATR-IR experiment, a Ge IRE with a freshly prepared gold layer was used. Control experiments with a bare Ge IRE revealed no NAC adsorption during several hours of exposure to a corresponding solution.

Data Acquisition: The spectrometer used for ATR-IR measurements was a Bruker Equinox 55 Fourier transform infrared (FTIR) spectrometer equipped with a liquid-nitrogen-cooled narrow band mercury cadmium telluride (MCT) detector. The solutions, stored in separate bubble tanks, were introduced into a home-built liquid flow-through cell with a total volume of 0.077 mL leaving a gap of 250 μm between the IRE and the polished steel surface. A more detailed description of the ATR-IR cell can be found elsewhere.[33,45] All ATR-IR spectra reported herein were performed at room temperature (298 K) and were recorded with 4 cm^{-1} resolution at a 40 kHz sampling rate.

ATR-IR and Modulation Experiments: Typical ATR-IR (modulation) experiments started with an inflow of solvent (ethanol) over the gold-coated Ge IRE until no variation in the spectrum could be detected (after about 5 min). The corresponding background spectrum, recorded by co-adding 200 interferograms, served as the reference for all subsequent (modulation) experiments. In order to study the adsorption and self-assembling of NAC on gold, NAC dissolved in ethanol (about 0.6 mM for all ATR-IR measurements reported herein) was allowed to flow at 0.18 mL min^{-1} over the gold-coated Ge IRE. Spectral changes were followed in situ for up to two hours by recording spectra at time intervals of about 5 min. A solution ATR-IR spectrum of the analyte proline was obtained by performing a modulation experiment on a bare Ge IRE. The flow of L-proline dissolved in ethanol (0.04 M) during the first half period was replaced by an equally long flow of solvent (ethanol) during the second half period of the modulation experiment. An analogous modulation experiment was repeated with the gold-coated Ge IRE, in order to investigate the interaction of proline with the "bare" gold surface. For these modulation experiments, a period of $T = 120.7$ s at a flow rate of 0.5 mL min^{-1} was used. In order to study the intermolecular interactions between each of the two proline enantiomers and the NAC SAM, concentration modulation experiments were performed. D-proline (0.04 M) and ethanol were periodically flowed over the chiral NAC modified gold surface. An analogous modulation experiment was performed with the other enantiomer, L-proline, at the same concentration. These modulation experiments, denoted by "D(L)-proline versus ethanol", were performed using a modulation period of $T = 72.4$ s, and a flow rate of 0.5 mL min^{-1}. Finally, the enantioselective discrimination between the NAC SAM (selector) and the analyte molecule proline (selectand) was probed by an absolute configuration modulation experiment. In this experiment, denoted "D- versus L-proline", D- and L-proline (both at 0.04 M) were allowed to flow periodically over the NAC SAM, starting with an inflow of D-proline. Absolute configuration modulation experiments were performed using a modulation period of $T = 362.3$ s and a flow rate of 0.18 mL min^{-1}.

All of the modulation experiments reported herein consisted of two initial "dummy loops" to let the system reach a new, quasistationary state, followed by averaging over four measurement loops (periods). During one measurement period (loop), 60 infrared spectra were recorded at a 40 kHz sampling rate using the rapid scan acquisition mode of the FTIR spectrometer. For each spectrum, 6, 10, and 30 interferograms were averaged, resulting in modulation periods of $T = 72.4$, 120.7, and 362.3 s, respectively. A digital PSD according to Equation (1) was then used to transform a set of time-resolved spectra to phase-resolved spectra.

$$A_k^{\phi_k^{PSD}}(\tilde{\nu}) = \frac{2}{T}\int_0^T A(\tilde{\nu},t)\sin(k\omega t + \phi_k^{PSD})dt \qquad (1)$$

where $k = 1,2,3,\ldots$ determines the demodulation frequency, that is, fundamental, first harmonic, and so on; T is the modulation period; $\tilde{\nu}$ denotes the wavenumber; ω the stimulation frequency; and ϕ_k^{PSD} the demodulation phase angle. With a set of time-resolved spectra $A(\tilde{\nu},t)$, Equation (1) can be evaluated for different phase angles ϕ_k^{PSD} resulting in a series of phase-resolved spectra $A_k^{\phi_k^{PSD}}$. Only spectra demodulated at the fundamental frequency ($k = 1$) are reported here. A more detailed description of the modulation technique can be found elsewhere.[32,33,42]

DFT Calculations for *N*-Acetyl-L-cysteine and Proline: DFT calculations were performed using the hybrid functional B3PW91[46,47] with a 6–31G basis set.[48] GAUSSIAN03 was used for all calculations.[49] Solvent (ethanol) effects were accounted for by performing optimizations using a PCM.[50] Structure optimizations were performed for neutral (uncharged) NAC and the zwitterionic form of proline, since these prevail in ethanol. For reasons that are discussed in the Results and Discussion Section, structure optimization and vibrational analysis was also performed for NAC in the deprotonated state, that is, in the anionic form. Finally, the interaction complexes between NAC (anionic) and the two proline enantiomers were considered at the same level of theory. More computational details are given in the Results and Discussion Section.

Acknowledgements

Financial support from the Swiss National Science Foundation and grants of computer time from the Swiss National Supercomputing Centre (CSCS) Manno are gratefully acknowledged. The use of sputtering facilities at the Swiss Center for Electronics and Microtechnology in Neuchâtel (CSEM) is kindly acknowledged.

Keywords: chirality · density functional calculations · enantioselectivity · IR spectroscopy · self-assembly

[1] S. Ahuja, *Chiral Separations by Chromatography*, Oxford University Press, Washington, DC, **2000**.
[2] T. Bürgi, A. Baiker, *Acc. Chem. Res.* **2004**, *37*, 909.
[3] D. Y. Murzin, P. Maki-Arvela, E. Toukoniitty, T. Salmi, *Catal. Rev.—Sci. Eng.* **2005**, *47*, 175.
[4] C. F. McFadden, P. S. Cremer, A. J. Gellman, *Langmuir* **1996**, *12*, 2483.
[5] J. D. Horvath, A. J. Gellman, *J. Am. Chem. Soc.* **2002**, *124*, 2384.
[6] J. D. Horvath, A. Koritnik, P. Kamakoti, D. S. Sholl, A. J. Gellman, *J. Am. Chem. Soc.* **2004**, *126*, 14988.
[7] R. M. Hazen, D. S. Sholl, *Nat. Mater.* **2003**, *2*, 367.
[8] G. A. Attard, *J. Phys. Chem. B* **2001**, *105*, 3158.
[9] M. O. Lorenzo, C. J. Baddeley, C. Muryn, R. Raval, *Nature* **2000**, *404*, 376.
[10] M. O. Lorenzo, S. Haq, T. Bertrams, P. Murray, R. Raval, C. J. Baddeley, *J. Phys. Chem. B* **1999**, *103*, 10661.
[11] D. Ferri, T. Bürgi, *J. Am. Chem. Soc.* **2001**, *123*, 12074.
[12] N. Bonalumi, T. Bürgi, A. Baiker, *J. Am. Chem. Soc.* **2003**, *125*, 13342.
[13] M. Schunack, E. Laegsgaard, I. Steengaard, I. Johannsen, F. Besenbacher, *Angew. Chem.* **2001**, *113*, 2693; *Angew. Chem. Int. Ed.* **2001**, *40*, 2623.
[14] A. Kühnle, T. R. Linderoth, B. Hammer, F. Besenbacher, *Nature* **2002**, *415*, 891.
[15] K.-H. Ernst, Y. Kuster, R. Fasel, M. Müller, U. Ellerbeck, *Chirality* **2001**, *13*, 675.
[16] R. Fasel, J. Wider, C. Quitmann, K. H. Ernst, T. Greber, *Angew. Chem.* **2004**, *116*, 2913; *Angew. Chem. Int. Ed.* **2004**, *43*, 2853.
[17] D. S. Sholl, *Langmuir* **1998**, *14*, 862.
[18] D. Stacchiola, L. Burkholder, W. T. Tysoe, *J. Mol. Catal A: Chem.* **2004**, *216*, 215.
[19] P. Messina, A. Dmitriev, N. Lin, H. Spillmann, M. Abel, J. V. Barth, K. Kern, *J. Am. Chem. Soc.* **2002**, *124*, 14000.
[20] R. B. Rankin, D. S. Sholl, *Surf. Sci.* **2004**, *548*, 301.
[21] R. B. Rankin, D. S. Sholl, *Surf. Sci.* **2005**, *574*, L1.

[22] R. B. Rankin, D. S. Sholl, *J. Phys. Chem. B* **2005**, *109*, 16764.
[23] R. McKendry, M.-E. Theoclitou, T. Rayment, C. Abell, *Nature* **1998**, *391*, 566.
[24] T. Nakanishi, N. Yamakawa, T. Asahi, T. Osaka, B. Ohtani, K. Uosaki, *J. Am. Chem. Soc.* **2002**, *124*, 740.
[25] K. Bodenhöfer, A. Hierlemann, J. Seemann, G. Gauglitz, B. Koppenhoefer, W. Göpel, *Nature* **1997**, *387*, 577.
[26] R. M. Hazen, T. R. Filley, G. A. Goodfriend, *Proc. Nat. Acad. Sci. USA* **2001**, *98*, 5487.
[27] D. A. M. Zaia, *Amino Acids* **2004**, *27*, 113.
[28] M. Kauranen, T. Verbiest, J. J. Maki, A. Persoons, *J. Chem. Phys.* **1994**, *101*, 8193.
[29] J. M. Hicks, T. Petralli-Mallow, *Appl. Phys. B: Lasers Opt.* **1999**, *68*, 589.
[30] I. Yagi, M. Chiba, K. Uosaki, *J. Am. Chem. Soc.* **2005**, *127*, 12743.
[31] N. J. Harrick, *Internal Reflection Spectroscopy*, Interscience Publishers, New York, **1967**.
[32] D. Baurecht, U. P. Fringeli, *Rev. Sci. Instrum.* **2001**, *72*, 3782.
[33] T. Bürgi, A. Baiker, *J. Phys. Chem. B* **2002**, *106*, 10649.
[34] R. Wirz, T. Bürgi, A. Baiker, *Langmuir* **2003**, *19*, 785.
[35] R. Wirz, T. Bürgi, W. Lindner, A. Baiker, *Anal. Chem.* **2004**, *76*, 5319.
[36] B. Ohtani, A. Shintani, K. Uosaki, *J. Am. Chem. Soc.* **1999**, *121*, 6515.
[37] T. Nakanishi, N. Yamakawa, T. Asahi, N. Shibata, B. Ohtani, T. Osaka, *Chirality* **2004**, *16*, S36.
[38] M. Bieri, T. Bürgi, *J. Phys. Chem. B* **2005**, *109*, 10243.
[39] T. Helgaker, E. Eggerud, H. J. A. Jensen, *Chem. Phys. Lett.* **1990**, *173*, 145.
[40] M. Dewar, W. Thiel, *J. Am. Chem. Soc.* **1977**, *99*, 4499.
[41] M. Bieri, T. Bürgi, *J. Phys. Chem. B* **2005**, *109*, 10243.
[42] M. Bieri, T. Bürgi, *Langmuir* **2005**, *21*, 1354.
[43] E. M. Marti, C. Methivier, C. M. Pradier, *Langmuir* **2004**, *20*, 10223.
[44] A. Pintar, R. Malacea, C. Pinel, G. Fogassy, M. Besson, *Appl. Catal. A* **2004**, *264*, 1.
[45] A. Urakawa, R. Wirz, T. Bürgi, A. Baiker, *J. Phys. Chem. B* **2003**, *107*, 13061.
[46] A. D. Becke, *J. Chem. Phys.* **1993**, *98*, 5648.
[47] J. P. Perdew, J. A. Chevary, S. H. Vosko, K. A. Jackson, M. R. Pederson, D. J. Singh, C. Fiolhais, *Phys. Rev. B* **1992**, *46*, 6671.
[48] R. Ditchfield, W. J. Hehre, J. A. Pople, *J. Chem. Phys.* **1971**, *54*, 724.
[49] M. J. Frisch, G. W. Trucks, H. B. Schlegel, G. E. Scuseria, M. A. Robb, J. R. Cheeseman, J. A. Montgomery, T. Vreven, K. N. Kudin, J. C. Burant, J. M. Millam, S. S. Iyengar, J. Tomasi, V. Barone, B. Mennucci, M. Cossi, G. Scalmani, N. Rega, G. A. Petersson, H. Nakatsuji, M. Hada, M. Ehara, K. Toyota, R. Fukuda, J. Hasegawa, M. Ishida, T. Nakajima, Y. Honda, O. Kitao, H. Nakai, M. Klene, X. Li, J. E. Knox, H. P. Hratchian, J. B. Cross, C. Adamo, J. Jaramillo, R. Gomperts, R. E. Stratmann, O. Yazyev, A. J. Austin, R. Cammi, C. Pomelli, J. W. Ochterski, P. Y. Ayala, K. Morokuma, G. A. Voth, P. Salvador, J. J. Dannenberg, V. G. Zakrzewski, S. Dapprich, A. D. Daniels, M. C. Strain, O. Farkas, D. K. Malick, A. D. Rabuck, K. Raghavachari, J. B. Foresman, J. V. Ortiz, Q. Cui, A. G. Baboul, S. Clifford, J. Cioslowski, B. B. Stefanov, G. Liu, A. Liashenko, P. Piskorz, I. Komaromi, R. L. Martin, D. J. Fox, T. Keith, M. A. Al-Laham, C. Y. Peng, A. Nanayakkara, M. Challacombe, P. M. W. Gill, B. Johnson, W. Chen, M. W. Wong, C. Gonzalez, J. A. Pople, Rev. C.01 ed., Gaussian, Inc., Wallingford CT, **2003**.
[50] M. T. Cancès, B. Mennucci, J. Tomasi, *J. Chem. Phys.* **1997**, *107*, 3032.

Received: August 26, 2005

Part IV

Catalysis

Preface

The investigation of catalytic reactions by *in situ* or *operando* spectroscopy is a promising strategy to obtain molecular-level information on the transformation of reactants into products and on the state of the catalyst under working conditions. Nevertheless, it is a difficult and challenging task, and the difficulty is even more pronounced in heterogeneous catalysis, where the reaction occurs at the solid–gas or solid–liquid interface. The complexity of these interfaces arises due to species, *e.g.* solvent and support, that are not directly related to a reaction. These so-called spectators may give rise to strong signals and hamper detection of important reaction intermediates or even lead to misinterpretation of spectroscopic results. Thus, to determine whether a species is an intermediate or a spectator requires more sophisticated methods.
It has been demonstrated that ATR-IR in combination with modulation excitation spectroscopy (MES) is a powerful tool to overcome these problems. MES, that is the periodic stimulation of the catalyst sample and phase-sensitive detection of the response significantly increases sensitivity, helps to disentangle complex spectra and catch reaction intermediates at the catalytic interface.

The following chapter reports on 2-propanol oxidation over Pd/Al_2O_3 investigated by ATR-MES combined with online UV-vis spectroscopy. By admitting dissolved oxygen and hydrogen the catalyst was driven fast between oxidized and reduced states and the response of the catalytic interface was followed in time with the goal of catching intermediates. Besides the oxidation product acetone and water that forms, when hydrogen and oxygen are simultaneously adsorbed on the catalyst surface, 2-propoxide was detected as reaction intermediate. The assignment of the latter was further confirmed by density functional theory (DFT) calculations.

Chapter 1

Time-Resolved *in Situ* ATR Spectroscopy of 2-Propanol Oxidation over Pd/Al_2O_3: Evidence for 2-Propoxide Intermediate

Thomas Bürgi and Marco Bieri

Published in J. Phys. Chem. B, Volume 108(35), pp. 13364–13369, doi: 10.1021/jp048187u, 2004.

13364 *J. Phys. Chem. B* **2004,** *108,* 13364−13369

Time-Resolved in Situ ATR Spectroscopy of 2-Propanol Oxidation over Pd/Al_2O_3: Evidence for 2-Propoxide Intermediate

Thomas Bürgi* and Marco Bieri

Institut de Chimie, Faculté des Sciences, Université de Neuchâtel, Rue Emilie-Argand 11, 2007-Neuchâtel, Switzerland

Received: April 26, 2004; In Final Form: June 15, 2004

In situ attenuated total reflection infrared spectroscopy in a flow-through cell combined with online UV−vis spectroscopy was used to investigate the oxidation of 2-propanol over Pd/Al_2O_3 catalyst. The state of the catalyst was driven fast between reduced and oxidized by admitting alternately dissolved hydrogen and oxygen, and the response of the catalytic solid−liquid interface was followed in time. Besides the oxidation product acetone and the water that forms, when hydrogen and oxygen are simultaneously adsorbed on the catalyst surface, an additional species was observed with a characteristic band at ∼1065 cm^{-1}. On the basis of the transient character of the adsorbate and density functional theory calculations, we assign this species to adsorbed 2-propoxide. Its observation indicates that the second dehydrogenation step is rate limiting in an oxidative dehydrogenation mechanism. The results furthermore show that adsorbed hydrogen and oxygen limit the dissociative adsorption of 2-propanol and that 2-propoxide can be hydrogenated back to the reactant in the presence of adsorbed hydrogen.

Introduction

The investigation of heterogeneous catalytic reactions by in situ or operando spectroscopy is a promising strategy to obtain molecular level information on the transformation of reactants into products and on the state of the catalyst under working conditions. The driving force for such research is, besides pure curiosity, the hope that a rigorous understanding of the reaction mechanism helps the rational design of better catalyst materials and processes. Development of spectroscopic techniques that can be applied in situ is currently making progress.[1,2]

A big challenge for in situ spectroscopy in heterogeneous catalysis is related to the complexity of the relevant interfaces. Pure observation of a species at a working catalytic interface does not a priori reveal its importance in the reaction mechanism. To determine whether a species is an intermediate or a spectator requires more effort. On the other hand, identification of the nature of reaction intermediates is perhaps the most direct way to uncover the reaction mechanism. Unfortunately, such intermediates are not easily observable due to their usually short lifetime and low abundance. One way to "catch" intermediates is the sudden change of a reaction parameter. For example, an intermediate in the hydrogenation of ethylene over Pt/Al_2O_3 was observed at the solid−gas interface after a short pulse of the reactant.[3] This intermediate, which was assigned to ethyl, had a lifetime of around 100 ms.

We have recently applied attenuated total reflection (ATR) infrared spectroscopy[4] to study catalytic solid−liquid interfaces, which proved to be a sensitive tool for the investigation of model[5−7] and real powder catalysts.[8,9] The combination with modulation excitation spectroscopy,[10] that is, the periodic stimulation of the catalyst sample and phase-sensitive detection of the response, further increases sensitivity and helps to disentangle complex spectra of the catalytic solid−liquid interface.[8] Applying relatively fast concentration stimulation at a solid−liquid interface in order to "catch" intermediates is limited by convection and diffusion processes in the fluid. Still, relatively fast stimulation is possible when using a carefully designed low volume flow-through cell.[11]

In this paper we use ATR to investigate the oxidation of 2-propanol to acetone by oxygen over a Pd/Al_2O_3 catalyst. By admitting dissolved hydrogen and oxygen, the Pd catalyst is switched fast between two states and the response of the catalytic interface is followed in time with the goal of catching intermediates. The evolution of the reaction product is traced by both ATR infrared and online UV spectroscopies.

Selective oxidation of alcohols over noble metal catalysts proceeds under mild conditions and is an attractive synthetic route for fine chemical production.[12−14] The reaction was proposed to proceed via a dehydrogenation mechanism:[12,15] The alcohol adsorbs on the metal catalyst and is dehydrogenated in two subsequent steps. The resulting adsorbed aldehyde or ketone is then desorbing. The role of the oxygen is the oxidation of adsorbed hydrogen. Support for this view stems from the observation that during reaction the catalyst surface is covered by hydrogen, even in the presence of oxygen.[16−19] Furthermore, an isotope effect was found for α-deuterated and nondeuterated 2-propanol.[16] Another proposed pathway involves a direct reaction between the adsorbed substrate and adsorbed oxygen.[20] Although direct spectroscopic information on the catalyst solid−liquid interface during alcohol oxidation has been reported recently,[21,22] reaction intermediates on the catalyst surface have not been identified up to now.

Experimental Section

Catalyst and Chemicals. A 5% Pd/Al_2O_3 catalyst (Johnson Matthey, Type 324) was used. Before measurements the catalyst

* Corresponding author. Telephone: ++41 32 718 24 12. Fax: ++41 32 718 25 11. E-mail: thomas.burgi@unine.ch.

10.1021/jp048187u CCC: $27.50
Published on Web 08/10/2004

was reduced in situ by hydrogen. 2-Propanol (Merck p.a.) was used as supplied. Nitrogen (99.995%), hydrogen (99.995%), and oxygen (99.998%) gases (CarbaGas) were used to saturate the solvents.

Thin Film Preparation. A slurry of the catalyst powder was prepared from about 20 mg of catalyst and 5 mL of 2-propanol. Films of the catalyst powder were prepared by dropping the slurry onto a ZnSe internal reflection element (IRE; 52 × 20 × 2 mm, KOMLAS). The solvent was allowed to evaporate, and the procedure was repeated totally three times. After drying for several minutes at 50 °C in air, loose catalyst particles were removed by flowing 2-propanol over the IRE. After drying in air the film was ready for use. The amount of catalyst exposed to the solvent was between 1 and 1.5 mg.

In Situ Spectroscopy. ATR spectra were recorded using a home-built stainless steel flow-through cell with a volume of 0.077 mL and a gap between IRE and polished steel surface of the cell of 250 μm.[8] The cell has two inlets, which allows the rapid change between two different fluids at the entrance of the flow compartment. The cell was mounted on an attachment for ATR measurements (Wilks Scientific) within the sample compartment of a Bruker EQUINOX-55 Fourier transform infrared (FT-IR) spectrometer equipped with a narrow band MCT detector. Spectra were recorded at 4 cm^{-1} resolution. The ATR cell can be cooled or heated; however, all measurements reported here were performed at room temperature. The ATR cell corresponds to the one described in more detail elsewhere.[11] In addition to the previously reported setup, the ATR cell effluent was directly coupled into a home-built UV−vis flow-through cell. This cell consists of two stainless steel tees connected by a Teflon tube. The light from a deuterium halogen source (Avantes) is guided to one end of the cell via an optical fiber. The transmitted light is collected at the other end of the cell and coupled into a second optical fiber, which guides the light to an UV−vis spectrometer (Avantes) equipped with a 2024 pixel CCD detector array and a resolution of 2.4 nm. Typical integration time for one spectrum is 10 ms. The path length of the UV−vis transmission cell is 4 cm. The solvent was saturated with gases in two separate glass bubble tanks and was flowed through the cells and over the sample by means of a peristaltic pump (ISMATEC, Reglo 100) located after the UV−vis cell. The flow rate was varied between 0.85 and 2.7 mL/min. Two pneumatically actuated three-way Teflon valves (PARKER PV-1-2324) were used to control the solvent flow from the two tanks. Stainless steel tubing was used. A schematic setup of the experiment is given in Figure 1.

Modulation Excitation Spectroscopy and Data Acquisition. The catalytic system was stimulated by periodically admitting 2-propanol saturated with hydrogen and oxygen. During one modulation period (flow of hydrogen-saturated 2-propanol followed by an equally long flow of oxygen-saturated 2-propanol), 60 and 20 infrared spectra, respectively, were recorded at 80 kHz sampling rate using the rapid scan acquisition mode of the FT-IR spectrometer. For each spectrum several scans were averaged. Several modulation periods (5−30) were applied before data acquisition was started. Infrared spectra were then averaged over several periods (5−60). UV−vis spectra of the cell effluent were recorded simultaneously and synchronized with IR spectra acquisition. Before every scan of the IR spectrometer the UV−vis spectrometer was triggered to record one scan. As for the IR several scans were averaged such that for one modulation period a total of 60 and 20 spectra, respectively, were obtained. In contrast to the IR the UV−vis spectra were not directly averaged over the modulation periods.

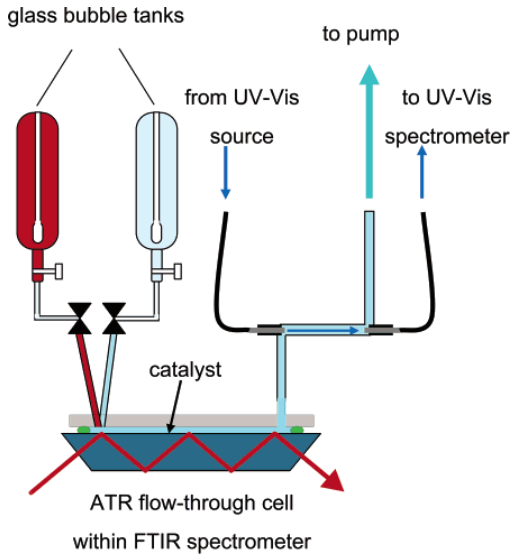

Figure 1. Schematic setup of the in situ attenuated total reflection (ATR) experiment with online fiber optics UV−vis analysis of reaction products.

Time-resolved IR and UV−vis spectra were also demodulated using a digital phase-sensitive detection according to eq 1:

$$A_k^{\phi_k^{PSD}}(\tilde{\nu}) = \frac{2}{T}\int_0^T A(\tilde{\nu},t)\sin(k\omega t + \phi_k^{PSD})\,dt \qquad (1)$$

$$k = 1, 2, \ldots$$

Here $\tilde{\nu}$ is the wavenumber, ω is the stimulation frequency, T is the modulation period, and ϕ_k^{PSD} is the demodulation phase angle. With one set of time-resolved spectra eq 1 can be evaluated for different phase angles ϕ_k^{PSD}, resulting in a series of phase-resolved absorbance spectra. The quantity k determines the frequency at which the time-dependent signals $A(\tilde{\nu},t)$ (IR or UV−vis) are demodulated, i.e., the fundamental of the stimulation frequency ($k = 1$), first harmonic ($k = 2$), and so on. A more detailed description of the modulation technique applied here can be found elsewhere.[8,23]

Typically experiments were performed as follows: 2-Propanol in the two glass bubble tanks was saturated with nitrogen before one tank was saturated with hydrogen and one with oxygen. Hydrogen-saturated 2-propanol was then flowed first over the sample for 10 min. Afterward the flow was changed between hydrogen- and oxygen-saturated 2-propanol five times (each flow for about 1 min). After that treatment modulation experiments were started. Several consecutive modulation experiments were performed with the same catalyst layer. The catalyst layer was however freshly prepared every day.

Results

Figure 2 shows different ATR spectra (not demodulated). Spectrum a was recorded during a modulation experiment when switching from hydrogen- to oxygen-saturated 2-propanol. Spectra b and c were recorded while flowing acetone in 2-propanol (saturated with nitrogen) over the bare IRE and over the IRE coated with catalyst, respectively. Spectrum d is an ATR spectrum of 2-propanol. Comparing spectrum a with spectra b and c allows identification of the oxidation product acetone in the spectra recorded in situ (Figure 2a). Specifically, strong bands in the ATR-IR spectra marked with open circles

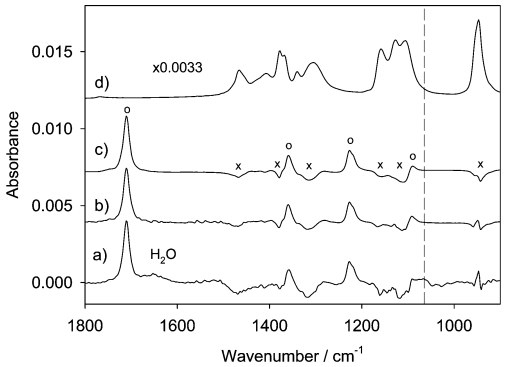

Figure 2. (a) ATR spectrum recorded during a modulation experiment (modulation period $T = 180$ s, flow rate 0.85 mL/min). The spectrum was recorded in the transient period while changing from hydrogen- to oxygen-saturated 2-propanol. The reference was recorded while flowing hydrogen-saturated 2-propanol. Spectra b and c were recorded while flowing acetone dissolved in 2-propanol over the clean IRE and the IRE covered with catalyst, respectively. The reference for spectra b and c was recorded while flowing 2-propanol over the clean IRE and the IRE covered with catalyst, respectively. Spectrum d shows an ATR spectrum of 2-propanol (background empty ATR cell). Open circles (○) indicate the most prominent bands associated with dissolved acetone. Crosses (×) mark regions of strong 2-propanol absorption. The dashed vertical line indicates a band that belongs neither to 2-propanol nor to acetone.

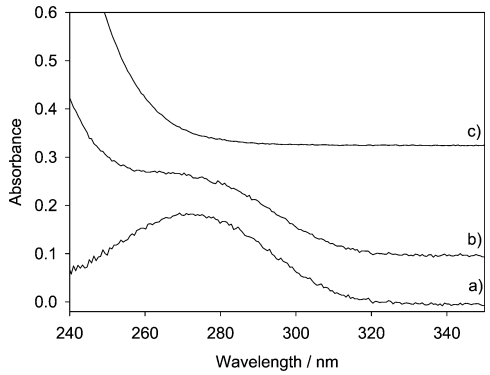

Figure 3. (a) UV spectrum of acetone in 2-propanol recorded with the online UV−vis spectrometer schematically shown in Figure 1. (b) UV spectrum recorded online during the transient period while changing from hydrogen- to oxygen-saturated 2-propanol (for conditions see Figure 2). (c) UV spectrum recorded online while flowing oxygen-saturated 2-propanol. The reference for spectra b and c was recorded while flowing hydrogen-saturated 2-propanol.

are associated with dissolved acetone. The negative signals marked with crosses are due to 2-propanol. When acetone is formed (Figure 2a) or admitted to the cell (Figure 2b,c), the concentration of 2-propanol slightly decreases, leading to negative signals. Besides the oxidation product acetone and the negative signals due to 2-propanol, two other features are evident in spectrum a recorded in situ: a broad band associated with water at ∼1650 cm^{-1} and a feature at 1065 cm^{-1} (dashed vertical line), which are associated neither with acetone nor with 2-propanol. Water forms in the transient period when both hydrogen and oxygen are adsorbed. The nature of the species associated with the band at 1065 cm^{-1} will be discussed below.

In the UV−vis spectra shown in Figure 3 acetone gives rise to a band centered at 270 nm. Figure 3a is the UV spectrum of a solution of acetone in 2-propanol. Spectra b and c were recorded online, with spectrum b in the transient period while changing from hydrogen- to oxygen-saturated 2-propanol and spectrum c while flowing oxygen-saturated solvent. The reference for spectra b and c was hydrogen-saturated 2-propanol. The prominent signal below 260 nm arises due to dissolved oxygen.

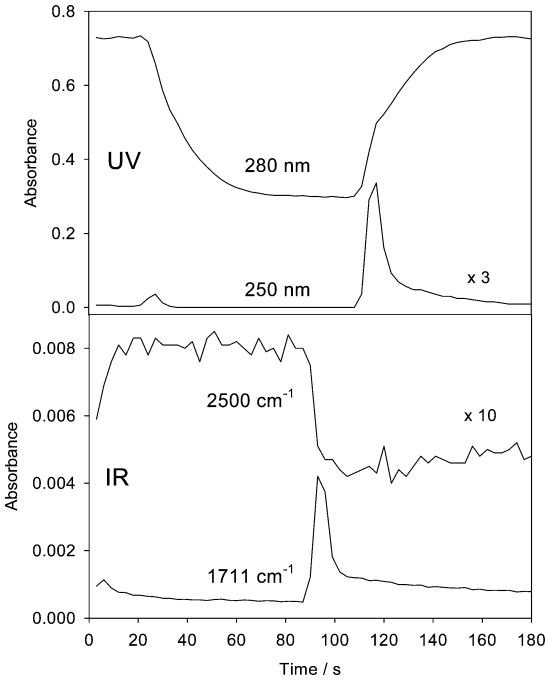

Figure 4. Selected ATR and UV signals as a function of time for a modulation experiment with a modulation period of 180 s and flow rate of 0.85 mL/min (60 spectra/period). At $t = 0$ the flow at the entrance of the ATR cell was switched from oxygen- to hydrogen-saturated 2-propanol. At $t = 90$ s ($T/2$) the flow was switched back to oxygen-saturated 2-propanol. The ATR signals were averaged over five modulation periods, whereas the UV signal was not averaged and represents only one out of the five cycles. Note that the signals in the UV are retarded with respect to the ones observed in the ATR-IR, since the UV spectra are recorded at the outlet of the ATR cell (see Figure 1).

Figure 4 shows the time dependence of some signals in the IR and UV. The absorbance at 1711 cm^{-1} is associated with the strongest signal of acetone in the infrared. The absorbance at 2500 cm^{-1}, which is far from any strong molecular absorption, reflects the change in the catalyst state. It has been shown recently that the Pd catalyst itself responds to the oxidative and reductive conditions. This results in a broad absorption in the ATR spectra over the whole mid-infrared region due to the changes in the optical constants of the strongly absorbing Pd when the latter changes its state.[22] Also shown is the absorbance in the UV at 280 (acetone) and 250 nm (oxygen). The maximum absorbance in the UV−vis corresponds to an acetone concentration of 0.0024 mol/L, as determined by comparison with solutions of known concentration. The corresponding value for the ATR is 0.0104 mol/L. The discrepancy is due to the fact that the acetone is formed within the catalyst layer, which is selectively probed by the ATR. Note that at a volumetric flow rate of 0.85 mL/min, as applied in the experiment shown in Figure 4, the mean residence time in the ATR cell is only 5.4 s. Figure 4 reveals that acetone is predominantly formed when changing from hydrogen- to oxygen-saturated 2-propanol. Considerably less acetone is formed when changing from oxygen to hydrogen.

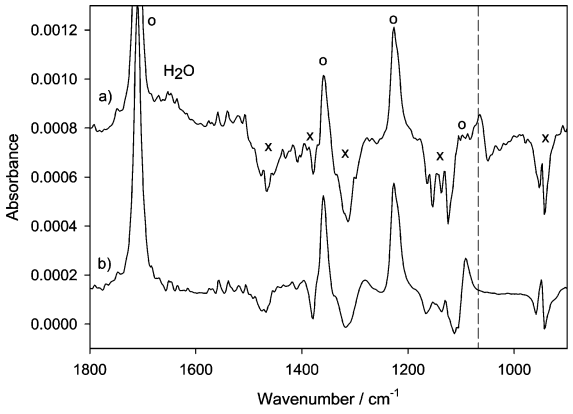

Figure 5. (a) Demodulated ATR spectrum of a modulation experiment. Modulation period $T = 12$ s; flow rate 2.7 mL /min. At $t = 0$ the flow at the entrance of the ATR cell was switched from oxygen- to hydrogen-saturated 2-propanol. At $t = 6$ s ($T/2$) the flow was switched back to oxygen-saturated 2-propanol. The signal was averaged over 20 periods with 20 spectra/period. The time-resolved spectra were then demodulated according to eq 1. For comparison a (time-resolved) spectrum is shown (trace b) that was recorded while flowing acetone dissolved in 2-propanol over the IRE covered with catalyst. Open circles (○) indicate the most prominent bands associated with dissolved acetone. Crosses (×) mark regions of strong 2-propanol absorption. The dashed vertical line indicates a band that belongs neither to 2-propanol nor to acetone.

Figure 5a shows a demodulated ATR spectrum for a fast modulation experiment (hydrogen−oxygen−hydrogen..., $T =$ 12 s). For comparison a (time-resolved) spectrum, recorded while flowing acetone dissolved in 2-propanol over the catalyst, is shown in Figure 5b. Careful inspection of the two spectra reveals a band at 1065 cm^{-1} for spectrum a, which is missing in spectrum b. Figure 6 reveals that the species associated with the band at 1065 cm^{-1} has a time dependence similar to the one of the reaction product acetone. Figure 2 shows that this band is not associated with dissolved or adsorbed acetone. Also, 2-propanol (Figure 2) does not have absorption bands at this frequency, which could lead to signals due to incomplete compensation. Besides the band at 1065 cm^{-1}, the ones associated with acetone and water, and the features associated with 2-propanol, no other signals with a similar time dependence could be observed.

A possible intermediate in the oxidation reaction is adsorbed 2-propoxide. Indeed, alkoxide species on metal surfaces exhibit strong C−O stretching vibrations in the frequency range between 1000 and 1100 cm^{-1}.[24−28] For 2-propoxide on Ni(100) a band at ∼1090 cm^{-1}, which was assigned to the C−O stretching vibration, is the most prominent feature in the frequency range between 1000 and 1600 cm^{-1}.[28] To corroborate the assignment of the band observed in our spectra at 1065 cm^{-1} to a 2-propoxide intermediate, we have performed density functional theory (DFT) calculations for both 2-propanol and 2-propoxide on Pd. The calculations were performed with Gaussian03.[29] The b3pw91 hybrid functional[30] was used with a 6-31G(d,p)[31] basis set for C, O, and H and LANL2DZ[32] for Pd. The Pd surface was replaced by three Pd atoms in order to simulate adsorption on 3-fold sites. This simple approach is expected to yield qualitative information concerning adsorbate vibrations, since the latter are relatively insensitive to cluster size, in contrast to other properties such as adsorption energies.[33] Figure 7 shows an ATR spectrum of liquid 2-propanol together with the calculated spectra for 2-propanol and 2-propoxide on Pd. A comparison between experimental and calculated spectra for 2-propanol reveals general good agreement with the exception

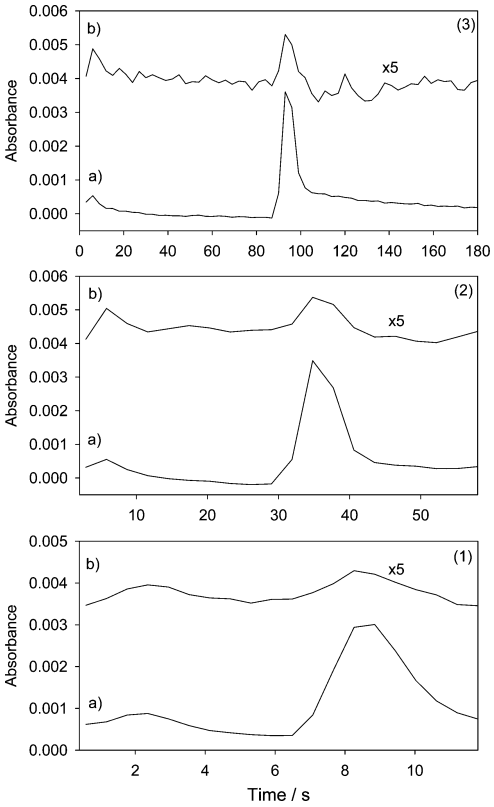

Figure 6. ATR signals as a function of time of (a) acetone (1711 cm^{-1} band) and (b) the species associated with the band at 1065 cm^{-1} for different modulation experiments (hydrogen-, oxygen-, hydrogen-saturated 2-propanol). (1) $T = 12$ s, flow rate 2.7 mL/min, averaged over 60 periods, 20 spectra/period. (2) $T = 58$ s, flow rate 0.85 mL/min, averaged over five periods, 20 spectra/period. (3) $T = 180$ s, flow rate 0.85 mL/min, averaged over five periods, 60 spectra/period.

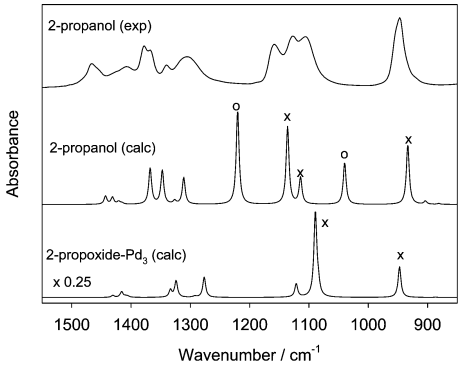

Figure 7. ATR spectrum of 2-propanol, together with calculated infrared spectra for 2-propanol and 2-propoxide on Pd. The b3pw91 method was used with a 6-31G(d,p) basis set for C, O, and H and LANL2DZ for Pd. The calculated infrared intensities were convoluted with a Lorentzian line shape. Calculated frequencies were scaled by a factor of 0.95 in order to account for the overestimation of the fundamental vibrational frequencies due to the neglect of anharmonicity, electron correlation, and basis set effect.[37] Open circles (○) indicate bands containing C−O−H bending character. Crosses (×) indicate bands with C−O stretching character (see text for more details).

of the two modes calculated at 1219 and 1040 cm^{-1} that contain C−O−H bending character. These modes are strongly affected by intermolecular interactions in the liquid state. This result is

in agreement with a previous report.[34] The three modes at 932, 1114, and 1136 cm^{-1} all contain significant C−O stretching character. The 2-propoxide species has a different spectrum. Besides the disappearance of the C−O−H bending modes, the modes containing C−O stretching character are affected. Most of the C−O stretching intensity is now condensed in a mode with a frequency calculated slightly below 1090 cm^{-1}, which becomes by far the strongest band in this frequency region. This mode is red-shifted compared to the corresponding modes in 2-propanol. Based on the calculated spectra of 2-propanol and 2-propoxide, we would expect a strong signal of 2-propoxide due to a C−O vibration red-shifted by 25−45 cm^{-1} with respect to the corresponding bands in 2-propanol. In the experimental spectrum of liquid 2-propanol the corresponding bands are found slightly above 1100 cm^{-1}. Therefore, the observed band at 1065 cm^{-1} in the ATR spectra recorded during reaction is consistent with a 2-propoxide adsorbed on Pd. Figure 7 reveals that a 2-propoxide species should also exhibit signals due to C−H modes. However, these signals are difficult to observe, since the corresponding frequency range is crowded by vibrations due to 2-propanol and acetone.

Discussion

In situ ATR spectroscopy of the catalytic solid−liquid interface combined with online UV−vis analysis of the reaction products, as schematically shown in Figure 1, proved to be a powerful tool for time-resolved investigations. Figure 4 shows that the signal of the reaction product acetone in the UV is delayed by 21 s with respect to the corresponding ATR-IR signal. This delay is caused by the flow of the fluid from the ATR to the UV cell. The full width at half-maximum of the two signals is 8.5 s in the ATR and 10 s in the UV, respectively, reflecting a fast response of the combined system.

Besides the reaction product acetone that is observed in the infrared and the UV spectra and some water that is formed from hydrogen and oxygen on the Pd surface, another band at 1065 cm^{-1} is observed that has the same time dependence as the reaction product. Based on control experiments, which show that this band is associated with neither adsorbed acetone nor 2-propanol, DFT calculations, and comparison with previously reported spectra of 2-propoxide, we assign the band to 2-propoxide adsorbed on Pd. Figure 6 furthermore shows that the 1065 cm^{-1} band is associated with a transient species. We should also note that this band was not observed for similar experiments in the absence of 2-propanol.

Our experiments strongly indicate that 2-propoxide is an intermediate in the oxidation of 2-propanol to acetone. Hence the initial step in the oxidation of the alcohol is its dissociative adsorption, which leads to adsorbed alkoxide and hydrogen. This step requires free surface sites. Not surprisingly the rate of product formation is coupled to the abundance of the intermediate on the catalyst surface. When the abundance of the intermediate on the surface is high, the product can be observed. In the presence of dissolved hydrogen the catalyst surface is covered with hydrogen, thus preventing dissociative adsorption of the alcohol. In the presence of oxygen under our conditions the Pd surface is covered by oxygen. This state is referred to as "over-oxidized" and also prevents dissociative adsorption of the alcohol.[35,36] In our experiments the 2-propoxide abundance had a maximum between the two extreme states of the catalyst surface. The change between the two states of the catalyst is sharp in our experiments and can be followed via the broad absorption over the whole mid-infrared region (Figure 4, signal at 2500 cm^{-1}) due to the slight alteration of the optical constants of the strongly absorbing metal particles.[22] In this transient period, stimulated by changing the dissolved gas, adsorbed hydrogen and oxygen react to water, which is also observed in our experiment (band at ∼1650 cm^{-1}, Figures 2 and 5). This opens up free sites on the catalyst surface, onto which the alcohol can dissociatively adsorb. Note that the reaction between oxygen and hydrogen on the catalyst surface also takes place under conditions where the hydrogen is not supplied externally, since the dissociative adsorption of the alcohol also leads to adsorbed hydrogen.

The results presented above strongly indicate that the key to high activity of the catalyst is its ability to dissociatively adsorb the alcohol reactant. This is in agreement with experimental observations that identify the concentration of oxygen as critical reaction parameter.[12,19] A delicate balance between dissociative adsorption of the reactant and the adsorption of oxygen is crucial for high activity. If the concentration of oxygen on the surface gets too high, the rate of dissociative adsorption of the alcohol decreases, due to fewer available sites. As a consequence, less hydrogen is available on the surface, which can react with adsorbed oxygen, and fewer sites are freed for the further adsorption of the reactant. The catalyst runs into an "over-oxidized" state.

Both acetone and 2-propoxide are detected when changing between oxygen and hydrogen and vice versa. However, Figure 6 reveals that the relative amount of the two species is different in the two cases. When changing from oxygen to hydrogen only a little acetone is formed, whereas the signal assigned to the 2-propoxide intermediate is still relatively strong. This holds for different conditions (flow rates, modulation periods), as Figure 6 shows. This means that not all the adsorbed intermediate is transformed to product and that the fraction that is transformed is higher when switching from hydrogen to oxygen. An explanation for this behavior is the back-reaction of 2-propoxide to 2-propanol in the presence of hydrogen on the surface. The importance of this reaction channel is different for the two transient periods (hydrogen → oxygen and oxygen → hydrogen). Support for this view comes from the fastest modulation experiment reported in Figure 6 (bottom), which indicates that the maximum of the 2-propoxide signal is sightly shifted toward the hydrogen-rich region of the transient periods with respect to the signal of the acetone product. Hence, too much hydrogen on the surface not only blocks adsorption sites for the dissociative adsorption of the alcohol but also promotes the reaction of the alkoxide intermediate back to the alcohol reactant.

The observation of an alkoxide species in the ATR spectra shows that this species is relatively abundant on the catalyst surface and therefore strongly indicates that the second dehydrogenation step, which yields adsorbed acetone, is rate limiting. This is in agreement with the observed isotope effect for the oxidation rate of α-deuterated and nondeuterated 2-propanol.[16]

Conclusions

The combination of attenuated total reflection (ATR) infrared spectroscopy in a low volume flow-through cell with online UV−vis analysis of the reaction product is well suited to following fast changes taking place at a catalytic solid−liquid interface. Application of the technique to the oxidation of 2-propanol over a Pd/Al_2O_3 catalyst allows the simultaneous observation of (1) dissolved reaction product acetone (by ATR and UV), (2) changes of the state of the Pd catalyst induced by adsorption of hydrogen and oxygen, respectively, and (3) adsorbed species at the catalytic interface. In transient experiments an adsorbed species can be observed in the ATR spectra

simultaneously with acetone formation. Based on the transient character of the species and density functional theory calculations, it is assigned to 2-propoxide intermediate. The intermediate is observed when both hydrogen and oxygen are present on the catalyst, which leads to the formation of water and frees up sites for the dissociative adsorption of the 2-propanol. The ratio between 2-propoxide and acetone is different when changing the dissolved gas from hydrogen to oxygen or vice versa, which indicates that the intermediate can be hydrogenated back to the reactant favored by high hydrogen coverage. The concentration of oxygen is decisive for fast oxidation. At too high oxygen concentration no free sites are available for the dissociative adsorption of the alcohol (the catalyst is "over-oxidized"); at too low oxygen concentration the surface coverage of hydrogen is large and blocks adsorption sites and furthermore promotes the hydrogenation of the alkoxide intermediate. The observations support an oxidative dehydrogenation mechanism and indicate that the second dehydrogenation step is rate limiting. The results furthermore reveal the importance of transient methods for the investigation of reaction intermediates and that such experiments are feasible also at solid−liquid interfaces, where response is usually limited by diffusion.

Acknowledgment. Grants of computer time by the Swiss National Supercomputer Centre in Manno and financial support by the Swiss National Science Foundation are kindly acknowledged.

References and Notes

(1) Weckhuysen, B. M. *J. Chem. Soc., Chem. Commun.* **2002**, 97.
(2) Weckhuysen, B. M. *In Situ Spectroscopy of Catalysts*; American Scientific Publishers: San Diego, CA, 2004.
(3) Ko, M. K.; Frei, H. *J. Phys. Chem. B* **2004**, *108*, 1805.
(4) Harrick, N. J. *Internal reflection spectroscopy*; Interscience Publishers: New York, 1967.
(5) Ferri, D.; Bürgi, T.; Baiker, A. *J. Phys. Chem. B* **2001**, *105*, 3187.
(6) Ferri, D.; Bürgi, T. *J. Am. Chem. Soc.* **2001**, *123*, 12074.
(7) Bonalumi, N.; Bürgi, T.; Baiker, A. *J. Am. Chem. Soc.* **2003**, *125*, 13342.
(8) Bürgi, T.; Baiker, A. *J. Phys. Chem. B* **2002**, *106*, 10649.
(9) Gisler, A.; Bürgi, T.; Baiker, A. *Phys. Chem. Chem. Phys.* **2003**, *5*, 3539.
(10) Baurecht, D.; Fringeli, U. P. *Rev. Sci. Instrum.* **2001**, *72*, 3782.
(11) Urakawa, A.; Wirz, R.; Bürgi, T.; Baiker, A. *J. Phys. Chem. B* **2003**, *107*, 13061.
(12) Besson, M.; Gallezot, P. *Catal. Today* **2000**, *57*, 127.
(13) Mallat, T.; Baiker, A. *Catal. Today* **1994**, *19*, 247.
(14) Vinke, P.; deWit, D.; deGoede, A. T. J. W.; vanBekkum, H. In *New Developments in Selective Oxidation by Heterogeneous Catalysis*; Ruiz, P., Delmon, B., Eds.; Elsevier: Amsterdam, 1992; Vol. 72; p 1.
(15) Heyns, K.; Paulsen, H. *Angew. Chem.* **1957**, *69*, 600.
(16) Cosimo, R. D.; Whitesides, G. M. *J. Phys. Chem.* **1989**, *93*, 768.
(17) Müller, E.; Schwabe, K. *Z. Elektrochem. Angew. Phys. Chem.* **1928**, *34*, 170.
(18) Mallat, T.; Bodnar, Z.; Baiker, A. In *Catalytic Selective Oxidation*; Oyama, S. T., Hightower, J. W., Eds.; American Chemical Society: Washington, DC, 1993; Vol. 523, p 308.
(19) Mallat, T.; Baiker, A. *Catal. Today* **1995**, *24*, 143.
(20) Tillaart, J. A. A. v. d.; Kuster, B. F. M.; Marin, G. B. *Appl. Catal. A: Gen.* **1994**, *120*, 127.
(21) Keresszegi, C.; Bürgi, T.; Mallat, T.; Baiker, A. *J. Catal.* **2002**, *211*, 244.
(22) Bürgi, T.; Wirz, R.; Baiker, A. *J. Phys. Chem. B* **2003**, *107*, 6774.
(23) Wirz, R.; Bürgi, T.; Baiker, A. *Langmuir* **2003**, *19*, 785.
(24) Yee, A.; Morrison, S. J.; Idriss, H. *J. Catal.* **1999**, *186*, 279.
(25) Shorthouse, L. J.; Roberts, A. J.; Raval, R. *Surf. Sci.* **2001**, *480*, 37.
(26) Stacchiola, D.; Burkholder, L.; Tysoe, W. T. *J. Mol. Catal A: Chem.* **2004**, *216*, 215.
(27) Davis, J. L.; Barteau, M. A. *Surf. Sci.* **1990**, *235*, 235.
(28) Zaera, F.; Guevremont, J. M.; Gleason, N. R. *J. Phys. Chem. B* **2001**, *105*, 2257.
(29) Frisch, M. J.; Trucks, G. W.; Schlegel, H. B.; Scuseria, G. E.; Robb, M. A.; Cheeseman, J. R.; Montgomery, J. A.; Vreven, T.; Kudin, K. N.; Burant, J. C.; Millam, J. M.; Iyengar, S. S.; Tomasi, J.; Barone, V.; Mennucci, B.; Cossi, M.; Scalmani, G.; Rega, N.; Petersson, G. A.; Nakatsuji, H.; Hada, M.; Ehara, M.; Toyota, K.; Fukuda, R.; Hasegawa, J.; Ishida, M.; Nakajima, T.; Honda, Y.; Kitao, O.; Nakai, H.; Klene, M.; Li, X.; Knox, J. E.; Hratchian, H. P.; Cross, J. B.; Adamo, C.; Jaramillo, J.; Gomperts, R.; Stratmann, R. E.; Yazyev, O.; Austin, A. J.; Cammi, R.; Pomelli, C.; Ochterski, J. W.; Ayala, P. Y.; Morokuma, K.; Voth, G. A.; Salvador, P.; Dannenberg, J. J.; Zakrzewski, V. G.; Dapprich, S.; Daniels, A. D.; Strain, M. C.; Farkas, O.; Malick, D. K.; Rabuck, A. D.; Raghavachari, K.; Foresman, J. B.; Ortiz, J. V.; Cui, Q.; Baboul, A. G.; Clifford, S.; Cioslowski, J.; Stefanov, B. B.; Liu, G.; Liashenko, A.; Piskorz, P.; Komaromi, I.; Martin, R. L.; Fox, D. J.; Keith, T.; Al-Laham, M. A.; Peng, C. Y.; Nanayakkara, A.; Challacombe, M.; Gill, P. M. W.; Johnson, B.; Chen, W.; Wong, M. W.; Gonzalez, C.; Pople, J. A. *Gaussian03*, Rev. B.05 ed.; Gaussian, Inc.: Pittsburgh, PA, 2003.
(30) Becke, A. D. *J. Chem. Phys.* **1993**, *98*, 5648.
(31) Ditchfield, R.; Hehre, W. J.; Pople, J. A. *J. Chem. Phys.* **1971**, *54*, 724.
(32) Hay, P. J.; Wadt, W. R. *J. Chem. Phys.* **1985**, *82*, 270.
(33) Neurock, M. *Top. Catal.* **1999**, *9*, 135.
(34) Uvdal, P.; MacKerell, A. D.; Wiegand, B. C.; Friend, C. M. *Phys. Rev. B* **1995**, *51*, 7844.
(35) vanDam, H. E.; Kieboom, A. P. G.; vanBekkum, H. *Appl. Catal.* **1987**, *33*, 361.
(36) Dijkgraaf, P. J. M.; Rijk, M. J. M.; Meuldijk, J.; Wiele, K. v. d. *J. Catal.* **1988**, *112*, 329.
(37) Scott, A. P.; Radom, L. *J. Phys. Chem.* **1996**, *100*, 16502.

Part V

Appendix

Appendix A

Modeling the Flow-Field within the ATR-IR Flow Reactor

For the investigation of chemical reactions at solid–liquid interfaces, reactant concentration modulation seems to be particularly promising. However, for fast concentration modulation, mass transport of dissolved molecules from the bulk phase to the solid–liquid interface has to be considered. In this case, the concentration at the interface may vary significantly not only with time, but also in space. To correctly extract and quantify the kinetics of the chemical step such as adsorption or surface reaction (see Appendix B on page 123) from concentration modulation experiments, mass transport within the ATR-IR flow-through reactor has to be accounted for.

In section A.1, a model based on finite element method (FEM) implemented in Comsol Multiphysics [COMSOL, 1994–2006, Zimmerman, 2004] is presented that was used to simulate the flow-field within the ATR-IR reactor. Refer to Chapter 2, Subsection 2.2.3 on page 11 for a description of the ATR-IR experimental setup.

A.1 The 3D Fluid-Flow Model

In a moving fluid, mass balance of a solute species in the bulk is described by the convection–diffusion equation [Bird et al., 1960]:

$$\frac{\partial c}{\partial t} = -(\mathbf{v} \cdot \nabla c) + D\,\nabla^2 c \tag{A.1}$$

where c denotes the bulk concentration of a solute species and D is the diffusion coefficient. Note that the convective term on the right hand side in Equation A.1 depends on the fluid velocity $\mathbf{v}$.

In order to study the flow-field within the ATR-IR chemical reactor, a FEM model using the real three-dimensional geometry was developed. Figure A.1 on the following page shows the geometry used for the 3D fluid-flow model. In order to reduce computing time and thanks to Comsol Multiphyiscs' unique features to handle symmetry, only half of the ATR-IR flow reactor geometry was used for modeling. At the circular inlet tube (boundary denoted by an arrow in Figure A.1) fully developed laminar flow was assumed.

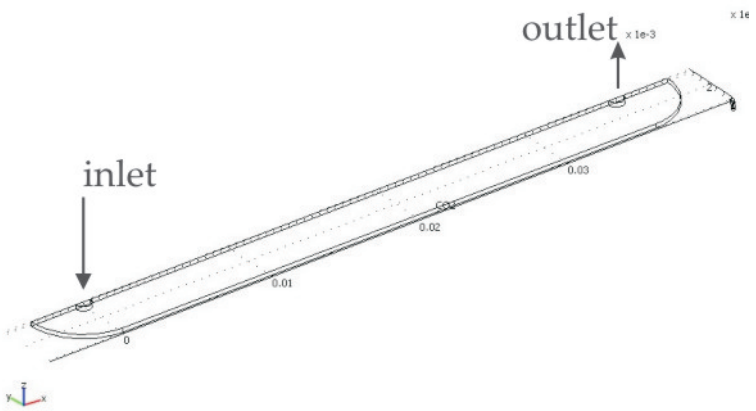

Figure A.1: Three-dimensional geometry of the ATR-IR flow reactor used for the fluid-flow model. The arrows denote the position of the in- and outlet, respectively.

Steady-state momentum balance yields the following analytical expression for the flow through a circular tube [Bird et al., 1960]:

$$u(r) = u_{\max}\left[1 - \left(\frac{r}{R}\right)^2\right] \tag{A.2}$$

where r is the distance from the center of the circular cross section, R is the radius of the inlet tube and $u_{\max}$ is the maximum inflow velocity. The latter is related to the volumetric flow rate ϕ_V by the following expression:

$$u_{\max} = 2\,\langle u\rangle = 2\,\frac{\phi_V}{A} \tag{A.3}$$

where $\langle u\rangle$ is the average flow velocity and $A = \pi R^2$ is the cross sectional area of the circular tube. It should be noted that Equation A.3 is valid only for flow through a circular tube.

The domain equation defined over the three-dimensional geometry shown in Figure A.1 is expressed by the famous Navier–Stokes equation that assumes isothermal flow of an incompressible Newtonian fluid [Bird et al., 1960]:

$$\rho\,\frac{\mathrm{D}}{\mathrm{D}t}\mathbf{v} = -\nabla p + \mu\nabla^2\mathbf{v} + \rho\mathbf{g} \tag{A.4}$$

In Equation A.4, ρ and μ denote the fluid density and dynamic viscosity, respectively, p is the pressure and $\rho\mathbf{g}$ is the external force per unit volume. The time-derivative $\mathrm{D}\,(\mathrm{D}t)^{-1}$ of the fluid velocity $\mathbf{v}$ is the *substantial time derivative*, defined as:

$$\frac{\mathrm{D}}{\mathrm{D}t}\mathbf{v} = \frac{\partial\mathbf{v}}{\partial t} + (\mathbf{v}\cdot\nabla\mathbf{v}) \tag{A.5}$$

Table A.1 on the facing page summarizes the parameters used for the model.

Symbol	Value	Unit	Comments
$u_{\max}$	2.1	$\mathrm{cm\,s^{-1}}$	Maximum inflow velocity corresponding to a volumetric flow rate of $\phi_V = 0.5\,\mathrm{mL\,min^{-1}}$. Typically used for modulation experiments.
ρ	789	$\mathrm{kg\,m^{-3}}$	Density of ethanol (at 20°C).[a]
μ	$1.2 \cdot 10^{-3}$	Pa s	Dynamic viscosity of ethanol (at 20°C).[a]

[a] Physical quantities taken from CRC Handbook of Chemistry and Physics, 84th edition.

Table A.1: Parameters used for the 3D fluid-flow model.

The model was solved in incompressible Navier–Stokes application mode using a stationary, nonlinear solver (UMFPACK). Ethanol (EtOH) is a widely used solvent (*e.g.* to investigate self-assembled monolayers) and the corresponding properties were taken for the model (see Table A.1). Model outputs are presented in the next section.

A.2 Model Results

The calculated flow-field (represented by the vector $\mathbf{v}$) within the ATR-IR flow reactor is presented and discussed by different cross section plots. The cross section plots refer to the reference orientation of the modeled geometry (see coordinate system on the left side at the bottom in Figure A.1 on the facing page). Specifically, the x-axis points along the direction of flow. The $x-y$ plane defines the surface boundary of the internal reflection element (IRE) and the z-axis points along the surface normal.

Figure A.2 on page 121 shows a cross section plot of the x-component (v_x) of the flow-field along the z-axis, *i.e.* between the IRE surface at $z = 0$ and the steel surface at $z = 265\,\mu$m. The velocity distribution shows the well-known and expected parabolic profile for flow between two parallel plates and is further an indication for laminar flow under the applied conditions. Laminar flow conditions are further confirmed by a calculated Reynold's number (Re) of about 2.5 within the cell, which is well below the turbulent regime (Re around 2100, [Bird et al., 1960]).

Figure A.3 on page 121 shows cross section plots of the y-component (top) and the x-component (bottom) of the flow-field calculated along the direction of flow (x-axis, see also Figure A.1 on the preceding page for the orientation) in the center of the cell between inlet and outlet (indicated by vertical dashed lines). The flow profile indicates a large homogenous flow-field between the in- and outlet. Expected variations are visible in the vicinity of the in- and outlets due to the in- and outflow of the fluid. However, the y-component is nearly zero and the x-component constant between in- and outlet, indicating a homogeneous flow-field. Variations in the flow-field with an almost stagnating flow behind the in- and outlet were further observed experimentally [Urakawa et al., 2003].

In conclusion, the fluid-flow model predicts well defined flow conditions within the ATR-IR flow cell for a commonly used flow rate of $\phi_V = 0.5\,\mathrm{mL\,min^{-1}}$, which is a prerequisite for the quantification of chemical reactions at the solid–liquid interface. The model further allows one to assess the maximum velocity of the moving fluid within the cell. In the present case, a maximum velocity of about $7.3\,\mathrm{mm\,s^{-1}}$ can

be expected for a flow rate of 0.5 $\mathrm{mL\,min^{-1}}$. Due to the calculated homogeneous flow-field, the 3D fluid-flow model finally legitimizes the use of a simplified geometry. In fact, Urakawa et al. [2003] showed in previous work that mass transport of solute molecules can successfully be described by convection and diffusion using a reduced two-dimensional geometry. In the next chapter, an advanced model based on FEM will be presented that further couples adsorption, surface diffusion and desorption to transport of species to the surface.

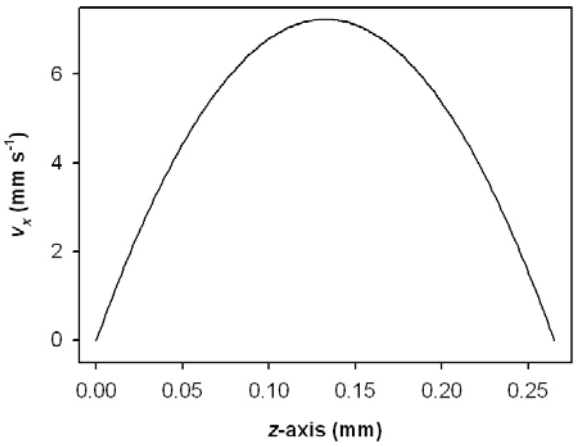

Figure A.2: Calculated velocity profile of the x-component of the flow-field along the z-axis.

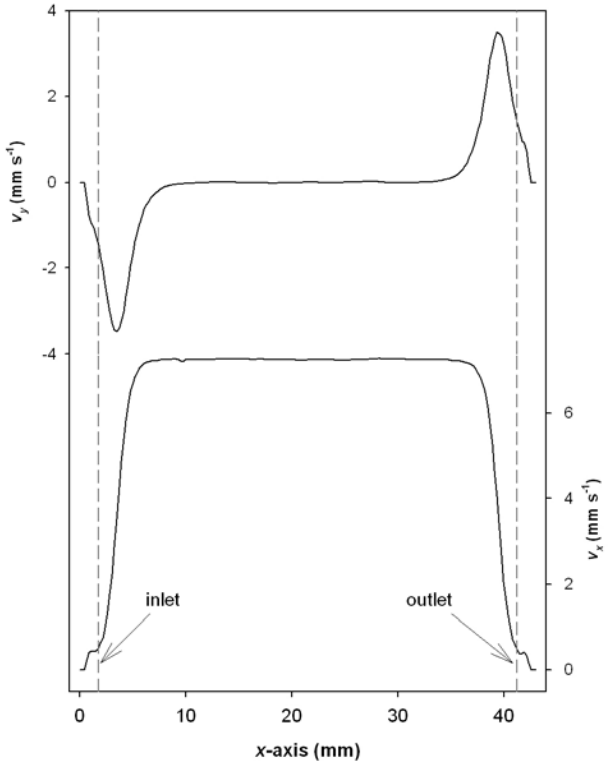

Figure A.3: Calculated flow-field between the in- and outlet (indicated by vertical dashed lines). The velocity profile was calculated along the x-axis in the center (*i.e.* at $y = 1.75\,\text{mm}$ and $z = 132.5\,\mu\text{m}$) of the ATR-IR flow reactor. The y-component of the flow-field is depicted on top and the velocity profile of the x-component at the bottom.

Appendix B

Modeling Mass Transport and Surface Reactions

The FEM model presented in the following uses a simplified, two-dimensional geometry of the ATR-IR flow reactor and couples adsorption, surface diffusion and desorption to mass transport of solute species to the surface. The model allows one to quantitatively assess adsorption and desorption kinetics from experimental data, fully accounting for mass transport within the flow-through reactor.

B.1 The 2D Transport and Adsorption Model

Figure B.1 on the following page shows the definition of the transport and adsorption model. The domain between in- and outlet has an orthorhombic geometry with an overall length of $L = 36\,\mathrm{mm}$, a width $w = 7\,\mathrm{mm}$ and a height of $h = 265\,\mu\mathrm{m}$ (distance between IRE and steel surface). Furthermore, the x-axis points in direction of flow and the $x{-}y$ plane defines the (IRE) surface boundary. In order to reduce the geometry to two dimensions, the y-axis was omitted and the domain equations were defined in the $x{-}z$ plane.

The following assumptions/simplifications were made for the transport and adsorption model:

- Laminar flow.
- Incompressible Newtonian fluid.
- Because of the reduced, two-dimensional geometry (z denotes the direction perpendicular to the surface and x the direction of the flow within the cell), there are no concentration variations in the y-direction and no velocity variations in the x- or y-direction.
- Interaction between solute molecules is neglected.

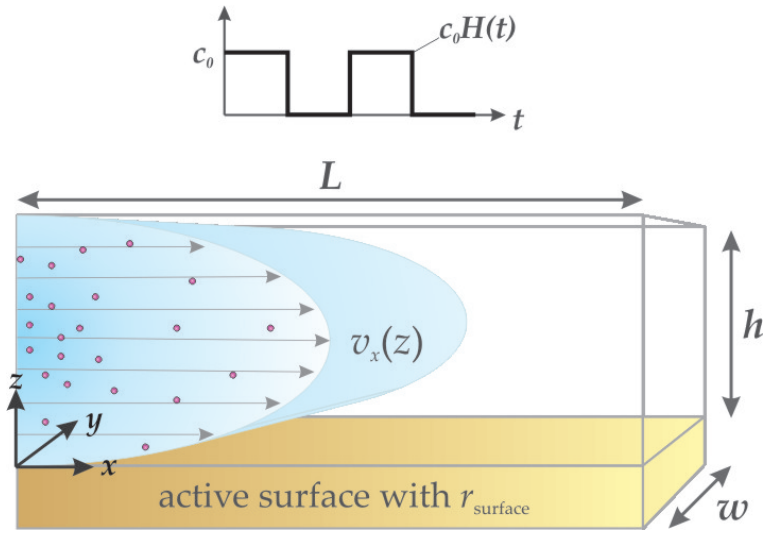

Figure B.1: Definition of the transport and adsorption model.

Steady-state momentum balance for laminar flow between two parallel plates yields the following velocity profile which can be expressed in terms of the volumetric flow rate ϕ_V [Bird et al., 1960]:

$$v_x(z) = \frac{6\phi_V}{wh^3}(hz - z^2) \tag{B.1}$$

where w is the width and h the height of the simplified 2D flow-through cell geometry. Mass balance of solute species in the bulk is then expressed by the convection–diffusion equation:

$$\frac{\partial c}{\partial t} = -v_x(z)\,\frac{\partial c}{\partial x} + D\left(\frac{\partial^2 c}{\partial x^2} + \frac{\partial^2 c}{\partial z^2}\right) \tag{B.2}$$

The flux of the solute species in the bulk is expressed by

$$J = v_x(z)\,c - D\left(\frac{\partial c}{\partial x} + \frac{\partial c}{\partial z}\right) \tag{B.3}$$

where c denotes the bulk concentration of the solute molecules and D is the diffusion coefficient.
On the surface boundary (see Figure B.1), the following reaction rate is defined:

$$r_{\text{surface}} = \frac{\mathrm{d}\theta}{\mathrm{d}t} = -k_{\text{ads}}\,c\,\theta + k_{\text{des}}\,c_s \tag{B.4}$$

In Equation B.4, θ is the surface concentration of active sites, c_s is the concentration of adsorbed molecules and k_{ads} and k_{des}, respectively, denote the rate constants for adsorption and desorption, respectively. It should be noted that the surface reaction rate described by Equation B.4 corresponds to the well-known first-order Langmuir model [Langmuir, 1918].

In the first term on the right hand side in Equation B.4 on the facing page, the surface concentration of active sites θ can be written as the difference between the total number of active sites θ_0 and the surface concentration c_s of adsorbed molecules leading to

$$r_{\text{surface}} = \frac{\mathrm{d}\theta}{\mathrm{d}t} = -k_{\text{ads}}\, c\,(\theta_0 - c_s) + k_{\text{des}}\, c_s \tag{B.5}$$

The mass balance for the surface, including surface diffusion and the surface reaction rate given by Equation B.5 is:

$$\frac{\partial c_s}{\partial t} = D_s \frac{\partial^2 c_s}{\partial x^2} + k_{\text{ads}}\, c\,(\theta_0 - c_s) - k_{\text{des}}\, c_s \tag{B.6}$$

where D_s is the surface diffusion coefficient.

The following initial and boundary conditions hold for the transport and adsorption model:

Initial conditions:

$$0 \leq x \leq L, \quad 0 \leq z \leq h \tag{B.7}$$

$$c(t=0) = c_0, \quad c_s(t=0) = 0 \tag{B.8}$$

where L denotes the length between the in- and outlet and h the height of the cell. The initial bulk concentration of solute species at $t = 0$ is denoted by c_0.

Boundary conditions:
On the reactive surface, *i.e.* at $z = 0$, the boundary condition for the bulk couples the surface reaction rate with the flux of reactive species according to:

$$J = v_x(z)\, c - D\left(\frac{\partial c}{\partial x} + \frac{\partial c}{\partial z}\right) = -k_{\text{ads}}\, c\,(\theta_0 - c_s) + k_{\text{des}}\, c_s \tag{B.9}$$

Other boundary conditions are:

$$z = h, \quad J = 0 \tag{B.10}$$

$$\text{inlet}\,(x=0), \quad c = c_0\, H(t) \tag{B.11}$$

$$\text{outlet}\,(x=L), \quad J = v_x(z)\, c \tag{B.12}$$

In boundary condition B.11, the concentration modulation $H(t)$ is represented by a smoothed Heaviside function (see also Figure B.1 on the preceding page for a pictorial representation of the concentration modulation).

Table B.1 on the following page summarizes the parameters used for the 2D transport and adsorption model. The model was solved using COMSOL Multiphysics' unique feature, that is the coupling of phenomena defined in different geometric dimensions.

Symbol	Comments
ϕ_V	Volumetric flow rate.
c_0	Initial bulk concentration of solute species.
ω	Modulation frequency.
D	Bulk diffusion coefficient.
D_s	Surface diffusion coefficient.
θ_0	Total number of active sites for adsorption, expressed in terms of moles per unit surface.
k_{ads}	Rate constant of adsorption. *Tunable parameter.*
k_{des}	Rate constant of desorption. *Tunable parameter.*

Table B.1: Parameters for the 2D transport and adsorption model.

In the present case, convection–diffusion, defined in a 2D domain was coupled to surface reactions defined at the 1D boundary of the 2D domain. More information can be found in the software manual. The 2D transport and adsorption model was finally used to calculate the bulk concentration c of solute species at the surface boundary, *i.e.* at $z = 0$, and the surface concentration c_s of adsorbed molecules, fully accounting for mass transport within the flow-through cell. Since, in an ATR-IR experiment, the measured signal is integrated over the IRE at the interface, the corresponding model outputs of c and c_s, respectively, were integrated over the surface boundary accordingly.

B.2 Model Results

The discussion of model results in this section is twofold. First, model results will be presented that are related to an active surface with an arbitrary large number of active adsorption sites. These model results have rather demonstrative character. The second type of results to be discussed are related to enantiodiscrimination between an L-glutathione (GSH) self-assembled monolayer (SAM) and proline (see also Part III, Chapter 1 on page 81). The model was successfully applied to extract the different rate constants of adsorption/desorption of proline enantiomers on/from the GSH SAM [Bieri and Bürgi, 2005a].

B.2.1 Surface with Large Number of Active Sites for Adsorption

Figure B.2 on the facing page shows a surface plot of the bulk concentration within the defined 2D domain. The plot was calculated eight seconds after an inflow of dissolved molecules ($c_0 = 0.3$mM) over an active surface with an arbitrary large amount of active sites for adsorption θ_0. Furthermore, the rate constant for desorption k_{des} was set to zero, which is reasonable for thiol adsorption on gold. As can be seen from Figures B.2 and B.3, the applied conditions lead to the formation of a so-called depletion layer in the vicinity of the active surface. Figure B.2, and the corresponding cross section plot along the distance from A. to B. depicted in Figure B.3, clearly show that the bulk concentration rapidly falls off at the surface. That is, the surface consumes molecules from the bulk and depletes the concentration at the interface.

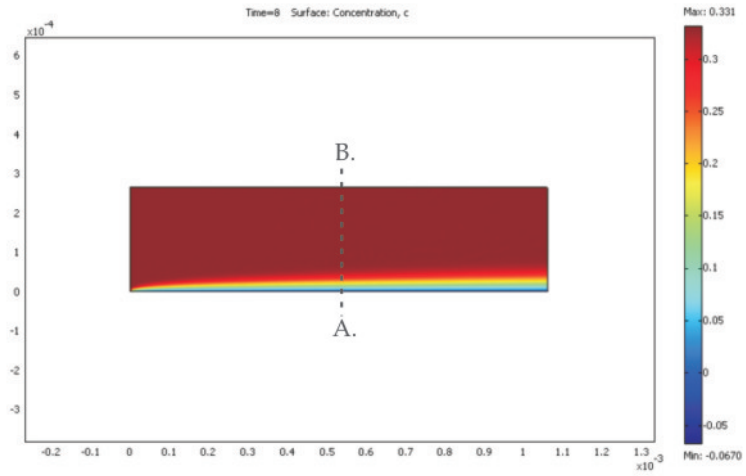

Figure B.2: Surface plot of bulk concentration in the 2D domain eight seconds after a flow of dissolved molecules (0.3 mM) over an active surface with an arbitrary large amount of active sites for adsorption. The vertical dashed line between A. and B. refers to the cross section plot of the bulk concentration depicted in Figure B.3.

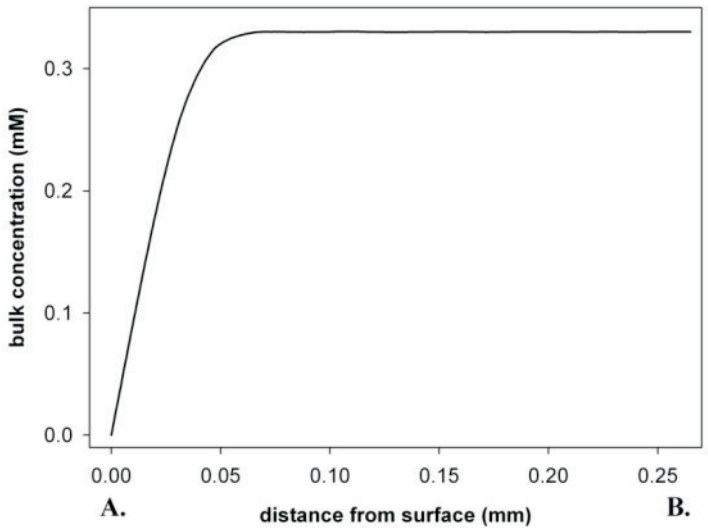

Figure B.3: Cross section plot of bulk concentration in direction from A. to B. (see Figure B.2).

This effect is particularly observed in stagnant fluids at low bulk concentration and/or elevated adsorption rates. In order to get adsorbed on the surface, molecules first have to overcome the depletion layer by diffusion, which finally limits the overall surface reaction rate. Diffusion limitation is mathematically accounted for by the first-order Langmuir diffusion-limited adsorption model [Peterlinz and Georgiadis, 1996, Rahn and Hallock, 1995].

B.2.2 Enantiodiscrimination between an L-Glutathione Self-Assembled Monolayer and Proline

Finally, and most importantly, the transport and adsorption model was successfully applied to assess intrinsic rate constants of adsorption and desorption, respectively, from experimental data. A brief discussion of the model outputs from a rather technical perspective is given in this section and a more detailed (spectroscopic) interpretation of the results is found in Part III, Chapter 1 on page 81.

In order to learn more about L-glutathione (GSH)–proline enantiodiscriminating intermolecular interactions, "EtOH vs. D(L)-proline" modulation experiments were performed. In this type of modulation experiments, EtOH and the proline enantiomers were allowed to periodically flow over the chiral GSH SAM while ATR-IR spectra were recorded *in situ*. The time dependence of selected ATR-IR signals is depicted in Figure B.4 on the next page where thin solid lines refer to L-proline and thin dashed lines to D-proline. The signals on top refer to bulk species, *i.e.* represent the concentration variation of dissolved proline at the interface, whereas the signals at the bottom are related to variation in surface concentration due to adsorption/desorption of proline on/from the GSH SAM. In other words, the signals on top are forced by convection–diffusion and the signals at the bottom, on the other hand, reflect adsorption and desorption kinetics, respectively.

In order to fit the experimental data and to quantitatively assess adsorption/desorption kinetics, the applied conditions were taken as fixed model parameters (see also Table B.1 on page 126), notably a flow rate of $\phi_V = 0.18\,\mathrm{mL\,min^{-1}}$, an initial concentration $c_0 = 4.3\,\mathrm{mM}$ and a modulation frequency $\omega = 2.8\,\mathrm{mHz}$. Furthermore, the total number of active sites θ_0 was assumed to be $10^{15}\,\mathrm{molecules\,cm^{-2}}$. The diffusion coefficient of solute species (proline in this case) was estimated according to the Stokes–Einstein equation [Robinson and Stokes, 1965]:

$$D = \frac{kT}{6\pi\mu a} \approx 3.7 \cdot 10^{-6}\,\mathrm{cm^2\,s^{-1}} \tag{B.13}$$

where $\mu = 1.2 \cdot 10^{-3}\,\mathrm{Pa\,s}$ is the dynamic viscosity of EtOH and a is the radius of the solute molecule approximated as a sphere. The sphere radius of proline was derived from DFT calculations and taken as $a \approx 5$ Å. The surface diffusion coefficient D_s was further estimated to be three orders of magnitude smaller than the bulk diffusion coefficient D. Finally, k_{ads} and k_{des} were used as tunable parameters.

As can be seen from Figure B.4, the model captures the different system responses of the bulk phase and surface well (smooth bold solid lines are model outputs). That is, the curves on top are the calculated bulk concentrations c of D- and L-proline, respectively, integrated over the surface boundary at $z = 0$, and the curves at the

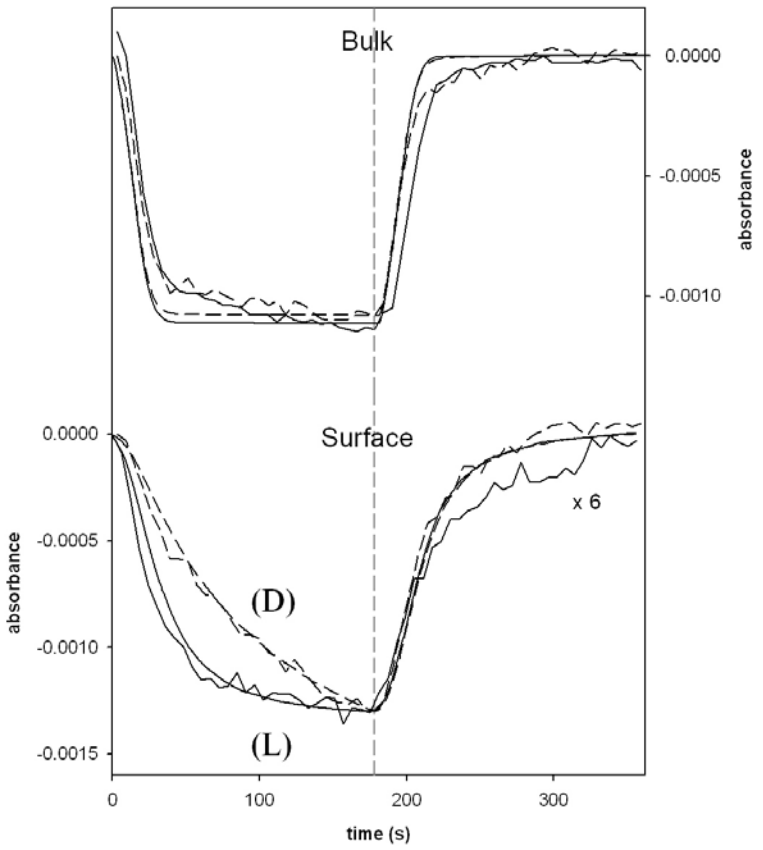

Figure B.4: Time dependence of selected ATR-IR signals obtained from "ethanol (EtOH) vs. D(L)-proline" modulation experiments. The signals on top denote bulk species whereas the signals at the bottom refer to species adsorbed on the surface (with dashed lines referring to D-proline and solid lines to L-proline). Smooth bold lines represent model outputs.

bottom represent the calculated surface concentration c_s of adsorbed D(L)-proline, integrated over the surface boundary. It is further important to notice that the bulk concentration c and the concentration c_s of adsorbed molecules were calculated during one and the same model run for one species (*i.e.* D- or L-proline).

Close inspection of the results shows discrepancies between model outputs and experiment, which are explainable by small volumes in the ATR-IR cell behind in- and outlet, where the fluid is almost stagnating [Urakawa et al., 2003]. Larger deviations are also apparent in the right lower half of Figure B.4. The corresponding signals are related to adsorption of D- and L-proline, respectively. Since the applied model assumes simple Langmuir kinetics (see Equation B.4 on page 124), the observed discrepancy may indicate a more complicated adsorption process (*e.g.* involving intermolecular interactions) that is not completely captured by the model.

Extracting the rate constants of adsorption, k_{ads}, and desorption, k_{des}, respectively, finally allows one to calculate $\Delta\Delta G^o$ of adsorption for D- and L-proline according to

$$\Delta\Delta G^o = -RT \ln \frac{K_{\mathrm{D}}}{K_{\mathrm{L}}} \tag{B.14}$$

where $K_{\mathrm{D,L}} = k_{\mathrm{ads(D,L)}}[k_{\mathrm{des(D,L)}}]^{-1}$. Evaluating Equation B.14 for $T = 298\,\mathrm{K}$ yields a $\Delta\Delta G^o \approx -5.0\,\mathrm{kJ\,mol^{-1}}$ and shows that the GSH SAM is able to discriminate between the proline enantiomers. Refer to Part III, Chapter 1 on page 81 for further detailed discussion of the results.

Appendix C

Quantitative Determination of the Orientation of an Adsorbate on a Surface Based on DFT Calculations

In this chapter a quantitative method is presented that allows one to estimate the average orientation of molecules adsorbed on a surface. The method fully relies on density functional theory (DFT) calculations and makes use of the calculated transition dipole moments associated with each normal mode of vibration. In order to demonstrate the principle of the method, ethylene (C_2H_4) is used as an illustrative example.

C.1 Normal Mode Analysis of Ethylene

C.1.1 Group Theory Considerations

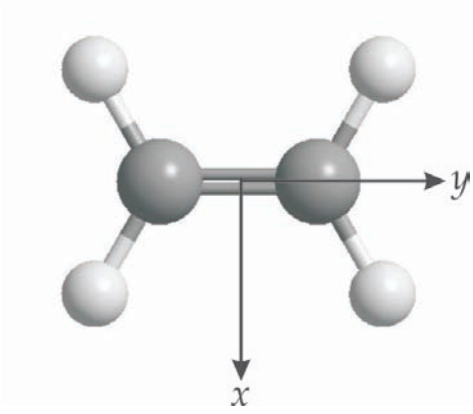

Figure C.1: Structure of ethylene and coordinate system used for group theory considerations.

Ethylene (see Figure C.1) has a symmetric structure that belongs to the $\mathscr{D}_{2h}$ point group. The molecule has $3N - 6 = 12$ normal modes of vibration. Applying group theory enables determination of the IR active vibrational modes that ultimately are

of interest here. In this section the treatment of group theory on ethylene is briefly outlined. More information can be found in Bright Wilson et al. [1980] and Cotton [1990].

For the $\mathscr{D}_{2h}$ point group, the way of assigning the subscript labels of the B-species is ambiguous. For planar $\mathscr{D}_{2h}$ molecules, the convention on symmetry notations proposed by Mulliken [1955] should be followed. However, for simplicity and to keep things consistent, the orientation shown in Figure C.1 on the previous page was used both for group theory consideration and DFT calculations (see Figure C.3 on page 135).

Table C.1 on the next page represents the character table of the $\mathscr{D}_{2h}$ point group with the elaborated reducible representation Γ_t for the 18 Cartesian displacement coordinates of ethylene.

$$a_i = \frac{1}{h} \sum_R \chi(R)\chi_i(R) \tag{C.1}$$

Equation C.1 gives an explicit expression for the number of times a_i the ith irreducible representation occurs in a reducible representation. The characters χ and χ_i of the reducible and irreducible representation, respectively, refer to the corresponding operation R and h is the order of the group. For ethylene, applying Equation C.1 gives

$$\Gamma_t = 3\mathrm{a_g} + 3\mathrm{b_{1g}} + 1\mathrm{b_{2g}} + 2\mathrm{b_{3g}} + 1\mathrm{a_u} + 2\mathrm{b_{1u}} + 3\mathrm{b_{2u}} + 3\mathrm{b_{3u}} \tag{C.2}$$

The irreducible representation Γ_{vib} for the normal modes of vibration is now easily obtained by subtracting the translational (x, y, z) and rotational (R_x, R_y, R_z) motions from Γ_t, which yields:

$$\Gamma_{\mathrm{vib}} = 3\mathrm{a_g} + 2\mathrm{b_{1g}} + 1\mathrm{b_{3g}} + 1\mathrm{a_u} + 1\mathrm{b_{1u}} + 2\mathrm{b_{2u}} + 2\mathrm{b_{3u}} \tag{C.3}$$

Inspecting Table C.1 on the next page shows that z, y and x transform as $\mathrm{b_{1u}}$, $\mathrm{b_{2u}}$ and $\mathrm{b_{3u}}$, respectively. Therefore, ethylene only has five IR active normal modes of vibration, notably:

$$\Gamma_{\mathrm{vib,IR}} = 1\mathrm{b_{1u}} + 2\mathrm{b_{2u}} + 2\mathrm{b_{3u}} \tag{C.4}$$

C.1.2 Normal Mode Analysis Based on DFT Calculations

Structure optimization and subsequent vibrational analysis was performed using the hybrid functional B3PW91 [Becke, 1993, Perdew et al., 1992] with a 6-31G basis set [Ditchfield et al., 1971]. The calculations were performed on GAUSSIAN03 [Frisch et al., 2003] and frequencies were afterward scaled by 0.95. Table C.2 on the facing page summarizes the calculated normal modes of vibration of ethylene. For simplicity, only the five IR active modes are presented. Beside the calculated frequency (in wavenumbers) and the assignment, each mode is further denoted by a label that will be used for the following discussion.

$\mathscr{D}_{\mathbf{2h}}$	E	$C_2(z)$	$C_2(y)$	$C_2(x)$	i	$\sigma(xy)$	$\sigma(xz)$	$\sigma(yz)$		
a_g	1	1	1	1	1	1	1	1		x^2, y^2, z^2
b_{1g}	1	1	−1	−1	1	1	−1	−1	R_z	xy
b_{2g}	1	−1	1	−1	1	−1	1	−1	R_y	xz
b_{3g}	1	−1	−1	1	1	−1	−1	1	R_x	yz
a_u	1	1	1	1	−1	−1	−1	−1		
b_{1u}	1	1	−1	−1	−1	−1	1	1	z	
b_{2u}	1	−1	1	−1	−1	1	−1	1	y	
b_{3u}	1	−1	−1	1	−1	1	1	−1	x	
Γ_t	18	0	−2	0	0	6	0	2		

Table C.1: The character table for the symmetry group $\mathscr{D}_{2h}$ with the characters for the representation Γ_t generated from the $3N = 18$ Cartesian displacement coordinates of ethylene.

Label	**Symmetry**	**Frequency**	**Assignment**
I.	b_{3u}	3099	$\nu_{as}(-CH)$
II.	b_{2u}	3003	$\nu_{as}(-CH)$
III.	b_{2u}	1413	$\delta(-CH_2)$ scissoring
IV.	b_{1u}	926	$\delta(-CH_2)$ wagging
V.	b_{3u}	790	$\delta(-CH_2)$ rocking

Table C.2: Calculated normal mode frequencies (given in wavenumbers /cm^{-1}) of ethylene, after scaling by 0.95.

C.2 Orientation of an Adsorbate on a Metal Surface

In the classical picture of light absorption, the intensity of a vibrational mode is given by

$$I \propto (\vec{E} \cdot \vec{\mu})^2 \tag{C.5}$$

which can be expressed as

$$I \propto |\vec{E}|^2 \cdot |\vec{\mu}|^2 \cdot \cos^2(\theta) \tag{C.6}$$

where $\vec{E}$ is the electric field vector, $\vec{\mu}$ is the transition dipole moment vector of a given normal mode of vibration and θ is the angle between the two vectors. Obviously, Equation C.6 tells that the intensity of light absorption depends on the mutual orientation of these vectors.

Equation C.6 forms the basis for orientation measurements. On a metal, shown as a deposit on the IRE in Figure C.2 on the following page, left side, the electric field is polarized perpendicular to the surface which leads to the metal surface selection rule [Greenler, 1966]. The latter states that only vibrations associated with a transition dipole moment vector component perpendicular to the surface can be observed (Figure C.2, right side). This rule is generally applied for external reflection, but its

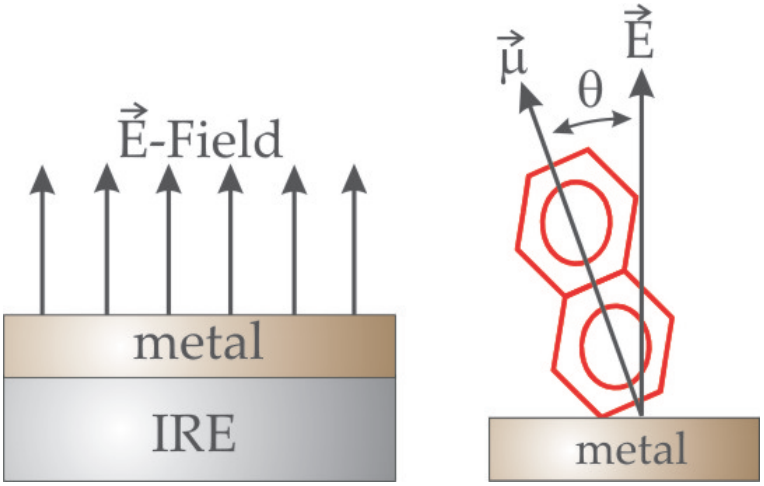

Figure C.2: On a metal, here shown as a thin deposit on the IRE, the electric field is polarized perpendicular to the surface (left picture). This leads to the metal surface selection rule [Greenler, 1966] which states that only vibrations associated with a transition dipole moment vector component perpendicular to the surface can be observed (right picture).

validity for internal reflection has been demonstrated [Hutter et al., 2003, Osawa et al., 1993].

In order to simulate the influence of orientation on the IR spectra, the transition dipole moment vector $\vec{\mu}$ for each normal mode has to be determined in the (arbitrarily defined) molecular coordinate system. For symmetric molecules (like *e.g.* ethylene) the direction of some transition dipole moment vectors can be determined by symmetry considerations [Fringeli et al., 1998, Street and Gellman, 1997]. However, for more complex and/or asymmetric molecular structures this approach fails and computational methods may turn out to be useful.

For displaying the transition dipole moment vectors for a normal mode analysis, the command `IOp(7/33=1)` has to be specified in the corresponding GAUSSIAN input file. The vectors are represented in a molecular coordinate system with the coordinate axes pointing along the principal axes of inertia of the molecule (GAUSSIAN standard orientation). In the reference orientation, the molecular coordinate system (x_m, y_m, z_m) coincides with the fixed surface coordinate system (x, y, z). The coordinate systems are depicted in Figure C.3 on the next page for the reference orientation.

To simulate the impact of different orientations on the spectra, the molecular coordinate system was allowed to rotate around the x- and y-axis, respectively, of the surface coordinate system, by defining the rotation angles α and β, respectively. A rotation around α, followed by a rotation around β, is mathematically described by the following orthogonal transformation matrix:

$$\mathbf{R}_{\alpha,\beta} = \begin{pmatrix} \cos\beta & \sin\beta\sin\alpha & \sin\beta\cos\alpha \\ 0 & \cos\alpha & -\sin\alpha \\ -\sin\beta & \cos\beta\sin\alpha & \cos\beta\cos\alpha \end{pmatrix} \tag{C.7}$$

Due to the surface selection rule for metals, only the z-component of the transition dipole moment μ_z contributes to the intensity of a vibrational band. Therefore,

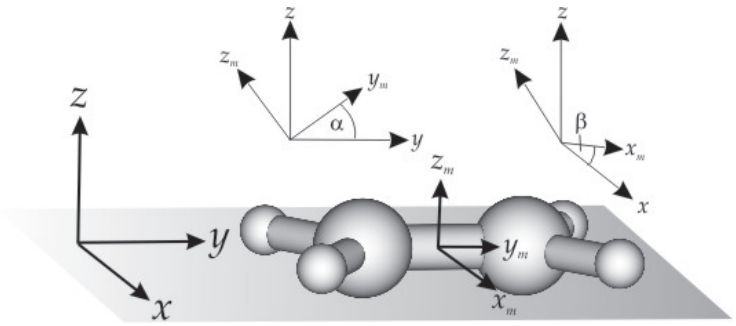

Figure C.3: Reference orientation of ethylene. The fixed surface coordinate system (x, y, z) and the molecular coordinate system given by the GAUSSIAN standard orientation and with the axes (x_m, y_m, z_m) pointing along the principal axes of inertia of the molecule, originally have the same orientation. By changing the rotation angles α and β, respectively, the molecular coordinate system is allowed to rotate around the x- and y-axis, respectively, of the surface coordinate system.

Equation C.5 on page 133 further simplifies to:

$$I \propto \mu_z^2 \tag{C.8}$$

It should be noted here that μ_z depends on the orientation of the molecular coordinate system and therefore on the rotation angles α and β, respectively.

By using a normalized Lorentzian band shape (half-width at half-maximum $\gamma = 5\,\mathrm{cm}^{-1}$), the IR spectra for different molecule orientations were calculated according to [Shinohara et al., 2004]:

$$I(\nu) = \sum_{i=1}^{N} \mu_{z,i}^2 \, \frac{\gamma}{\pi} \, \frac{1}{(\nu - \nu_{\mathrm{calc},i})^2 + \gamma^2} \tag{C.9}$$

where N is the total number of vibrational modes and $\nu_{\mathrm{calc},i}$ is the calculated frequency of mode i. The calculation of IR spectra for different orientations was finally performed using a self-made MATLAB program [The MathWorks, 1994–2006].

In order to simplify the following discussion of the spectra, the orientations of (IR active) transition dipole moments with respect to the molecular coordinate system but also the angles they define with respect to each other are summarized in Tables C.3 and C.4 on the next page.

The angle θ between two transition dipole moment vectors is calculated by using the vector dot product:

$$\cos\theta = \frac{\vec{\mu}_m \cdot \vec{\mu}_n}{|\vec{\mu}_m| \cdot |\vec{\mu}_n|} \tag{C.10}$$

where $\vec{\mu}_{m,n}$ denotes a pair of transition dipole moment vectors. Calculated angles (in degrees) are listed in Table C.4 on the following page.

Tables C.3 and C.4 show that all of the transition dipole moment vectors of ethylene are pointing along a principal axis of inertia of the molecule and hence are parallel and orthogonal, respectively, with respect to each other. Furthermore, it is evident that the DFT calculations give an accurate result for the calculated vectors in this

Label	Symmetry	Assignment	μ_x	μ_y	μ_z
I.	b_{3u}	$\nu_{as}(-CH)$	5.44	0.00	0.00
II.	b_{2u}	$\nu_{as}(-CH)$	0.01	4.31	0.00
III.	b_{2u}	$\delta(-CH_2)$ scissoring	0.00	−2.56	0.00
IV.	b_{1u}	$\delta(-CH_2)$ wagging	0.00	0.00	−9.74
V.	b_{3u}	$\delta(-CH_2)$ rocking	−1.08	0.00	0.00

Table C.3: Calculated transition dipole moment vectors (rounded to two digits after decimal point) of ethylene. The components of $\vec{\mu}$ are given with respect to the molecular coordinate system (x_m, y_m, z_m) depicted in Figure C.3 on the previous page. Note the agreement between the transformation of the modes derived by group theory and calculated components of $\vec{\mu}$ derived by DFT.

	I.	II.	III.	IV.	V.
I.	0	89.94	89.99	90.00	179.94
II.		0	179.93	90.00	90.12
III.			0	90.00	89.95
IV.				0	90.00
V.					0

Table C.4: Calculated angles in degrees (rounded to two digits after decimal point) between the five IR active transition dipole moment vectors of ethylene.

particular example with only small errors < 0.14 % (*i.e.* small deviations from 90.00 and 180.00°, respectively).

C.2.1 Discussion of Simulated IR Spectra of an Adsorbate on a Metal Surface

The effect of different orientation angles α and β on the calculated spectra is illustrated in Figure C.4 on the next page for different orientation angles α in the upper half and β in the lower half, respectively. Note that, while rotating around one orientation angle, the other was fixed at 0°. It should be noted that the transformation matrix represented by Equation C.7 on page 134 defines rotations in counterclockwise direction for positive angles α and β, respectively.

The reference orientation is the one depicted in Figure C.3 on the previous page with the corresponding angles $\alpha = \beta = 0°$. For clarity, subsequent spectra are shifted to lower wavenumbers and Roman Numbers label the IR active vibrational bands of ethylene (see also Table C.2 on page 133).

The simulated spectra for different orientation angles α in the upper half in Figure C.4 on the next page show that the bands II. and III. continuously increase in intensity with increasing α while the strong band with label IV. is disappearing for $\alpha = 90°$. Furthermore, it is also obvious that the bands I. and V. do not show up in the spectra. On the other hand, by changing the angle β the signal labeled I. and the weak band V. are appearing while the one labeled IV. again is disappearing

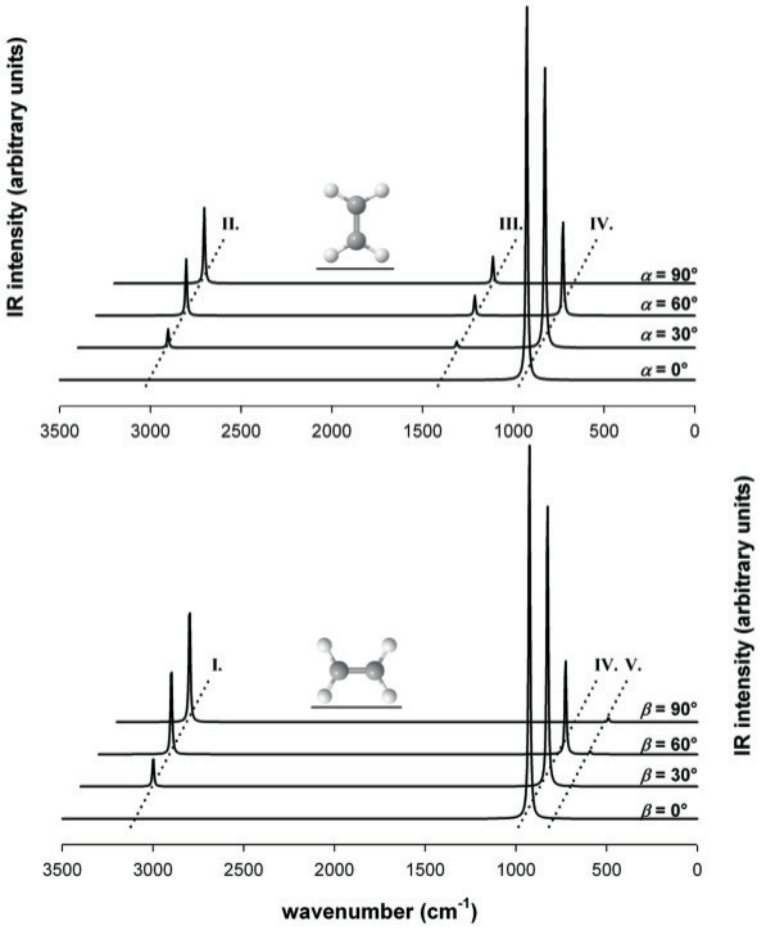

Figure C.4: Simulated IR spectra of ethylene for different orientations of the molecule with respect to the metal surface (see Figure C.3 on page 135 for the reference orientation of the molecular and fixed surface coordinate system). Rotations were performed around the x- and y-axis corresponding to the orientation angles α and β. Note that while one orientation angle was changed, the other was fixed at 0°. For clarity, subsequent spectra are shifted to lower wavenumbers and Roman Numbers denote the IR active vibrational bands as listed in Table C.2 on page 133. For $\alpha = 90°$, $\beta = 0°$ and $\alpha = 0°$, $\beta = 90°$, respectively, pictorial representations show the two orthogonal surface orientations of ethylene.

for $\beta = 90°$, which is evident by inspecting the lower part of Figure C.4.
The appearance/disappearance of the bands in the spectra in Figure C.4 is easily explained by inspecting Table C.3 on the facing page with the components of the transition dipole moment vectors, and bearing in mind that the intensity of a vibrational band of an adsorbate on a metal surface is proportional to the square of the component perpendicular to the surface (μ_z^2).

A rotation around the x-axis defined by changing the angle α leaves the x-component μ_x unchanged but alters the components μ_y and μ_z of the corresponding transition dipole moment vectors. By these arguments, only the modes labeled II., III. and IV.

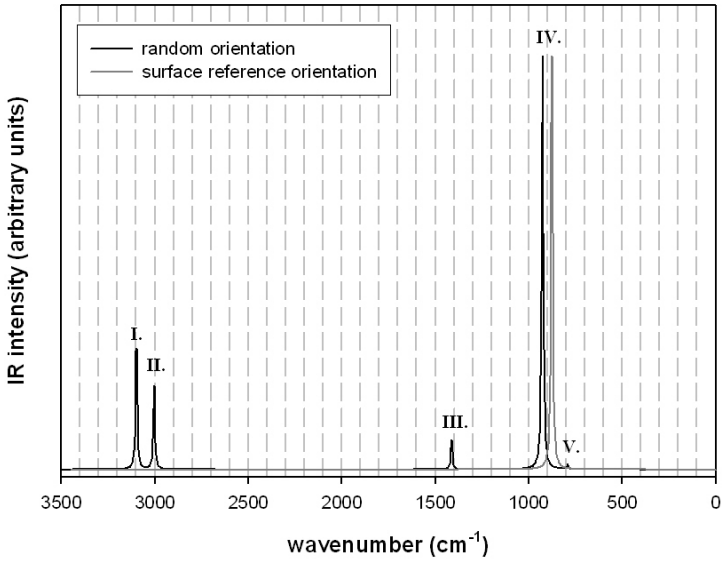

Figure C.5: Calculated IR spectra referring to random orientation and the surface reference orientation depicted in Figure C.3 on page 135. For clarity, the surface spectrum is shifted to lower wavenumbers and Roman Numbers denote the IR active vibrational bands as listed in Table C.2 on page 133.

will be affected by the rotation, as can be seen in the upper half of Figure C.4.

Analogously, based on the same arguments, a rotation around the y-axis (defined by the angle β) leaves the μ_y unchanged but affects the other components of $\vec{\mu}$. Therefore, the intensity of the modes I. IV. and V. will change by this kind of rotation, which is evident by inspecting the lower half in the figure.

However, in order to elaborate the (average) orientation of molecules within an adsorbate layer, a spectrum referring to random orientation is required. Experimentally, this is accessible by measuring a spectrum of the dissolved molecule in the liquid or in the gas phase. Theoretically, an ordinary normal mode analysis returns the calculated IR intensities for random orientation in gas phase or a more sophisticated treatment allows one to include solvent effects by using the Onsager model [Onsager, 1936], a polarizable continuum model, PCM [Cancès et al., 1997] or even more advanced methods.

An experimentally accessible parameter directly related to the orientation is the intensity ratio of two vibrational bands for random (liquid phase) and surface orientation, as expressed by the following equation [Street and Gellman, 1997, 1996]:

$$R_{\text{exp}} = \frac{(I_m^s / I_n^s)}{(I_m^r / I_n^r)} \tag{C.11}$$

where $I_{m,n}$ denotes the measured integrated intensity of vibrational bands m and n, respectively, and the superscripts s and r, respectively, refer to surface and randomly oriented (dissolved) species, respectively. The determination of the orientation finally relies on the comparison between experimental and calculated R-values. The goal is

to find a corresponding quantity R_{calc}, analogously defined as R_{exp} in Equation C.11, for the calculated IR spectra for random and surface orientation by using the angles α and β as tunable parameters.

Figure C.5 on the preceding page shows calculated spectra of ethylene for random orientation and the surface reference orientation depicted in Figure C.3 on page 135. An equivalent experimental spectrum would ultimately lead to the conclusion that the molecule is adsorbed on the surface in the mode shown in Figure C.3 since the surface spectrum only shows the vibrational band with an associated pure z-component of $\vec{\mu}$.

C.3 Orientation of an Adsorbate on a Surface Using Polarized Light

C.3.1 Light Absorption and Dichroic Ratio

In order to quantitatively derive the orientation of molecules within an adsorbate layer on a non-metallic surface, polarized light has to be used for ATR-IR experiments. Figure C.6 shows the definition of the coordinate system fixed to the internal reflection element (IRE). According to this coordinate system, parallel polarized incident light (pp) results in the x- and z-components of the electric field of the evanescent wave (E_x and E_z), while perpendicular (vertical) polarized light (vp) produces the y-component (E_y).

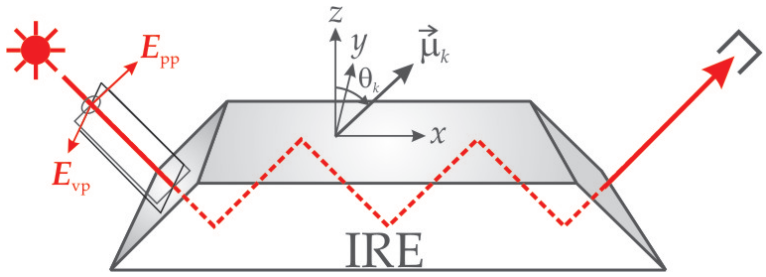

Figure C.6: ATR setup with the IRE-fixed coordinate system. E_{pp} and E_{vp} denote the parallel and perpendicular polarized components of the light incident to the IRE. E_{pp} results in the E_x- and E_z-components of the evanescent field, while E_{vp} results in the E_y-component. $\vec{\mu}_k$ denotes the transition dipole moment vector of the kth vibrational mode within a molecule and θ_k is the tilt angle between $\vec{\mu}_k$ and the z-axis of the IRE coordinate system.

In most optical orientation measurements the dichroic ratio R_k, defined by Equation C.12, is used as the relevant parameter

$$R_k = \frac{\langle A_{k,\,\text{pp}} \rangle}{\langle A_{k,\,\text{vp}} \rangle} \tag{C.12}$$

where $A_{k,\text{pp}}$ and $A_{k,\text{vp}}$ are the integrated absorbances of a given band for parallel and perpendicular polarized incident light, respectively.

For uniaxial alignment, *i.e.* for isotropic arrangement of molecules around the z-axis (surface normal) the dichroic ratio R_k can further be expressed as [Fringeli et al., 2001, 1998, Fringeli, 1992]:

$$R_k = \frac{\langle A_{k,\,\mathrm{pp}}\rangle}{\langle A_{k,\,\mathrm{vp}}\rangle} = \frac{E_x^2}{E_y^2} + 2\,\frac{E_z^2}{E_y^2}\,\frac{\langle\overline{\cos^2\theta_k}\rangle}{1-\langle\overline{\cos^2\theta_k}\rangle} \tag{C.13}$$

where θ_k denotes the tilt angle between the direction of the transition moment and the z-axis (see Figure C.6).
Solving Equation C.13 for $\langle\overline{\cos^2\theta_k}\rangle$ yields

$$\langle\overline{\cos^2\theta_k}\rangle = \frac{E_x^2 - \langle R_k\rangle\cdot E_y^2}{E_x^2 - \langle R_k\rangle\cdot E_y^2 - 2E_z^2} \tag{C.14}$$

C.3.2 Simulation of ATR-IR Spectra for Parallel and Perpendicular Polarized Light Using DFT Calculations

As stated in Section C.2 on page 133, normal mode analysis based on DFT calculations yields the transition dipole moment vectors for each normal mode of vibration and the latter are represented in the molecular coordinate system given by the GAUSSIAN standard orientation. Therefore, all the prerequisites are met to simulate the intensities of vibrational bands of an adsorbate for parallel and perpendicular polarized light, accounting for different orientations of the molecule on the surface.

The basic relation for orientation measurements, Equation C.5 on page 133, reads for parallel (pp) and perpendicular (vp) polarized light as follows:

$$I_{\mathrm{pp}} \propto (E_x\cdot\mu_x + E_z\cdot\mu_z)^2, \quad \text{and} \quad I_{\mathrm{vp}} \propto (E_y\cdot\mu_y)^2 \tag{C.15}$$

The transition moment components in Equation C.15 depend on the orientation of the molecular coordinate system with respect to the fixed surface coordinate system. That is, the set of transition moment vectors is first transformed by the orthogonal matrix given by Equation C.7 on page 134 by specifying the angles α and β accordingly.

Uniaxial alignment, *i.e.* isotropic arrangement of molecules around the z-axis is then numerically performed by a complete rotation of the set of transition moment vectors around the z-axis according to the following transformation matrix:

$$\mathbf{R}_\gamma = \begin{pmatrix} \cos\gamma & -\sin\gamma & 0 \\ \sin\gamma & \cos\gamma & 0 \\ 0 & 0 & 1 \end{pmatrix} \tag{C.16}$$

where the rotation angle γ runs from 0 to 360° in steps of less than 0.01° to produce accurate numerical results.

The components of the transition moments are then projected onto the electric field vectors for parallel and perpendicular polarization, respectively, and the intensities represented by Equation C.15 are averaged for a complete rotation around the z-axis. The relative electric field components E_x, E_y and E_z of the evanescent are calculated according to the Fresnel's equations [Born and Wolf, 1979, Harrick, 1967].

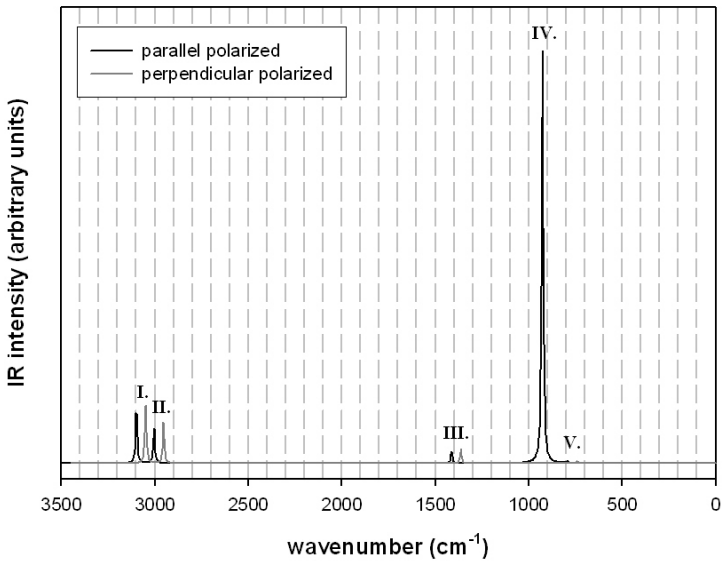

Figure C.7: Calculated ATR-IR spectra referring to the surface reference orientation depicted in Figure C.3 on page 135. The spectrum for parallel polarization is depicted as black trace and the one for perpendicular polarization as grey trace. For clarity, the spectrum for perpendicular polarized light is shifted to lower wavenumbers and Roman Numbers denote the IR active vibrational bands as listed in Table C.2 on page 133.

The components depend on the angle of incidence of the light, the optical constants of the internal reflection element (n_1), the adsorbate film (n_2) and the bulk medium (n_3).

An example of a calculated ATR-IR spectrum for parallel and perpendicular polarized light is given for ethylene in the reference orientation depicted in Figure C.3 on page 135 (refer to Subsection C.1.2 on page 132 for the discussion of vibrational modes of ethylene). The calculated ATR-IR spectra are depicted in Figure C.7 for parallel (black trace) and perpendicular (grey trace) polarized light. Numerical values for the optical constants were taken as $n_1 = 4.0$, $n_2 = 1.45$ and $n_3 = 1.41$ and the angle of incidence was assumed to be 45°. According to the Fresnel's equations the relative electric field components are calculated as $E_x = 1.40$, $E_y = 1.51$ and $E_z = 1.53$. Furthermore, the five IR active modes of ethylene are labeled with Roman Numbers (see Table C.2 on page 133).

As expected, all of the modes (besides the one labeled IV.) having a transition dipole moment component either in x- or y-direction show up in the spectra for parallel and perpendicular polarization. Furthermore, the intensities are slightly increased for perpendicular polarization since the related field component E_y is slightly larger than the E_x-component.

The mode IV. with a pure z-component of the transition moment consistently does not appear in the calculated ATR-IR spectrum (for the reference orientation) for perpendicular polarized light.

C.4 Conclusions

In this chapter, a novel approach, fully based on DFT calculations was presented that allows one to quantitatively determine the orientation of an adsorbate on a surface by simulating the ATR-IR spectra. This approach may be particularly useful in cases of rather complex and/or asymmetric molecular structures where *e.g.* symmetry considerations fail to derive the orientation of the transition moments. For example, the method was successfully applied in order to estimate the orientation of *N*-acetyl-L-cysteine adsorbed on a gold surface [Bieri and Bürgi, 2005b, see also Part II, Chapter 3 on page 55].

However, this chapter is concluded by also stating the limitations of the method. First of all, it has to be noted that ATR-IR spectroscopy gives, due to the nature of the technique, no spatial information of the interface probed. In case of the investigation of an adsorbate layer on a surface this means that recorded spectra refer to the *average* orientation of the molecules on the surface, *i.e.* the method cannot distinguish between sites (like *e.g.* islands) of different orientation. A similar problem occurs when the (same) molecule exists in different ionic forms on the surface and the observed spectrum is a superposition of two or multiple phases.

Furthermore, the described analysis assumes that the magnitudes of the transition dipole moment vectors $\vec{\mu}$ are the same in solution and in the adsorbate layer. In other words, the conformation of the molecule in solution and adsorbed on the surface should be virtually the same, which implies that molecule–surface interaction is negligible. This may be experimentally verified by inspecting the positions of prominent vibrational bands, since conformational changes result in significant band shifts.

A promising way to estimate the orientation of adsorbed molecules is to take account of experimental spectra recorded at the beginning of adsorption and self-assembly, respectively, since intermolecular interactions are supposed to have a negligible effect on the molecular structure at low surface coverage. In addition, a rather rigid part or group within the molecule (like *e.g.* the amide group in case of *N*-acetyl-L-cysteine) may be used as a pointer for the orientation analysis.

References

A. D. Becke. Density-functional Thermochemistry. III. The Role of Exact Exchange. *J. Chem. Phys.*, 98(7):5648–5652, 1993.

M. Bieri and T. Bürgi. Probing Enantiospecific Interactions between Proline and an L-Glutathione Self-Assembled Monolayer by Modulation Excitation ATR-IR Spectroscopy. *J. Phys. Chem. B*, 109(20):10243–10250, 2005a.

M. Bieri and T. Bürgi. Adsorption Kinetics, Orientation and Self-Assembling of *N*-Acetyl-L-cysteine on Gold: A Combined ATR-IR, PM-IRRAS and QCM Study. *J. Phys. Chem. B*, 109(47):22476–22485, 2005b.

R. B. Bird, W. E. Stewart, and E. N. Lightfoot. *Transport Phenomena.* John Wiley & Sons, New York, 1960.

M. Born and E. Wolf. *Principles of Optics.* Pergamon, 3rd edition, 1979.

E. Bright Wilson, J. C. Decius, and P. C. Cross. *Molecular Vibrations.* Dover Publications, Inc., 1980.

M. T. Cancès, B. Mennucci, and J. Tomasi. A New Integral Equation Formalism for the Polarizable Continuum Model: Theoretical Background and Applications to Isotropic and Anisotropic Dielectrics. *J. Chem. Phys.*, 107(8):3032–3041, 1997.

COMSOL. COMSOL Multiphysics, 1994–2006.

F. A. Cotton. *Chemical Applications of Group Theory, 3rd edition.* John Wiley & Sons, 1990.

R. Ditchfield, W. J. Hehre, and J. A. Pople. Self-Consistent Molecular-Orbital Methods. IX. Extended Gaussian-Type Basis for Molecular-Orbital Studies of Organic Molecules. *J. Chem. Phys.*, 54(2):724–728, 1971.

U. P. Fringeli. In Situ Infrared Attenuated Total Reflection Membrane Spectroscopy. In F. Mirabella, editor, *Internal Reflection Spectroscopy: Theory and Applications*, pages 255–324. Marcel Dekker Inc., New York, 1992.

U. P. Fringeli, J. Goette, G. Reiter, M. Siam, and D. Baurecht. Structural Investigations of Oriented Membrane Assemblies by FTIR-ATR Spectroscopy. In J. A. deHaseth, editor, *AIP Conference Proceedings, 430(Fourier Transform Spectroscopy).* Am. Inst. of Phys., 1998.

U. P. Fringeli, D. Baurecht, M. Siam, G. Reiter, M. Schwarzott, T. Bürgi, and P. Brüesch. ATR Spectroscopy of Thin Films. In H. S. Nalwa, editor, *Handbook of Thin Film Materials*, volume 2, pages 191–229. Academic Press, New York, 2001.

M. J. Frisch, G. W. Trucks, H. B. Schlegel, G. E. Scuseria, M. A. Robb, J. R. Cheeseman, J. A. Montgomery, T. Vreven, K. N. Kudin, J. C. Burant, J. M. Millam, S. S. Iyengar, J. Tomasi, V. Barone, B. Mennucci, M. Cossi, G. Scalmani, N. Rega, G. A. Petersson, H. Nakatsuji, M. Hada, M. Ehara, K. Toyota, R. Fukuda, J. Hasegawa, H. Ishida, T. Nakajima, Y. Honda, O. Kitao, H. Nakai, M. Klene, X. Li, J. E. Knox, H. P. Hratchian, J. B. Cross, C. Adamo, J. Jaramillo, R. Gomperts, R. E. Stratmann, O. Yazyev, A. J. Austin, R. Cammi, C. Pomelli, J. Ochterski, P. Y. Ayala, K. Morokuma, G. A. Voth, P. Salvador, J. J. Dannenberg, V. G. Zakrzewski, S. Dapprich, A. D. Daniels, M. C. Strain, O. Farkas, D. K. Malick, A. D. Rabuck, K. Raghavachari, J. B. Foresman, J. V. Ortiz, Q. Cui, A. G. Baboul, S. Clifford, J. Cioslowski, B. B. Stefanov, G. Liu, A. Liashenko, P. Piskorz, I. Komaromi, R. L. Martin, D. J. Fox, T. Keith, M. A. Al-Laham, C. Y. Peng, A. Nanayakkara, M. Challacombe, P. M. W. Gill, B. Johnson, W. Chen, M. W. Wong, C. Gonzalez, and J. A. Pople. *GAUSSIAN03*, Rev. D.01, 2003.

R. G. Greenler. Infrared Study of Adsorbed Molecules on Metal Surfaces by Reflection Techniques. *J. Chem. Phys.*, 44(1):310–315, 1966.

N. J. Harrick. *Internal Reflection Spectroscopy.* Interscience Publishers, New York, 1967.

E. Hutter, K. A. Assiongbon, J. H. Fendler, and D. Roy. Fourier Transform Infrared Spectroscopy Using Polarization Modulation and Polarization Selective Techniques for Internal and External Reflection Geometries: Investigation of Self-Assembled Octadecylmercaptan on a Thin Gold Film. *J. Phys. Chem. B*, 107(31):7812–7819, 2003.

I. Langmuir. The Adsorption of Gases on Plane Surfaces of Glass, Mica and Platinum. *J. Am. Chem. Soc.*, 40:1361–1402, 1918.

R. S. Mulliken. Report on Notation for the Spectra of Polyatomic Molecules. *J. Chem. Phys.*, 23:1997, 1955.

L. Onsager. Electric Moments of Molecules in Liquids. *J. Am. Chem. Soc.*, 58:1486–1493, 1936.

M. Osawa, K.-I. Ataka, K. Yoshii, and T. Yotsuyanagi. Surface-Enhanced Infrared ATR Spectroscopy for in Situ Studies of Electrode/Electrolyte Interfaces. *J. El. Spectr. Rel. Phenom.*, 64/65:371–379, 1993.

J. P. Perdew, J. A. Chevary, S. H. Vosko, K. A. Jackson, M. R. Pederson, D. J. Singh, and C. Fiolhais. Atoms, Molecules, Solids, and Surfaces: Applications of the Generalized Gradient Approximation for Exchange and Correlation. *Phys. Rev. B*, 46(11):6671–6687, 1992.

K. A. Peterlinz and R. Georgiadis. In Situ Kinetics of Self-Assembly by Surface Plasmon Resonance Spectroscopy. *Langmuir*, 12(20):4731–4740, 1996.

J. R. Rahn and R. B. Hallock. Antibody Binding to Antigen-Coated Substrates Studied with Surface Plasmon Oscillations. *Langmuir*, 11:650–654, 1995.

R. A. Robinson and R. H. Stokes. *Electrolyte Solutions, 2nd Edition.* Butterworths, Washington, D.C., 1965.

H. Shinohara, T. Kasahara, K. Kadokura, Y. Uryu, and K. Itoh. Infrared Reflection Absorption Spectroscopic Study on the Rotational Isomerism of Methyl Propyl Ether on Cu(110) and Ag(110). *J. Phys. Chem. B*, 108:3584–3591, 2004.

S. C. Street and A. J. Gellman. Quantitative Adsorbate Orientation from Vibrational Spectra: Ethoxides on Cu(111). *J. Chem. Phys.*, 105(16):7158–7170, 1996.

S. C. Street and A. J. Gellman. Orientation of Physisorbed Fluoropropenes on Cu(111). *J. Phys. Chem. B*, 101:1389–1395, 1997.

The MathWorks. *MATLAB*, 1994–2006.

A. Urakawa, R. Wirz, T. Bürgi, and A. Baiker. ATR-IR Flow-Through Cell for Concentration Modulation Excitation Spectroscopy: Diffusion Experiments and Simulations. *J. Phys. Chem. B*, 107(47):13061–13068, 2003.

W. B. J. Zimmerman. *Process Modeling and Simulation with Finite Element Methods.* World Scientific, 2004.

Acknowledgement

Many Thanks to ...

... Prof. Thomas Bürgi for giving me the chance to work in a very interesting interdisciplinary field of research. I am grateful for his advice and many interesting and fruitful discussions that stimulated my work. I am further grateful for the freedom Thomas offered me during the PhD and the chance for attending various international conferences and workshops.

... Silvia Angeloni-Suter, Natallia Shalkevich, Dr. Qiaoling Li, Cyrille Gautier, Igor Dolamic and Julien Boudon for the agreeable working atmosphere. I thank Cyrille for his patience and assistance in chemistry problems. Thanks to Julien for developing and maintaining the nice group website.

... Prof. Fritz Stoeckli for providing laboratory facilities with stable environment for quartz crystal microbalance analyses.

... the Swiss Center for Electronics and Microtechnology (CSEM) in Neuchâtel for using sputtering facilities. Many thanks to Mireille Leboeuf and Dr. Massoud Dadras for advice and assistance in AFM and STM measurements.

... Dr. Deborah Gonzalez Mantero and Alejandro Castillejo for the many funny and non-scientific conversations.

... the secretary staff of the Department of Chemistry/Microtechnology for the help in administrative problems and Philippe Stauffer and André Floreano for help in technical problems.

... the Swiss National Supercomputing Centre (CSCS) for grants of computing time and the Swiss National Science Foundation for financial support.

... Dipl. Ing. ETH Marcel Perrinjaquet for his knowledge in data management and for printing many conference posters.

... Nicole for her love, friendship and support over the last years.

... my parents for their generous and endless support during my education and for supporting me throughout my life.

List of Publications

Articles Published in Reviewed Journals

T. Bürgi and M. Bieri. Time-Resolved *In Situ* ATR Spectroscopy of 2-Propanol Oxidation over Pd/Al_2O_3: Evidence for 2-Propoxide Intermediate. *J. Phys. Chem. B*, 108(35):13364–13369, 2004.

M. Bieri and T. Bürgi. L-Glutathione Chemisorption on Gold and Acid/Base Induced Structural Changes: A PM-IRRAS and Time-Resolved *In Situ* ATR-IR Spectroscopic Study. *Langmuir*, 21(4):1354–1363, 2005.

M. Bieri and T. Bürgi. Probing Enantiospecific Interactions between Proline and an L-Glutathione Self-Assembled Monolayer by Modulation Excitation ATR-IR Spectroscopy. *J. Phys. Chem. B*, 109(20):10243–10250, 2005.

M. Bieri and T. Bürgi. Adsorption Kinetics, Orientation and Self-Assembling of *N*-Acetyl-L-cysteine on Gold: A Combined ATR-IR, PM-IRRAS and QCM Study. *J. Phys. Chem. B*, 109(47):22476–22485, 2005.

M. Bieri and T. Bürgi. Adsorption Kinetics of L-Glutathione on Gold and Structural Changes during Self-Assembly: An *In Situ* ATR-IR and QCM Study. *Phys. Chem. Chem. Phys.*, 8(4):513–520, 2006. ***Paper highlighted as issue cover***.

M. Bieri and T. Bürgi. Enantiodiscrimination between an *N*-Acetyl-L-cysteine SAM and Proline: An *In Situ* Spectroscopic and Computational Study. *ChemPhysChem*, 7(2):514–523, 2006.

M. Bieri and T. Bürgi. D-Penicillamine Adsorption on Gold: An *In Situ* ATR-IR Spectroscopic and QCM Study. *Langmuir*, 22(20):8379–8386, 2006.

C. Gautier, M. Bieri, I. Dolamic, S. Angeloni, J. Boudon and T. Bürgi. Probing Chiral Nanoparticles and Surfaces by Infrared Spectroscopy. *Chimia*, 60(11):777–782, 2006. Invited article.

M. Bieri, C. Gautier and T. Bürgi. Probing Chiral Interfaces by Infrared Spectroscopic Methods. *Phys. Chem. Chem. Phys.*, 9(6):671–685, 2007. Invited article.

M. Bieri and T. Bürgi. What can Group Theory and Computational Methods tell about the IR Spectrum of an Adsorbate on a Metal Surface? *J. Chem. Educ.*, submitted for publication.

Conference Abstracts

M. Bieri and T. Bürgi. Quantitative Assessment of the Difference in Free Standard Energy of Reaction ($\Delta\Delta G^O$) between two Enantiomers of a Chiral Molecule and a Chiral Surface Using a Convection–Diffusion Model Coupled to Surface Reactions. COMSOL Multiphysics Conference, Paris, 2005.

M. Bieri and T. Bürgi. *In Situ* ATR-IR Modulation Excitation Spectroscopy: A Powerful Tool to Investigate the Properties of Chiral Self-Assembled Monolayers at Solid–Liquid Interfaces. European Conference on Surface Science, ECOSS24, Paris, 2006.

Curriculum Vitæ

Marco Bieri, born September 6th, 1975, in Bern, Switzerland.

Education

1982–1986	Primary School, Kehrsatz.
1986–1991	Secondary School, Kehrsatz.
1991–1995	Gymnasium Köniz, Matura Type C (University Entrance Exam).
1996–2001	Studies in Physics at University of Bern, Switzerland. Minor subjects: Mathematics and Geography.
06/2001	Diploma (M.Sc.) in Physics, Climate and Environmental Physics, University of Bern, Switzerland. Thesis Advisors: Prof. B. Stauffer and Prof. T. F. Stocker.
2003–2007	PhD Study in Physical Chemistry, University of Neuchâtel, Switzerland. Thesis Advisor: Prof. T. Bürgi.

Professional

2000–2001	Assistant in Operational Weather Forecast, METEOTEST Bern, Switzerland.
2001–2003	Research Associate at the Division of Length and Optics, Swiss Federal Office of Metrology and Accreditation (METAS), Switzerland.
2003–2007	Teaching Assistant in Physical Chemistry for Second and Third Year Students in Standard and Advanced Practical Classes.

Conferences and Workshops

06/2003	American Society for Precision Engineering (ASPE) Summer Topical Meeting on Coordinate Measuring Machines, UNC Charlotte, NC, USA. *Oral Presentation.*
12/2003	Workshop on Application of Special Techniques in FT-IR ATR Spectroscopy, University of Vienna, Austria (Prof. U. P. Fringeli).

Conferences and Workshops (*continued*)

04/2004	Comsol Multiphysics Modeling Course, Grenoble, France.
09/2005	Swiss National Supercomputing Centre (CSCS) User Day, Manno, Switzerland. *Poster Presentation.*
10/2005	Swiss Chemical Society (SCS) Fall Meeting, Lausanne, Switzerland. *Poster Presentation.*
11/2005	Comsol Multiphysics Conference 2005, Paris, France. *Oral Presentation.*
09/2006	European Conference on Surface Science (Ecoss24), Paris, France. *Oral Presentation.*
09/2006	Summer School on Computational Quantum Dynamics in Chemistry, Swiss National Supercomputing Centre (CSCS), Manno, Switzerland.
10/2006	Swiss Chemical Society (SCS) Fall Meeting, Zurich, Switzerland. *Poster Presentation.*
10/2006	Empa PhD-Symposium 2006, St. Gallen, Switzerland. *Poster Presentation.*
01/2007	Swiss User Group Surfaces and Interfaces (SAOG), 23$^{\text{rd}}$ Annual Meeting, Fribourg, Switzerland.

Fireworks Ended, Spectators Gone Away . . .
Ah, How Vast and Dark!

Masaoka Tsunenori Shiki (1867–1902)